CONFINED ACOUSTIC PHONONS IN SI NANOMEMBRANES: IMPACT ON THERMAL PROPERTIES

Emigdio Chávez Ángel

M.Sc. Physics

Tesi Doctoral
Programa de Doctorat en Física

Thesis Director: Prof. Dr. Clivia M. Sotomayor Torres

Supervisor: Prof. Dr. Jordi Mompart

Departament de Física

Facultat de Ciències

Research supported by the
Comisión Nacional Científica y Tecnológica de Chile (CONICYT)

2014

…"Gobernar es educar"…
Pedro Aguirre Cerda,
Presidente de Chile, 1938-1944

…"La educación es un bien de consumo"…
Sebastián Piñera Echenique,
Presidente de Chile 2010-2014

…"Vamos a invertir primero en educación, segundo en educación, tercero en educación.
Un pueblo educado tiene las mejores opciones en la vida y es muy difícil que lo engañen los corruptos y mentirosos"…
José Mujica Cordano,
Presidente de Uruguay, 2010-2015

Antes de votar: lea, mire, y juzgue

A mi Madre

ACKNOWLEDGMENTS

The author expresses his gratitude to the Chilean government for a research fellowship through the Comisión Nacional Científica y Tecnológica de Chile, CONICYT, Becas Chile 2010. Additionally, the author acknowledge the financial support from the FP7 projects NANOFUNCTION (grant nr. 257375), NANOPOWER (grant nr. 256 959) and MERGING (grant nr. 309150), as well as the Spanish MINECO projects nanoTHERM (grant nr. CSD2010-0044), ACPHIN (FIS2009-10150) and TAPHOR (MAT2012-31392).

First of all, I would like to express my deepest gratitude to my thesis director Prof. Dr Clivia M. Sotomayor Torres and all my colleagues in the Phononic and Photonic Nanostructures group, P2N, at the Catalan Institute of Nanoscience and nanotechnology, ICN2, especially to Dr. Francesc Alzina, Dr Juan Sebastian Reparaz and Dr Jordi Gomis Bresco for their great contribution of the development of this work. Also, I would like to thank to Dr John Cuffe from Massachusetts Institute of Technology, MIT, for providing helpful discussions during the development of this work.

I would like to thanks to our collaborators from Technical Research Centre of Finland, VTT, Dr Andrey Shchepetov, Dr Mika Prunnila, and Prof. Dr Jouni Ahopelto for providing silicon membranes.

I would like to thanks Dr Thomas Dekorsy and his group from University of Konstanz, Konstanz, Germany for the measurement of phonon lifetime accepting me for two stay abroad in his group.

I would like to thank to Prof. Dr Bahram Djafari-Rouhani from the Institut d'Electronique, de Microélectronique et de Nanotechnologie (IEMN), Lille, France, and Prof. Dr El Houssaine El Boudouti from the Institut d'Electronique, de Microélectronique et de Nanotechnologie

(IEMN), Lille, France, and the LDOM, Faculté des Sciences, Université Mohamed I, Oujda, Morocco, for their contributions to the understanding of the dispersion relation in phononic crystals and the development of the PWE method.

I would like to thank to Prof. Dr. Gang Chen, Prof. Dr. Keith Nelson, Dr. John Cuffe and Mr. Jeffrey Eliason from Massachusetts Institute of Technology (MIT) for the measurements of thermal diffusivity using the Transient Thermal Gradient method.

I would like to thank all my friends and colleagues from ICN2 especially to Dr Francesc Alzina, Dr Claudia Simão, Dr Erwan Guillotel, MsC Noèlia Arias, Dr Jordi Gomis-Bresco, Dr. Markus Raphael Wagner, Dr Bartlomiej Graczykowski, Dr Juan Sebastian Reparaz, Dr Juan Sierra, Dr Nikolaos Kehagias and Ms Sweta Bhansali for their great contribution to my scientific and social life. In particular, I would like to thank Jordi, whose ability to create new devices, equipment, experimental methods etc. is inspiriting. Especial acknowledge to Noèlia and Erwan for their indispensable work for the scientific development of group. El meu més profund agraïment a Francesc per proporcionar les fructíferes discussions científiques i també per tota l'ajuda brindada durant el desenvolupament d'aquest treball.

I am also grateful to Clivia for providing me this great opportunity to work in Europe. Without her, nothing of the work developed in this thesis would have been possible.

Finalmente quisiera agradecer a mi familia, especialmente a mi madre, Delcira Ángel, quien a pesar de todas las penurias pasadas nunca se cansó de decirme “estudia”, la educación es el bien más preciado que te puedo dejar. Por eso y muchas cosas más siempre estaré agradecido de mi vieja. Of course, my sincere thanks to Alexandra, who arrived in my darkest hours to put meaning to silence and mute to my fatigue.

Y como diría el Gran Gustavo Cerati,

Gracias totales…

ABSTRACT

The miniaturization trend of the technology has led to power level densities in excess 100 watts/cm^2, which are in the order of the heat produced in a nuclear reactor. The need for new cooling techniques has positioned the thermal management on the stage the last years. Moreover, the engineering of the thermal conduction opens a route to energy harvesting through, for example, thermoelectric generation. As a consequence, control and engineering of phonons in the nanoscale is essential for tuning desirable physical properties in a device in the quest to find a suitable compromise between performance and power consumption.

In the present work we study theoretically and experimentally the thickness-dependence of the thermal properties of silicon membranes with thicknesses ranging from 9 to 2000 nm. We investigate the dispersion relations and the corresponding modification of the phase velocities of the acoustic modes using inelastic Brillouin light scattering spectroscopy. A reduction of the phase/group velocities of the fundamental flexural mode by more than one order of magnitude compared to bulk values was observed and is theoretically explained. In addition, the lifetime of the coherent acoustic phonon modes with frequencies up to 500 GHz was also studied using state-of-the-art ultrafast pump-probe: asynchronous optical sampling (ASOPS). We have observed that the lifetime of the first-order dilatational mode decreases significantly from ~ 4.7 ns to 5 ps with decreasing membrane thickness from ~ 194 to 8 nm. Finally, the thermal conductivity of membranes was investigated using three different contactless techniques known as single-laser Raman thermometry, two-laser Raman thermometry and transient thermal gradient. We have found that the thermal conductivity of the membranes gradually reduces with their thickness, reaching values as low as 9 Wm^{-1}K^{-1} for the thinnest membrane.

In order to account for the observed thermal behaviour of the silicon membranes we have developed different theoretical approaches to explain the size dependence of thermal properties.

The simulation of acoustic dispersion was carried out by using models based on an elastic continuum approach, Debye and fitting approaches. The size dependence of the lifetimes was modelled considering intrinsic phonon-phonon processes and extrinsic phonon scatterings. The thermal conductivity was modelled using a modified 2D Debye approach (Huang model), Srivastava-Callaway-Debye model and Fuchs-Sondheimer approach.

Our observations have significant consequences for Si-based technology, establishing the foundation to investigate the thermal properties in others low-dimensional systems. In addition, this study would provide design guidelines and enable new approaches for thermal management at nanometric scales.

TABLE OF CONTENTS

Acknowledgments....i

Abstract....v

Table of contents....vii

List of figures....xiii

List of tables....xxiii

List of publications and presentations....xxv

Published and accepted articles....xxv

Non-related articles....xxvii

Book chapters....xxvii

In preparation articles....xxviii

Oral Presentations....xxviii

List of acronyms....xxxi

Chapter I: Introduction and Objectives....1

1.1 Nanoscale thermal conductivity....3

1.2 Phonon confinement....8

1.4 Thesis Outline....10

Chapter II: Acoustic Waves....11

2.1 Elastic continuum model....11

2.1.1 Boundary conditions and confined waves....13

Lamb waves 15

Symmetric and antisymmetric modes 16

Shear Waves 21

2.1.2 Layered systems 22

From one layer to N layers 23

Example 24

Chapter III: Anharmonicity and Thermal Conductivity 27

3.1 Harmonic effect in crystals 27

3.2 Phonon-phonon interaction 28

3.2.1 Normal and Umklapp process 31

Selection Rules: Normal and Umklapp processes. 34

3.3 Phonon lifetime: relaxation time approximation 35

3.3 Evaluation of phonon relaxation times 37

3.3.1 Extrinsic relaxation times 38

Boundary scattering 38

Impurity scattering 40

3.3.2 Intrinsic relaxation times 41

Phonon density of states 44

Einstein and Debye approximations 45

3.4.3 Phonon-phonon interaction and the Debye approximation 47

Numerical simulations 52

Bulk Umklapp-processes 52

Intrinsic sound absorption: Akhieser and Landau-Rumer mechanisms 57

3.4 Thermal conductivity: modelling and approximations 58

3.4.1 Specific heat capacity 60

3.4.2 Thermal conductivity in low dimensional systems 61

Modified Debye-Callaway-Srivastava model: complete phonon-phonon scheme 61

Fuchs-Sondheimer model: correction of the thermal conductivity expression 63

Huang model: modified dispersion relation and correction of the thermal conductivity expression 64

3.5 Phonon confinement and modification of specific heat capacity 68

3.5.1 Modification of the specific heat capacity 68

3.6 Use of modified dispersion relation: defining criteria 72

Chapter IV: Fabrication and Experimental Techniques 74

4.1 Fabrication of ultrathin freestanding silicon membranes 74

4.2 Advanced methods of characterizing phonon dispersion, lifetimes and thermal conductivity 76

4.2.1 Brillouin scattering 76

4.2.2 Pump-and-probe ultrafast spectroscopy. 82

Generation and detection of high-frequency phonons 82

Asynchronous Optical Sampling: ASOPS 84

4.2.3 Raman Thermometry 86

Single Laser Raman Thermometry: 1LRT 87

Measurement of the absorbed power 91

Measurement of the temperature field by two-laser Raman thermometry: 2LRT 92

4.2.4 Transient thermal grating (TTG) 94

Chapter V: Modelling and Experimental Results 99

5.1 Acoustic phonons dispersion relation in ultrathin silicon membranes 99

5.1.1 Flexural mode dispersion 100

5.2 Phonon lifetime: measurements and simulations. 102

5.2.1 Lifetimes of Confined Acoustic Phonons in Ultrathin Silicon Membranes 103

5.2.2 Phonon lifetime: theoretical results 105

5.3 Thermal conductivity: measurements and simulations 114

5.3.1 Reduction of the thermal conductivity in free-standing silicon nano-membranes investigated by non-invasive Raman thermometry 116

5.3.2 A novel contactless technique for thermal field mapping and thermal conductivity determination: Two-Laser Raman Thermometry 122

5.3.3 Transient thermal grating measurements: temperature dependence of thermal diffusivity 129

5.4 Thermal rectification 131

5.4.1 Modelling of thermal rectification in Si and Ge thin films 132

Chapter VI: Conclusions and Future Work 137

6.1 Thesis Summary 137

6.2 Future work 140

Appendix I: Elastic continuum model 145

I.1 Strain 145

I.2 Stress 148

I.3 Hooke's law 151

I.4 From strain-stress relation to equations of motion 153

I.5 Boundary conditions and Lamb waves 154

Appendix II: ahnarmonicity and Thermal conductivity 157

II.1 Harmonic effect in crystals 157

II.2 Thermal conductivity models 159

II.2.1 Boltzmann equation 159

II.2.2 Kinetic theory 161

II.2.3 Cattaneo equation: hyperbolic heat equation. 165

II.2.4 Callaway model 166

II.2.5 Holland model 170

II.2.6 Holland-Callaway modifications 172

II. 3 Boundary scattering processes 173

Appendix III: Modeling of thermal transport 177

III.1 Calculation of thermal conductivity 177

III.2 Modelling of thermal transport: 2LRT and FEM simulations 180

Curriculum Vitae 187

References 189

LIST OF FIGURES

Figure 2.1 *Schematic representation of longitudinal and transversal waves* 12

Figure 2.2 *Left: Scheme of a free-standing membrane. Right: Symmetric and antisymmetric waves.* 15

Figure 2.3 *Decomposition of longitudinal and transverse wavevectors.* 16

Figure 2.4 *(a) Dimensionless acoustic dispersion relation, f·a, and (b) group velocity, v_g, of Si membrane for dilatational (red dotted lines, DW), flexural (black solid lines, FW) and shear (blue dashed lines, SW) waves as a function of the dimensionless in-plane wavevector, $q_{//}$·a.* .. 19

Figure 2.5 *Out-of-plane component of the wavevector, the red solid and blue dotted lines are q_l and q_t wavevector component respectively for dilatational (a) and flexural (b) waves.* 20

Figure 2.6 *Scheme of layered system*.. 23

Figure 2.7 *Scheme of symmetric three-layer system. Here “b” is the thickness of layer 1 and 3, and “a” is the thickness of layer 2 of layered system* 25

Figure 3.1 *Diagrammatic representation of coordinates of a lattice point.*.............................. 28

Figure 3.2 *Diagrammatic representation of a phonon-phonon interaction.* 32

Figure 3.3 *Diagrammatic representation of Normal and Umklapp processes, left and right respectively.*.. 33

Figure 3.4 *Construction for intersection of three phonons in a line for N process, adapted from ref.* [7].. 34

Figure 3.5 *Construction of the intersection of three phonons in a line to illustrate Umklapp-process.*... 35

Figure 3.6 *Wavelength-dependent specularity* $p(\lambda)$ *as a function of phonon wavelength* λ *for roughness values of* η *= 0.5 nm (black),* η *= 1 nm (red),* η *= 2 nm (blue).* 39

Figure 3.7 *Schematic representation of three phonon-phonon scattering processes.* 41

Figure 3.8 *(a-f): Areas of Integration in the x-x' plane allowed for U-processes. Where* $x_{i = 1 \text{ to } 6}$ *are given in Table 3.2* 50

Figure 3.9 *Areas of Integration in the x-x' plane allowed for N-processes. Where* $x_{i = 1 \text{ to } 6}$ *are given in Table 3.2* 51

Figure 3.10 *Relaxation rate,* $1/\tau_U$*, for bulk silicon at room temperature via class I (a) and class II (b) event.* 53

Figure 3.11 *Relative contribution to the total intrinsic relaxation time for each processes and event* 53

Figure 3.12 *Total relaxation rate for Umklapp-processes. Grey dotted line denotes the different zones where each processes dominate.* 54

Figure 3.13 *Relaxation rate as a function of temperature and reduced wavevector for different phonon-phonon processes.* 55

Figure 3.14 *Total relaxation rate for class I event as a function of temperature and reduced wavevector: (a) three-dimensional plot, (b) contour plot (isoline).* 56

Figure 3.15. *Total relaxation rate for class II event as a function of temperature and reduced wavevector: (a) three-dimensional plot, (b) contour plot (isoline).* 56

Figure 3.16 *Modelling and comparison of thermal conductivity of free-standing silicon nanowires ref.* [45] 63

Figure 3.17 *Number of discrete modes for 10 nm thick Si membrane as a function of the dimensionless in-plane wavevector.* 66

Figure 3.18 *Specific heat of Si as a function of temperature for the bulk (blue dashed line) and for 1 to 120 nm thick free standing membrane.* 69

Figure 3.19 *(a) Specific heat capacity and temperature dependence of flexural (red line), shear (blue line) and dilatational (black line) polarizations for a 10 nm thick silicon membrane. For comparison the dependence of the Si bulk is also plotted (green line). (b) Contributions of each polarization to the total specific heat for 10 nm and 1 nm thick silicon membrane. The solid (dotted) black, solid (dotted) red and solid (dotted) blue lines represent the polarization contribution of flexural, shear and dilatational modes, respectively for 10 nm (1 nm) thick Si membrane.* 70

Figure 3.20 *(a) Normalized specific heat capacity as a function of temperature the blue line illustrates the bulk values. (b) Specific heat as a function of the membrane thickness at 300, 10, 4 and 1 K.* 70

Figure 3.21 *Spectral density of the heat capacity of a 10 nm thick Si membrane at 30 K (a) and 300 K (b) as a function of frequency.* 71

Figure 3.22 *Lattice thermal energy (red solid line) and spacing energy (black solid and grey dashed lines) as a function of the temperature and thickness, respectively. (b) Magnified image of the low temperature/thickness regime plotted in linear scale.* 73

Figure 4.1 *(a) Typical SOI wafers used in the fabrication of the free-standing membranes with a few 100s nm thick SOI film and BOX layer. (b) The SOI film is thinned by thermal oxidation. The thermal process creates compressive stress in the film, as shown by the arrows. (c) After release the membrane is relaxed and tends to buckle. (d) Optical micrograph of a released 1.4x1.4 mm^2 membrane with thickness of 9 nm. Courtesy of Prof. Dr. Jouni Ahopelto.* 75

Figure 4.2 *Wavevector conservation in the photoelastic backscattering configuration.* 79

Figure 4.3 *Wavevector conservation in backscattering configuration via the ripple effect.* 79

Figure 4.4 *(a) Schematics of apparatus used for backscattering configuration, (b) Photograph of apparatus used for backscattering configuration. TPFI is a Tandem Fabry-Perot Interferometer* 80

Figure 4.5 *Schematic of Tandem Fabry-Perot Interferometer, TPFI, manufactured by JRS* 81

Figure 4.6 *Typical Brillouin spectra recorded for 200 nm thick free-standing Si membrane. The first two peaks nearest the central quasi-elastic peak are identified as the zero-order flexural, A0, and dilatational, S0, modes. The others belongs to first, and second order dilatational modes, S1 and S2, respectively. Adapted from J. Cuffe and E. Chavez et at.* [21,137]............... 81

Figure 4.7 *Schematic of the response of a semiconductor to an ultra-short pulse. Electrons are excited from the valence band, VB, to the conduction band, CB, where they decay rapidly to the bottom of the conduction band through electron-electron collisions and phonon emission. The dynamics are then described by a slower decay involving electron-hole pair recombination, carrier diffusion, and thermal diffusion. Courtesy of Dr. John Cuffe.* 84

Figure 4.8 *Schematic pump-probe experiment: (a) Mechanical delay and (b) ASOPS with two mode-locked lasers, adapted from J. Cuffe* [136] 85

Figure 4.9 *Schematic time delay between pump and probe pulses. From Gigaoptics GmbH website.* 86

Figure 4.10 *Schematic examples of Raman spectra as thermometer: (a) typical Raman spectrum showing the anti-Stokes, Rayleigh, and Stokes signal, (b) Redshift and broadening of the linewidth due to temperature increasing, adapted from* [154]. 88

Figure 4.11 *Scheme of the Raman thermometry method.* 90

Figure 4.12 *Schematic configuration for the incident, reflected and transmitted power measurements.* 92

Figure 4.13 *Schematic configuration of the Two-Laser Raman Thermometry Technique developed in this work.* 94

Figure 4.14 *Typical time trace from a 400 nm thick Si membrane. The electronic response of the sample is seen, which decays quickly to leave the thermal response. This decay can then be fitted to extract the decay time, which is proportional to the thermal diffusivity. Courtesy of Dr. J. Cuffe.* 95

Figure 4.15 *Schematics of Four-beam Transient Thermal Grating apparatus adapted from Johnson et al.* [173]. *The angle between the pump beams is controlled by splitting the beams with a diffraction grating (phase mask) with a well-defined pitch. The pump beams are later blocked, while the signal from the probe beam that is diffracted from the thermal diffraction grating is recorded. This signal is mixed with an attenuated reference beam for heterodyne detection.* 97

Figure 5.1 *Brillouin spectra as function of the angle of incidence, showing for the fundamental flexural mode of a 17.5 nm Si membrane.* 101

Figure 5.2 *Dispersion relation and phase velocity of the zero order flexural mode of a 17.5 nm silicon membrane: experimental results (blue dots), simulation (black solid line) and quadratic fit (red dashed line). Inset (a): Schematic representation of the displacement fields of the flexural mode, courtesy of Dr. Jordi Gomis-Bresco.* 102

Figure 5.3 *Fractional change in reflectivity as a function of time in the 100 nm silicon membrane. The sharp initial change is due to the electronic response of the membrane. The subsequent weaker oscillations are due to the excited acoustic modes. (b) Close-up of the acoustic modes after subtraction of the electronic response for membranes with 100 and 30 nm thickness shown by the green and red line, respectively. The sinusoidal decay of the reflectivity due to the first-order dilatational mode is clearly observed as a function of time, with a faster* *decay observed for the thinner membrane. The time trace of the 30 nm membrane has been magnified by a factor of 10 for clarity. Adapted from J. Cuffe et al.* [23]. 104

Figure 5.4 *Experimental and theoretical phonon lifetime of the first-order dilatational mode in free-standing silicon membranes as a function of frequency. Experimental data of free-standing silicon membranes with thickness values ranging from approximately 194 to 8 nm (red dots)* [23] *and 222 nm (black dot)* [180]. *Green line: extrinsic boundary scattering processes. Blue line intrinsic three-phonon normal scattering processes. The total contribution, calculated using Matthiessen's rule, is shown by the solid black-dashed line. Adapted from J. Cuffe et al.* [23]. 105

Figure 5.5 *Phonon-phonon processes in Si membranes: (a) Intrinsic relaxation rate as function of the frequency. (b) Relative contribution to the total intrinsic lifetime of each phonon-phonon processes as a function of the frequency.* 108

Figure 5.6 *(a) Thermal conductivity of Si membranes normalized to the Si bulk value as function of the thickness. The experimental data were obtained from thermal transient gradient (black dots), Raman thermometry (red dots) and two-laser Raman thermometry (green dot) methods, respectively* [184–186]. *The theoretical description of the data using the Fuchs-Sondheimer model is shown in blue solid line. (b) Theoretical lifetime of the thermal phonon,* τ_{TH}*, as a function of thickness: black line includes modification of thermal phonon lifetime due to the decrease of the thermal conductivity, blue and red lines: constant thermal phonon lifetime of 17 and 6 ps are shown for comparison.* 110

Figure 5.7 *Experimental and theoretical phonon lifetime of the first-order dilatational mode in free-standing silicon membranes as a function of frequency. Data of free-standing Si membranes with thickness ranging from 194 to 8 nm (green dots) were taken from Reference* [23] *and the data point for a 222 nm thick membrane (violet dot) was taken from* *reference* [180]. *Solid blue (a), red (b) and black lines (c) are the intrinsic Akhieser attenuation dependence calculated for thermal phonon lifetimes of 17 ps (a) and 6 ps (b), whereas (c) includes the thickness-dependent.* 112

Figure 5.8 *(a) Frequency dependence of the Q-factor for different values of the lifetime of the thermal phonon: bulk values,* $\tau_{TH,bulk} = 3\kappa_{bulk}/(C_V v^2)$*, 50% of the bulk value,* $\tau_{TH} = 0.5\tau_{TH,bulk}$ *and 10% of the bulk value,* $\tau_{TH} = 0.1\tau_{TH,bulk}$*. (b) Experimental and theoretical quality factor of different phonon modes in a Si nano-resonator. The experimental data (red dots) were taken from the Reference* [187]*, blue-solid line shows the best fit. Inset SEM image of the nano-resonator, courtesy of Dr. J. Gomis-Bresco.* 113

Figure 5.9 *Typical thermal conductivity measurement diagram* 115

Figure 5.10 *Theoretical and experimental absorptance, A, reflectance, R, and transmittance, T, as a function of membrane thickness. The solids lines are calculation obtained from Fabry-Perot simulations, courtesy of Dr. Francesc Alzina. The solid dots are experimental data points. Inset: diagrammatic Fabry-Perot effect in membranes* 118

Figure 5.11 *Calibration of the Raman shift of the LO Si mode as function of the temperature: the red and green dots were extracted from the References* [156,186]*, respectively.* 119

Figure 5.12 *Raman shift (right axis) of the longitudinal optical (LO) Si phonon of the membranes as a function of the absorbed power and membrane thickness. The left axis represent the temperature obtained from the temperature dependence of the LO mode extracted from the slope of the Figure 5.11.* 119

Figure 5.13 *Thermal conductivity of the membranes,* $\kappa_{film}/\kappa_{bulk}$*, normalized to the bulk Si value as a function of the thickness (solid red dots). As reference previous work in SOI* [2–4] *and membranes using TTG* [184] *are also shown. The theoretical description of the data using the* *modification of the dispersion relation, Srivastava and Fuchs-Sondheimer models are shown in green dotted, black dashed and blue solid lines, respectively.*.. 120

Figure 5.14 *Three-dimensional contour plot of the thermal field distribution of a 250 nm thick free-standing Si membrane. The isoline distribution of the thermal field is also shown in a lower plane. The colour bar indicates the maximum temperatures reaches.*..................................... 123

Figure 5.15 *Vertical and horizontal temperature cuts of the isoline thermal field distribution of a 250 nm thick free-standing Si membrane. Note the high symmetric distribution in temperature from both cuts.*... 124

Figure 5.16 *Comparison of the temperature map measured and simulated for a 1 µm thick silicon membrane. The solid lines represent theoretical curves with different thermal conductivity values ranging from the bulk values (1) and decreasing progressively to 65% of the bulk values (0.65).* 125

Figure 5.17 *Experimental temperature profile measured in a 1 µm thick Si membrane (green and purple dots). The purple dots come from of the negative part of the Figure 5.16 mirror reflected to the right side.*... 126

Figure 5.18 *Comparison of the temperature map measured and simulated for a 2 µm thick silicon membrane. The solid lines represent theoretical curves with thermal conductivity value of 118* $WK^{-1}m^{-1}$. 127

Figure 5.19 *Comparison of the measured and simulated temperature map for a 250 nm thick silicon membrane. The solid red line represents theoretical curves with thermal conductivity value of 81*$WK^{-1}m^{-1}$*. The bulk limit, black solid line, is shown by comparison.*....................... 127

Figure 5.20 *Theoretical and experimental thermal conductivity of the Si membranes, normalized to the bulk Si value,* $\kappa_{film}/\kappa_{bulk}$*, as a function of thickness. The green solid dots show* *this work (2LRT) and as reference previous work data on SOI* [2–4] *and Si membranes using TTG* [184], *and Single-Raman thermometry, 1LRT, are also shown.* 128

Figure 5.21 *Thermal diffusivity as a function of grating spacing in a 200 nm thick Si membrane at different temperatures.* 130

Figure 5.22 *Temperature dependence of the thermal diffusivity for 100 and 200 nm thick Si membranes. The Si bulk values are also shown for comparison* [191,192] 131

Figure 5.23 *Two-segment schemes for thermal rectification: (a) In-plane Si-Si or Si-Ge configuration. (b) Out-of- plane Si-Ge configuration.* 133

Figure 5.24 *Temperature dependence of the in-plane (a) and out-of-plane (b) thermal conductivity of Si and Ge thin films. All curves were calculated with a mass-defect scattering parameter (Γ) reflecting the natural isotope concentration, with the exception of the 500 nm thick Si film for which an increased mass-defect scattering was introduced (10Γ).* 134

Figure 5.25 *Calculated in-plane thermal rectification coefficient of (a) 500-200 nm Si-Si, (b) 800-200 nm Ge-Si and (c) 80 -15 nm Ge-Si systems. Calculated out-of-plane thermal rectification of a 100-20 nm Si-Ge system. For each configuration* T_H, *was fixed and the low temperature was varied.* 135

Figure 6.1 *SEM image of the ordered (a) and disorder (b) phononic crystal for thermal properties analysis. Courtesy of Dr. Marianna Sledzinska.* 142

Figure I.1 *Sectioned solid under external loading* 148

Figure I.2 *Stress components* 148

Figure I.3 *Traction on arbitrary orientation* 149

Figure I.4 *Typical graph of non-linear equation of dilatational waves for a fixed dimensionless wavevector, Q = 0.5, as a function of reduced frequency* 156

Figure II.1 *Silicon dispersion relation, adapted from* [212]. 170

Figure II.2 *Schematic phonon spectrum showing zone division, 0.5b, and the extension into second Brillouin zone. Adapted from* [104]. 172

Figure III.1 *(a) Phonon dispersion relation of bulk silicon and germanium systems: experimental results (red and blue dots) from Ref.* [176] *and second-order polynomial fit (red and blue solid line). (b) Red and blue lines: calculated temperature-dependence of the lattice thermal conductivity of bulk silicon and germanium, respectively. Red and blue dots: the experimental data of silicon and germanium bulk respectively obtained from Ref.* [70].......... 180

Figure III.2 *Normalized intensity of the monochromatic light with wavelength of 407 nm as a function of travelled distance in bulk silicon. Three different stars at 250 (red), 1000 (blue) and 2000 (green) nm are included to rough comparison with the thicknesses of the studied membranes. Inset: idem in double logarithmic scale for better visualization of the graph.* 182

Figure III.3 *Absorptance (A), reflectance (R), and transmittance (T) as a function of the thickness of the membranes. Solid black, red and blue lines are the calculated A, R and T coefficient considering the Fabry-Perot effect. For comparison the bulk limit of the A and R coefficients are shown in dashed grey and pink lines, respectively. Note that the oscillating behaviour is more appreciable at small thicknesses (a), while larger thicknesses the absorption reaches quietly the bulk values (b). Courtesy of Dr Francesc Alzina.* 183

Figure III.4 *Temperature dependence of the bulk silicon thermal conductivity. The experimental data (red dots) were obtained from Ref.* [214]. *The solid blue line is a second-order polynomial adjust.* 184

Figure III.5 *(a) Geometry of the sample used in the simulations. (b) Representative simulated temperature field.* 185

LIST OF TABLES

Table 1.1 *Thermal conductivity measurements in Si nanostructures* 7

Table 3.1 *N and U-processes interactions. s is the polarization, L and T are the longitudinal and transverse polarization, respectively. The processes described in the last row is only valid for N-Processes* 49

Table 3.2 *Limit values for areas of integration in the x-x' space, with S_L and S_T longitudinal and transversal sound speed respectively.* 50

Table 3.3 *Silicon parameters used in the simulation of Umklapp-processes in the bulk system.*52

Table III.1 *Silicon and Germanium parameters used in the calculations*. 179

LIST OF PUBLICATIONS AND PRESENTATIONS

Published and accepted articles

1. J. Gomis-Bresco, D. Navarro-Urrios, M. Oudich, S. El-Jallal, A. Griol, D. Puerto, **E. Chavez**, Y. Pennec, B. Djafari-Rouhani, F. Alzina, A. Martínez, C. M. Sotomayor Torres, "A 1D optomechanical crystal with a complete phononic band gap", Arxiv: 1401.1691v2, 2014. **Accepted in Nat. Commun.**

2. E. Chávez-Ángel, R.A. Zarate, J. Gomis-Bresco, F. Alzina, C.M. Sotomayor Torres, "*Modification of Akhieser mechanism in Si nanomembranes and thermal conductivity dependence of the Q-factor of high frequency nanoresonators*", **Accepted in Semicond. Sci. Tech.**

3. J.S. Reparaz, **E. Chávez-Ángel,** M. R. Wagner, J. Gomis-Bresco, B. Graczykowski, F. Alzina, and C. M. Sotomayor Torres**,** "*Novel high resolution contactless technique for thermal field mapping and thermal conductivity determination: Two-Laser Raman Thermometry*", Rev. Sci. Instr., Vol. 85, 034901, 2014.

4. V. A. Shah, S. D. Rhead, J. E. Halpin, O. Trushkevych, **E. Chávez-Ángel**, A. Shchepetov, V. Kachkanov, N. R. Wilson, M Myronov, J. S. Reparaz, R. S. Edwards, M.R. Wagner, F. Alzina, I. P. Dolbnya, D. H. Patchett, P. S. Allred, M.J. Prest, P.M. Gammon, M. Prunnila, T. E. Whall, E. H. C. Parker, C.M. Sotomayor Torres, D. R. Leadley, "High quality single crystal Ge nano-membranes for opto-electronic integrated circuitry", J. Appl. Phys. Vol. 115, 144307, 2014.

5. E. Chávez-Ángel, J. S. Reparaz, J. Gomis-Bresco, M. R. Wagner, J. Cuffe, B. Graczykowski, A. Shchepetov, H. Jiang, M. Prunnila, J. Ahopelto, F. Alzina and C. M. Sotomayor Torres, "*Reduction of the thermal conductivity in free-standing silicon nano-membranes investigated by non-invasive Raman thermometry*", APL Mat., Vol. 2, 012113, 2014.

6. J. Cuffe, O. Ristow, **E. Chávez**, A. Shchepetov, P-O. Chapuis, F. Alzina, M. Hettich, M. Prunnila, J. Ahopelto, T. Dekorsy and C. M. Sotomayor Torres, "*Lifetime of Confined Acoustic Phonons in Ultra-Thin Silicon Membranes*", Phys. Rev Lett., Vol. 110, 095503, 2013.

7. **E. Chávez**, J. Gomis-Bresco, F. Alzina, J.S. Reparaz, V.A. Shah, M. Myronov, D.R. Leadley and C.M. Sotomayor Torres, "*Flexural mode dispersion in ultra-thin Ge membranes*", 14th International Conference on *Ultimate Integration on Silicon (ULIS)*, Vol. 185, 2013.

8. **E. Chávez-Ángel**, F. Alzina, C.M. Sotomayor Torres, "*Modelling of thermal rectification in Si and Ge thin films*", ASME 2013 International Mechanical Engineering Congress and Exposition: Heat Transfer and Thermal Engineering, Vol. 8C, V08CT09A013, 2013.

9. J. Cuffe, **E. Chávez**, A. Shchepetov, P.O. Chapuis, El Houssaine El Boudouti, F. Alzina, T. Kehoe, J. Gomis-Bresco, D. Dudek, Y. Pennec, B. Djafari-Rouhani, M. Prunnila, J. Ahopelto, and C.M. Sotomayor Torres, "*Phonons in Slow Motion: Dispersion Relations in Ultra-Thin Si Membranes*", Nano Lett., Vol. 12, 3569, 2012.

10. **E. Chávez**, J. Cuffe, F. Alzina and C.M. Sotomayor Torres, "*Calculation of the specific heat capacity in free-standing silicon membranes*", J. Phys.: Conf. Ser., Vol. 395, 012105, 2012.

11. J. Cuffe, **E. Chávez**, A. Shchepetov, P.O. Chapuis, El Houssaine El Boudouti, F. Alzina, T. Kehoe, J. Gomis-Bresco, D. Dudek, Y. Pennec, B. Djafari-Rouhani, M. Prunnila, J. Ahopelto, and C.M. Sotomayor Torres "*Effect of the phonon confinement on the dispersion relation and the heat capacity in nanoscale Si membranes*", ASME 2012 International Mechanical Engineering Congress and Exposition: Micro- and Nano-Systems Engineering and Packaging, Vol. 9, 1081, 2012.

Non-related articles

12. S. Fuentes, F. Cespedes, P. Muñoz, **E. Chávez** and L. Padilla-Campos, "*Synthesis and structural characterization of nanocrystalline $BaTiO_3$ at various calcination temperature*" J. Chil. Chem. Soc. Vol 58, 2077, 2013.

13. S. Fuentes, **E. Chávez**, L. Padilla-Campos and D.E. Diaz-Droguett, "*Influence of reactant type on the Sr incorporation grade and structural characteristics of $Ba_{1-x}Sr_xTiO_3$ (x=0−1) grown by sol–gel-hydrothermal synthesis*" Ceramics International, Vol. 39, 8823, 2013.

14. E. Chávez, S. Fuentes, R. A. Zarate, L. Padilla-Campos, "*Structural analysis of nanocrystalline $BaTiO_3$*", Journal of Molecular Structure, Vol. 984, 131, 2010.

Book chapters

15. M. Mouis, **E. Chávez-Ángel**, F. Alzina, A. Shchepetov, J. Ahopelto, C. M. Sotomayor Torres, A. Nassiopoulou, M. V. Costache, S. O. Valenzuela, B. Viala, D. Zakharov, Wensi Wang, Beyond CMOS Nanodevices 1, Chapter 7: "*Thermal Energy Harvesting*", John Wiley & sons, Inc., pp. 135-219, 2014.

16. D. Leadley, V. Shah, J. Ahopelto, F. Alzina, **E. Chávez-Ángel**, J. Muhonen, M. Myronov, A. G. Nassiopoulou, H. Nguyen, E. Parker, J. Pekola, M. Prest, M. Prunnila, J. S. Reaparaz, C.M. Sotomayor Torres, K. Valalaki and T. Whall, BEYOND-CMOS NANODEVICES 1, Chapter 12: "*Thermal isolator through nanostructuring*", John Wiley & sons, Inc., pp. 331-363, 2014.

In preparation articles

17. F. Alzina, **E. Chávez-Ángel**, J.S. Reparaz, J. Cuffe, J. Gomis-Bresco, A. Shchepetov, J. Ahopelto, and C. M. Sotomayor Torres, Invited review article: "*Silicon membranes: a model system to study heat transport*", to be published in APL Mat.

Oral Presentations

1. **E. Chávez,** F. Alzina and C. M. Sotomayor Torres, "*Modelling of thermal rectification in Si and Ge thin films*" European Material Research Society 2014 spring meeting, E-MRS 2014, May 26-30, 2014, Lille, France.

2. **E. Chávez-Ángel**, F. Alzina and C. M. Sotomayor Torres, "*Modelling of thermal rectification in Si and Ge thin films*" ASME 2013 International Mechanical Engineering Congress and Exposition, ASME-IMECE 2103, Nov. 15-21, 2013, San Diego, USA.

3. **E. Chávez**, J.S. Reparaz, J. Cuffe, J. Gomis-Bresco, M. R. Wagner, A. Shchepetov, M. Prunnila, J. Ahopelto, F. Alzina and C. M. Sotomayor Torres, *"Thermal properties of silicon ultra-thin membranes: A theoretical and experimental approach"* 2nd edition of largest European Event in Nanoscience and nanotechnology, ImageNano 2013, April 23-26, 2013, Bilbao, Spain.

4. **E. Chávez**, J. Cuffe, F. Alzina, J. S. Reparaz, W. Khunsin, A. Goñi, C. M. Sotomayor Torres, "*Calculation of thermal properties in silicon nanostructures*" XVIII Simposio Chileno de Física, Nov. 21-23, 2012, La Serena, Chile.

5. **E. Chávez**, J. Cuffe, F. Alzina, C.M. Sotomayor, "*Specific heat of ultra-thin free standing silicon membranes*" 6th European Thermal Sciences Conference, Eurotherm 2012, September 04-07, 2012, Poitiers, France.

6. **E. Chávez**, J. Cuffe, F. Alzina, C.M. Sotomayor, "*Heat capacity on free standing membranes included native oxide*", XIV International Conference on Phonon Scattering in Condensed Matter, Phonons 2012, July 8-12, 2012, Ann Arbor, MI USA.

7. **E. Chávez**, P.O. Chapuis, J. Cuffe, F. Alzina, C.M. Sotomayor-Torres "*Relaxation rate in ultra-thin silicon membranes*", Summer School: "Energy Harvesting at micro and nanoscale", NiPS Summer School 2011, August 1-4, Workshop "Energy Management at Micro and Nanoscale", August 4-5, Perugia, Italy.

8. **E. Chávez**, P.O. Chapuis, J. Cuffe, F. Alzina, C.M. Sotomayor-Torres "*Acoustic phonon relaxation rates in nanometer-scale membranes*", Phononics 2011: First International Conference on Phononic Crystals, Metamaterials and Optomechanics, Phononics 2011, May 29th to June 2nd 2011, Santa Fé, New Mexico, USA.

LIST OF ACRONYMS

1D	One dimensional
2D	Two dimensional
3D	Three dimensional
1-LRT	Single-laser Raman thermometry
2-LRT	Two-laser Raman thermometry
a	Thickness of the membrane
A	Absorptance
ASOPS	Asynchronous optical sampling
BHS	Buffered hydrofluoric acid
BOX	Buried oxide layer
BLS	Brillouin light scattering
BTE	Boltzmann transport equation
CCD	Charge-couple device
CW	Continuous wave
DOS	Density of States
DSP	Double side polished
DW	Dilatational waves
FEM	Finite element method
FDTR	Frequency-domain thermoreflectance
FPI	Fabry-Pérot interferometer
FW	Flexural waves
FWHM	Full-width-half-maximum
LA (L)	Longitudinal acoustic
HF	Hydrofluoric acid
ILS	Inelastic light scattering
LO	Longitudinal optic
MFP	Mean free path
PBTE	Phonon Boltzmann transport equation
R	Reflectance
RIE	Reactive ion etching
SAW	Surface acoustic wave

SEM	Scanning electronic microscopy
SOI	Silicon-on-insulator
SW	Shear waves
T	Transmittance
TA (T)	Transverse acoustic
TDTR	Time-domain thermoreflectance
TMAH	Tetramethyl ammonium hydroxide
TPFI	Tandem Fabry-Pérot interferometer
TTG	Transient thermal grating
Q-factor	Quality factor

CHAPTER I: INTRODUCTION AND OBJECTIVES

Due to the large variety of promising technological applications, the concept of nanotechnology has become one of the most important and exciting fields encompassing many disciplines such as physics, chemistry, biology, medicine, engineering among others. At nanometric scales, material properties can be dramatically modified in comparison with their bulk counterpart. This is, in part, due to the effects of quantum confinement and to the increase of surface-volume ratio. For example, a spherical particle with size of 30 nm has 5% of its atoms on its surface; at 10 nm this percentage has increased by 20% while at 5 nm atoms at the surface account for almost 50% the total number [1]. These factors can either enhance or degrade elastic, reactive, thermal, optical and electrical characteristics among others.

Great innovations in controlled micro and nanofabrication have led to the realization of novel materials, development of processes and unveiling of new phenomena at nanoscale which, in turn, have spurred technology growth at an astounding pace, while offering us the first building blocks for the next green-industrial revolution.

In this sense, the control of the charge and heat transport in low-dimensional semiconductor structures has become a cornerstone in the development of this next technology revolution. This is in part motivated by the increasing importance of thermal management as a consequence of the large power densities resulting from the continuous miniaturization of electronics components. Moreover, the engineering of the thermal conduction opens a route to energy harvesting through, for example, thermoelectric generation. As a consequence, control and engineering of phonons in the nanoscale is essential for tuning desirable physical properties in a device in the quest to find a suitable compromise between performance and power consumption.

Developments arising from confinement of electronic charge and light in nanostructures have been widely researched in the context of information and communication technology. In contrast, progress in the study of phonons as main actors in heat conductivity, carrier electronic mobility, detection limits and emission time-scales, among others, has been slower in rate and smaller volume. An example of the still poor state-of-the-art on this topic it that until now essential parameters remains unknowns such as: the frequency-dependence of the Grüneisen parameter, accurate measurements of phonon lifetime and/or phonon mean free path, the influence of constant [2–5] or frequency-dependent surface roughness parameter [6,7], the limit of diffusive/ballistic thermal transport and their associated temperature and thickness transition, to name but a few. One example of this limited state-of-the-art is that only last year an experimental proof of the effective phonon mean free path in bulk silicon was obtained [8].

The lack of the knowledge of these parameters is due, in part, to substantial challenges associated with their quantitative experimental determination and the corresponding theoretical model. In this sense, one set of structures that are attracting increasing attention for thermal studies is free-standing membranes. These include solids plates (slabs) or rods (bars) connected to solid substrate by the extremities. From one-atom thick layers, e. g. graphene [9], to high purity and single-crystal structure, e.g. Si membranes [10], these structures have found use in a wide variety of interesting and important applications, including very sensitive forces [11], mass [12] and pressure sensors, low-loss macromolecule separators [13], bolometers platform [14,15] and optomechanical cavities [16] among others.

In addition, as there is no interference from a substrate and as they can be fabricated with precise, controlled and reproducible fabrication processes, these nanoscale objects facilitate the experimental analysis and comparison with theoretical models and are a text-book example of a nanoscale system. Their physical properties, e.g. electrical and thermal properties, can be dramatically different compared to a thick sample or bulk counterpart, by orders of magnitude. All these characteristics are of special interest from experimental and theoretical point of view.

1.1 Nanoscale thermal conductivity

The understanding of heat propagation and thermal properties in low-dimensional nanostructures has motivated increasing research activity and, undoubtedly, the thermal conductivity, κ, is one of the most important and fundamental physical quantities.

The thermal conductivity of a material governs its ability to transport heat and plays a fundamental role in the design and performance of the technological devices. The dominant carrier of the heat energy depends on the type of material. It can be transported via charge carriers (electrons), lattice waves (phonons), electromagnetic waves (photons), or spin waves (magnons). For non-metal, semiconductor and alloy materials the dominant conduction carrier is the lattice thermal conduction, i.e., by phonons. A phonon is a pseudo-particle which represents quantized modes of the vibrational energy of an atom or group of atoms in a lattice. Considering that phonons are pseudo-particles, it is possible to associate to each of them an energy $\hbar\omega$ and a pseudo-momentum $p = \hbar q$, which obey Bose-Einstein statistics [17].

Similarly to the electron case, the phonon energy can be represented as a dispersion relation, i.e., a relationship between the phonon frequency and its wavevector. The slope of a dispersion relation curves determines the phonon group velocity, $v_g = d\omega/dq$. For the bulk case, the dispersion relation of phonons with short wavevector can be considered linear and the slope represents the sound velocity in the material. However, when we decrease the characteristic dimensions of the material, this linear dependence no longer holds, and many discrete modes appear leading to the quantization of the phonon energy. This spatial confinement affects the phonon group velocity, density of states, specific heat capacity, electron-phonon and phonon-phonon interactions, etc. [18–23]. Moreover the decrease in dimension sets an upper limit to the phonon mean free path, because the acoustic wave cannot continue to travel in the media due to the boundaries.

The recent experimental and theoretical reports point to an enhancement of the thermoelectricity figure of merit, $ZT = S^2\sigma T/\kappa$ (where S is the Seebeck coefficient, σ the electrical conductivity κ the thermal conductivity and T is the temperature), in thin films [24–28], nanowires [29–33], superlattices [34–37] and suspended phononic crystals [38–40]. This is primarily a result of the thermal conductivity decrease compared to the bulk counterpart, without a corresponding decrease in electrical properties. The reduction of the thermal conductivity in these systems has been associated with two principal factors: (*i*) the modification of the acoustic dispersion relation due to the additional periodicity (superlattices and phononic crystal structures) [41–43] or spatial confinement of the phonon modes (thin films and nanowires) [44–47] and (*ii*) the shortening of the phonon mean free path due to the diffuse scattering of phonons at the boundaries [2,48–50].

To model heat transfer in nanostructures, advanced theoretical models are required which correctly take into account the frequency dependence of phonon properties. The majority of the models of the thermal conductivity are derived from the phonon Boltzmann transport equation (PBTE) under the single mode relaxation-time approximation [17]. For low-dimensional systems Zou et al. [51] classified the theoretical models into three types. The first one takes the bulk formulation for the thermal conductivity, introduces the modified dispersion relation caused by the spatial confinement and adds a boundary scattering rate to the total scattering rate through Mattiessen's rule [44]. The second one uses the bulk dispersion relation and derives an exact solution of the PBTE after introducing the diffusive boundaries conditions, according to a Knudsen flow model [2,48,52]. The third model, proposed by Zou et al. [51], is a combination of these two approaches. This model takes the modified expression of the thermal conductivity including the Knudsen flow model in addition to the modified dispersion relation. More recently Huang et al. [46] developed one- and two-dimensional expressions for the thermal conductivity of nanowire and thin films, which include the modified expression of the relaxation time due to the boundaries.

The experimental measurement of the thermal conductivity involves two steps: the introduction of thermal energy into the system (heating) and the detection of the change of temperature or related physical properties due to the increase in thermal energy (sensing). Both heating and sensing can be measured, mainly, by electrical, optical and/or the combination of both methods. In Table 1.1 a summary of main measurements of Si nanostructures performed in the last ten years is given.

Reference	Type of Nanostructure	Relevant Dimensions [nm]	Type of measurement	Temperature [K]	Thermal conductivity at 300 K [W K^{-1} m^{-1}]
Ma et al. [53] (2013)	Inverse opals	18-38	Electrical, 3ω	30-400	0.6-1.3
Grauby et al. [54] (2013)	Nanowires	50 & 200	Electrical, 3ω-SThM	Room temperature	22-150
Claudio et al. [55] (2012)	Nanostructured Bulk	30-40	Electrical, commercial	2-300	15-24
Feser et al. [56] (2012)	Nanowires	110-150	Optical, TDTR	Room temperature	12-40
Marconnet et al. [57] (2012)	Periodic porous nanobridge	196	Electrical, 3ω	Room temperature	3.4-112

Reference	Type of Nanostructure	Relevant Dimensions [nm]	Type of measurement	Temperature [K]	Thermal conductivity at 300 K [W K^{-1} m^{-1}]
Weisse et al. [58] (2012)	Porous nanowires	300-350	Optical, TDTR	Room temperature	51-142
Kim et al. [59] (2012)	Free-standing phononic crystal	500	Electrical, Joule heating	Room temperature	32.6
Fang et al. [60] (2012)	Mesoporous nanocrystalline thin films	140-340	Electrical, 3ω	25-315	0.23-0.32
Liu et al. [61] (2011)	Free-standing membrane	500 & 700	Optical, Raman thermometry	Room temperature	118 & 123
Wang et al. [62] (2011)	Nanocrystals	64-550	Electrical, 3ω	16-310	8-79
Yu et al. [38] (2010)	Free-standing phononic nanomesh	22-25	Electrical, suspended heater & detector	80-320	1.5-17
Doerk et al. [63] (2010)	Nanowires	30-300	Optical, Raman thermometry	Room temperature	10-81
Tang et al. [39] (2010)	Holey Si	100	Electrical, suspended heater & detector	20-300	1.7-51
Schmotz et al. [64] (2010)	Free-standing membrane	340	Optical, thermal transient grating	Room temperature	136

Reference	Type of Nanostructure	Relevant Dimensions [nm]	Type of measurement	Temperature [K]	Thermal conductivity at 300 K [W K^{-1} m^{-1}]
Hochbaum et at. [30] (2008)	Nanowires	20-300	Electrical, suspended heater & detector	20-320	2.5-8.5
Boukai et al. [29] (2008)	Nanowires	10 & 20	Electrical, suspended heater & detector	100-300	0.76 & 5.7
Hao et al. [65] (2006)	Thin films	50 and 80	Electrical, suspended heater & detector	Room temperature	32 & 38
Ju [66] (2005)	Thin films	20-50	Electrical, on substrate heater & detector	Room temperature	30-55
Liu et at. [4] (2005)	Free-standing membranes	30	Electrical, Joule heating	300-450	30
Liu et al. [49] (2004)	Free-Standing membrane	20 & 100	Electrical, Joule heating	20-300	22 & 60
Li et al. [45] (2003)	Nanowires	22-115	Electrical, suspended heater & detector	20-320	6.7-40.7

Table 1.1 *Thermal conductivity measurements in Si nanostructures*

The first thermal conductivity models for bulk systems [67–70] were based on the solution of the phonon Boltzmann transport equation (PBTE) under the single mode relaxation time approximation. This approach provides the simplest picture of phonon interactions considering that each phonon mode has a single relaxation time independent of others modes, i.e., it assumes that all other phonon have their equilibrium distribution [17]. The calculation of the thermal conductivity in semiconductor material implies the knowledge of three major frequency-dependent parameters, i.e., ***specific heat***, C_V, ***phonon group velocity***, v_g, and the ***phonon mean***

free path, Λ. The expression for thermal conductivity from the kinetic theory of gases is given by

$$\kappa = \frac{1}{3} C_V v_g \Lambda \qquad [1.1]$$

Taking into consideration the contribution of each mode q with transverse (T) or longitudinal (L) polarization s, Equation [1.1] becomes:

$$\kappa = \frac{\hbar^2}{3VK_B T^2} \sum_{qs} v_{qs}^2 \omega_{qs}^2 \tau_{qs} n_{qs} (n_{qs} + 1) \qquad [1.2]$$

where $\hbar$ is the reduced Plack's constant, V the total volume, T the temperature, K_B is the Boltzmann constant, ω_{qs} the phonon frequency, v_{qs} the group velocity, n_{qs} the Bose-Einstein equilibrium phonon distribution function and $\tau_{qs} = \Lambda_{qs}/v_{qs}$ the total relaxation time of each mode. From Equation [1.2] it is clear that to model the lattice thermal conductivity we need the dispersion relation, the total relaxation time of each mode and a numerical scheme for performing the integration within the Brillouin zone. The phonon dispersion relation can be calculated through several methods. However, the calculation of the intrinsic relaxation time and the summation over the Brillouin zone can be very time-consuming and the knowledge of the anharmonic phonon-phonon scattering strengths is not yet sufficiently-well established [71].

1.2 Phonon confinement

Acoustic phonons play an essential role in almost all the physical properties of a crystal. The statistics of phonons and their interaction with others particles sets a limit to some properties, such as: electrical and thermal conductivity, sound transmission, reflectivity of ionic crystals, inelastic scattering of light, scattering of X-Rays and neutrons, linewidth of quantum dot emission, maximum power carried by optical fibers and so on [72,73]. In this sense, the engineering of new devices able to generate and control phonons becomes an essential issue in the development of future technologies.

The pioneering studies of confined waves were performed by Lord Rayleigh [74] in 1885. He demonstrated, theoretically, the existence of surfaces acoustics waves, SAW, which propagates along the plane surface of an isotropic solid half-space. These waves are non-dispersive, with a velocity slightly smaller than of the bulk shear waves and their amplitudes decaying exponentially from the surface, i.e., these waves are confined in the surface. Years later, following the results of Lord Rayleigh others scientists developed this topic, particularly Pochhammer, Love, Sezawa, Stoneley, Lamb, among others. Following the Pochhammer and Rayleigh's work Horace Lamb [75] described the characteristics of waves propagating in free-standing plates.

Early experiments to detect optical phonons in confined systems were performed by Fasol in 1988 [76], who used Raman scattering techniques to show that the wave vector of optical phonons of a ten monolayer thick AlAs/GaAs/AlAs superlattice are confined and can only take values given by $q_z = n\pi/L_z$, where L_z is the thickness of the layers. This early experiment demonstrated not only that phonons are confined in nanostructures but also that the measurement of phonon wave vectors are well described by relatively simple continuum models of phonon confinement. Concerning to membranes, technically an acoustic cavity, first experimental observation of confined acoustic phonons of nanometre-scale membranes was reported in 1987 in suspended 20 nm thick Au films [77]. Other works in free-standing membranes has been reported on 100 and 200 nm in SiN films in 2003 [78] and 30 nm Si films in 2004 [79].

1.4 Thesis Outline

In this thesis we report the study of thermal properties in free-standing silicon membranes. In Chapter II, an analytical model for wave propagation in isotropic free-standing membranes is developed. There the main concepts of the elastic continuum theory are described. Chapter III theoretical models of the thermal properties are developed, including phonon lifetime, phonon density of states, heat capacity and thermal conductivity. Chapter IV the fabrication of the samples and the different characterization techniques used for the study the phonon-dependent properties are described. The experimental results and their theoretical description are developed in Chapter V. Finally, the conclusion, the summary of the main results and future extension of this work are shown in the Chapter VI.

CHAPTER II: ACOUSTIC WAVES

In this chapter, a semi-analytical model for wave propagation in free-standing membrane is developed. The free-standing membrane consists of a solid plate, slab, connected to a solid substrate by the extremities. The membrane system is treated as a semi-infinite system, i.e., with infinite extensions in x and y directions but with a finite extension in the z component. The acoustic waves sustained by this system are solutions of the elasticity equation of the material with stress-free conditions at the boundaries at $z = \pm a/2$, where a is the thickness of the membrane. In addition, the acoustic wave propagation and the phonon dispersion relation in a layered system are calculated.

2.1 Elastic continuum model

To calculate the dispersion relation the elastic continuum model is often used. In this model, the discrete nature of the atomic lattice is ignored and the material treated as a continuum. This model can be derived from the theory of lattice vibrations by considering that the lattice deformations vary slowly on a scale determined by the range of the inter-atomic forces [80], and is usually valid provided that the wavelength of elastic waves, λ, is significantly larger than the atomic lattice constant, a_0, i.e., $\lambda/a_0 \geq 20$. This corresponds to wavelengths approximately longer than 10 nm, or frequencies smaller than approximately 100 GHz [81].

Within this model, a displacement of the material causes a strain, which can be described in terms of the strain tensor, S, and is related to the gradient of the displacement, $\partial U_i/\partial x_i$. In the presence of the strain, the material generates internal forces that return it to its original positions, i.e., the equilibrium state. These forces are expressed in terms of the stress tensor, *T*, which is related to the *S* tensor through the elastic constant tensor, *C*, as:

$$T_{ij} = C_{ijkl} S_{kl} \qquad [2.1]$$

where C_{ijkl} is a fourth order tensor, which has 81 components, but only 36 of these components are independent, due to symmetry considerations [69,82–84]. In isotropic materials, waves can travel equally well in all directions, and the elastic constant tensor can be further simplified to have two independent components.

As shown in the Figure 2.1, depending on the type of displacement, there are two types of acoustic waves. First, longitudinal waves (LA) are such that the displacement is parallel to the propagation direction. Second, transverse or shear waves (TA) have their displacement in a plane parallel to the wavefront and consequently normal to the propagation direction.

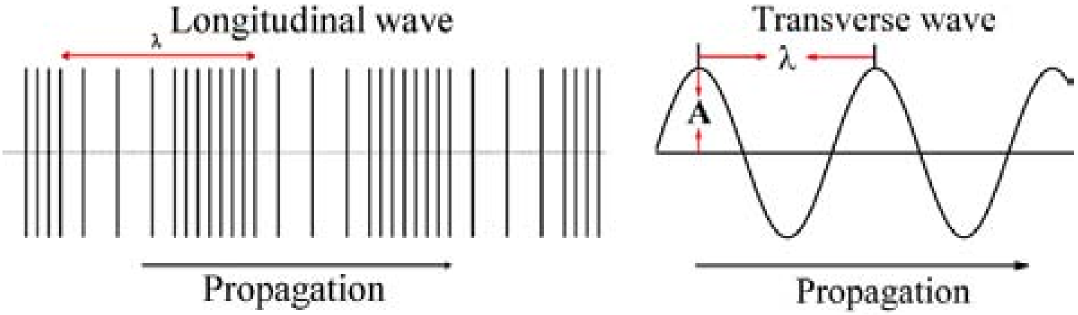

Figure 2.1 *Schematic representation of longitudinal and transversal waves*

The elastic continuum model provides an adequate description of elastics waves and can be used to describe confinement effects in nanostructures when the dimensions become comparable to the wavelength. A full description of the propagation of acoustic waves according to the continuum elasticity model is given in a number of comprehensive textbooks, by authors such as Auld [82], Nayfeh [69], Sadd [83] and Rose [84]. A detailed analysis and development of the associated equations is described in Appendix I.

By describing strain S in terms of the displacement U and the stress T in terms of the strain component S_{ij}, the equation of motion can be written purely in terms of the displacement and the C tensor as:

$$\rho \frac{\partial^2 U_i}{\partial t^2} = \frac{1}{2}\frac{\partial}{\partial x_j}\left[C_{ijkl}\left(\frac{\partial U_k}{\partial x_l} + \frac{\partial U_l}{\partial x_k}\right)\right] \qquad [2.2]$$

In isotropic materials, waves can travel equally well in all directions, and the elastic constant tensor can be further simplified to have two independent components:

$$T_{ij} = \lambda S_{kk}\delta_{ij} + 2\mu S_{ij} \qquad [2.3]$$

where λ is called Lamé's constant and μ is referred to as the shear modulus. Then the equation of motion is given by:

$$\frac{\partial^2 U}{\partial t^2} = v_T^2 \nabla^2 U + (v_L^2 - v_T^2)\nabla \cdot (\nabla U) \qquad [2.4]$$

where $U = (u, v, w)$ is the amplitude of the displacement vector, $v_L = [(l + 2\mu)/\rho]^{1/2}$ and $v_T = [\mu/\rho]^{1/2}$ are the longitudinal and transversal velocities of acoustic waves in a given continuum medium, respectively.

2.1.1 Boundary conditions and confined waves

The introduction of boundary conditions in infinite media changes the nature of the acoustic propagation. SAW [74] are solution of the wave equation with stress-free boundary condition on the surface. These waves are non-dispersive and they have two components corresponding to bulk shear and longitudinal waves, with a velocity lower than the bulk shear waves. The atomic displacement forming those waves occurs in the sagittal plane, that is, the plane normal to the propagation direction and their amplitude decays exponentially from the surface. The motion of individual atoms is taken to be elliptical.

Following Rayleigh's work other scientist developed this topic, particularly Love and Sezawa. Love found a purely shear waves, SW, with displacement normal to the sagittal plane existing in a half-space covered with a layer of softer material [85]. Sezawa found that SAW, with displacement in the sagittal plane, could exist in layered system [86]. Rayleigh, Love and Sezawa waves all occur in surface-wave-based devices.

Following the same concept Lamb described propagating waves in isotropic stress-free plates, i.e., plate waves [75]. The waves sustained by this type of structures are solutions of the elasticity equation of material with stress-free conditions at the boundaries at $z = \pm a/2$, where a is the thickness of the plate, with infinite extent in x and y directions. For unsupported plates the normal components of the stress tensor vanish at the surface. This system has two types of solutions: solutions with displacements confined to the sagittal xz plane, which are called Lamb waves and solutions with displacements perpendicular to the sagittal plane are called shear waves, SW. Lamb waves can be further divided into two categories of modes. Those with out-of-plane symmetric and antisymmetric displacements with respect to midplane of the plate are known as dilatational waves, DW, and flexural waves, FW, respectively.

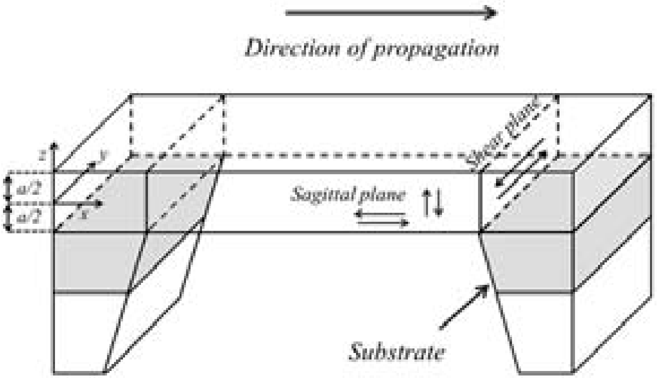

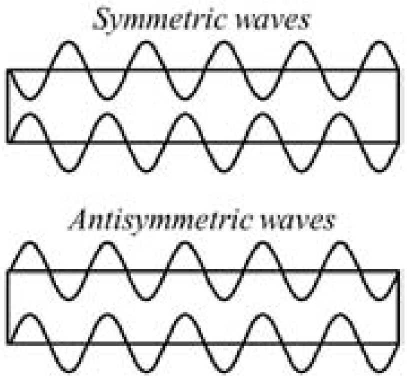

Figure 2.2 *Left: Scheme of a free-standing membrane. Right: Symmetric and antisymmetric waves.*

Lamb waves

The classical problem of Lamb's wave propagation is associated with a wave motion in a stress-free and isotropic plate. The solution of this system can be uncoupled between two fields: shear waves (*0, v, 0*) and sagittal waves (*u, 0, w*). The displacement fields of the sagittal waves are frequently written using the Helmholtz decomposition [82]. This consists in a linear combination of a scalar, ϕ, and vectorial, ψ, potentials functions:

$$U_i = \frac{\partial \phi}{\partial x_i} + \varepsilon_{ijk} \frac{\partial \psi_k}{\partial x_j} \qquad [2.5]$$

where ε_{ijk} is the Levi-Civita tensor and the scalar and vectorial potential correspond to irrotational and rotational fields, respectively. Introducing this solution in the equation of motion, Equation [2.4], is possible to uncouple the potentials generating two harmonic equations:

$$\nabla^2 \phi = \frac{1}{v_L^2} \frac{\partial^2 \phi}{\partial t^2} \qquad [2.6]$$

$$\nabla^2 \psi_i = \frac{1}{v_T^2} \frac{\partial^2 \psi_i}{\partial t^2} \qquad [2.7]$$

which has the typically plane wave solutions:

$$\begin{aligned} \phi &= \Phi(z) \exp[i(q_{//} x - \omega t)] \\ \psi &= \Psi(z) \exp[i(q_{//} x - \omega t)] \end{aligned} \qquad [2.8]$$

These equations represent travelling waves in the x direction, parallel to the surface, and standing waves in z direction. Finally, substituting these solutions in the Equations [2.6] and [2.7], respectively, leads to solutions for $\Phi(z)$ and $\Psi(z)$ as:

$$\begin{aligned} \Phi(\mathrm{z}) &= A_1 \sin(q_l z) + A_2 \cos(q_l z) \\ \Psi(\mathrm{z}) &= B_1 \sin(q_t z) + B_2 \cos(q_t z) \end{aligned} \qquad [2.9]$$

where q_l and q_t are the perpendicular component of the wavevector expressed as:

$$q_l^2 = \omega^2 / v_L^2 - q_{//}^2 \text{ and } q_l^2 = \omega^2 / v_L^2 - q_{//}^2 \qquad [2.10]$$

Finally, the displacements can be written in terms of the potentials. These solutions split in to two sets of modes: symmetric and antisymmetric modes with respect to midplane.

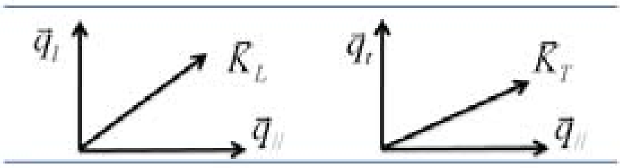

Figure 2.3 *Decomposition of longitudinal and transverse wavevectors.*

Symmetric and antisymmetric modes

For displacement in the plane direction, the motion will be symmetric or antisymmetric depending if the u components contain cosines or sines, respectively. The same rule applies to displacement perpendicular to plane.

Symmetric modes

$$\begin{aligned}\Phi &= A_2\cos(q_l z)\\ \Psi &= B_1\sin(q_t z)\\ u &= iq_{//}A_2\cos(q_l z) - q_t B_1\cos(q_t z)\\ w &= -q_l A_2\sin(q_l z) + iq_{//}B_1\sin(q_t z)\end{aligned} \qquad [2.11]$$

Antisymmetric modes

$$\begin{aligned}\Phi &= A_1\sin(q_l z)\\ \Psi &= B_2\cos(q_t z)\\ u &= iq_{//}A_1\sin(q_l z) + q_t B_2\sin(q_t z)\\ w &= q_l A_1\cos(q_l z) + iq_{//}B_2\cos(q_t z)\end{aligned} \qquad [2.12]$$

For symmetric (antisymmetric) modes, note that the wave motion are symmetric (antisymmetric) in *u* and antisymmetric (symmetric) in *w*.

This separation is only valid and possible for waves propagating along a symmetry axis of the plate. For multi-layer structures this separation is only possible if this symmetry exists in the system itself.

Once the displacements field are obtained the boundary conditions can be introduced. This gives homogenous systems of two equations for the two unknowns: A_2, B_1 for the symmetric case and A_1, B_2 for the antisymmetric case. The non-trivial solutions require that the determinant of the matrix coefficient vanishes in order to ensure solutions yielding the expression:

$$\frac{4q_{//}^2 q_{l,n} q_{t,n}}{(q_{t,n}^2 - q_{//}^2)^2} = -\left(\frac{\tan(q_{t,n}a/2)}{\tan(q_{l,n}a/2)}\right)^{\pm 1} \qquad [2.13]$$

where the exponents $+1$ and -1 correspond to symmetric and antisymmetric modes, respectively. The parameters q_l and q_t represent the longitudinal and transverse perpendicular component of the wavevector. The dispersion relation is found through the relationship between two perpendicular wavevectors:

$$\omega_n^2 = v_L^2\left(q_{//}^2 + q_{l,n}^2\right) = v_T^2\left(q_{//}^2 + q_{t,n}^2\right) \qquad [2.14]$$

The parallel wave vector, $q_{//}$, is numerically equal to ω/v_{ph}, where v_{ph} is the phase velocity of the mode with a frequency $f = \omega/2\pi$. By introducing Equation [2.14] in Equation [2.13] a non-linear equation is obtained, where for each value of $q_{//}$ there are many values for $q_{t,n}$ and $q_{l,n}$.

The solutions for $q_{l,n}$ and $q_{t,n}$ will be real or purely imaginary depending of the values taken by $q_{//}$. For real values of $q_{//}$, the values of q_t and q_l will be real if $\omega \geq v_{T,L}q_{//}$. The real values of q_l and q_t imply that the waves are propagating without damping, i.e., propagating waves. The pure imaginary values of q_l and q_t imply that the waves decay in the perpendicular direction. Such waves are called surface or Rayleigh waves, because their propagation is on the plane.

Other possibility is that $q_{//}$ can be take complex values. Taking $q_{//} = q^{re} + iq^{im}$ the time-harmonic factor becomes:

$$\exp\left(i(q^{re}x - \omega t)\right)\exp\left(-q^{im}x\right) \qquad [2.15]$$

Depending of the value taken by q^{im} there are three possible types of waves:

i. $q^{im} < 0$, waves which grow with distance, growing waves.

ii. $q^{im} = 0$, waves which propagate without damping, propagating waves.

iii. $q^{im} > 0$, waves which decay exponentially with distance, evanescent waves.

Growing waves (*i*) are waves the amplitude increases of which exponentially with the distance and physically have no meaning. Propagating waves (*ii*) are waves the amplitude of which does not change in the media. Evanescent waves (*iii*) are waves the amplitude of which decreases with distance from their source or upon interaction with a scattering centre.

To calculate the dispersion relation it is necessary to employ a numerical approach in order to solve the Equations [2.14] and [2.13]. A complete scheme to solve this system is described in the Appendix I.

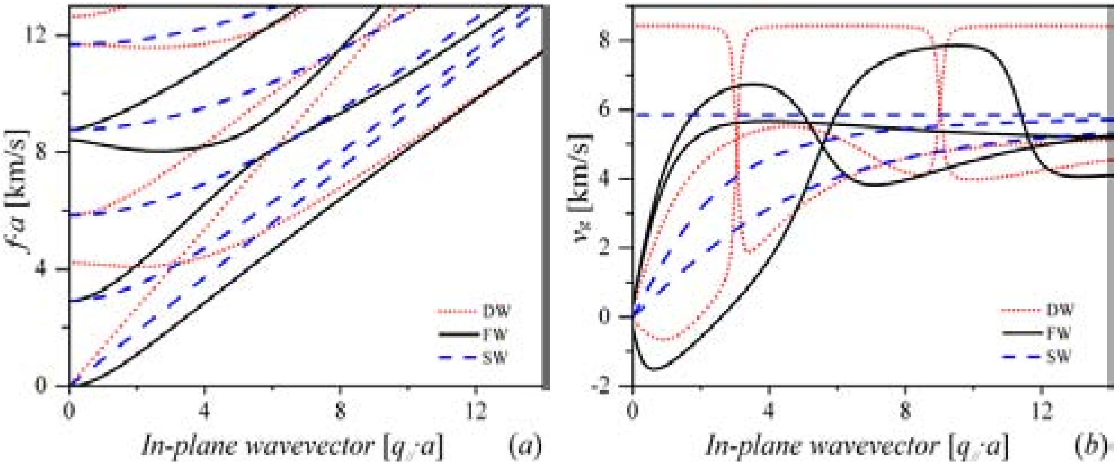

Figure 2.4 *(a) Dimensionless acoustic dispersion relation, f·a, and (b) group velocity,* v_g*, of Si membrane for dilatational (red dotted lines, DW), flexural (black solid lines, FW) and shear (blue dashed lines, SW) waves as a function of the dimensionless in-plane wavevector,* $q_{//}\cdot a$*.*

Figure 2.4 shows the phonons dispersion relation (*a*) and group velocity (*b*) of a Si membrane. An interesting characteristic of the dispersion relation can be observed for small values of $q_{//}$. In this regime the fundamental modes of the dilatational and flexural waves can be approximated by linear and quadratic dependences, respectively [87]. This dependence will be found to be important when determining the thermal properties in the low temperature regime, where these modes became the most populated states.

The values of perpendicular wavevector, q_l and q_t, for dilatational (*a*) and flexural (*b*) waves are shown in Figure 2.5. The values of q_l and q_t above the abscissa are real and below it are pure imaginary.

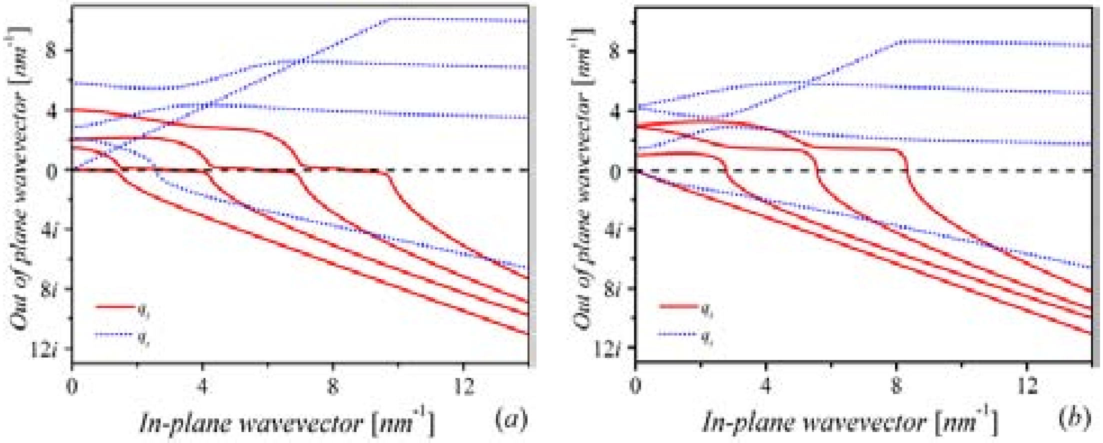

Figure 2.5 *Out-of-plane component of the wavevector, the red solid and blue dotted lines are q_l and q_t wavevector component respectively for dilatational (a) and flexural (b) waves.*

The linear behaviour of the zero-order dilatational mode is due to the pure imaginary values of perpendicular components of the wavevector, q_l and q_t, respectively. This means that the zero-order dilatational mode has terms extended throughout the width of the membranes (harmonic function, i.e., sine and cosines in q_t) as well as terms localized on the surface of the membranes (hyperbolic sine and cosines in q_l). On the other hand, the quadratic behaviour of the zero-order flexural mode is due to the fact that both values of the perpendicular wavevector have pure imaginary solutions, thus the acoustics vibrations are essentially localized on the surface and their amplitudes decrease exponentially from the surface to the interior of the membrane. The other of solutions of the system are divided in three types of behaviour:

i. Real solution of perpendicular wavevector, q_t and q_l.

ii. Real solution of q_t and pure imaginary solution of q_l.

iii. Pure imaginary solution of q_t and q_l.

The solution (*i*) means that these waves are extended throughout of the membrane, and commonly are called propagating waves. The solution (*ii*) means that there are waves extended throughout of the membrane (propagating waves) and waves localized on the surface (evanescent waves), which we will call them mixed waves. The solution (*iii*) means that all the waves are propagating in the plane of the membrane and decay towards the center (pure evanescent waves). Other kind of solutions are the standing waves obtained for long wavelength, $q_{//} \rightarrow 0$, or thin membranes, $d \rightarrow 0$, which behave like a confined standing wave between the surface of the membrane formed by the superposition of two counter-propagating plane waves [18].

Finally, all solutions of the system are harmonic waves which propagate through the crystal and result in a movement in the material. For this movement two types of velocity can be defined: the phase velocity, $v_{ph} = \omega/q_{//}$, as the speed of moving the points of equal phase and the group velocity, $v_g = \mathrm{d}\omega/\mathrm{d}q_{//}$, which is the speed of moving the wavefront (pulse wave formed of different frequency). Both quantities are approximately equal for the zero order modes in the limits $q_{//} \rightarrow 0$ and $q_{//} \rightarrow \infty$.

Shear Waves

These waves have only non-zero component perpendicular to sagittal plane $U = (0, v, 0)$. If solutions are taken as $v = \mathrm{V}(z)\exp[i(q_{//}x-\omega t)]$, the elastic equation can be written as:

$$\frac{d^2}{dz^2}\mathrm{V}(z) + (\omega^2 - S_T^2 q_{//}^2)\mathrm{V}(z) = 0 \qquad [2.16]$$

Taking stress-free as boundary conditions and defining $(v_T q_z)^2 = \omega^2 - (v_T q_{//})^2$, the solutions can be expressed in terms of:

$$V(\mathrm{z}) \propto \begin{cases} \cos(q_{z,n}z), & \mathrm{n = odd} \\ \sin(q_{z,n}z), & \mathrm{n = even} \end{cases} \quad \text{with } q_{z,n} = n\pi/a \qquad [2.17]$$

These modes are similar to the transverse modes in the bulk and their quantization is based on the simple integer half-wavelength fits in a plate of thickness a. Finally, the dispersion relation is generated for the expression $\omega = v_T (q^2_{//} + (n\pi/a)^2)^{1/2}$.

The solutions of shear waves are completely analytical and they only depend on the other n of the branches. Figure 2.4 shows the acoustic dispersion relation (a) and group velocity (b) of shear waves, SW, for a free-standing silicon membrane.

2.1.2 Layered systems

The problem of guided waves in layered systems can be used in multiple situations, e.g.: coating materials, painted structures, geological systems, multilayer systems, oxide materials, among others. Early studies on this topic were performed by Love in 1911 [85], who adding another interface to the “Rayleigh’s problem”, found out that shear waves can exist in the layer only when it is attached to a solid half-space of a different material. In 1924, Stoneley generalized the problem studying the propagation of waves at the interface of two solid half-spaces [88].

The first significant work on the wave propagation in multilayer media was done by Thomson [89] in 1950, who introduced a transfer matrix method. This method consists of reducing the layered systems into six equations, relating the boundary conditions at the first interface to the boundary conditions at the last interface, in the process, the equations for the intermediates interfaces are eliminated so that the fields in the layers of the plate are described solely of the external conditions. Others alternatives methods are: Global matrix proposed by Knopoff [90], plane wave expansion or Green functions.

From one layer to N layers

A simple solution to describe a layered system can be arrived at through the method proposed by Donetti et al. [91]. It consists of linear combinations of single layer solutions for each layer. The number of solutions used will be in according to the number of interfaces. For example, if the system consists in N layers, the number of interfaces will be N + 1. Two of these interfaces correspond to boundary and N − 1 to junctions between the layers. Then, the total number of equation generates will be 6N. Six equations are related to the boundary condition, e.g. stress-free or clamped surfaces and the other 6N − 6 equations correspond to the continuity condition of the displacement and stress field in each interface.

Separating the waves in shear and sagittal waves, the system is reduced to 4N sagittal equations and 2N shear equations. If the system has symmetry with respect to the midplane, the number of equation is reduced again in N shear equations and 2N sagittal equations. Taking into account the number of equations needed to express the solutions with the same number of unknowns, i.e., give the number of waves that will be used for each layer.

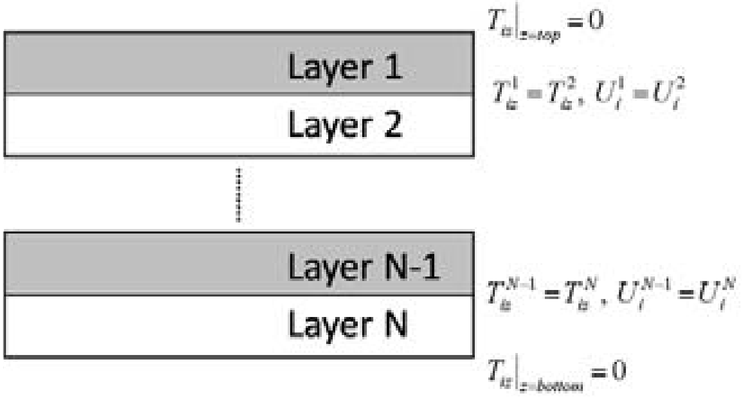
$T_{iz}|_{z=top}=0$
Layer 1
Layer 2
$T_{iz}^{1}=T_{iz}^{2},\ U_i^{1}=U_i^{2}$
Layer N-1
Layer N
$T_{iz}^{N-1}=T_{iz}^{N},\ U_i^{N-1}=U_i^{N}$
$T_{iz}|_{z=bottom}=0$

Figure 2.6 *Scheme of layered system*

Example

Consider the system shown in Figure 2.7, here the number of layer is three, i.e., the total number of equations necessary to describe the system is 18, of which twelve are sagittal and six are shear equations. If the first and last layers are equals, the system has symmetry with respect of the midplane. Then, the numbers of independent equations is only six. Finally the solutions for each layer will be given as:

$$\begin{aligned} u_{1,3}(z) &= DW_x + FW_x \\ w_{1,3}(z) &= DW_z + FW_z \\ u_2(z) &= DW_x \text{ or } FW_x \\ w_2(z) &= DW_z \text{ or } FW_z \end{aligned} \qquad [2.18]$$

where u_i (w_i) is the x (z) component of the amplitude of displacement in the media i and $DW_x(z)$ ($FW_x(z)$) is symmetrical (antisymmetrical) solution in x (z) component. Expanding Equation [2.18], the solutions are:

$$\begin{aligned} u_{1,3}(z) &= iA_{1,3}q_{//}\sin(q_{l1,3}z) + B_{1,3}q_{t1,3}\sin(q_{t1,3}z) + iC_{1,3}q_{//}\cos(q_{l1,3}z) \\ &\quad - D_{1,3}q_{t1,3}\cos(q_{t1,3}z) \\ w_{1,3}(z) &= A_{1,3}q_{l1,3}\cos(q_{l1,3}z) + iB_{1,3}q_{//}\cos(q_{t1,3}z) - C_{1,3}q_{l1}\sin(q_{l1,3}z) \\ &\quad + iD_{1,3}q_{//}\sin(q_{t1,3}z) \\ u_2(z) &= iA_2q_{//}\cos(q_{l2}z) - B_2q_{t2}\cos(q_{t2}z) \;\; or \;\; iA_2q_{//}\sin(q_{l2}z) + B_2q_{t2}\sin(q_{t2}z) \\ w_2(z) &= -A_2q_{l2}\sin(q_{l2}z) + iB_2q_{//}\sin(q_{t2}z) \;\; or \;\; A_2q_{l2}\cos(q_{l2}z) + iB_2q_{//}\cos(q_{t2}z) \end{aligned} \qquad [2.19]$$

with linear dispersion relation given by:

$$\omega^2 = v_{Li}^2(q_{li}^2 + q_{//}^2) = v_{Ti}^2(q_{ti}^2 + q_{//}^2), \; i = 1, 2, 3 \qquad [2.20]$$

where A_1, A_2, A_3, B_1, B_2, B_3, C_1, C_3, D_1, D_3 are the unknowns. Note that in the intermediate layer only one type of symmetric or antisymmetric wave is used, due to the symmetry of the system. This implies that symmetric and antisymmetric wave solutions can be decoupled.

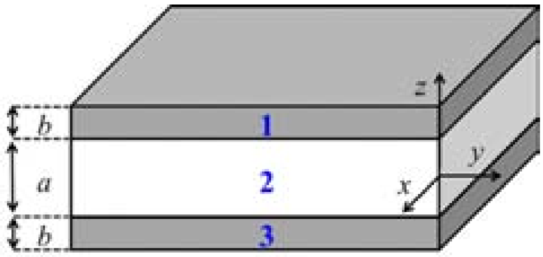

Figure 2.7 *Scheme of symmetric three-layer system. Here "b" is the thickness of layer 1 and 3, and "a" is the thickness of layer 2 of layered system*

Finally, continuity and boundary conditions are applied at the interface and external surfaces, respectively. This produces a system of six linear equations with six unknowns. The dispersion relation will be given by setting to zero the determinant of the matrix of the corresponding system.

CHAPTER III: ANHARMONICITY AND THERMAL CONDUCTIVITY

Considering the wave-particle duality, it is possible to express lattice waves as quanta of vibrational energy, i.e., as a particle. The associated particle is the phonon[*] and it represents the discretization of vibrational energy of an atom or group of them.

In a crystalline system, all the thermodynamic properties are linked to the statistics of phonons. There are several of approaches to describe the phonons in a solid crystal. The most common it is assume that the amplitude of the atomic displacement is smaller than the interatomic distance. This leads to the harmonic approximation of the Hamiltonian, which is sufficiently accurate to describe most of the properties of the crystal at low temperatures. However, as increases the temperature certain properties cannot be explained using only harmonic terms. At higher temperatures the harmonic approximation breaks down and the introduction of the anharmonic theory is required to explain physical properties.

3.1 Harmonic effect in crystals

At temperatures lower than the melting point, the assumption of small oscillations appears to be reasonable for solid crystals. However, this description is poor and it does not represent adequately the system.

Under the harmonic approximation, the phonon states are stationary. This implies that a phonon distribution, which carries a thermal current, will remain unaltered in the course of time. Then, the thermal current will be forever unchanged, i.e., a perfect harmonic crystal will have an infinite thermal conductivity. However, the thermal conductivity in a real crystal cannot be infinite for several reasons given the inevitable imperfections, impurities and boundaries. Even, if the crystal were perfect and infinity, the presence of anharmonic terms in the interatomic potential would produce interaction between the phonons, setting a limit to the mean free path and, consequently, to the thermal conductivity [72].

---

[*] To be more precise, the term phonon is not a particle but rather it is quasi-particle since it needs a medium to propagate.

3.2 Phonon-phonon interaction

Let us consider the most general case of the lattice with a basis. The atoms are labelled by two symbols, *l* and *b*, where *l* is the vector from the origin to the cell and *b* is the basis vector to the atom in the cell (see Figure 3.1).

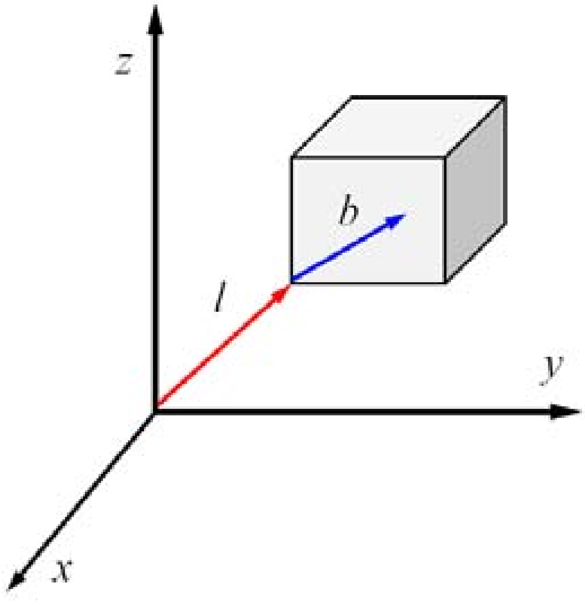

Figure 3.1 *Diagrammatic representation of coordinates of a lattice point.*

Using a Taylor expansion, the potential energy of the system, ϕ, can be written as a power series around its minimum:

$$
\begin{aligned}
V = V_0 &+ \sum_{lb,\alpha} \left.\frac{\partial \phi}{\partial u_\alpha(lb)}\right|_0 u_\alpha(lb) + \frac{1}{2}\sum_{\substack{lb,l'b'\\ \alpha,\beta}} \left.\frac{\partial^2 \phi}{\partial u_\alpha(lb)\partial u_\beta(l'b')}\right|_0 u_\alpha(lb)u_\beta(l'b') \\
&+ \frac{1}{3!}\sum_{\substack{lb,l'b',l''b''\\ \alpha,\beta,\gamma}} \left.\frac{\partial^3 \phi}{\partial u_\alpha(lb)\partial u_\beta(l'b')\partial u_\gamma(l''b'')}\right|_0 u_\alpha(lb)u_\beta(l'b')u_\gamma(l''b'') + \text{....higher order terms}
\end{aligned}
\qquad [3.1]
$$

where $u_\alpha(lb)$ is the displacement of the atom α in the cell l in the position b. The first term is a constant, which can be set as zero; the second term is zero because the system is in the minimum of its energy, i.e. equilibrium configuration; the third term represent the interatomic force constant, harmonic term; and the last one represents the anharmonic term or perturbation of the Hamiltonian.

This last term is responsible for the phonon-phonon interaction and, depending of case, it could contain terms higher than the cubic one. By introducing higher-order terms in the Hamiltonian these could be included as perturbations of the classical Hamiltonian. This leads to transitions between eigenstates, i.e., the creation and destruction of particles. If the anharmonic terms are sufficiently small compared to the harmonic terms, it is possible to calculate the effect of the perturbation using the perturbation theory. Then, the anharmonic part can be written as a perturbation of the harmonic Hamiltonian, such as:

$$
\begin{aligned}
&H_{pp} = \frac{1}{3!}\sum_{lb;l'b';l''b''} \eta_{l,b}\eta_{l',b'}\eta_{l'',b''} \otimes A_{l,b;l',b';l'',b''} \\
&u_\alpha(lb) \rightarrow \eta_{l,b} \\
&A_{l,b;l',b';l'',b''} = \frac{\partial^3 \phi}{\partial \eta_{l,b}\partial \eta_{l',b'}\partial \eta_{l'',b''}}
\end{aligned}
\qquad [3.2]
$$

Which expressed in terms of the wave operator, i.e., using a Fourier transform, can be rewritten as:

$$H_{pp} = \frac{1}{3!}(N_0\Omega)^{-3/2} \sum_{\substack{qb;q'b'\\q''b''}} \sum_{l,l',l''} e^{-i(ql+q'l'+q''l'')} \Lambda_{l,b}\Lambda_{l',b'}\Lambda_{l'',b''} \otimes A_{l,b;l',b';l'',b''} \qquad [3.3]$$

where N_0 represents the number of units cell, Ω the volume of each unit cell and $\Lambda_{l,b}$ is the Fourier transform of $\eta_{l,b}$.

Considering the crystal symmetry, it is convenient to change the summations over *l'* and *l''* to those over new variables *h'* and *h''*, defined by *l' = l + h'* and *l'' = l + h''*. Then substituting in Equation [3.3] the Hamiltonian becomes:

$$\begin{aligned} H_{pp} &= \frac{1}{3!}(N_0\Omega)^{-1/2} \sum_{\substack{qb;q'b'\\q''b''}} \sum_{l} e^{-i(q+q'+q'')l} \Lambda_{l,b}\Lambda_{l',b'}\Lambda_{l'',b''} \otimes F_{l,b;l',b';l'',b''} \\ F_{l,b;l',b';l'',b''} &\equiv \sum_{hh'} e^{-i(q'h'+q''h'')} A_{l,b;l+h',b';l+h'',b''} \end{aligned} \qquad [3.4]$$

Applying the orthogonal properties of the crystal the summation over *l* has to vanish unless:

$$\delta_{l,q} = \frac{1}{N_0\Omega}\sum_{l} e^{-i(q+q'+q'')l} \begin{cases} =1 & if \quad q+q'+q''=G \\ =0 & if \quad q+q'+q''\neq G \end{cases} \qquad [3.5]$$

where *G* is a reciprocal lattice vector. Then, the perturbed Hamiltonian is given by

$$H_{pp} = \frac{1}{3!}(N_0\Omega)^{-3/2} \sum_{\substack{qb;q'b'\\q''b''}} \delta_{G,q+q'+q''} \Lambda_{l,b}\Lambda_{l',b'}\Lambda_{l'',b''} \otimes F_{l,b;l',b';l'',b''} \qquad [3.6]$$

Using second quantization, it is possible to express the unperturbed and perturbed Hamiltonian as a combination of creation, a^{*}_{qs}, and annihilation, a_{qs}, operators given by:

$$H_0 = (N_0\Omega)^{-1/2} \sum_{qs} \hbar\omega_{qs}\left(a^{*}_{qs}a_{qs} + \frac{1}{2}\right) \qquad [3.7]$$

$$H_{pp} = \frac{1}{3!} \sum_{qs;q's'q''s''} \delta_{G,q+q'+q''} \psi_{qs;q's';q''s''} \left(a^{*}_{qs} - a_{-qs}\right)\left(a^{*}_{q's'} - a_{-q's'}\right)\left(a^{*}_{q''s''} - a_{-q''s''}\right) \qquad [3.8]$$

where $\psi_{qs;q's';q''s''}$ is a scalar quantity, resulting from annihilation-creation transformation, defined by

$$\psi_{q,s;q',s';q'',s''} = i\left(\frac{\hbar^3}{N_0\Omega\omega_{qs}\omega_{q's'}\omega_{q''s''}}\right)^{1/2} \sum_{bb'b''} \frac{e_{q,b,s}e_{q',b',s'}e_{q'',b'',s''} \otimes F_{l,b;l',b';l'',b''}}{\sqrt{m_b m_{b'} m_{b''}}} \qquad [3.9]$$

where m is the atomic mass of the atom localized in the position b.

This factor is an average of the Fourier transformed tensor projected on the directions of the polarizations vectors $e_{q,b,s}$.

Therefore, the effect of anharmonicity is to introduce interactions among the independent phonons of a crystal. In first-order perturbation approximation, the cubic term in the potential causes interactions of three phonons and in second-order, interactions involving four phonons. Similarly, the quartic term causes, in first-order perturbation, four phonon interactions, etc.

3.2.1 Normal and Umklapp process

Solving all the combination of the expression [3.8] four basic processes can be distinguished:

i. Annihilation of two phonons and creation of third phonon: $a_{-qs}\, a_{-q's'}\, a^*_{q''s''}$.

ii. Annihilation of one phonon and creation of two phonons: $a_{-qs}\, a^*_{q's'}\, a^*_{q''s''}$.

iii. Simultaneous creation of three phonons: $a^*_{qs}\, a^*_{q's'}\, a^*_{q''s''}$.

iv. Simultaneous annihilation of three phonons: $a_{-qs}\, a_{-q's'}\, a_{-q''s''}$.

However, only the combinations (*i*) and (*ii*) are permitted because they satisfy energy conservation, while processes (*iii*) and (*iv*) are forbidden because they violate it. Nevertheless, processes (*iii*) and (*iv*) have to be taken into account to develop higher-order terms in the perturbed Hamiltonian.

These operators basically create and destroy different phonons states. For example, the combination $a_{-qs}\, a_{-q's'}\, a^{*}_{q's''}$ has the effect of reducing by unity the number of the quanta in the modes ($-q$, s), ($-q'$, s') and increasing by unity the number in the mode (q'', s''), i.e., it creates a phonon in (q'', s'') destroying two phonons, in the sates ($-q$, s) and ($-q'$, s') (See Figure 3.2). However, this interaction is limited by the Kronecker delta, which vanishes unless:

$$q + q' + q'' = G \qquad [3.10]$$

where q, q' and q'' are restricted to the first Brillouin zone.

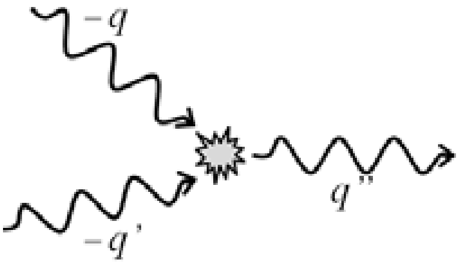

Figure 3.2 *Diagrammatic representation of a phonon-phonon interaction.*

If $G = 0$ the wavevector of the created phonon is the result of the vectorial sum of the wavevectors of the phonons being destroyed. This interaction is known as normal processes, N-processes. In these processes the energy and the momentum of the phonons are conserved, thus, there is no contribution to the thermal resistance.

When $G \neq 0$ the interaction is denominated Umklapprozesse, U-processes, and it indicates that the phonons “flip over” in the process [92]. In the U-processes, in opposite to N-processes, the momentum is not conserved, which produces a thermal resistance. Figure 3.3 shows a diagram of N and U-processes.

The argument for U-processes can be interpreted, as a collision of two phonons with "large" wavevectors *q* and *q'*, which generating a third phonon with a wavevector outside the Brillouin zone, which can be brought back into the Brillouin zone by the addition of a *G* vector.

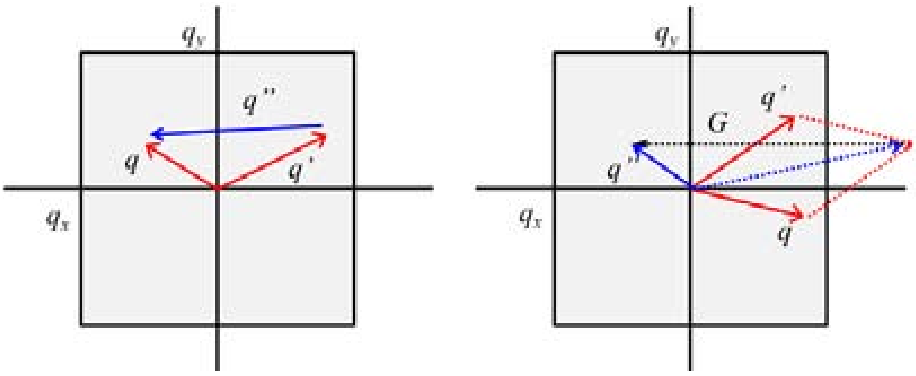

Figure 3.3 *Diagrammatic representation of Normal and Umklapp processes, left and right respectively.*

As discussed above, the introduction of cubic or higher order terms in the potential causes phonon-phonon interactions, if terms were absent, there would be not heat diffusion. This is simply because the carriers of the heat are the phonons. Their collision introduce anharmonic terms, otherwise, the thermal conductivity of a crystal would be infinite. Others consequences of the introduction of anharmonic terms include:

i. Deviations of the temperature dependence of specific heat at high temperatures.

ii. Electron-phonon and phonon-phonon interaction.

iii. Temperature dependence of phonon frequencies (thermal expansion).

iv. Finite phonon lifetimes.

Selection Rules: Normal and Umklapp processes.

As been mentioned above, the N-processes occur when momentum is conserved, i.e., the vectorial sum of the wavevectors lie inside of the first Brillouin zone. One graphic example of these selection rules is show in Figure 3.4. There, the phonon frequency is represented as a function of wavevector, for a given radial direction from the centre to the border of the Brillouin zone. Where *O* is the origin of dispersion relation and *O'* corresponds to the chosen value *q* with polarization *s*. At this point, the same dispersion relation is drawn again but with origin at *O'*. This results in the intersections of curves $O't_1'$, $O't_2'$, $O'l'$ and Ot_1'', Ot_2'', Ol'' at the points Q_1, Q_2 and Q_3, with values q'' and ω'' that satisfying the selection rules for momentum and energy in N-processes.

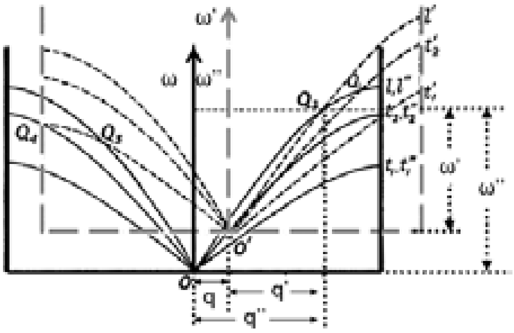

Figure 3.4 *Construction for intersection of three phonons in a line for N process, adapted from ref.* [7].

Usually the shape of dispersion relation is such that they are upwardly convex and tend to have a horizontal tangent at the border of the Brillouin zone, visually in this region there are not intersections between the branches, i.e., "*there is no process in which all three phonons belong to the same polarization branch of the spectrum*" [7]. However, this statement is only valid for U-processes, because, the dispersion relation of low frequency phonons can be approximate as Debye-like dispersion, allowing the normal interaction processes of the phonons with the same polarization [17,93–95].

If the index l and t are relabelled as longitudinal, L, and transverse, T, polarization, respectively, based the Figure 3.4 it is possible to define two types of interactions in the points Q_1 and Q_2:

$$\begin{aligned} Q_1 &: T + T \leftrightarrow L \\ Q_2 &: T + L \leftrightarrow L \end{aligned} \qquad [3.11]$$

This generates another rule: "*the created phonon must lie in a higher branch than one at least of the destroyed phonons*" [7]. Similarly, it is possible to establish a different selection rule for U-processes, with, the condition that the intersections points have to be outside of Brillouin zone (see Figure 3.5).

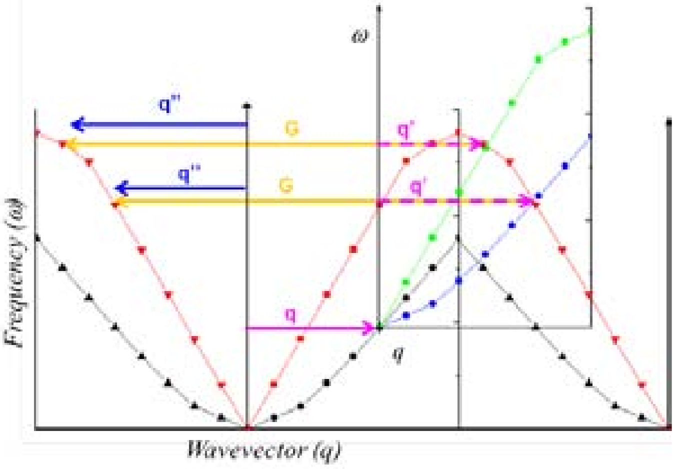

Figure 3.5 *Construction of the intersection of three phonons in a line to illustrate Umklapp-process.*

3.3 Phonon lifetime: relaxation time approximation

The term relaxation is used to describe how a state or ensemble of states returns to equilibrium state. If a system in equilibrium is subjected to an external perturbation, such as a temperature change, the system is perturbed and the lagging time it takes to return to equilibrium is called relaxation time.

The phonon attenuation time or lifetime refers to the time taken by a phonon and/or wavepacked of them to be scattered, attenuated or absorbed. In a solid crystal a variety of mechanisms exists including: impurities, isotopes, defects, dislocations, boundaries as well as collision with other quasi-particles or excitations such as electrons, magnons, photons or other phonons.

Depending on the nature of the scattering mechanism they can be divided in two interaction types: inelastic scattering and elastic scattering. Typically, the scattering due to impurities, isotopes, defects, dislocations or boundaries are treated as elastics scattering, because they only produce a change of the direction in the phonon path. The scattering resulting from collisions with other particles, i.e., “ons”-phonon interaction, are treated as inelastic scattering. Mathematically, these scatterings are a consequence of the anharmonic terms in the interatomic potential.

As discussed before, the phonon-phonon interaction can be divided in two process Normal and Umklapp processes. Both processes are governed by energy and momentum conservation rules.

$$\omega + \omega' \leftrightarrow \omega'' \qquad [3.12]$$

$$q + q' \leftrightarrow q'' \qquad \text{N processes} \qquad [3.13]$$

$$q + q' \leftrightarrow q'' + G \qquad \text{U processes} \qquad [3.14]$$

The N-processes do not lead to a thermal resistance because the momentum is conserved, but they change the distribution in the phonon frequency, thus indirectly affecting to other scattering process which depends on frequency, such as impurity or U-processes. Therefore, these processes indirectly contribute to thermal conductivity.

Assuming that each process is independent from each other, the effective relaxation time, τ, can be expressed using the Mattheissen's rule:

$$\frac{1}{\tau}=\frac{1}{\tau_U}+\frac{1}{\tau_B}+\frac{1}{\tau_I}+\cdots=\sum_i \tau_i^{-1} \qquad [3.15]$$

where τ_U is relaxation time for Umklapp processes, τ_B the contribution of boundary scattering and τ_I the contribution of impurity scattering.

3.3 Evaluation of phonon relaxation times

Finite sample size, the imperfections such as inhomogeneity, isotopes differences, dislocations, and anharmonicity in the crystal potential provide the main phonon-scattering sources in non-metallic solids. Each scattering mechanism contributes to limiting the lifetime of the phonons. These mechanisms give rise to intrinsic relaxation time (due to anharmonicity) or to extrinsic relaxation times (due to the medium).

In particular, the phonon lifetime limits value of the quality factor of micro/nano-scaled mechanical resonators. Moreover, as mention above, they are a necessary input parameter for accurate calculations of nanoscale thermal transport. Although, the fundamental understanding of the phonon lifetime is well established the testing of these models against experimental data has been challenging due to the complexity of the models, the use of fitting parameters that still remains unknowns, e.g. the Grüneisen parameter, and also due to the few experimental reports of phonon lifetime in the gigahertz and terahertz regimes.

3.3.1 Extrinsic relaxation times

Boundary scattering

The main extrinsic scattering mechanism in the nanoscale is the surface roughness scattering. The effect of boundary scattering due to surface roughness may be introduced through a boundary condition on the steady-state Boltzmann transport equation [7]. An extended explanation of this formalism can be found in Appendix II.

Intuitively, the boundary condition is that all the phonons which reach the boundary at an arbitrary position, r_B, will be reflected with the normal component of their velocity reversed, v_n. Introducing a displaced Bose-Einstein distribution function $n_{qs} = n_{qs,0} + g_{qs}(r)$, where $n_{qs,0}$ is the equilibrium distribution, the boundary condition can be derived to have the following form:

$$g_{qs}(r_B)\Big|_{v_n} = p g_{q's}(r_B)\Big|_{-v_n} \qquad [3.16]$$

In this treatment, the effect of the roughness is described by a single phenomenological parameter, p, which represents the "polish" of the surface, with $p = 0$ for perfectly rough surfaces and $p = 1$ for perfectly smooth surfaces. For the case of thin films and/or membrane, it is possible derive a phonon wavelength-dependent specularity $p(\lambda)$ by considering a plane wave normally incident on the boundary, i.e., standing waves. The change in phase ϕ of the wave reflected from the boundary is related to the roughness, and varies thickness of the membrane, as:

$$\phi(x) = \frac{4\pi}{\lambda} y(x) \qquad [3.17]$$

where x is the direction parallel to the membrane surface, and $y(x)$ is a continuous function representing the deviation of the height of the surface from a reference plane. From this, the wavelength-dependent specularity can be derived by considering the auto-correlation function of the phase [7], $p(\lambda) = \exp(-\pi\bar{\phi}^2) = \exp(-16\pi^2\eta^2/\lambda^2)$, where η is the root mean square deviation of $y(x)$, sometimes known as the *asperity*, henceforth referred to as the *roughness*. The physical interpretation of this expression is that phonons with shorter wavelengths will be more affected by the surface roughness than longer wavelength phonons.

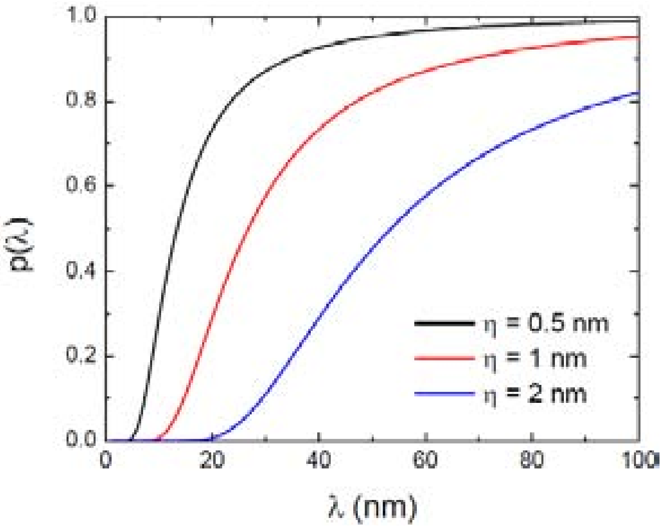

Figure 3.6 *Wavelength-dependent specularity p(λ) as a function of phonon wavelength λ for roughness values of η = 0.5 nm (black), η = 1 nm (red), η = 2 nm (blue).*

Once the wavelength-dependent specularity $p(\lambda)$ is determined, it is possible to calculate the effective mean free path in the membrane. After considering multiple reflections from the boundary in series, the mean free path can be written as:

$$\Lambda = \frac{1+p(\lambda)}{1-p(\lambda)}\Lambda_0 \qquad [3.18]$$

where Λ_0 is the characteristic dimension of the structure, i.e. the thickness of the film. Considering that the mean free path can expressed in terms of group velocity and lifetime,

$\Lambda = \tau_B v_g$, it is possible to express the boundary relaxation time as a function of the thickness of the film, a, the group velocity, v_g, the wavelength, λ, and the roughness parameter, η, such as:

$$\tau_B = \frac{\Lambda}{v_g} = \frac{a}{v_g}\frac{1+\exp(-16\pi^2\eta^2/\lambda^2)}{1-\exp(-16\pi^2\eta^2/\lambda^2)} = \frac{a}{v_g}\coth\left(\frac{8\pi^2\eta^2}{\lambda^2}\right) \qquad [3.19]$$

Impurity scattering

This scattering process is a consequence of the internal imperfections of the crystal, such as: atomic mass differences, substitutional and interstitial impurities, changes in atomic forces constants or vacancy defects. The impurity scattering mechanisms are assumed to change the phonon wavevector and/or polarization, but not its energy, i.e. $\omega_{qs} = \omega_{q's'}$. The transition of probability of these occurrences is governed by the Fermi's golden rule.

For phonons with wavelength larger than imperfection typical size, the scattering is essentially of Rayleigh type. Therefore, the scattering time is inversely proportional to the fourth power of frequency. The relaxation time can be expressed following the Rayleigh regime in radiation theory [17]

$$\tau_{q,s}^{-1}(md) = \frac{\Gamma V_0}{4\pi v_{g,s}^3}\omega_{q,s}^4 \qquad [3.20]$$

$$\Gamma_{md} = \sum_i fi\left[\left(1-\frac{M_i}{\bar{M}}\right)^2 + 2\left(\frac{\Delta g_i}{g} - 6.4\gamma\frac{\Delta\delta_i}{\delta}\right)^2\right] \qquad [3.21]$$

where V_0 is the volume per atom and Γ is determined from the nature of the imperfection, $\bar{M}$ the average atomic mass and f_i the fraction of the unit cells having atomic mass M_i. The fractional spatial extent of the imperfection is expressed as $\Delta\delta_i/\delta$, $\Delta g_i/g$. They represent the fractional stiffness constant of the nearest-neighbour bonds from the imperfection to the host crystal and γ is an average anharmonicity of bonds linking the imperfection.

3.3.2 Intrinsic relaxation times

As seen above, the inclusion of anharmonicity in the Hamiltonian leads to phonon-phonon interactions which become increasingly important as the temperature increases.

Limiting the crystals anharmonicity to the cubic terms, the relaxation time associated to three-phonon interactions can be treated using the first-order perturbation theory and four-phonon interactions using second-order perturbation theory. In general, four-phonon processes are ignored because their small contribution to the thermal conductivity [96]. In the literature the anharmonic relaxation time has been expressed as a product of frequency and temperature $\tau_{ph} \propto \omega^n T^m$, where the exponents are chosen depending of temperature range. However, with a systematic theoretical approach this relationship is subtancially more complexbecoming a continuous function over the entire range of frequencies and temperature.

According to the type of interaction, three-phonon processes can be classified in two classes [17], as shown in Figure 3.7. In **class I** two phonons are annihilated and one phonon is created and in **class II** one phonon is annihilated and two phonons are created.

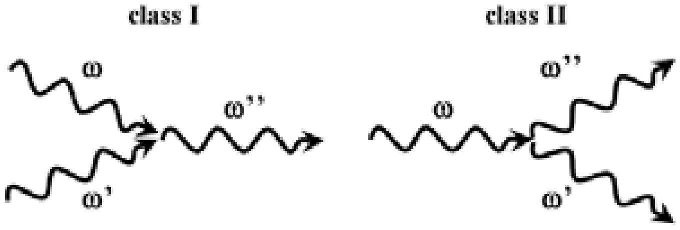

Figure 3.7 *Schematic representation of three phonon-phonon scattering processes.*

The phonon-phonon scattering rates can be studied by applying Fermi's golden rule, which is based on first order time-dependent perturbation theory. Where the probability of the initial state goes to the final state is given by

$$W_{qq'q''} = \frac{2\pi}{\hbar} \left| \langle f | H_{pp} | i \rangle \right|^2 \delta\left(E_f - E_i\right) \qquad [3.22]$$

where H_{pp} is given by Equation [3.8]; i and f correspond to the initial and final states of the phonon distributions; and the delta Dirac function ensures the energy conservation.

Depending of the class of the event the delta energy is

$$\begin{aligned} E_f - E_i &= \hbar\left(\omega_{q''s''} - \omega_{qs} - \omega_{q's'}\right) \text{ for class I} \\ E_f - E_i &= \hbar\left(\omega_{qs} - \omega_{q's'} - \omega_{q''s''}\right) \text{ for class II} \end{aligned} \qquad [3.23]$$

The scattering rates due to class I and II and their reverses contribute to phonon scattering can be expressed in term of collisional part of BTE given by:

$$\left.\frac{\partial n_{qs}}{\partial t}\right|_{col} = \frac{n_{qs} - n_{qs,0}}{\tau_{qs}} = \sum_{q's',q''s''} \left[\left(W^{(I)}_{qs,q's',q''s''} - W^{(I,reverse)}_{q''s'',qs,q's'} \right) + \frac{1}{2}\left(W^{(II)}_{qs,q's',q''s''} - W^{(II,reverse)}_{q''s'',qs,q's'} \right) \right] \qquad [3.24]$$

where the factor 1/2 is due to the indistinguishability between processes where *q'* and *q''* switch places and change the phonon distributions. As an example, the calculations of the matrix element due to a class I process give:

$$\begin{aligned} W^{(I)}_{qs,q's',q''s''} = \frac{2\pi}{\hbar^2} &\left| \langle n_{qs} - 1, n_{q's'} - 1, n_{q''s''} + 1 | H_{pp} | n_{qs}, n_{q's'}, n_{q''s''} \rangle \right|^2 \\ &\times \delta\left(\omega_{qs} - \omega_{q's'} - \omega_{q''s''}\right) \end{aligned} \qquad [3.25]$$

In an isotropic continuum model in the Debye approach, the anharmonic perturbation has eight combinations. Once the annihilator and creator operators are bracketed between the initial and final state (see Equation [3.25]), there are only three combinations in class I, which give non-zero matrix elements. Then, the equation for class I reduces to:

$$W^{(I)}_{qs,q's',q"s"} = \frac{\pi\hbar}{4\rho^3 N_0 \Omega} \frac{qq'q''}{v_s v_{s'} v_{s"}} \left|A^{ss's"}_{qq'q"}\right|^2 n_{qs} n_{q's'} \left(n_{q"s"}+1\right) \times \delta_{q+q'+q",G} \delta(\omega_{qs} - \omega_{q's'} - \omega_{q"s"}) \qquad [3.26]$$

where $|A^{s,s',s"}_{q,q',q"}|^2$ are the Fourier components of the phonon coupling constants, giving the three-phonon scattering strength. In same way it is possible to define the expression for the transition probability in class II:

$$W^{(II)}_{qs,q's',q"s"} = \frac{\pi\hbar}{4\rho^3 N_0 \Omega} \frac{qq'q''}{v_s v_{s'} v_{s"}} \left|A^{ss's"}_{qq'q"}\right|^2 (n_{qs}+1) n_{q's'} n_{q"s"} \times \delta_{q+q'+q",G} \delta(\omega_{qs} - \omega_{q's'} - \omega_{q"s"}) \qquad [3.27]$$

Finally, using the single-mode relaxation time approximation, assuming that only the phonon in the mode *qs* has a displaced distribution function, i.e., $n_{qs} = n_{qs,0} + \psi_{qs} n_{qs,0}(n_{qs,0} + 1)$, and that all other phonons have their equilibrium distribution, i.e., $\psi_{q's'} = \psi_{q''s''} = 0$, then under these considerations Equation [3.24] can be write as:

$$\tau^{-1}_{qs} = \frac{\pi\hbar}{4\rho^3 N_0 \Omega} \sum_{q'p',q"p"} \left[\left|A^{ss's"}_{qq'q"}\right|^2 \frac{qq'q''}{v_s v_{s'} v_{s"}} \left\{ \frac{n_{q's',0}\left(n_{q"s",0}+1\right)}{n_{qs,0}+1} \delta(\omega_{\mathrm{qs}} + \omega_{\mathrm{q's'}} - \omega_{\mathrm{q"s"}}) \times \delta_{s+s'+s",G} + \frac{1}{2} \frac{n_{q's',0} n_{q"s",0}}{n_{qs,0}} \delta(\omega_{\mathrm{qs}} - \omega_{\mathrm{q's'}} - \omega_{\mathrm{q"s"}}) \delta_{q+G,q'+q"} \right\} \right] \qquad [3.28]$$

where three-phonon scattering strengths, $|A^{s,s',s"}_{q,q',q"}|^2$, can be approximated as [71]:

$$\left|A^{ss's"}_{qq'q"}\right|^2 = \frac{4\rho^2}{\overline{v}^2} \gamma_s^2 v_s^2 v_{s'}^2 v_{s"}^2 \qquad [3.29]$$

with γ_s as the mode-average Grüneisen's constant, $\overline{v}$ as the phonon average group velocity given by:

$$\bar{v} = \frac{\sum_{qs} v_{qs} n_{qs,0}}{\sum_{qs} n_{qs,0}} \qquad [3.30]$$

The real value of the Grüneisen parameter is not known with sufficient degree of accuracy, and sometimes it is treated as a semi-adjustable parameter.

Finally, to evaluate the phonon-phonon interaction, Equation [3.28] , it is necessary to express the sum in *q'*-space by an integral in all space:

$$\sum_{q's'} \rightarrow \sum_{s'} \int d^3 q' \qquad [3.31]$$

A numerical scheme to perform the integration within the Brillouin zone and the phonon density of state is required.

Phonon density of states

The phonon density of states is one of the most important quantities to determinate the thermal conductivity. Similarly to electronic density of states, this is defined as the number of states per unit frequency. In principle, the density of states may be computed exactly, by calculating the energies of all the allowed states in the specimen. But the complexity behind does not allow to calculate and approximation have to be made.

The number of allowed **q** values for which the phonon frequency is between ω and $\omega + d\omega$ is given by:

$$D(\omega)d\omega = \frac{N_0 \Omega}{8\pi^3} \int_{Shell} d^3\mathbf{q} \qquad [3.32]$$

where N_0 is the number of cells with a volume **Ω**. This integral goes over all the volume of the shell in the q-space bound by two constant surfaces ω and $\omega + d\omega$ [97]. To calculate the total volume of the shell, it is possible to approximate it as small and straight cylinder with basal area dS_ω and high $dq_\perp$,

$$\int_{shell} d^3\mathbf{q} = \int dS_\omega dq_\perp = \int dS_\omega \frac{d\omega}{|d\omega/dq|} = \int_{\omega=const.} \frac{dS_\omega}{|v_g|} d\omega \qquad [3.33]$$

Then the DOS is given by

$$D(\omega) = \frac{N_0\Omega}{8\pi^3} \int_{\omega=const.} \frac{dS_\omega}{|v_g|} \qquad [3.34]$$

Calculating $D(\omega)$ using the Equation [3.34] requires the full integration over all the Brillouin zone of the crystal, i.e., the full dispersion relation for all possible directions is also required. To avoid the full integration, symmetry properties can be used and the total integration is reduced to the irreducible part of the Brillouin zone. Although crystal symmetry properties can reduce the problem, the element of area still remains intractable and, in general, the only way to calculate this integral is numerically or making some approximations.

Einstein and Debye approximations

A very simple DOS model was proposed by Einstein in 1907. He considered a solid as an ensemble of independent quantum harmonic oscillators vibrating at the same frequency, ω_E. In this case, the density of states would be worth zero for $\omega \neq \omega_E$, or one for frequencies $\omega = \omega_E$.

Although the model reproduces quite well the expected behaviour of the heat capacity at high temperatures (T > Θ_D, where Θ_D is the Debye temperature), the Dulong-Pettit law or classical limit, it breaks down at low temperatures, (T > Θ_D/10). In this regime, Einstein formula predicts a faster decrease of heat capacity as compared to experimental data.

Based on the fact that at low temperature most of the excited phonons populate the short-wavevector or long-wavelength acoustic branches, Debye suggested that an isotropic and linear dispersion relation, $\omega_s(q) = v_s q$, can be used for all the normal modes lying within a sphere of radius q. Then the element of area, dS_ω, can be approximated by an element of area of a sphere of radius q:

$$dS_\omega = q^2 \sin(\theta) d\theta d\phi \qquad [3.35]$$

In addition, in the continuum approximation the phonon group velocity is the same as the phase velocity, $v_{g,qs} = v_s$, therefore the Equation [3.34] can be reduced to:

$$\begin{aligned} D(\omega_s) &= \frac{N_0 \Omega}{8\pi^3} \frac{q^2}{v_s} \iint \sin(\theta) d\theta d\phi \\ &= \frac{N_0 \Omega}{2\pi^2} \frac{\omega^2}{v_s^3} \end{aligned} \qquad [3.36]$$

There are two conventions regarding the normalization of the phonon DOS. It can be either normalized to unity or to the total number of vibrational modes, $3N$, where N is the number of atoms. Thus, it is possible to define an upper limit in wavevector, q_D, or equivalently in the frequency ω_D, which represents the maximum radius of a sphere which contains $3N$ modes:

$$\begin{aligned} 3N &= \frac{N_0 \Omega}{2\pi^2} \sum_s \frac{1}{v_s^3} \int_0^{\omega_D} \omega^2 d\omega \\ &= \frac{N_0 \Omega}{2\pi^2} \omega_D^3 \frac{1}{\bar{v}^3} \end{aligned} \qquad [3.37]$$

where $\bar{v}$ is an average of the sound velocity given by:

$$\frac{1}{\bar{v}^3} = \frac{1}{3}\sum_s \frac{1}{v_s^3} \qquad [3.38]$$

Using Equation [3.37] it is possible to define an average cut-off wavevector, q_D, and averaged frequency, ω_D, given by:

$$\omega_D = \bar{v} q_D = \bar{v}\left(\frac{6\pi^2 N}{N_0 \Omega}\right)^{1/3} \qquad [3.39]$$

Similarly, it is also possible to define the averaged Debye temperature, Θ_D, for the solid by the relation $k_B\Theta_D = \hbar\omega_D$. This represents the temperature at which the wavelength of vibration of the atoms in a crystal is equal to the length of the unit cell.

3.4.3 Phonon-phonon interaction and the Debye approximation

To calculate the phonon-phonon interaction a full knowledge of the realistic dispersion relation inside of the first Brillouin zone is necessary. The complex evaluation of this quantity usually makes does that the study of three-phonon processes intractable. Thus motivating the use of a much simpler model based on the Debye approximation. However, the continuum approach used in Debye's model does not allow for a physical picture of U-processes, because there is no concept of a reciprocal lattice vector in the continuum. To overcome this problem, Parrot [98] and Srivastava [99,100] designed the following expression for a pseudo-lattice wavevector, "*G*", in the continuum.

$$G = 2q_D \frac{q \pm q'}{|q \pm q'|} \qquad [3.40]$$

where q_D is the Debye radius and the +/– signs correspond to class I and II events, respectively. Including the linear dispersion relation leads two news N-processes such as: T + T → T and L + L → L, which are forbidden in non-linear dispersion relation [7].

In this model is possible to approximate the sum in *q'*-space by an integral in all space. Once this replacement is made, the sum in *q''* can be eliminated using the Kronecker delta function, then the sum in *q'* can be expressed by:

$$\sum_{q's'} \rightarrow \frac{N_0\Omega}{8\pi^3} \sum_{s'} \int d^3q' \qquad [3.41]$$

After some algebra, the expression for the relaxation time for class I and class II events is given by:

$$\begin{aligned} \tau_{qs}^{-1} = \frac{\pi\hbar}{4\rho^3 N_0\Omega} \frac{N_0\Omega}{8\pi^3} 2\pi \sum_{p',p'',G} \frac{1}{v_s v_{s'} v_{s''}} \int_0^{\pi} \sin\theta' d\theta' \int \left| A_{qq'q''}^{ss's''} \right|^2 qq'q''q'^2\, dq' \\ \times \left[\frac{n_{q's',0}\left(n_{q''s'',0}+1\right)}{n_{qs,0}+1} \delta(\omega_{\mathrm{qs}} + \omega_{\mathrm{q's'}} - \omega_{\mathrm{q''s''}}) \right. \\ \left. + \frac{1}{2} \frac{n_{q's',0}\, n_{q''s'',0}}{n_{qs,0}} \delta(\omega_{\mathrm{qs}} - \omega_{\mathrm{q's'}} - \omega_{\mathrm{q''s''}}) \right] \end{aligned} \qquad [3.42]$$

where $|q''| = |G - (q \pm q')|$ and G is equal zero for N-processes. Using the Equation [3.40] in the expression of *q''* the reduced form:

$$|q''| = (1-\varepsilon)q_D + \varepsilon\, |q \pm q'| \qquad [3.43]$$

with ε = +1/–1 for N/U-processes, respectively. Taken the three-phonon scattering strengths given in Equation [3.29] and a linear dispersion relation, the relaxation time is given by:

$$\tau_{qs}^{-1}=\frac{\hbar}{16\pi\rho^{3}}\sum_{s',s''}\frac{\left|A_{qq'q''}^{ss's''}\right|^{2}}{v_{s}v_{s'}v_{s''}^{2}}\int qq'q''q'^{2}\,dq'$$
$$\times\left[\frac{n_{q's',0}\left(n_{q''s'',0}+1\right)}{n_{qs,0}+1}\int_{0}^{\pi}\delta(q''\text{-}Cq-Dq')q''\sin\theta' d\theta' \right. \qquad [3.44]$$
$$\left.+\frac{1}{2}\frac{n_{q's',0}n_{q''s'',0}}{n_{qs,0}}\int_{0}^{\pi}\delta(q''\text{-}Cq+Dq')s''\sin\theta' d\theta'\right]$$

with $C = v_s/v_{s''}$ and D = $v_{s'}/v_{s''}$. The angular integral can be solve using the Dirac delta function properties [17], finally the expression for the relaxation time on Debye approach is given by:

$$\tau_{qs}^{-1}=\frac{\hbar q_{D}^{5}}{16\pi\rho^{3}}\sum_{s',s''}\frac{\left|A_{xx'x''}^{ss's''}\right|^{2}}{v_{s}v_{s'}v_{s''}^{2}}\left[\int\frac{n_{x's',0}\left(n_{x''_{+},0}+1\right)}{n_{xs,0}+1}x'^{2}\,x''_{+}(1-\varepsilon+\varepsilon(Cx+Dx'))dx'\right.$$
$$\left.+\frac{1}{2}\int\frac{n_{x's',0}n_{x''_{-},0}}{n_{xs,0}}x'^{2}\,x''_{-}(1-\varepsilon+\varepsilon(Cx-Dx'))dx'\right] \qquad [3.45]$$

with $x = q/q_D$, $x' = q'/q_D$, $x''_{\pm} = Cx \pm Dx'$, and $n_{x''\pm,0}$ is the Bose-Einstein distribution function evaluated in $x''_{\pm}$. The different scattering event for N and U-processes are summarized in Table 3.1.

The energy and momentum conservation rules for N and U-processes impose certain restriction on the integration of the x'. The areas of integration in the space $x - x'$ for U and N-processes are summarized in the Figure 3.8 and Figure 3.9

$\omega+\omega'\rightarrow\omega''$					$\omega\rightarrow\omega'+\omega''$				
s	*s'*	*s''*	*C*	*D*	*s*	*s'*	*s''*	*C*	*D*
L	*T*	*L*	1	v_T/v_L	*L*	*T*	*T*	v_L/v_T	1
T	*T*	*L*	v_T/v_L	v_T/v_L	*L*	*L*	*T*	v_L/v_T	v_L/v_T
T	*L*	*L*	v_T/v_L	1	*L*	*T*	*L*	1	v_T/v_L
L	*L*	*L*	1	1	*L*	*L*	*L*	1	1

Table 3.1 *N and U-processes interactions. s is the polarization, L and T are the longitudinal and transverse polarization, respectively. The processes described in the last row is only valid for N-Processes*

x_1	$(v_L - v_T)/(v_L + v_T)$	x_4	$(v_L - v_T)/v_L$
x_2	$(v_L - v_T)/v_T$	x_5	$2v_T/(v_L + v_T)$
x_3	$(v_L - v_T)/2v_L$	x_6	$(v_L + v_T)/2v_L$

Table 3.2 *Limit values for areas of integration in the x-x' space, with v_L and v_T longitudinal and transverse sound velocity, respectively.*

The new formulation can be simplified again to consider the high and low temperature limits, but this would not permit to see and to understand easily the interaction between the phonons in the crystal.

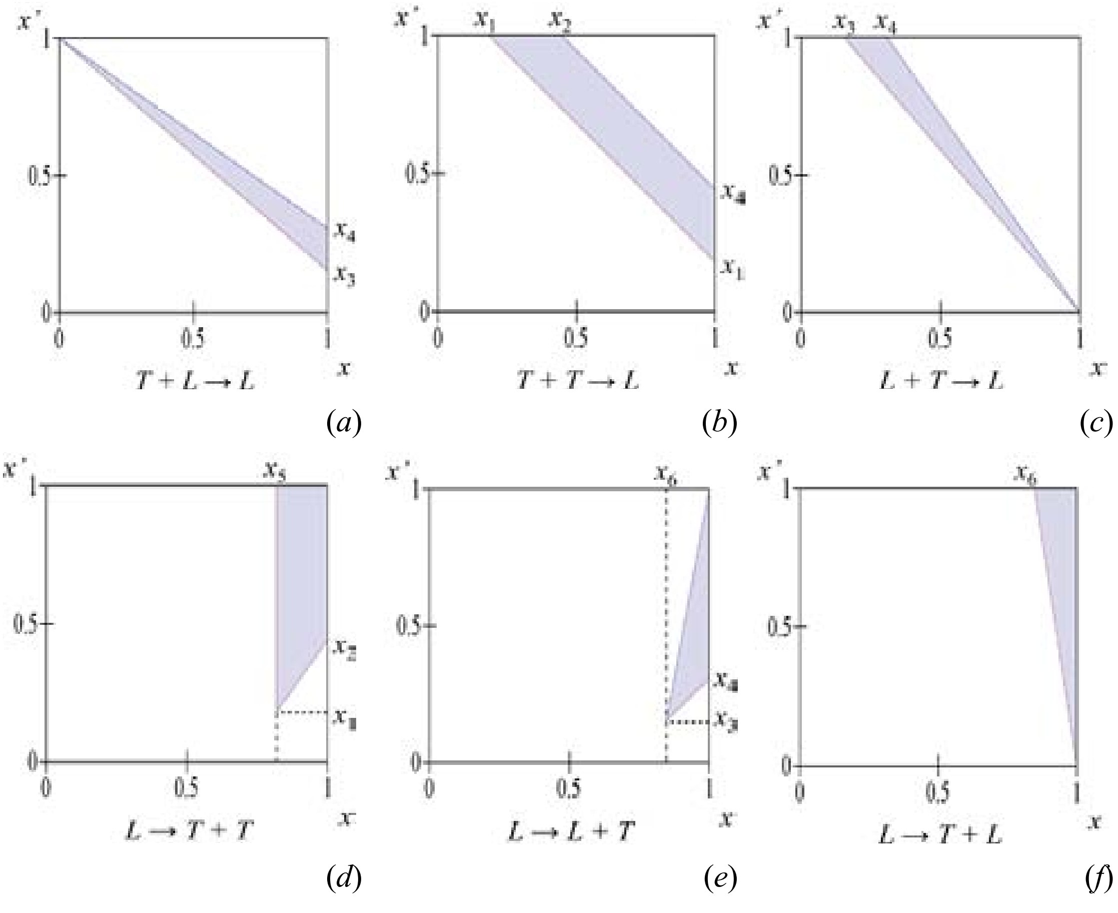

(*a*) (*b*) (*c*)

(*d*) (*e*) (*f*)

Figure 3.8 *(a-f): Areas of Integration in the x-x' plane allowed for U-processes. Where $x_{i = 1 \text{ to } 6}$ are given in Table 3.2*

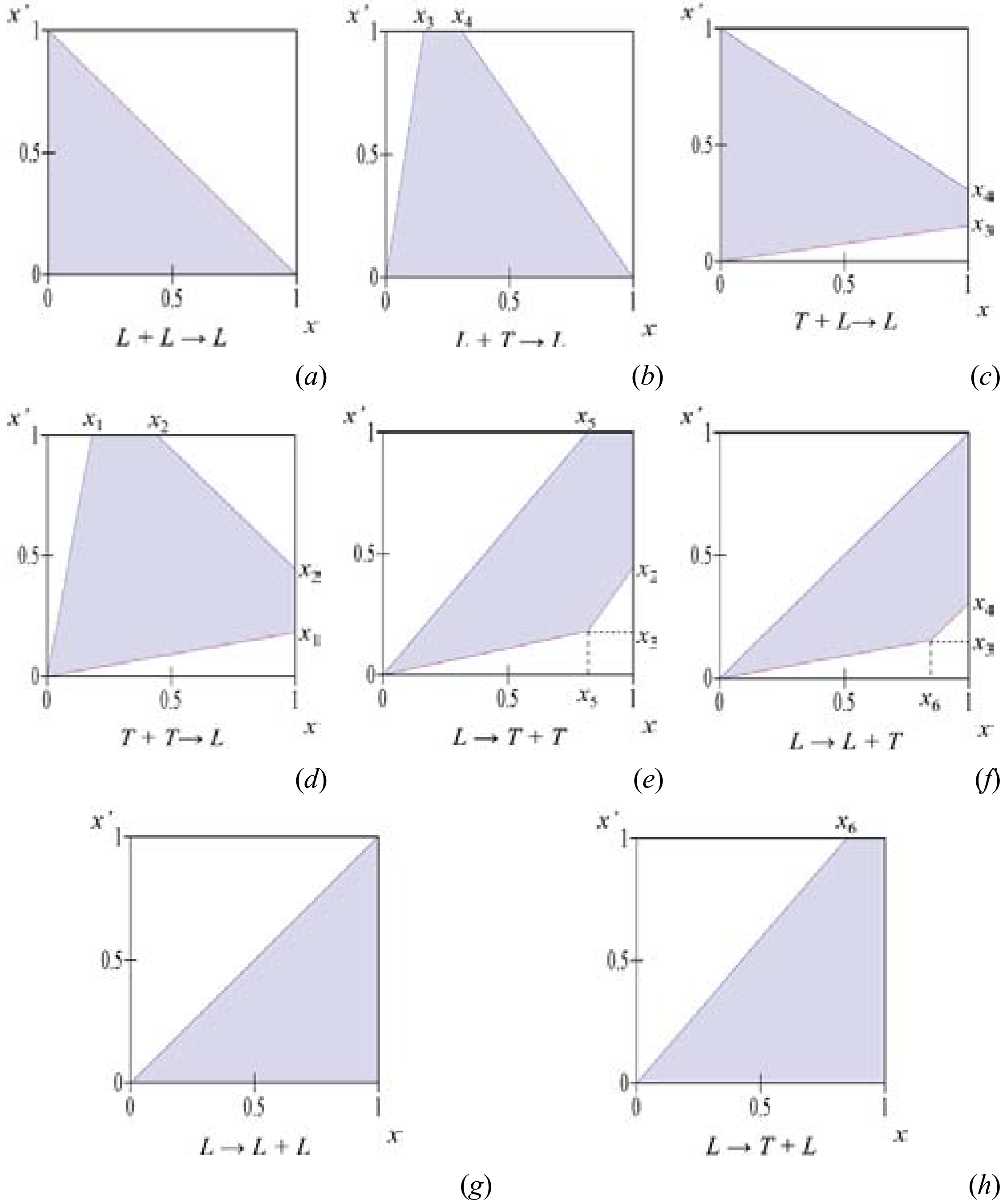

(*a*) (*b*) (*c*)

(*d*) (*e*) (*f*)

(*g*) (*h*)

Figure 3.9 *Areas of Integration in the x-x' plane allowed for N-processes. Where* $x_{i=1\ \mathrm{to}\ 6}$ *are given in Table 3.2*

Numerical simulations

As an example, simulations of U-processes were performed by using the Equation [3.45] under the Debye approach. The selection rules employed are show in Table 3.1, with the limit values for areas of integration show in Figure 3.8 and Figure 3.9. All simulations were performed using a computational algorithm developed using the commercial code MATLAB^{TM} and Mathematica. The material parameters used in the simulation are summarized in the Table 3.3

Parameter	Symbol	Value	Reference
Lattice constant	a_0	0.543 nm	[101]
Atomic mass	M	46.6×10^{-27}Kg	[101]
Density	ρ	2330 Kg/m^3	[101]
Averaged longitudinal Grüneisen parameter	γ_L	1.14	[102]
Averaged transverse Grüneisen parameter	γ_T	0.56	[102]
Longitudinal velocity	S_L	8440 m/s	[103]
Transversal velocity	S_T	5845 m/s	[103]
Debye radius	q_D	1.435×10^{10} m^{-1}	[17]

Table 3.3 *Silicon parameters used in the simulation of Umklapp-processes in the bulk system.*

Bulk Umklapp-processes

Figure 3.10 shows the relaxation rate, $1/\tau_U$, for class I and class II events at room temperature. The higher relaxation rate processes of class II are due to the allowed participation of only phonon with large energies in these events.

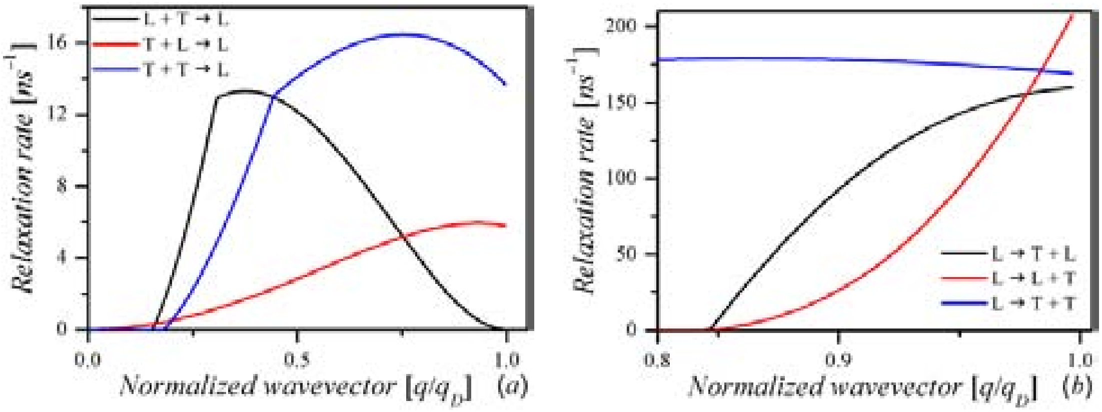

Figure 3.10 *Relaxation rate, $1/\tau_U$, for bulk silicon at room temperature via class I (a) and class II (b) event.*

Figure 3.11 shows the contribution to the total intrinsic relaxation time of each process. For class I events, Figure 3.11*a*, the larger contribution comes from $L + T \rightarrow L$ process at small values of normalized wavevector. But, its contribution decreases as the normalized wavevector begin to take larger values, where the more important contribution comes from $T + T \rightarrow L$ process. For class II events, Figure 3.11*b*, the bigger contribution comes from $L \rightarrow T + T$ process. At large values of normalized wavevector the contribution of the three processes becomes comparable.

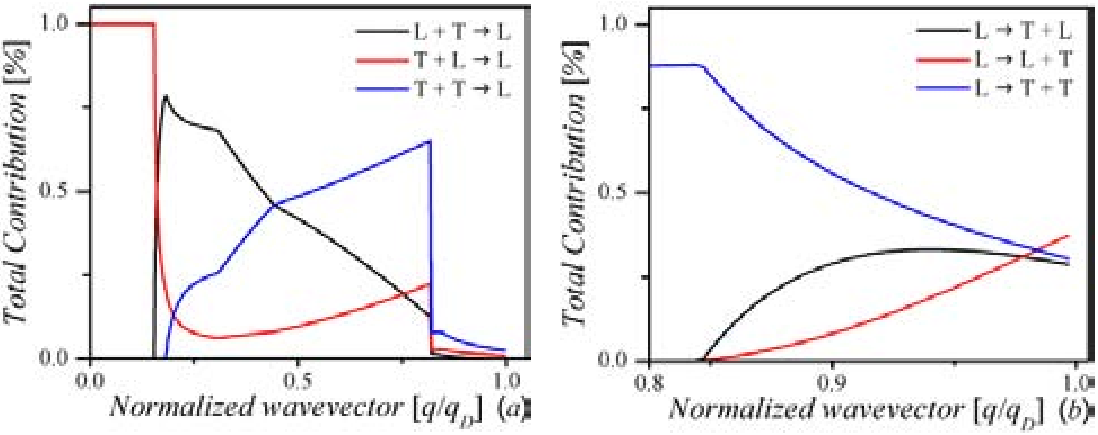

Figure 3.11 *Relative contribution to the total intrinsic relaxation time for each processes and event*

Figure 3.12 shows the total relaxation time for U-processes at room temperature. From this picture is possible to observe that for small normalized wavevector the contribution come from class I event and decrease dramatically at $q/q_D \approx 0.8$ where the more important contribution comes from class II events.

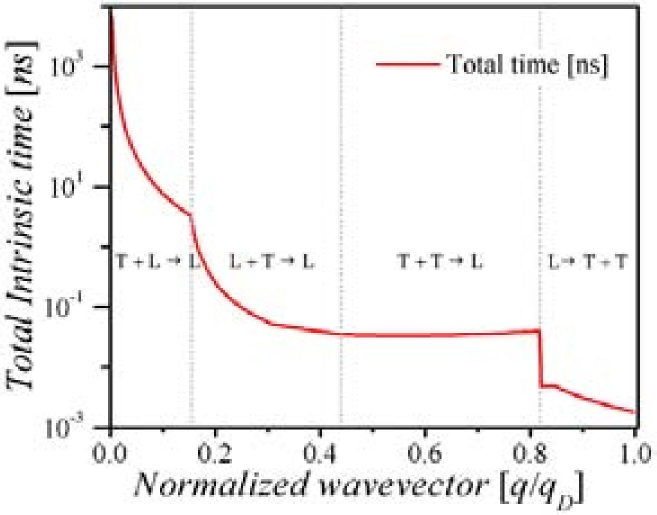

Figure 3.12 *Total relaxation rate for Umklapp-processes. Grey dotted line denotes the different zones where each processes dominate.*

The relaxation rate as function of temperature and reduced wavevector for different phonon-phonon processes is shown Figure 3.13. The important feature from these pictures is the increase of the relaxation rate as function of temperature. This is due to the fact that at high temperature the phonon population can be approximated by $n_{qp,0} \approx k_BT/\hbar\omega$ and the relaxation rate is directly proportional to temperature.

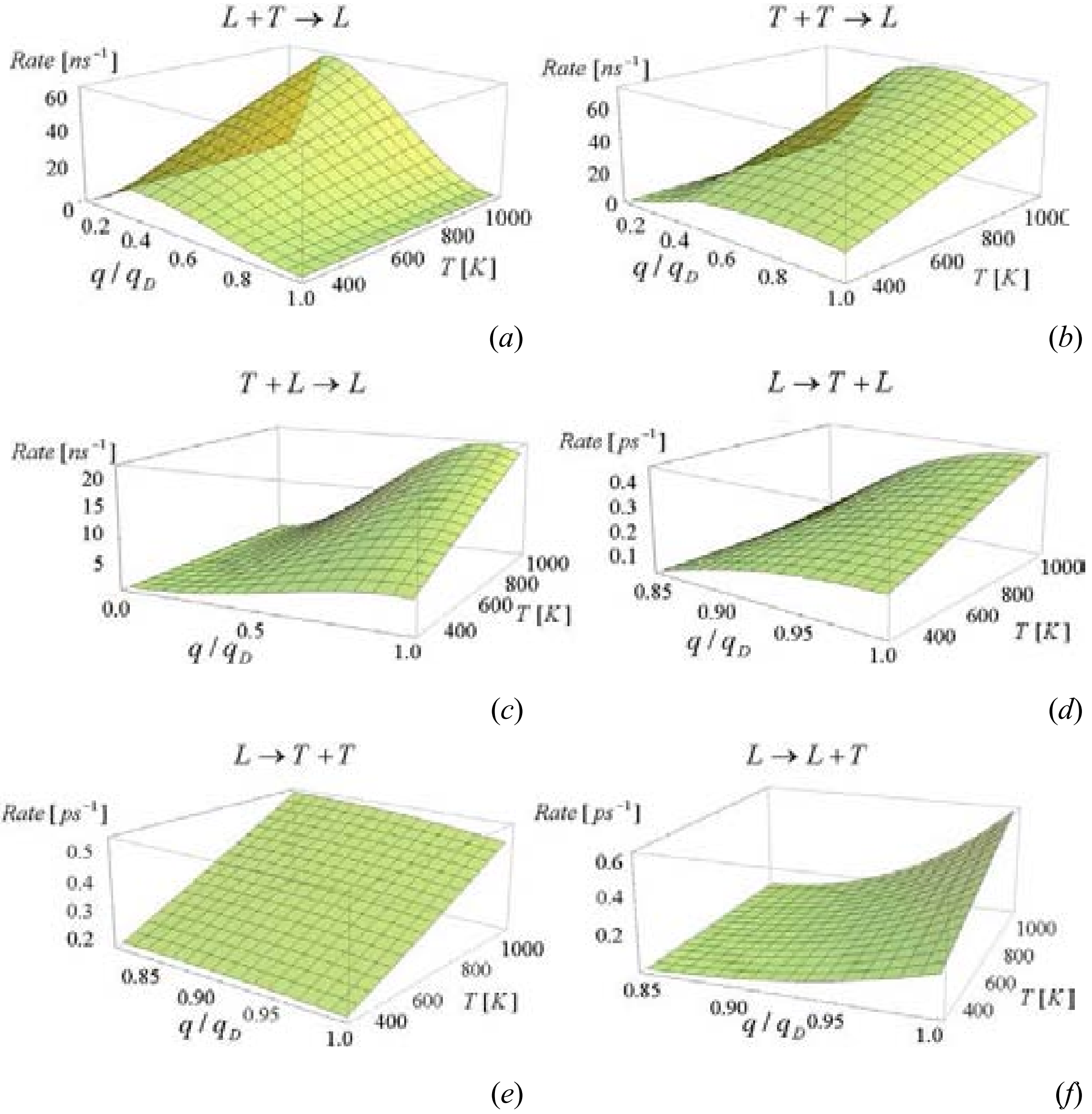

(*a*) (*b*)

(*c*) (*d*)

(*e*) (*f*)

Figure 3.13 *Relaxation rate as a function of temperature and reduced wavevector for different phonon-phonon processes.*

Figure 3.14 and Figure 3.15 show the total relaxation time, as a function of temperature and reduced wavevector, for class I and II respectively. The total contribution for each event was plotted separately because of the large difference between the two interactions. In general the class II event involves ultra-short time due to the high-frequency phonons involves in these processes.

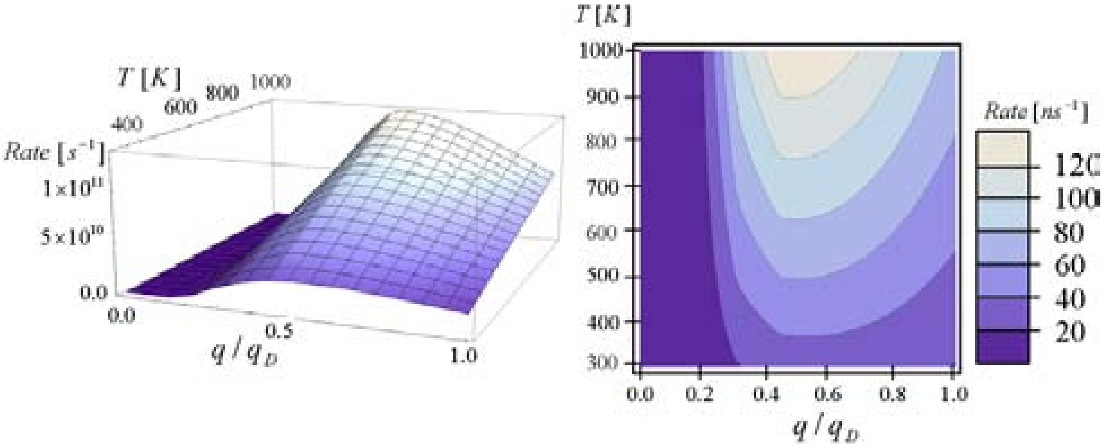

(*a*) (*b*)

Figure 3.14 *Total relaxation rate for class I event as a function of temperature and reduced wavevector: (a) three-dimensional plot, (b) contour plot (isoline).*

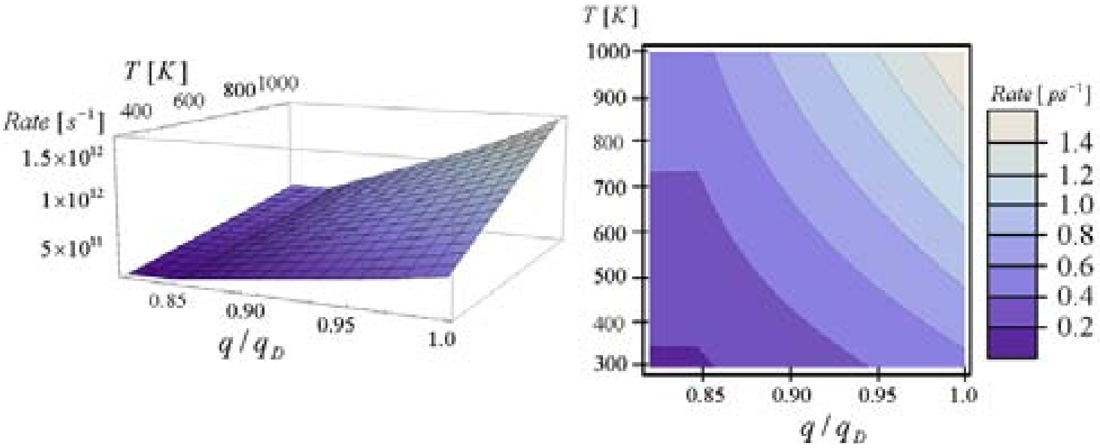

(*a*) (*b*)

Figure 3.15 *Total relaxation rate for class II event as a function of temperature and reduced wavevector: (a) three-dimensional plot, (b) contour plot (isoline).*

One consequence of the Debye approximation is an overestimation of the class II event. That is a consequence of the linear-like dispersion relation, which produces faster decay of the border zone phonons due to its energy is higher than the real one. In general to avoid this problem, it is possible to use the Holland approach [104], but the limits of the integration areas have to be redefined.

Intrinsic sound absorption: Akhieser and Landau-Rumer mechanisms

The intrinsic sound absorption[*] can be explained using two theoretical approaches: (*i*) Landau-Rumer or three-phonon scattering processes [105] and (*ii*) Akhieser mechanism or viscous damping mechanism [106]. The dominant processes will depend of two factors: the wavelength of the absorbed phonon, λ, and the mean free path of the thermal phonons, Λ_{mfp}, i.e. the average of the mean free path of thermally excited phonon in the crystal.

If the λ of the acoustic wave is much larger than the typical Λ_{mfp} of the thermal phonons, i.e. $f\tau_{TH} << 1$, we can assume that the acoustic wave is interacting with the whole of the thermal phonons. This range is known as the Akhieser regime. But if the λ is much smaller than the Λ_{mfp}, i.e., $f\tau_{TH} >> 1$, then the phonon attenuation is better described in the Landau-Rumer regime and the phonon attenuation is due to three-phonon interaction processes. The main difference between both approaches is the point of view how the sound wave is considered. In the Landau-Rumer approximation the sound wave is treated microscopically, i.e., as a phonon, whereas in the Akhieser approximation the sound wave is treated macroscopically. In general, the momentum associated to the interacting phonon is not enough to produce a collision that generates a phonon outside of the Brillouin zone. Then U-processes can be neglected in comparison with the N-processes and the Landau-Rumer and Akhieser mechanisms can be treated as pure N-processes.

In the Akhieser damping mechanism the sound of wave is considered as a macroscopic strain field in the crystal, a driving force, which produces a shift in the equilibrium distribution function of thermal phonons. The disturbed system will then tend to return to equilibrium through collision between thermal phonons leading to the absorption of the acoustic wave. Theoretically, the Akhieser mechanism can be obtained using the BTE under the relaxation time approximation for the collision part. For the case where the thermoelastic damping is negligible, the relaxation time can be written as [106–108]

---

[*] In general the sound absorption is related with acoustic phonon with frequency smaller than 1 THz

$$\tau_{AK}^{-1}(\omega_s) = \frac{C_V T}{2\rho v_s^2} \frac{\omega_s^2 \tau_{TH}}{(1+\omega_s^2 \tau_{TH}^2)} \left(\langle \gamma^2 \rangle - \langle \gamma \rangle^2 \right) \qquad [3.46]$$

where the lifetime of the thermal phonon can be approached by [109–111].

$$\tau_{TH} \approx \frac{3\kappa}{C_V \bar{v}^2} \qquad [3.47]$$

Originally, the Akhieser theory was developed for high temperatures where the average of the phonon mean free path of the thermal phonons is much less than the wavelength of the absorbed acoustic wave, i.e., $f\tau << 1$. Years later, the theory was developed in details by Woodruff and Ehrenreich [112] and Maris [107], who extended the limits to include values $f\tau > 1$ and $f\tau = 1$, respectively.

3.4 Thermal conductivity: modelling and approximations

The thermal conductivity, κ, is defined as the material ability to conduct heat and, in general, the total thermal conductivity can be expressed as a sum of all heat carrier contributions. In a semi-conductor, alloys and non-metallic media, the dominant carriers of the heat are lattice vibrations, i.e., phonons. In a macroscopic system, the thermal conductivity is related to the thermal flux through the Fourier´s law. This equation establishes a link between the heat flux, Q, and the temperature gradient, dT/dr, caused by it:

$$Q = \kappa \frac{dT}{dr} \qquad [3.48]$$

The calculation of the thermal conductivity is a major mathematical challenge due to the complexity of the variables involved. The first thermal conductivity models for bulk systems were based on the solution of phonon BTE under the single mode relaxation time approximation [67–70]. This approach provides the simplest picture of phonons interactions considering that each phonon mode has a single relaxation time independent of others modes, i.e., it assumes that all other phonons have their own undisturbed equilibrium distribution [17]. The calculation of the thermal conductivity in semiconductor materials imply the knowledge of three major frequency-dependent parameters, i.e., the specific heat, C_V, the phonon group velocity, v_g, and the phonon mean free path, $\Lambda = v_g \tau$. This leads to:

$$\kappa = \frac{1}{3}\sum_{qs} C_{V,qs} v_{g,qs} \Lambda_{qs} = \frac{1}{3}\sum_{qs} C_{V,qs} v_{g,qs}^2 \tau_{qs} \qquad [3.49]$$

The dispersion relation can be approximated using different approaches such as: the sine function approximation, *ab initio* simulations, Debye-like and Holland approximations, Brillouin zone boundary condition, fourth-order polynomial fit, etc. [17,104,113–115]. In general, due to the high symmetry of cubic semiconductor, it is assumed that the first Brillouin zone is isotropic, implying that the dispersion relation is identically for any wavevector direction and, consequently, it can be represented just by the (100) direction.

Finally, to calculate the thermal conductivity it is necessary to pass the summation in the q-space by an integral in the q-space:

$$\kappa_{bulk} = \frac{1}{3}\sum_{s} \int v_{g,qs}^2 \tau_{qs} C_{V,qs} D(\omega_s) d\omega_s \qquad [3.50]$$

where $D(\omega_s)$ is the phonon density of states, DOS. The determination of DOS in a particular system is a highly complex dynamic problem. But, as been above, this function is estimated by using simple and analytical models such as Einstein or Debye approximations.

3.4.1 Specific heat capacity

The specific heat capacity, C_V, of a solid is defined as the heat capacity, c_V, per unit volume, i.e. $C_V = c_V/N_0\Omega$. The heat capacity is defined as the amount of energy per unit mass or per unit volume to be supplied to a system to increase its temperature by one degree Kelvin or Celsius. It can be defined as the temperature derivative of the average energy, U:

$$c_V = \left.\frac{\partial U}{\partial T}\right|_V = \sum_{q,s} \hbar\omega_{qs} \frac{\partial n_{qs,0}}{\partial T} \qquad [3.51]$$

Using the Debye approach for the DOS, Equation [3.36], it is possible to replace the summation in the q-space to the integral in the q-space:

$$c_V = \frac{N_0\Omega\hbar^2}{2\pi^2 k_B T^2} \sum_s \frac{1}{v_s^3} \int_0^{\omega_D} \omega_s^4 n_s (n_s + 1) d\omega_s \qquad [3.52]$$

By introducing dimensionless quantities $x = \hbar\omega/k_BT$ and $x_D = \Theta_D/T$, it is possible to rewrite the heat capacity as:

$$c_V = 9Nk_B \frac{1}{x_D^3} \int_0^{x_D} x^4 \frac{e^x}{(e^x - 1)^2} dx \qquad [3.53]$$

An important characteristic of the heat capacity in the Debye expression is that it can recover the Dulong-Petit limit at high temperature and the T^3 behaviour for dielectric solids at low temperature. Some deviations of this power law can be found in layered-type materials, e.g. graphite, which exhibits a 2D-like behaviour at low temperature, namely, $c_V \sim T^2$, and in long molecular-chains of organic polymers which shows a 1D-like behaviour, i.e., $c_V \sim T$. Others deviations from T^3 can be found in metallic system due to the electronic contribution.

3.4.2 Thermal conductivity in low dimensional systems

It is well known that in thin films and nanostructures, compared to the bulk, the boundary scattering reduces the thermal conductivity. In the literature, this decrease has been associated to two main factors: (*i*) modification of the dispersion relation [41–47] and/or (*ii*) shortening of the phonon mean free path due to the diffuse scattering of phonons at the boundaries [2,48–50].

For low-dimensional systems Zou et al. [51] classified the theoretical models into three types. The first one takes the bulk formulation of the thermal conductivity, introduces the modified dispersion relation caused by the spatial confinement and adds a boundary scattering rate to the total scattering rate through Mattiessen's rule [44]. The second one uses the bulk dispersion relation and derives an exact solution to the PBTE after introducing diffusive boundaries conditions, according to the Knudsen flow model [2,48,52]. The third model, proposed by Zou et al. [51], is a combination of these two approaches. This model takes the modified expression of the thermal conductivity including the Knudsen flow model in addition to the modified dispersion relation. More recently Huang et al. [46] developed one- and two-dimensional expressions for the thermal conductivity of thin films and nanowire, which include the modified expression of the relaxation time due to the boundaries.

Modified Debye-Callaway-Srivastava model: complete phonon-phonon scheme

Depending of the model chosen, each result in a reasonable fit to the experimental data, but some assumptions and approximations could lead to an over/underestimation of the contribution of intrinsic phonon-phonon scattering processes. It is due to the typical approximation used for phonon-phonon scattering processes, i.e., $\tau^{-1} \propto T^m \omega^n$. However, this approach does not include any kind of phonon selection rules and certain kinds of forbidden phonon-phonon interactions appear incorrectly as allowed, such as Umklapp processes for zone-centre longitudinal phonons. In addition, some models completely exclude the contribution of the decay processes in Umklapp scattering processes.

From Equation [3.50] is clear that to model the lattice thermal conductivity dispersion relation, the total relaxation time of each mode and a numerical scheme for performing the integration within the Brillouin zone are required. The phonon dispersion relation can be calculated by several methods. However, the calculation of the intrinsic relaxation rates and the summation over the Brillouin zone can be very time-consuming and the necessary knowledge of the anharmonic phonon-phonon scattering strengths is not yet sufficiently well-established [71]. Taking these difficulties into account, Srivastava formulated a model of the lattice thermal conductivity based upon an isotropic continuum dispersion relation approximation limiting the Brillouin zone with the Debye radius. Under these approximations, Equation [3.50] reduces to a more tractable form:

$$\kappa = \frac{q_D^5 \hbar^2}{6\pi^2 k_B T^2} \sum_s v_s^4 \int_0^1 x^4 n_{xs} (n_{xs} + 1) \tau_{xs} dx \qquad [3.54]$$

with $\omega_s = v_s q$, q_D denotes the Debye radius cut-off and $x = q/q_D$ the reduced wavevector. The total relaxation time, τ_{xs}, and the distribution function, n_{xs}, are functions that depend on the reduced wavevector, x, and the polarization, s. Although the Debye model does not include optical modes or dispersion at large wavevectors, it is a good representation of almost 60% of the full acoustic dispersion relation. Moreover, this 60% represents the majority of the heat carrying phonons due to their relatively large group velocities and low scattering rates [116].

The total relaxation time is obtained by Mathessien's rule adding the boundary scattering processes derived from Equation [3.19]. As an example, the Figure 3.16 shows the good match between this theoretical model and experimental results in silicon nanowires.

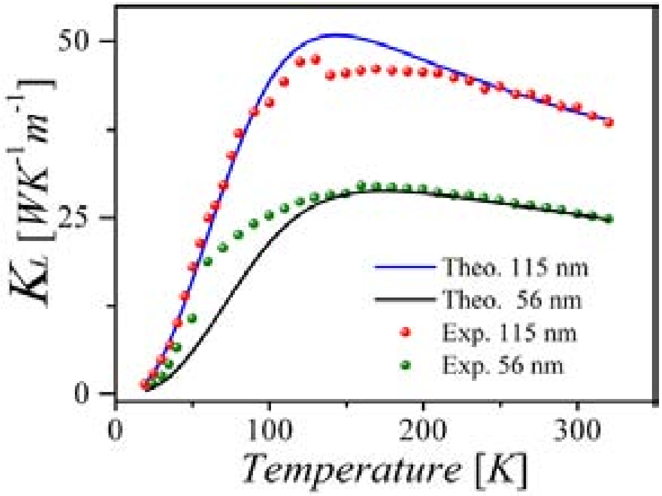

Figure 3.16 *Modelling and comparison of thermal conductivity of free-standing silicon nanowires ref.* [45]

Fuchs-Sondheimer model: correction of the thermal conductivity expression

The modelling of the reduction of the thermal conductivity is typically approached adding the phonon-boundary scattering term, τ_B, to the total relaxation time. It is estimated from the structure thicknesses and/or diameter, a, the phonon group velocity and the correction factor parameter which will depend of the geometry of the system, F, $\tau_B = Fa/v_g(q)$. Sometimes, a specularity factor, p, is added, which represents the surface polish quality of the film/wire [7,117]. However, the boundary scattering is a surface phenomenon and the addition of an extra term in the total relaxation time is not strictly rigorous. Instead, it is necessary to include the boundary effect on the phonon mean free path.

Based on the experimental results of Lovell [118] and the theoretical model of Thomson [119], Fuchs developed the first analytical solution of the size effect in the electrical conductivity of thin films [120]. He derived the effective electronic conductivity by solving the electronic-BTE with partially diffuse boundaries. It led to modification of the electronic distribution function results in a modified formulation of the electronic conductivity. Years later, Chambers extended the models for nanowires [121] and Sondheimer simplified the model for thin film and nanowires [122]. The same concept was extended and adapted for phonons to calculate the reduced thermal conductivity of thin films [2,6,49] and nanowires [52,123,124].

The thermal conductivity simulation of Si free-standing membranes is carried out, first, by deriving the lattice thermal conductivity of the bulk using the modified Callaway-Holland model, Equation [3.50], under the single-mode relaxation time approximation [68,104].

Then, once the thermal conductivity of bulk is determined, the effect of finite size is introduced through the Fuchs-Sondheimer boundary corrections:

$$\frac{\kappa_{film}}{\kappa_{bulk}} = 1 - \frac{3}{2}\frac{(1-p)}{\delta_s}\int_1^{\infty}(x^{-3}-x^{-5})\frac{1-e^{-x\delta_s}}{1-pe^{-x\delta_s}}\,dx \qquad [3.55]$$

where $p = \exp(4\eta^2 q^2)$ is the fraction of phonons specularly reflected by the boundaries, η is the root mean square deviation of the height of the surface from a reference plane [7] (roughness), $\delta_s = a/\Lambda_s$ is the inverse of Knudsen number and Λ_s is the bulk mean free path.

Huang model: modified dispersion relation and correction of the thermal conductivity expression

As discussed in Chapter II, the decrease in the structure dimension leads to the confinement of acoustics modes and the discretization of the acoustics spectrum, which results in a change in phonon propagation. The quantization of the dispersion relation leads to a modification of all frequency-dependence parameters which, in turn, results in changes in the phonon density of states, group velocity and phonon-phonon interaction. Based in this fact, Huang et al. [46] postulated a new lattice thermal conductivity model. The model included not only the modification of the dispersion relation and group velocity, but also, that of the specific heat capacity and, consequently, the Debye temperature. In addition, considering the boundary scattering effect, the lattice thermal conductivity expression also undergoes changes.

Due to the discretization of dispersion relation in the perpendicular component of the wavevector in a membrane, it is not possible to integrate over all q space. Therefore, to convert the sum to an integral over q-space, the summation along the perpendicular direction has to be made to keep also over the discrete number of modes m, i.e.:

$$\sum_{q,s} \rightarrow \sum_{m,s} \int \frac{A}{(2\pi)^2} d\bar{\mathbf{q}} \qquad [3.56]$$

with A the surface of the film. Taken the solution of the steady state relaxation time approximation of the BTE, Equation [II.12] of Appendix II, the thermal flux through of the film for a given direction can be written as:

$$\frac{Q}{\nabla T} = -\frac{1}{aA}\frac{A}{(2\pi)^2}\sum_{m,s}\int v_{g,q_{//}s}^2 \cos(\theta)^2 \hbar\omega_{q_{//}s}\tau_{q_{//}s}\frac{\partial n_{qs,0}}{\partial T} q_{//}dq_{//}d\theta \qquad [3.57]$$

By introducing the Fourier Law in the Equation [3.57], the lattice thermal conductivity of the film can be expressed as:

$$\kappa = \frac{1}{4\pi a}\sum_{m,s}\int v_g^2 \hbar\omega_{q_{//}s}\tau'_{q_{//}s}\frac{\partial n_{q_{//}s,0}}{\partial T} q_{//}dq_{//} \qquad [3.58]$$

The number of discrete modes, m, is limited by the material size [125]. However Huang et al. [20] suggested that for a given plane wave number $q_{//}$, the maximum number of allowed discrete modes is:

$$m(q_{//}) = \left[2\sqrt{q_D^2 - q_{//}^2}\,\frac{1}{(2\pi/a)}\right] + 1 \qquad [3.59]$$

where [x] is the Gauss notation that gives the largest integer less than or equal to x. The number one in Equation [3.59] counts the modes for $q_{//} = q_D$. The Figure 3.17 shows the number of discrete modes for 10 nm Si membranes.

Now, to calculate the thermal conductivity of our structure it is only necessary to know the dispersion relation and the total phonon lifetimes, i.e., $\tau_{q//s}{}^{-1} = \tau_U{}^{-1} + \tau_I{}^{-1} + \tau_B{}^{-1}$.

On the other hand, as has been shown in the Fuchs-Sondheimer model, the thermal conductivity expression must be corrected to account for the collision of phonons with the surface. However, for the case of membranes, only the phonon dispersion relation of waves traveling in the plane is allowed and it would seem that phonons cannot collide with the boundaries. However, this is unlikely to be the case because their amplitudes are strongly affected by the boundaries.

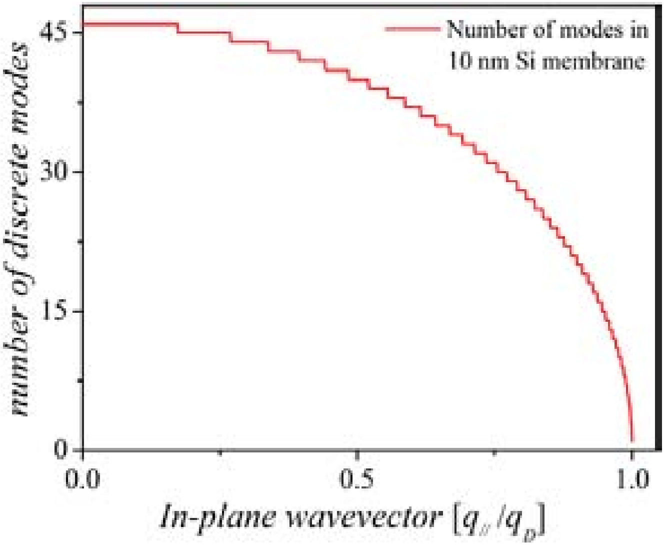

Figure 3.17 *Number of discrete modes for 10 nm thick Si membrane as a function of the dimensionless in-plane wavevector.*

In order to correct this expression, the boundary scattering will be viewed as a microscopic phenomenon and may be modelled using a characteristic relaxation time given by the Fuchs-Sondheimer corrections. The thermal conductivity of the film can be written as a correction of the bulk values due to the boundary, i.e., $\kappa_{film} = \kappa_{bulk} - F\kappa_{bulk}$, where F is the reduction function given by the Equation [3.55]. In this expression the phonon group velocity is considered as three-dimensional and this means that phonons collide with the boundaries.

$$\kappa_{film} = \kappa_{bulk} - F\kappa_{bulk} = \frac{1}{3}\sum_s \int (1-F)\tau_{\omega s} v_{g,\omega s}^2 \hbar\omega_s \frac{\partial n_{0,\omega s}}{\partial T} D(\omega_s) d\omega_s \qquad [3.60]$$

Since this expression takes into account the scattering due to the boundary, the total life time in this expression has to contain only Umklapp and impurity scattering processes, i.e., $1/\tau_{\omega s} = 1/\tau_{Us} + 1/\tau_{Is}$. Now, to derivate the boundary relaxation time, the lattice thermal conductivity of the thin film has to be rewritten in a suitable form akin to bulk materials, i.e.:

$$\kappa_{film} = \frac{1}{3}\sum_s \int \tau'_{\omega s} v_{g,\omega s}^2 \hbar\omega_s \frac{\partial n_{0,\omega s}}{\partial T} D(\omega_s) d\omega_s \qquad [3.61]$$

Finally, by comparing Equation [3.61] with [3.60], it found that:

$$\tau' = \tau(1-F) \qquad [3.62]$$

According to the Matthiessen's rule, it is now possible to define the boundary relaxation time as:

$$\tau_B = \tau\frac{(1-F)}{F} \qquad [3.63]$$

Finally, more realistic expression for the boundary lifetime is obtained. To compute the lattice thermal conductivity within this model it is just necessary to introduce the Equation [3.62] in the expression [3.58].

It is noteworthy that the derivation of the modified boundary relaxation time followed here is not equal to that in the Reference [46], because the reduction function used here is different although mathematically is the same and it does not have any major implications for the data analysis.

3.5 Phonon confinement and modification of specific heat capacity

The dispersion relation of a lower dimensional structure is not Debye-like and the acoustic dispersion relation is quantized. Therefore, all the frequency-dependent parameters could be affected, resulting in changes in the phonon density of states, group velocity and phonon-phonon interaction. In this section, the effect of the modified dispersion relation on the specific heat capacity will be examined.

3.5.1 Modification of the specific heat capacity

As seen in the Huang-model, the discretization of the dispersion relation does not allow the integration over all q values. Taking the discrete expression of the specific heat capacity, Equation [3.51], and replacing by the continuum through Equation [3.56], the specific heat capacity can be rewritten as [20,22]:

$$\begin{aligned} C_V &= \frac{1}{Aa}\sum_{m,s}\int_0^{q_D}\frac{(\hbar\omega_{q_{//}s})^2 n_{q_{//}s,0}(n_{q_{//}s,0}+1)}{k_B T^2}\frac{A}{(2\pi)^2}(2\pi)q_{//}dq_{//} \\ &= \frac{1}{2\pi a}\sum_{m,s}\int_0^{q_D} c(\omega_{q_{//}s})q_{//}dq_{//};\quad c(\omega_{q_{//}s}) = \frac{1}{k_B}\left(\frac{\hbar\omega_{q_{//}s}}{T}\right)^2 n_{q_{//}s,0}(n_{q_{//}s,0}+1) \end{aligned} \qquad [3.64]$$

where c($\omega_{q//s}$) is defined as the spectral density of the specific heat capacity representing the contribution to the specific heat by the states in the interval $\omega + d\omega$, the number of phonon modes is given by the Equation [3.59] and the dispersion relation is given by Equations [2.13] and [2.17]. Finally, the specific heat capacity is calculated from Equation [3.64] taking into consideration the phonon discretization as well as the contribution of each polarization, i.e., flexural, dilatational and shear modes.

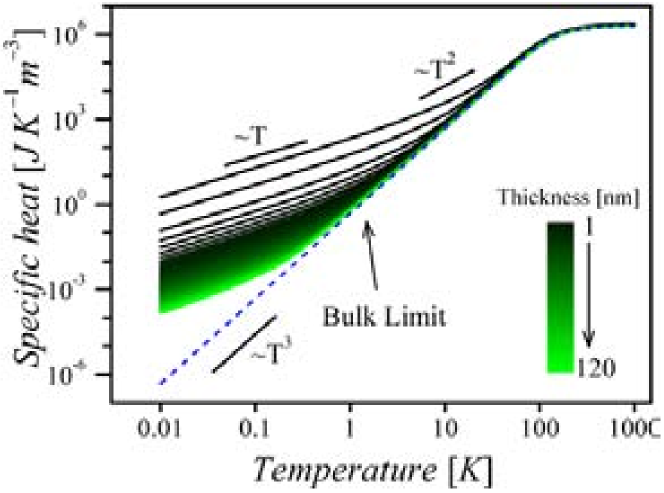

Figure 3.18 *Specific heat of Si as a function of temperature for the bulk (blue dashed line) and for 1 to 120 nm thick free standing membrane.*

Figure 3.18 shows the temperature dependence of the specific heat for Si membranes with thicknesses ranging from 1 to 120 nm. For comparison, the specific heat of the bulk Si is also plotted. As the membrane thickness increases, the bulk behaviour is recovered.

In the low temperature regime, a departure from $\propto$ T^3 is evident, approaching a linear dependence with decreasing membrane thickness. As shown in Figure 3.19 *a* and *b*, the linear dependence reflects the predominance of the fundamental flexural mode in this low temperature regime due to its quadratic dispersion. On the other hand, at higher temperatures the contribution of shear polarization becomes important, which for 10 nm, reaches the maximum contribution of around of 43% at 30 K, and the specific heat capacity becomes proportional to T^2. Above T > 400 K the contributions of all polarizations converge.

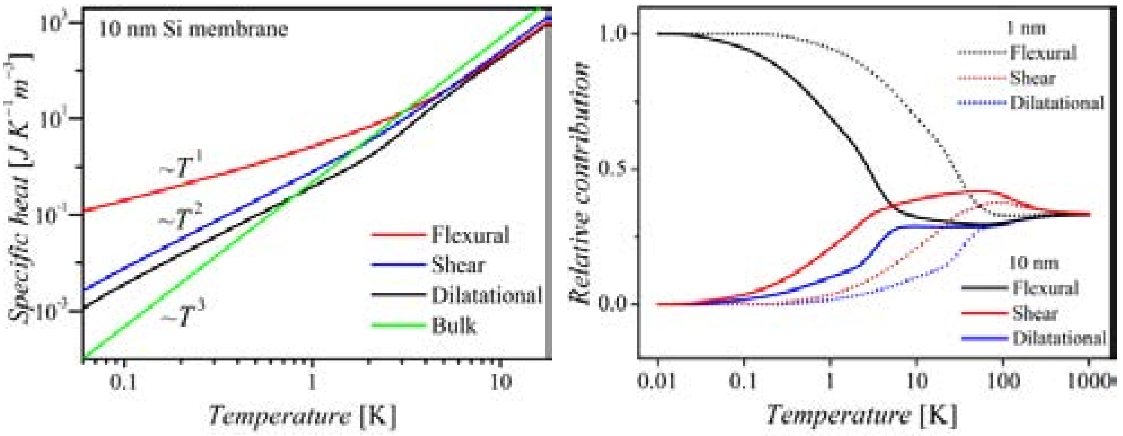

Figure 3.19 *(a) Specific heat capacity and temperature dependence of flexural (red line), shear (blue line) and dilatational (black line) polarizations for a 10 nm thick silicon membrane. For comparison the dependence of the Si bulk is also plotted (green line). (b) Contributions of each polarization to the total specific heat for 10 nm and 1 nm thick silicon membrane. The solid (dotted) black, solid (dotted) red and solid (dotted) blue lines represent the polarization contribution of flexural, shear and dilatational modes, respectively for 10 nm (1 nm) thick Si membrane.*

Figure 3.19*b* shows the specific heat as a function of thickness. Note that at low temperature the specific heat increases as the thickness decreases, reflecting the dominant role of flexural waves in the low temperature regime, whereas it remains virtually thickness-independent at room temperature.

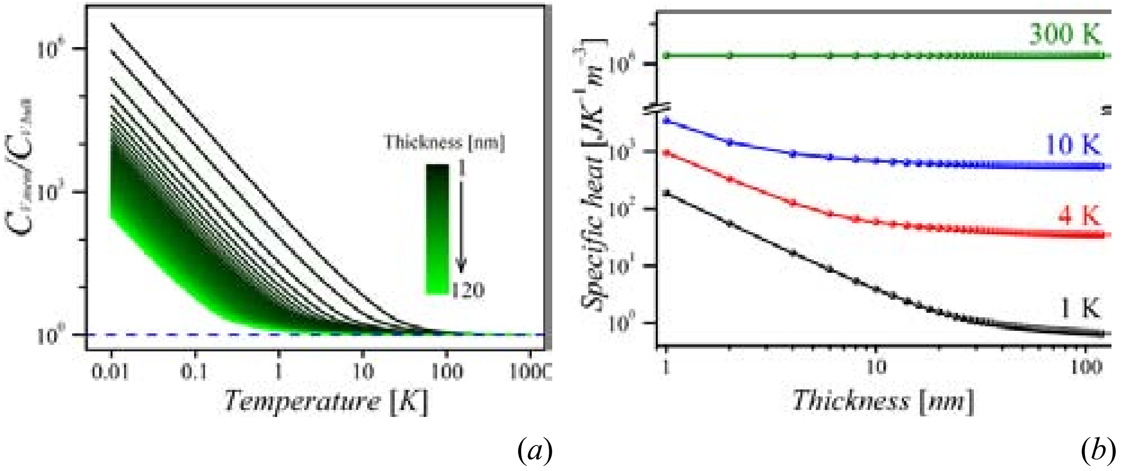

Figure 3.20 *(a) Normalized specific heat capacity as a function of temperature the blue line illustrates the bulk values. (b) Specific heat as a function of the membrane thickness at 300, 10, 4 and 1 K.*

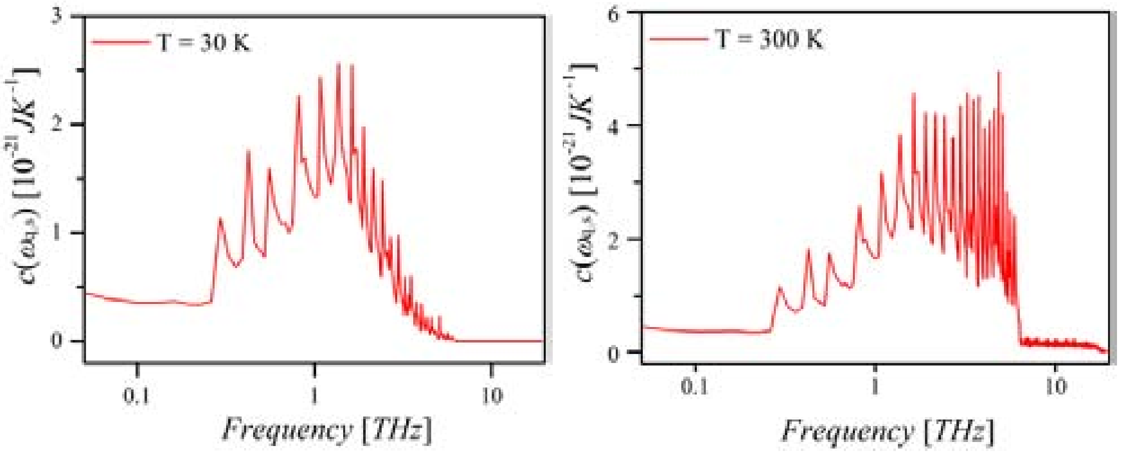

(*a*) (*b*)

Figure 3.21 *Spectral density of the heat capacity of a 10 nm thick Si membrane at 30 K (a) and 300 K (b) as a function of frequency.*

Figure 3.21*a* and *b* show the spectral density of the heat capacity as a function of frequency for a 10 nm thick Si membrane. The numerous peaks are due to regions of high density of states in the modified dispersion relation. It is seen that at room temperature the main contribution to the specific heat comes from the more energetic phonons (~ 1.6 to 6 THz), while at 30 K the main contribution comes from low-energy phonons (~ 0.3 to 1.3 THz).

The size effects in the specific heat capacity are most important at cryogenic temperatures and/or ultra-thin membranes (see Figure 3.18 and Figure 3.20*a*). At higher temperatures bulk values are quickly approached. From this result, two important questions arise: To what degree is *the modification of the dispersion relation important? When does it make sense to use the modified dispersion relation?*

3.6 Use of modified dispersion relation: defining criteria

Although there is no formal procedure for deciding when it is valid and/or useful to introduce of the modified dispersion relation, it is clear from Figure 3.18 and Figure 3.20*a* that it only affects the low temperature regime and smaller thicknesses.

To estimate when is useful to use the discretised relation, the comparison between the lattice thermal energy, $E_{TH} = k_B T$, and the energy spacing between the phonons branches, $\Delta E = \hbar\Delta\omega$ may be a suitable criterion. At the centre of the Brillouin zone this separation is approximately $\Delta E = \hbar\pi v_i/a$ where v_i can be the longitudinal or transverse sound velocity. The high temperature regime and/or in thicker systems the energy between the modes is always much smaller than the thermal lattice energy, hence many modes are occupied. In this case the dispersion relation and the phonon density of states may be approached by bulk-like behaviour. Figure 3.22 *a* and *b* show the lattice thermal and separation energy as a function of the temperature and thickness respectively. For $T > 15$ K and $a > 15$ nm it is clear that the lattice thermal energy is always much larger than the energy between the modes. In this regime the bulk-dispersion relation becomes a good approximation. However, the bulk dispersion relation is no longer a good approximation when the energy separation exceeds the thermal energy, that is, $Ta < \hbar\pi v_i/k_B$. It is in this regime that the modified dispersion relation plays a role in the thermal properties [126].

Taking these facts into consideration, the reduction of thermal conductivity in Si thin films can be attributed mainly to the shortening of the phonon mean free path due to the diffuse scattering of phonons at the boundaries [2,48–50], but in the low dimensions and/or low temperature regime effect of modification of the dispersion relation should be taken into account, including its effects on both group velocity and heat capacity [20,51,87].

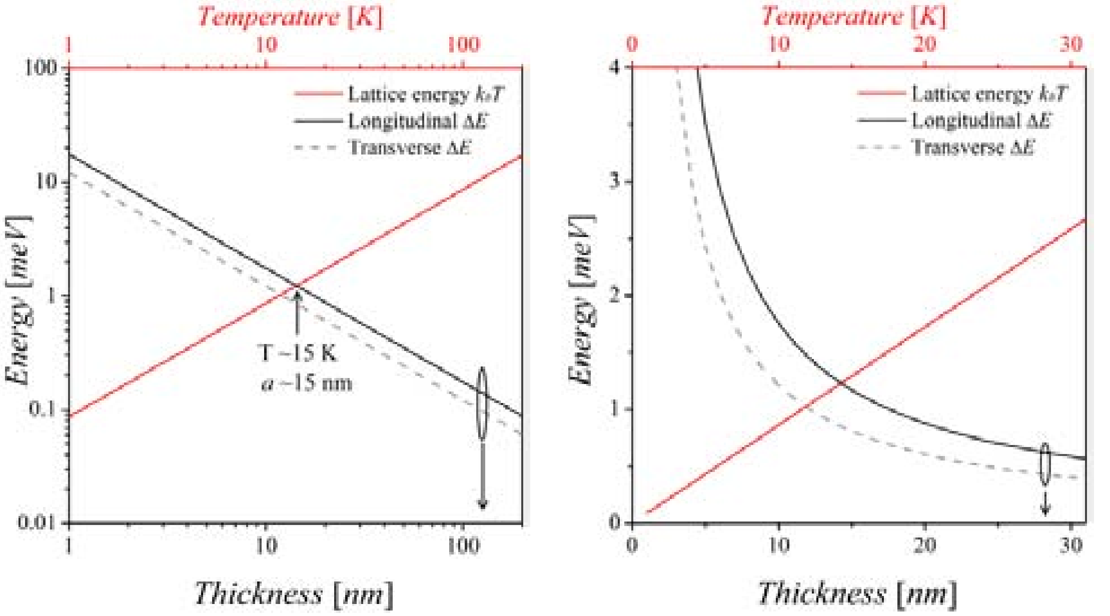

(*a*) (*b*)

Figure 3.22 *Lattice thermal energy (red solid line) and spacing energy (black solid and grey dashed lines) as a function of the temperature and thickness, respectively. (b) Magnified image of the low temperature/thickness regime plotted in linear scale.*

CHAPTER IV: FABRICATION AND EXPERIMENTAL TECHNIQUES

In the present chapter, the fabrication processes and characterization methods will be described. The silicon membranes used in this work were fabricated by collaborators from: the Technical Research Centre of Finland (VTT) in collaboration with Dr. Andrey Shchepetov, Dr. Mika Prunnila, and Prof. Dr. Jouni Ahopelto of the Technical Research Centre of Finland (VTT). Three Si membranes with thickness of 250, 1000 and 2000 nm were purchased from NORCADA Inc.

4.1 Fabrication of ultrathin freestanding silicon membranes

A convenient way to fabricate thin free-standing silicon membranes to investigate the thermal properties is to start with silicon-on-insulator (SOI) wafers. The fabrication processes developed at VTT for ultrathin Si membrane (< 100 nm) includes thinning of the SOI film by thermal oxidation, oxide removal and releasing the membrane by deep etching through the handle wafer and the buried oxide layer (BOX). The windows to be opened on the backside are defined by photolithography and, consequently, double side polished (DSP) SOI wafers are used. The thickness of the SOI film and BOX layer are typically a few hundreds of nm. The SOI film is thinned to the desired thickness by thermal oxidation which provides very accurate control of the film thickness and atomic layer sharp interfaces between silicon and silicon dioxide. The grown oxide can be selectively removed in hydrofluoric acid (HF) or in buffered HF (BHF). Windows are patterned to the back side of the wafer by optical lithography. The deep etching through the handle wafer can be done by wet etching in tetramethyl ammonium hydroxide (TMAH) bath or by reactive ion etching (RIE) or by combining both. In RIE SF_6

based chemistry provides good selectivity between silicon and oxide and for TMAH the selectivity is in practice infinite, leading in both cases to stopping of the deep etching at the handle wafer - BOX interface. The final removal of the BOX layer is carried out in BHF. During the fabrication process the thickness of the layers is controlled by an optical reflectometer with an accuracy better than 1 nm and confirmed by cross-sectional scanning electron microscopy (SEM). Using this process free-standing membranes with areas of several square millimetres and with thickness below 10 nm can be fabricated in a controlled manner, afforded by established silicon processing. The main process steps are schematically shown in Figure 4.1,

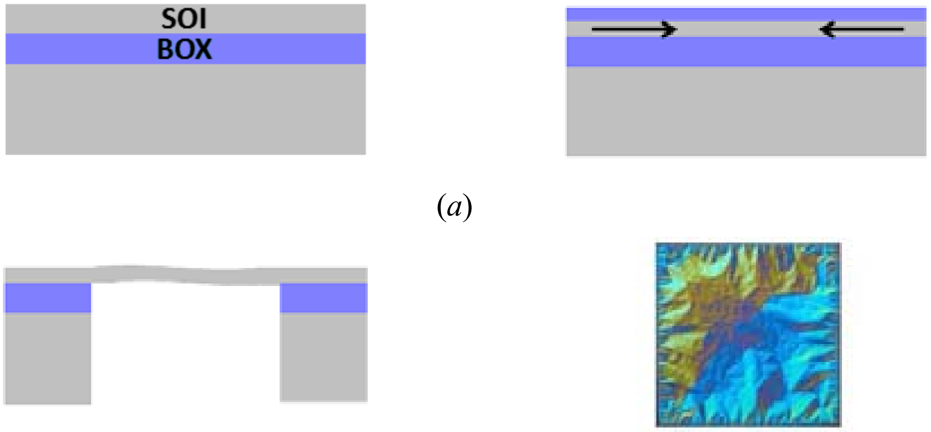

(*a*) (*b*)

(*c*) (*d*)

Figure 4.1 *(a) Typical SOI wafers used in the fabrication of the free-standing membranes with a few 100s nm thick SOI film and BOX layer. (b) The SOI film is thinned by thermal oxidation. The thermal process creates compressive stress in the film, as shown by the arrows. (c) After release the membrane is relaxed and tends to buckle. (d) Optical micrograph of a released 1.4x1.4 mm*^{2} *membrane with thickness of 9 nm. Courtesy of Prof. Dr. Jouni Ahopelto.*

However, the thermal processes used to thin the SOI film tend to create compressive stress in the film [127], leading to buckling of the membranes after the release. The buckling can be potentially detrimental for experimental work, especially for optical measurements, because the angle of incidence of the laser beam may not be well defined, and can also prevent the use of membranes in devices. In addition, the strain and, consequently, the elasto-mechanical properties of the membrane, cannot be tuned in a controlled manner because of the relaxation of the built-in stress. There are ways to overcome this problem and control the stress such as growing Si epitaxially on a SiGe buffer [128], oxide undercut [129], depositing thick SiN layers on top and bottom of the Si layer [130] or using SiN top frame [10].

This last approach avoids buckling and allows control of the strain. The strain can be tuned by varying the dimensions and layout of the frame and, consequently, the properties of the membrane can be engineered in controlled manner.

4.2 Advanced methods of characterizing phonon dispersion, lifetimes and thermal conductivity

In order to measure the main components of thermal transport: dispersion relations, lifetimes and thermal conductivity/diffusivity, advanced characterization techniques will be explained and discussed. Starting with the measurement of the dispersion relation and the detection of confined phonons to novel technique to measure thermal conductivity and transport regime.

4.2.1 Brillouin scattering

In order to determinate the impact of confinement effects on the thermal properties of nanostructures, the first step is the experimental determination of the phonon dispersion. It is crucial to measure the dependence of the phonon frequency on its propagation direction and magnitude and compare it with theory. Several questions must be answered: Is the elastic continuum model still valid at the nanoscale? Is quantum confinement important when the coherence of the scattered phonons is masked by boundary or grain effects?

The experimental technique to measure the transfer of energy and momentum between photons and phonons, is known generically as Inelastic Light Scattering (ILS), which allows a direct measurement of the energy or frequency of phonon, vibrational and rotational states of molecules, as well as plasmons, excitons and magnons. It is a non-contact, non-destructive method, with no pre- or post- processing required.

Historically, ILS by acoustic phonons has been known as Brillouin Light Scattering (BLS), while scattering from optical phonons, and vibrational and rotational states of molecules, has been known as Raman scattering. From the point of view of quantum theory, Brillouin scattering is simply the first-order Raman scattering associated with a transition in the vibrational states of the acoustic vibrations [131].

In practice, the difference among the ILS techniques is the apparatus used to access with enough resolution to the different frequency or energy ranges of the targeted quasiparticles or vibrations. The interaction of the quasiparticle with the photon causes a frequency down-shift (Stokes) or a frequency upshift (anti-Stokes) depending on whether the energy is given or absorbed by the photon. The typical frequency range accessed by BLS, extends from 500 MHz to several hundred GHz, which is suitable to access acoustic phonons.

In the quantum description of the interaction, the incident photon creates or annihilates a phonon and the energy and momentum of the phonon is equal to the difference in energy and momentum between the incident and scattered photons. Two main inelastic light scattering processes by acoustic phonons are present in nanostructured materials, namely, the *photoelastic* scattering mechanism, and the *ripple* scattering mechanism.

- Photoelastic (or elasto-optic) scattering occurs due to time-dependent fluctuations in the polarisability of a material, which are caused by acoustic phonons.

- The ripple scattering mechanism differs from the photoelastic one mainly in that the scattering strength does not depend directly on the strain, photoelastic constants, or polarisability of the material. Instead, the strength of the scattered signal is proportional to the normal displacement of the acoustic wave, or ripple, since the change in phase is caused by variations of the optical path length arising from the surface displacement. For this reason, the ripple scattering mechanism is stronger for surface acoustic waves, or waves which cause modulation at the surface, such as the flexural and dilatational waves in a membrane.

However, bulk waves will also cause surface displacement, and surface waves will also induce a strain, and therefore scatter light via the photoelastic effect; thus, in general, both effects must be taken into account. The relative importance of either effect is determined primarily by the scattering volume. Extensive discussions of both mechanisms can be found in references [132,133].

To measure a dispersion relation, both frequency and wavevector magnitude and direction are required. The wavevector of the phonon involved in the scattering process is determined by the angle of scattering, which is defined through the scattering apparatus and the mechanism responsible of the ILS.

The wavevector, q, involved in the scattering process depends on the scattering mechanism. In the general case of photoelastic scattering it is given by:

$$q = 2k\sin(\alpha/2) \qquad [4.1]$$

where k and q are the wavevectors of the incident photon within the material and the generated/absorbed phonon, respectively, and α is the angle between the incident and scattered light beams. In a backscattering configuration of α=180 degrees, Equation [4.1] becomes:

$$q = 2k \qquad [4.2]$$

where the magnitude of the wavevector is independent of the scattering angle and the direction of the wavevector within the sample is defined by Snell's law (See Figure 4.2).

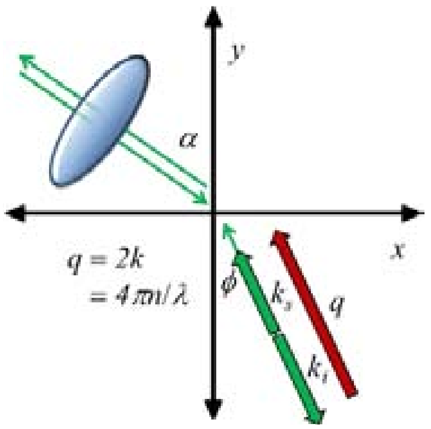

Figure 4.2 *Wavevector conservation in the photoelastic backscattering configuration.*

For the case of the ripple scattering, the wavevector of the phonon involved is given by:

$$q_x = k_{1i}^x - k_{1s}^x = 2k(\sin(\alpha_i) + \sin(\alpha_s)) \qquad [4.3]$$

where α_i and α_S are the incident and scattered angle, respectively, both defined with respect to the normal to the surface. For the backscattering configuration the previous relation becomes:

$$q = 2k\sin(\alpha) = \frac{4\pi}{\lambda}\sin(\alpha) \qquad [4.4]$$

In this case, the magnitude of the wavevector changes as a function of the angle, while the direction remains constant, parallel to the surface in the scattering plane (See Figure 4.3).

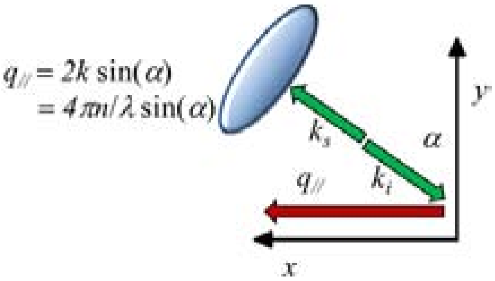

Figure 4.3 *Wavevector conservation in backscattering configuration via the ripple effect.*

The apparatus is shown in Figure 4.4 and it is built in a backscattering geometry. A small prism or beam splitter is used to direct the light towards the sample, with an achromatic lens to focus the light. As the scattering occurs at the focus of the lens, the backscattered light is collimated, and another lens placed after the prism is used to focus the light to the entrance pinhole of the spectrometer. A beam splitter is placed between the prism and the lens to form an image of the sample on a CCD camera.

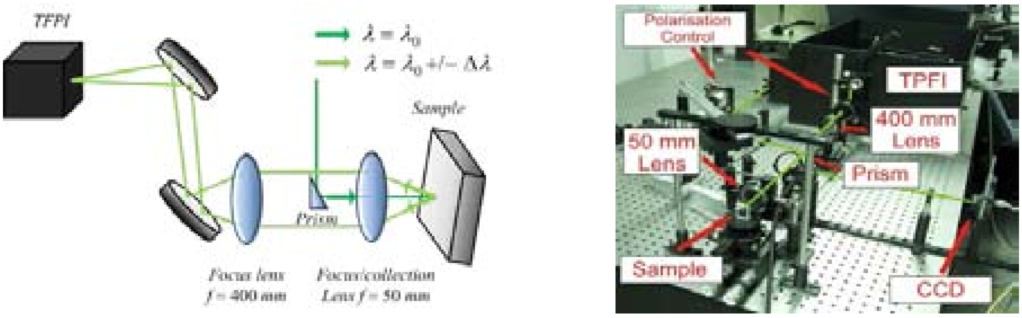

(*a*) (*b*)

Figure 4.4 *(a) Schematics of apparatus used for backscattering configuration, (b) Photograph of apparatus used for backscattering configuration. TPFI is a Tandem Fabry-Perot Interferometer*

For our experiment, the incident radiation was provided by a diode-pumped solid state laser (DPSSL) from Oxxius, with a free-space wavelength, λ, of 532.6 nm. The light inelastically scattered by optical and acoustic phonons undergoes an extremely small fractional change in frequency and a high-resolution spectrometer is required. The scattering light was analysed with a high resolution multipass (3+3) Tandem Fabry-Pérot Interferometer (TPFI) from JRS Scientific Instruments [134,135], which consists in two Fabry-Pérot Interferometers (FPIs) put in series (see Figure 4.5).

In ordinary FPIs the increase of the finesse is achieved by increasing the cavity length, but this reduces the free spectral range. The tandem configuration overcomes this problem since the two cavities can be configured, using two slightly different cavity lengths, to be both resonant just at a certain wavelength and detuned for the neighbouring supported modes. This greatly enhances the free spectral range, while maintain a high finesse.

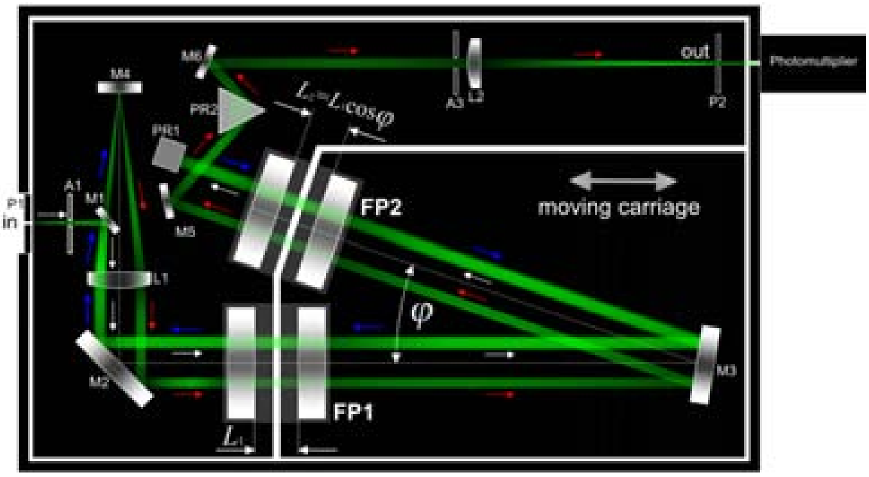

Figure 4.5 *Schematic of Tandem Fabry-Perot Interferometer, TPFI, manufactured by JRS Instruments, Sandercock showing path of light* [134,135]. *Courtesy of Dr. Bartlomiej Graczykowski.*

As example, the typical Brillouin spectrum of 200 nm thick Si membranes is shown in Figure 4.6. The spectra was taken using Olympus 10× objective, with a numerical aperture of NA = 0.25 and spot size measured at Full-Width-Half-Max (FWHM) of 12.5 μm was used as the focus and collection lens for the thicker membrane [136]. The main difference with respect to bulk counterpart is the multiples peaks observed in the membrane case. For bulk system just a single peak corresponding to the surface acoustic wave is seen.

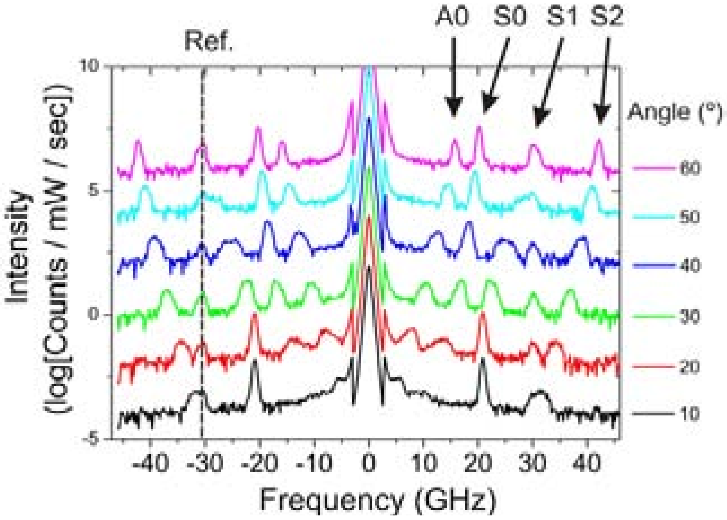

Figure 4.6 *Typical Brillouin spectra recorded for 200 nm thick free-standing Si membrane. The first two peaks nearest the central quasi-elastic peak are identified as the zero-order flexural, A0, and dilatational, S0, modes. The others belongs to first, and second order dilatational modes, S1 and S2, respectively. Adapted from J. Cuffe and E. Chavez et at.* [21,137]

4.2.2 Pump-and-probe ultrafast spectroscopy.

Understanding the lifetimes of heat carrying phonons is essential to engineering thermal transport. A phonon's lifetime refers to the time taken for a phonon or phonon wavepacket to scatter or be attenuated. The reason for this attenuation may be either collision with impurities or defects within the sample or the boundaries of the sample (extrinsic mechanisms), or due to the intrinsic anharmonicity of the lattice, which occurs even for perfect crystals. In conjunction with its group velocity, the phonon lifetimes defines how far a phonon can carry its energy, which is known as the phonon mean free path. Despite the fundamental importance of these parameters, accurate measurements of phonon lifetimes are challenging, and their values are unknown in most materials. Even though silicon is the most important material for nanoscale devices, there are few direct measurements of phonon lifetimes in the gigahertz to terahertz range [108]. Moreover, many open questions remain about the relative contributions of intrinsic and extrinsic scattering processes at high frequencies in both bulk and nanoscale structures [138–140].

Generation and detection of high-frequency phonons

One of the most fundamental approaches to measure phonon lifetimes is to first generate phonons with an impulse and then observe the rate at which they decay. As the dominant heat-carrying phonons at room temperature have frequencies of the order of 1 THz and above, one of the challenges relates to exciting high-frequency phonons. One of the primary tools that enabled the study of these phonons is ultrafast lasers, capable of generating very short pulses with very intense electric fields. These pulses, with durations of just a few picoseconds, and more recently down to sub-100 fs pulses, deliver very fast, powerful impulses, which generate high-frequency phonons. This development opened a field of study now known of picosecond acoustics or picosecond ultrasonic.

The light-matter interactions that cause ultra-short laser pulses to excite high frequency phonons constitute a rich and interesting field of study. The intense electric field of the short pulse interacts with the electron clouds of the material, which then generates strain through different mechanisms, depending on the material properties. The processes involved for semiconductors, such as silicon, are illustrated in Figure 4.7. The light pulse hits the sample, electrons are excited into the conduction band. These electrons decay rapidly while giving their energy to the lattice through phonon emission and come to equilibrium with the lattice at the bottom of the conduction band within ~ 1 ps. The subsequent dynamics then depend on carrier and thermal diffusion. The laser pulse causes strain via two separate mechanisms, namely thermal expansion, and the hydrostatic deformation potential. The thermal expansion is due to the anharmonicity of the lattice, whereas the deformation potential is due to the excitation of electrons into binding orbitals. In the case of bulk silicon, the stress caused by the deformation potential is about seven times greater than the thermal stress and is compressive [141]. These stress terms then lead to the generation of acoustic phonons. Often, metal layers are used as transducers, especially for transparent films which cannot absorb the radiation. Here, the dynamics are quite similar, except that electron-hole recombination is much faster.

To detect these phonons, the strain dependence of the reflectivity of many materials is exploited, which occurs due to a change in the refractive index caused by the elasto-optic or photoelastic coefficients of the material. For many pico-/femto-second experiments, one intense laser pulse will be used to excite phonons, while another weaker pulse or train of pulses is used to detect the corresponding change in reflectivity. These are collectively known as pump-probe measurements.

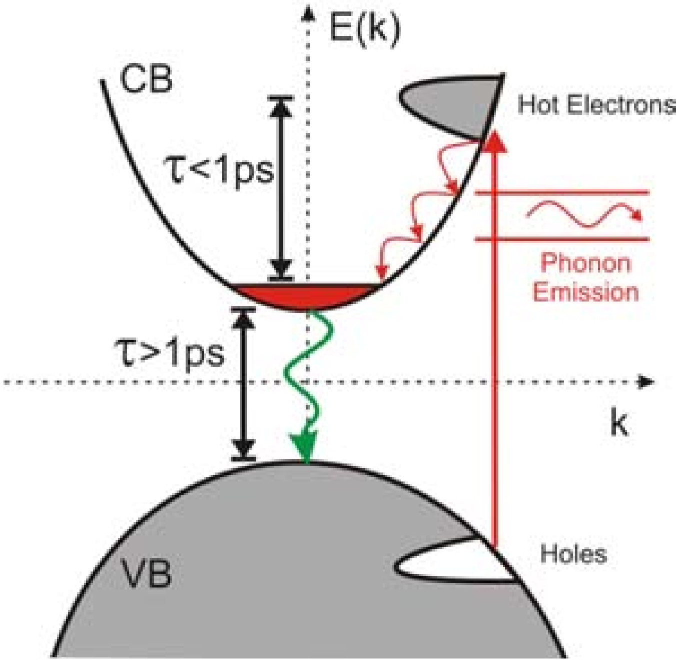

Figure 4.7 *Schematic of the response of a semiconductor to an ultra-short pulse. Electrons are excited from the valence band, VB, to the conduction band, CB, where they decay rapidly to the bottom of the conduction band through electron-electron collisions and phonon emission. The dynamics are then described by a slower decay involving electron-hole pair recombination, carrier diffusion, and thermal diffusion. Courtesy of Dr. John Cuffe.*

Asynchronous Optical Sampling: ASOPS

The first measurements involving the generation and detection of acoustic phonons by picoseconds laser pulses were performed in the 1980's [142,143]. The technique was then applied to measure the attenuation of phonons in amorphous SiO_2, for frequencies up to 440 GHz [144]. Recently, these experimental investigations have been extended to measure of phonons in superlattice cavities with frequencies of around 1 THz [145]. For bulk samples, the phonon lifetimes are expected to be limited by intrinsic anharmonicity, for which there are many models. The generation and detection of coherent acoustic phonons at high frequencies is an ideal method to investigate these mechanisms and their relative importance compared to extrinsic scattering in nanostructures.

One state-of-art technique of generation and detection coherent phonons is the Asynchronous Optical Sampling spectroscopy, ASOPS [146]. The ASOPS method is based on the traditional ultra-fast pump-probe techniques, but instead of the mechanical delay line for the temporal dephasing of the lasers, Figure 4.8 *a*, it produces pulses from two mode-locked femtosecond Ti:Sa lasers with slightly detuned repetition rates, Figure 4.8*b*.

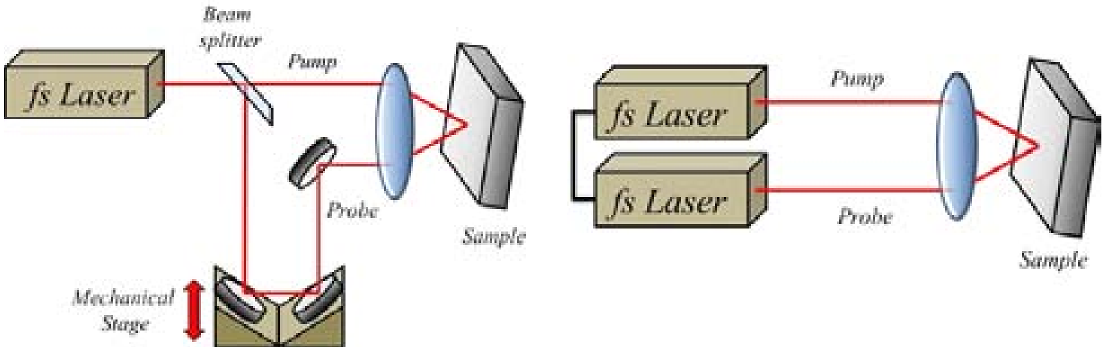

(*a*) (*b*)

Figure 4.8 *Schematic pump-probe experiment: (a) Mechanical delay and (b)ASOPS with two mode-locked lasers, adapted from J. Cuffe* [136]

To scan the dynamic of the system, the ASOPS technique uses the detuning of the repetition rate between the pump and probe pulses. This detuning creates a monotonically temporal window which allows scanning the dynamic of the system without the need the re-adjustment of the any mechanical stage. The scan rate is determinate by the difference in frequency, Δf_R, and the temporal window is given by the inverse of this difference, $1/ \Delta f_R$. For example, if the repetition rates of the pump and probe are 1 GHz and 0.999999 GHz, respectively, the temporal window will be of one nanosecond and it can be probed in 100 μs, see Figure 4.9. The typical resolution of the ASOPS could achieve values smaller than 100 fs [83].

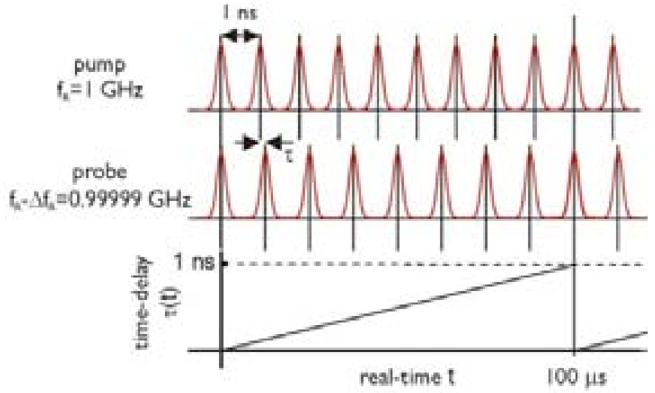

Figure 4.9 *Schematic time delay between pump and probe pulses. From Gigaoptics GmbH website.*

4.2.3 Raman Thermometry

The experimental measurement of the thermal conductivity involves two steps: the introduction of thermal energy into the system, heating, and the detection of the change of temperature or related physical properties due to the increase of the thermal energy, i.e., sensing. Both, heating and sensing, can be measured mainly by electrical or optical and/or a combination of both.

In recent years, novel contactless characterization techniques for thermal conductivity (or thermal diffusivity) determination have been developed. Their main advantage compared to electrical techniques is the lack of contacts and the pre-processing stage of the samples. Besides from the steady-state method for thermal conductivity determination, where good thermal contacts are mandatory [147], the well-established 3 ω technique for bulk and thin films samples [148] requires an initial lithography process followed by a metallic strip deposition and finally the bonding of electrical contacts. The later represents a good example of the drawbacks of contact techniques since, although the accuracy is in the order of $\approx$ 5%, the fabrication process sometimes results difficult, e.g., due to large roughness of the samples which can result in breakage of the metallic strip. Scanning thermal microscopy with higher spatial resolution is also an alternative, although the fabrication of the thermal tips is complex and expensive. Moreover, the physics behind the tip-sample interactions is far from being unravelled.

In consequence, many different groups have developed a variety of contactless advanced techniques such as, e.g., time-domain thermoreflectance (TDTR) [149,150], frequency-domain thermoreflectance (FDTR) [151], thermal transient grating (TTG) [152], the photoacoustic method [153], and Raman thermometry [61]. In addition, optical sensing methods might be able to collect information more selectively which could be used to distinguish between emission and scattering originated within a sample or its substrate and to measure local temperatures.

Single Laser Raman Thermometry: 1LRT

Single Laser Raman thermometry, 1LRT, is a contactless advanced technique for thermal conductivity determination based on the probe of the local temperature due to different physical mechanism. Accordingly, any aspect of phonons changing with temperature can be used to probe the thermal state of the system. These changes are reflected mainly in: the Stokes and anti-Stokes intensity components, the Raman peak position and linewidth (full width at half maximum, FWHM) associated with specific optical phonon modes, all of which vary with temperature, as is shown in Figure 4.10*a* and *b*.

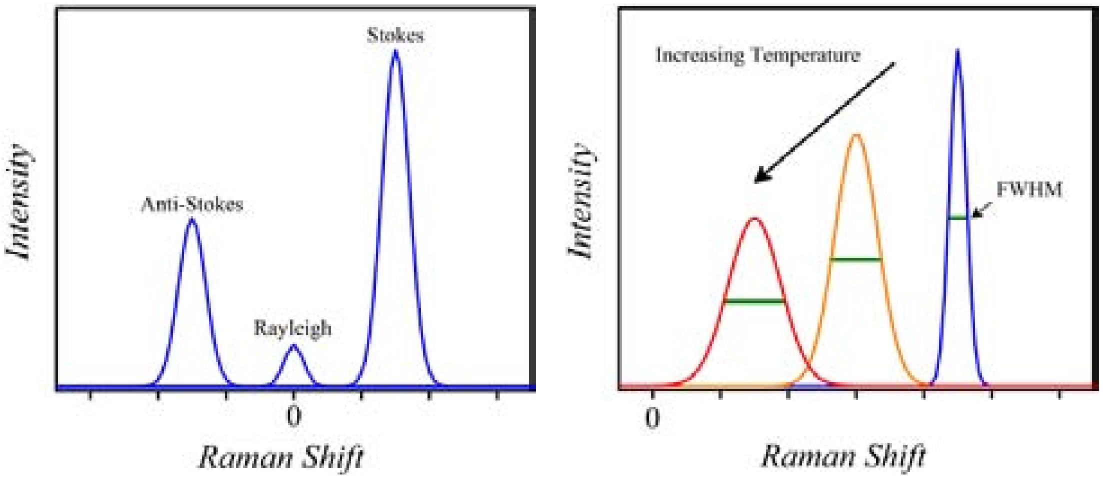

(*a*) (*b*)

Figure 4.10 *Schematic examples of Raman spectra as thermometer: (a) typical Raman spectrum showing the anti-Stokes, Rayleigh, and Stokes signal, (b) Redshift and broadening of the linewidth due to temperature increasing, adapted from* [154].

The first method, Stokes and anti-Stokes, is based on ratio of the intensities of Stokes and anti-Stokes processes, I_A/I_S, it is related to the phonon population. Which it is determinate by Boltzmann statistics:

$$\frac{I_A}{I_S} \cong \exp\left[\frac{\hbar\omega_{phonon}}{k_B T}\right] \qquad [4.5]$$

In Figure 4.10*a* the schematic change in the intensity, for a given temperature T, is shown. One of disadvantage of this method is that it is only accurate at higher temperatures and for materials with small phonon energies. Also intensity is a more difficult parameter to measure accurately and, more importantly, consistently. This method is possible with Raman as well as with Brillouin light scattering spectroscopy.

A second way to estimate the temperature from the Raman peak position and/or FWHM, both sensitive to the sample temperature given in the references [155,156]. To increase/decrease the temperature, the atoms are displaced from their equilibrium positions, resulting in an overall volumetric expansion or contraction of the lattice and a change in interatomic forces as a result of the anharmonicity of the bonds. This change in the interatomic force is reflected in the

Raman peaks position resulting in a red shift to lower wave numbers as the temperature increases. Similarly, the linewidth of the Raman spectrum is broadened as the temperature increases. This broadening is a consequence of the temperature-dependence of the phonon lifetime. In silicon, the Raman peak position, $\Delta\omega_{Raman}$, and Raman linewidth, $\Delta\Gamma_{Raman}$, depend linearly with the temperature [157] and can be simplified as:

$$\Delta\omega_{Raman}(T)/cm^{-1} = -0.022\ (\Delta T/K) \quad [4.6]$$

$$\Delta\Gamma_{Raman}(T)/cm^{-1} = -0.011\ (\Delta T/K) \quad [4.7]$$

There are some inconvenient when using this method. Sometimes it is less reliable due to other contributions to the Raman spectral line-shape, such as embedded strain, strain due to a thermal expansion mismatch, sample compositional/structural disorder, impurities and contamination of the sample as well as the presence of pseudo-phases and deformation of the material [158–161].

A main requirement to apply this technique is that the material should have a non-negligible Raman signal from any of its optical modes. For example, amorphous materials and metals exhibit poor Raman signal. On the contrary, most inorganic and organic semiconductors, electrical insulators, and polymers exhibit many optical Raman modes depending upon their symmetry. In any case, the temperature dependence of just one optical mode can serve as the local temperature probe.

The temperature of the focused spot can be easily obtained by fitting the spectral position of the observed Raman mode, given a previous calibration of its spectral position with temperature. A laser is focused onto the surface of a sample using a microscope objective with high numerical aperture (NA≈0.9) resulting in a spot of about 1 µm in diameter. Thus, increasing the incident laser power leads to local heating and, thus, to a red-shift of the observed

Raman mode. The temperature increase in the spot region for a given incident laser power will depend on the thermal properties of the investigated material.

Finally, the thermal conductivity of the sample can be extracted with a suitable heat diffusion model. For example, for bulk materials the three-dimensional heat equation has to be solved considering a Gaussian power source [162] (i.e., the incident laser), for thin films on a substrate the problem results analytically more complicated due to the interface resistances and heat reflections [163,164], for thin membranes the solution is much simpler since the heat equation can be reduced to two dimensions.

Figure 4.11 shows a simple example of the application of Raman thermometry in ultrathin suspended Si membranes. The schematics is a finite element simulation of the temperature distribution in a Si membrane upon heating with a Gaussian power source (the incident laser) in its central position (yellow=max, black=min temperature).

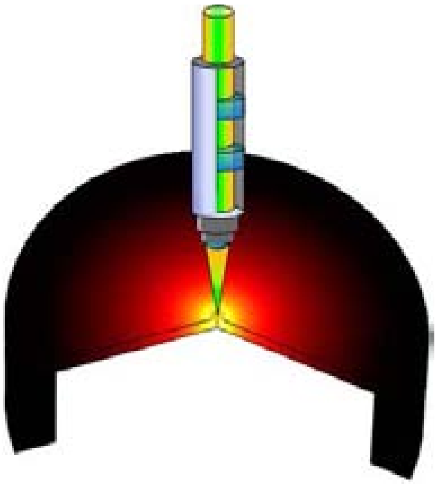

Figure 4.11 *Scheme of the Raman thermometry method.*

Considering that the typical thickness of the membranes, $d < 1$ µm, is much smaller than their lateral, L ~ 300 µm. The heat equation can be approximated as 2-dimensional model, i.e.:

$$-\nabla^2 T = \frac{g(x,y)}{\kappa} = \frac{P_{Abs}}{2\pi d\sigma^2\kappa}\exp\left(-\frac{r^2}{\sigma^2}\right) \qquad [4.8]$$

where $g(x,y)$ is a power generation function which, based on the laser profile, can be approximated by a Gaussian function and P_{Abs} is the absorbed laser power.

Measurement of the absorbed power

Due to multiple reflections in the membranes the power absorbed cannot approach to the bulk values. The membranes behave as Fabry-Pérot cavities.

In order to obtain the absorbed power in each membrane a home-made setup was build. This setup is able to measure simultaneously the incident light and reflectance, R, and transmittance, T, of the Si membranes. The reflectance and transmittance were obtained measuring the incident, P_I, reflected, P_R, and transmitted, P_T, powers after focusing the laser spot on the surface of the membranes using a 50× (NA = 0.55) microscope objective. The power absorptance, A, of each membrane was computed considering that:

$$\begin{aligned} A &= 1 - R - T \\ &= 1 - P_R / P_I - P_T / P_I \end{aligned} \quad [4.9]$$

The Figure 4.12 shows the schematic configuration of the incident, reflected and transmitted power measurements. The power measurements were performed using digital power and energy meters with 50 nW to 50 mW Si sensor, from Thorlabs company. The calibration of the setup was carried out by using a silver coated mirror, with reflectivity > 99.0 % at 514.5 nm.

The measurement of the scattered was also considered by using integrating spheres, but the contribution was negligible.

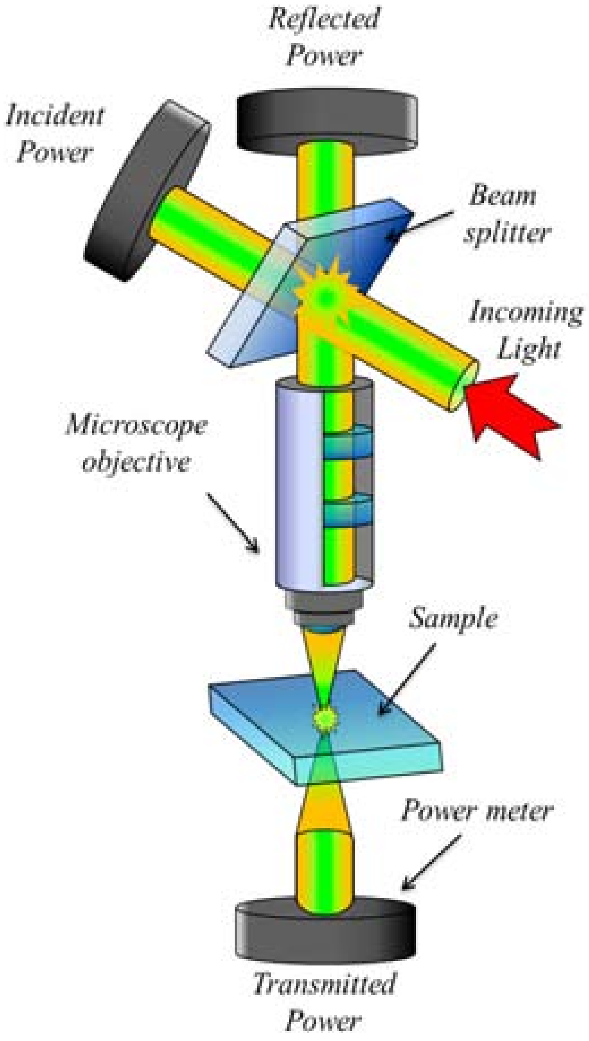
Reflected Power
Incident Power
Beam splitter
Incoming Light
Microscope objective
Sample
Power meter
Transmitted Power

Figure 4.12 *Schematic configuration for the incident reflected and transmitted power measurements.*

Measurement of the temperature field by two-laser Raman thermometry: 2LRT

The Raman thermometry technique is particularly useful for a quick and contactless determination of the thermal conductivity. However, there is a substantial amount of information that can be obtained studying the spatial dependence of the temperature distribution in the membranes, e.g., the heat transport regime. On a macroscopic length scale, heat transport is generally described as a diffusive process where the heat flow, *Q*, is driven by a temperature gradient, ∇T, following Fourier´s law of heat conduction: $Q = -\kappa \nabla \mathrm{T}$. However, this description fails if the material dimensions, L, become smaller than and/or in the order of the mean free path of the heat carriers, Λ. In the case of acoustic phonons in crystalline materials such as silicon, Λ can be several hundreds of nanometers at room temperature [8]. For shorter length scales, $\Lambda > L$, the heat flow will become quasi-ballistic driven by direct point-to-point transport of energy quanta [165]. In other words, in a large system ($\Lambda << L$) the heat can reach equilibrium whereas in a confined system dissipation leads to a local non-equilibrium. Past experiments have demonstrated the size dependence of ballistic thermal transport in nanostructures such as thin films, superlattices, nanowires and carbon nanotubes [3,30,165–169].

In order to investigate the transport behaviour in the nanoscale, we developed a novel and contactless technique: Two-Laser Raman Thermometry technique, 2LRT. This new technique is based on a two-laser approach to create and probe a thermal field in nanostructures. As is shown in Figure 4.13, while a *heating* laser with λ_1 is used to produce a hotspot, a *thermometer* laser with λ_2 measures the spatial distribution of the local temperature through the temperature dependent redshift of a Raman mode.

To apply this technique, the sample has to have a Raman active mode, with detectable temperature dependence. A calibration of the Raman shift versus temperature is essential. Moreover, the sample should have a reasonable absorbance in the spectral region of the heating laser to set up a temperature distribution. The absorbed has to be power measured by, e.g. the technique described for 1LRT above.

One of the main advantages of this technique compared to other contactless steady-state methods, e.g. infrared thermometry, is its sub-micrometer spatial resolution, given by the spot size of the probe laser ~ 500 nm with a 100× high NA microscope objective. In addition, the spatial resolution can be also improved using, for example, Tip Enhanced Raman Spectroscopy, TERS, which could reach resolution better than 10 nm [170,171].

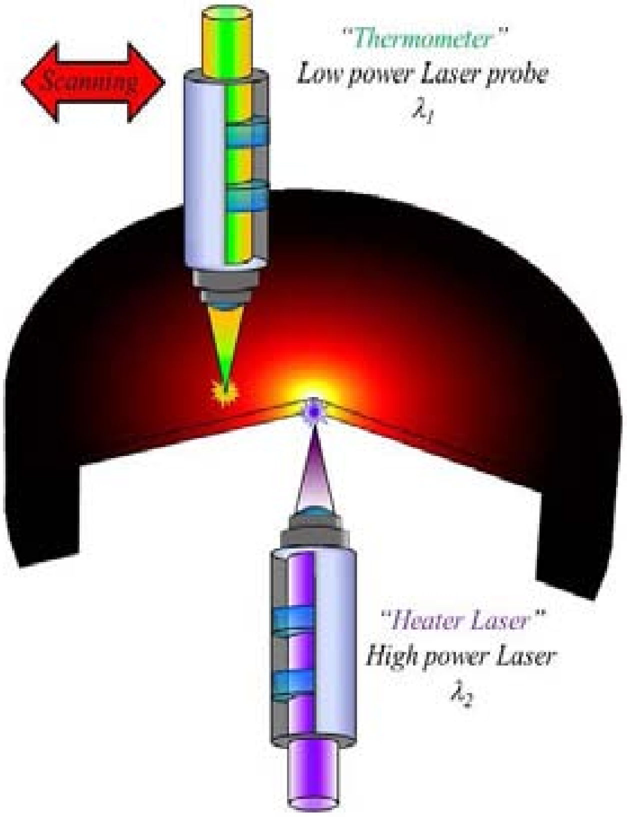

Figure 4.13 *Schematic configuration of the Two-Laser Raman Thermometry Technique developed in this work.*

Using the same concept of the two lasers, it is possible to vary slightly the setup to use different physical phenomena to detect the temperature such as: photoluminescence [172] or reflexion and transmission coefficient [64].

4.2.4 Transient thermal grating (TTG)

The TTG method is an optical technique for measuring thermal diffusivity. While the thermal conductivity is a measure of how well a material conducts heat, the diffusivity is related to how quickly a material conducts heat. The thermal conductivity of a sample is the product of its diffusivity and volumetric heat capacity.

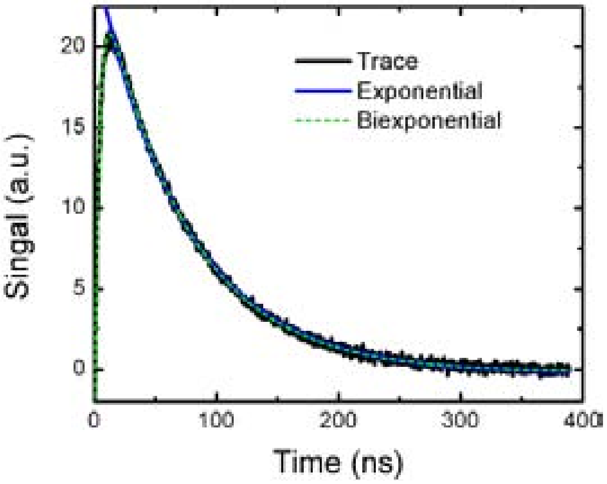

Figure 4.14 *Typical time trace from a 400 nm thick Si membrane. The electronic response of the sample is seen, which decays quickly to leave the thermal response. This decay can then be fitted to extract the decay time, which is proportional to the thermal diffusivity. Courtesy of Dr. John Cuffe.*

In this method, two short laser pulses are crossed at the sample to form an interference pattern. The absorption of the light causes a spatially periodic thermal grating, which in turn induces an optical phase and amplitude grating through the temperature dependence of the real and imaginary parts of the refractive index, respectively. A probe beam is diffracted from this transient grating and the thermal diffusivity can be determined from the rate of the signal decay. As the heat diffuses from the peak to the null of the grating, the diffraction efficiency of the optical grating decreases and the signal intensity decays exponentially with time, i.e., T(t) ~ $\exp[-q^2\alpha t]$ as shown in Figure 4.14.

The thermal decay can then be characterised by a decay time τ which is related to the thermal diffusivity α as:

$$\alpha = \frac{1}{q^2\tau} \qquad [4.10]$$

where $q = 2\pi/L$ is the grating wavevector corresponding to a grating period L. The grating period is controlled by the angle of incidence θ, and is given by:

$$L = \frac{\lambda}{2}\sin(\theta/2) \qquad [4.11]$$

The TTG method has a number of advantages. As no adsorbed metal layer is required, no electrical or thermal contact resistances are introduced in the measurement or analysis. Hence the diffusivity is measured, instead of to directly measuring the thermal conductivity, and this has the implication that the absolute power does not need to be measured, which can be challenging for many nanoscale objects. The thermal length scale can also easily be varied by changing the grating period, which is useful to ensure diffusive transport and can be used to observe ballistic phonon transport over micrometre distances in silicon at room temperature [173]. Finally, as the thermal grating is defined in the plane of the membrane, in-plane thermal transport is assured. Typical apparatus for performing a TTG measurement is shown in Figure 4.15.

For our measurements, the thermal grating was created by the interference of two crossing pulsed laser beams with pulse duration of 60 ps, repetition rate of 1 kHz and wavelength of 515 nm. This interference produces the diffraction of a third quasi-CW probe beam with a wavelength of 532 nm chopped to 64 µs. The diffracted probe beam is mixed with a fourth reference beam from the same laser source for the heterodyne detection. The thermal diffusivity is extracted from the decay signal of the quasi-CW probe beam for a given spacing of the thermal grating. The period of the thermal grating is varied by changing the angle of the two crossing beam, which can be changed from 4 to 25 µm.

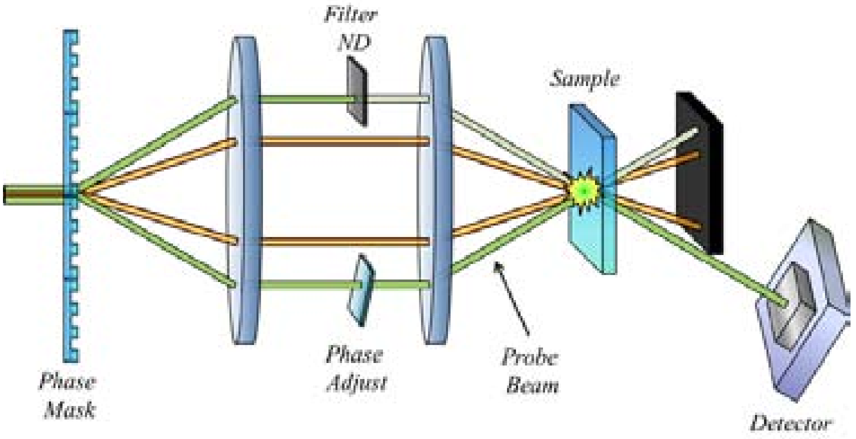
Filter
ND
Sample
Phase
Mask
Phase
Adjust
Probe
Beam
Detector

Figure 4.15 *Schematics of Four-beam Transient Thermal Grating apparatus adapted from Johnson et al.* [173]. *The angle between the pump beams is controlled by splitting the beams with a diffraction grating (phase mask) with a well-defined pitch. The pump beams are later blocked, while the signal from the probe beam that is diffracted from the thermal diffraction grating is recorded. This signal is mixed with an attenuated reference beam for heterodyne detection.*

CHAPTER V: MODELLING AND EXPERIMENTAL RESULTS

In this chapter, measurements of the phonon properties in free-standing membranes are shown. The results are dived into experimental and theoretical part. In the first part the measurement of acoustic dispersion relation, phonon lifetime and thermal transport are described. In the second part the theoretical models are discussed and compared with the experiments.

5.1 Acoustic phonons dispersion relation in ultrathin silicon membranes

In the present section the measurement of the flexural mode in ultra-thin Si membrane will be shown. These Si membranes were fabricated at the Technical Research Centre of Finland (VTT) in collaboration with Drs. Andrey Shchepetov and Mika Prunnila and Prof. Jouni Ahopelto of the Technical Research Centre of Finland (VTT).

The phonon dispersion relation was measured by angle-resolve Brillouin Light Scattering spectroscopy. This technique has been shown to be an adequate non-contact technique to detect confined phonons in thin films [174], free-standing membranes [21,137] and phononic crystals [175]. The measurements were taken in backscattering configuration, as described in section 4.2.1. The laser beam was focused on the sample by means of a long working distance 50x Olympus objective with N.A. = 0.55, that produces a spot size of about ~1.2 µm. The measurements were performed at room temperature with an incident power of 1.2 mW and α was varied in the 30º–75º range, which corresponds approximately, according to Equation [4.2], to the range of $q_{//}$~ 11.8–22.8 µm^{-1} corresponding to ~ 0.001% of the Brillouin zone.

5.1.1 Flexural mode dispersion

Figure 5.1 shows Brillouin spectra of 17.5 nm thick Si membrane for several scattering angle, α, between 30º to 70º displaying a single feature. This peak is identified as the zero-order flexural mode of the Si membrane. The flexural mode corresponds to in-phase vibrations which flexes the membrane (see the inset to Figure 5.2*a*). In thin membranes, the lowest flexural mode has been found to dominate in the Brillouin spectra. This is a consequence of three combined effects: the dominant ripple scattering mechanism [21,133], mode symmetry [78] and the enhancement of the phonons density of states [21,44].

The theoretical curves were calculated solving Equation [2.4] and using numerical root searching described in the Appendix I. The sound velocities used were 8440 m/s and 5840 m/s for longitudinal and transverse sound speed, respectively [176]. In addition, a fit to the experimental values with a quadratic dependence is displayed, which is a clear difference from the well-known linear dependence of the bulk acoustic phonons in this wavevector range.

Figure 5.2*b* shows the phase velocity as a function of the in-plane wavevector. An important characteristic from this data is the dramatic decay of the phase velocity compared to the bulk counterpart (8440 m/s and 5840 m/s for longitudinal and transverse, respectively) near to the zone centre of the Brillouin zone. This decay is due to the quadratic behaviour of the flexural mode, which leads to a linear dependence of the phase velocity with respect to in-plane wavevector [21,137].

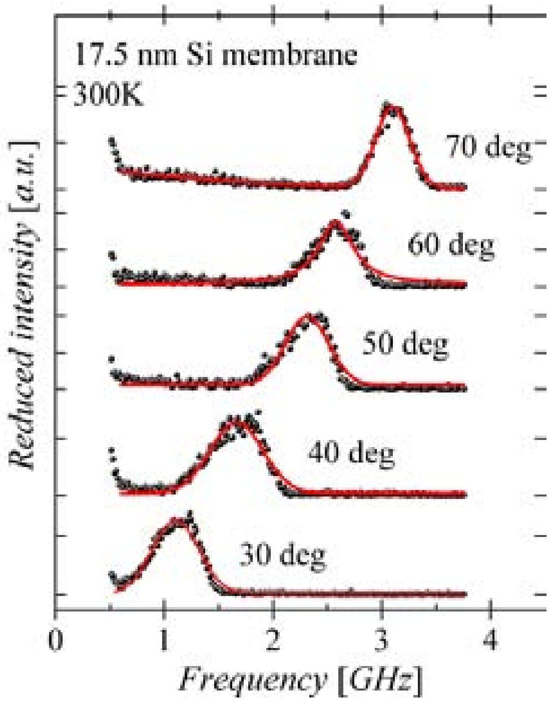

Figure 5.1 *Brillouin spectra as function of the angle of incidence, showing for the fundamental flexural mode of a 17.5 nm Si membrane.*

Moreover, as was shown in the Figure 3.18 and Figure 3.19*a*, this quadratic behaviour leads to departure of the specific heat capacity dependence from T^3 to T at temperatures below few Kelvins and in ultra-thin films [20,22], and to the thermal conductance approaching the ballistic limit, which displays in a $T^{3/2}$ dependence [177,178].

In summary, we have studied confinement effects on the flexural mode dispersion relation in 17.5 nm thick free-standing silicon membrane. We use angle-resolved Brillouin Light scattering spectroscopy to detect the low frequency (1 to 3 GHz) flexural mode as a function of the in-plane wavevector (~11-22 µm^{-1}). We have calculated the overall dispersion relation and found a good agreement with the experimental results for the fundamental flexural mode. We also demonstrated that the fundamental flexural wave dispersion in ultra-thin membranes can be described by simple quadratic wavevector dependence. This behaviour leads to a dramatic decrease of the group/phase velocity and has implications for the thermal properties of the system, specifically at the low temperature regime, where the fundamental flexural mode carries most of the heat.

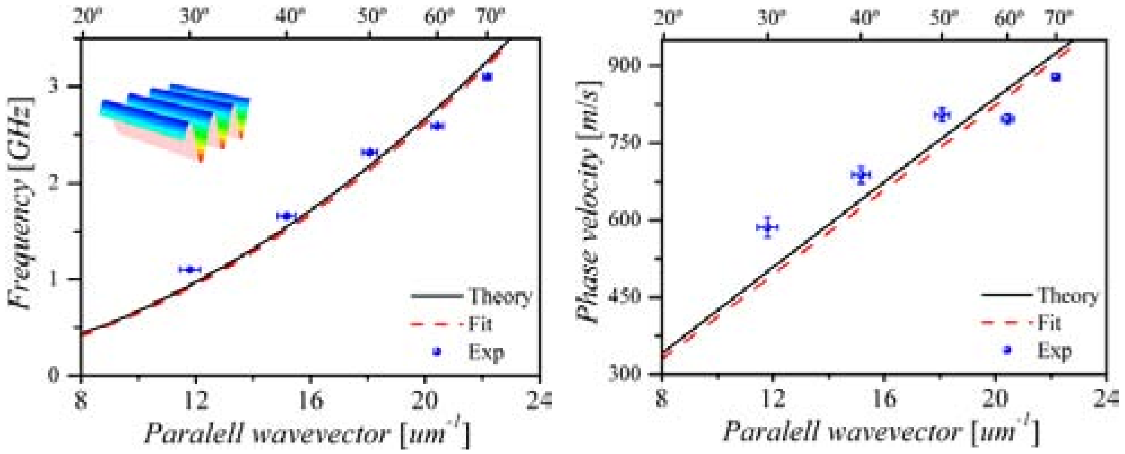

(*a*) (*b*)

Figure 5.2 *Dispersion relation and phase velocity of the zero order flexural mode of a 17.5 nm silicon membrane: experimental results (blue dots), simulation (black solid line) and quadratic fit (red dashed line). Inset (a): Schematic representation of the displacement fields of the flexural mode, courtesy of Dr. Jordi Gomis-Bresco.*

5.2 Phonon lifetime: measurements and simulations.

In this section measurements of frequency and lifetime of confined phonon will be shown. This work formed part of collaboration with the group of Prof. Dr. Thomas Dekorsky of the University of Konstanz, Konstanz, Germany. All this measurements were developed in collaboration with Dr. John Cuffe, Dr. Mike Hettich and Mr Oliver Ristow.

The measurements were performed by using ultra-fast pump-probe technique of Asynchronous Optical Sampling, ASOPS, described in the previous in the section 4.2.2. The samples investigated were silicon membranes over a large range of thickness from 7.7 ± 0.1 to 194 ± 1 nm, allowing the investigation of the trend of phonon lifetime with frequencies up to ~ 500 GHz. The analysis of the experimental data was carried out considering the intrinsic and extrinsic damping mechanism. The intrinsic phonon lifetimes were calculated by considering the Akhieser and the Landau-Rumer damping models. The extrinsic phonon lifetimes were modelled considering the surface roughness scattering mechanism including a wavelength-dependent specularity parameter.

5.2.1 Lifetimes of Confined Acoustic Phonons in Ultrathin Silicon Membranes

The ASOPS experiments were performed at room temperature in reflection configuration. The laser spot size on the membranes was about 1.7 μm in diameter and the wavelengths of the pump and probe beams were 780 and 810 nm, respectively. Due to the large optical penetration depth ~ 8 μm, the pump pulse causes a symmetric strain in the membrane via thermal expansion and the hydrostatic deformation potential [141,179], resulting in the excitation of the first-order dilatational mode at $q_{//} = 0$, which oscillates at a frequency of $f = v_L/2a$, where a is the thickness of the membrane.

As the dilatational mode changes temporarily the thickness of the membrane, it will modulate the reflectivity according with the well-known Fabry-Perot effect. Although the change in thickness is of the order of 1 pm and below, corresponding to a reflectivity change of about one part in 10^{-5}, the ASOPS technique is sufficiently sensitive to detect it. Other phenomena which can also change the reflectivity include the photoelastic effect, however, the change of the optical cavity thickness is the dominant contribution, due to the small photoelastic constant and volume of the silicon samples. The subsequent dynamics of the confined phonons are then observed by recording the light modulation induced by phonon-photon coupling in a one-dimensional photo-acoustic cavity.

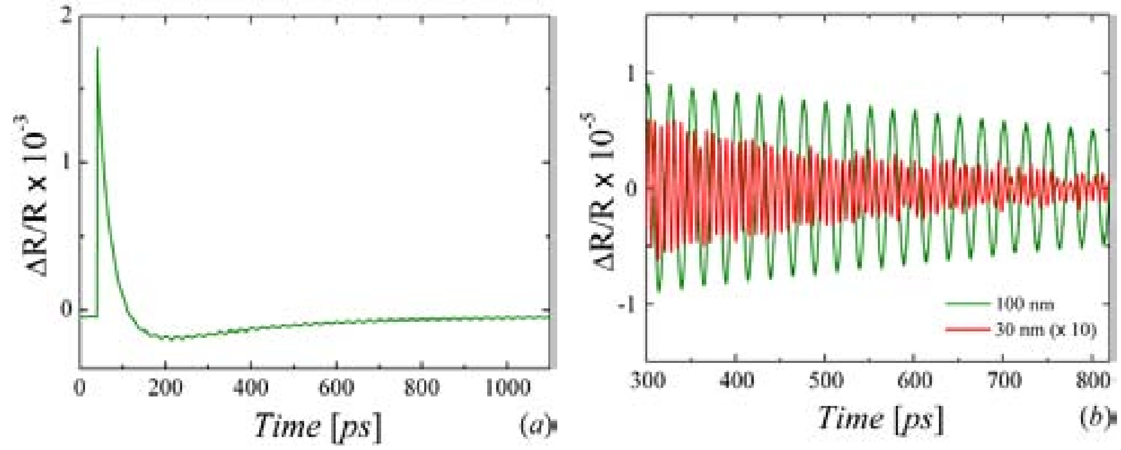

Figure 5.3 *Fractional change in reflectivity as a function of time in the 100 nm silicon membrane. The sharp initial change is due to the electronic response of the membrane. The subsequent weaker oscillations are due to the excited acoustic modes. (b) Close-up of the acoustic modes after subtraction of the electronic response for membranes with 100 and 30 nm thickness shown by the green and red line, respectively. The sinusoidal decay of the reflectivity due to the first-order dilatational mode is clearly observed as a function of time, with a faster decay observed for the thinner membrane. The time trace of the 30 nm membrane has been magnified by a factor of 10 for clarity. Adapted from J. Cuffe et al.* [23].

Figure 5.3*a* shows a typical time trace of the change in reflectivity induced by the laser pulse in a 100 nm silicon membrane. The initial spike is related to the electronic response, while the subsequent oscillations are due to the excited phonon modes. Figure 5.3*b* shows a close up of these modes, and a comparison for membranes of two different thickness values. It can be seen that the signal from the 30 nm membrane decays faster compared to that of the 100 nm one.

The electronic contribution can be modelled by a bi-exponential decay and subtracted to reveal the acoustic modes [180] as shown in Figure 5.3*b*. The phonon lifetime is then extracted by modelling the decay, assuming a damped harmonic oscillator of the form:

$$\frac{\Delta R}{R}(t) = A\sin(\omega t)\exp[-t/\tau] \qquad [5.1]$$

where ω is the phonon frequency, t the time and τ the phonon lifetime. Then, by fitting the decay curve with the Equation [5.1] the phonon lifetime is extracted. The results from all the membranes are shown in Figure 5.4. It can be seen that the phonon lifetime decreases dramatically with membrane thickness, corresponding to higher phonon frequencies.

These findings are compared with theories introduced in Chapter III considering both intrinsic phonon scattering and extrinsic surface roughness scattering. The intrinsic phonon lifetimes were modelled applying Fermi's golden rule to calculate three-phonon interaction probabilities [17] based upon a Debye model in the Srivastava approximation for Normal processes. The surface scattering was calculated following the approach of Ziman, including a wavelength-dependent specularity parameter and surface roughness fixed to η = 0.5 nm. The discussion of the theoretical models will be presented in the next section.

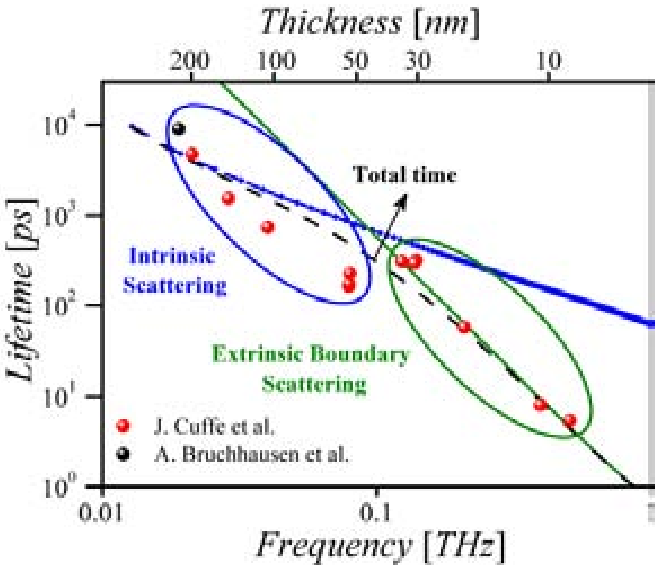

Figure 5.4 *Experimental and theoretical phonon lifetime of the first-order dilatational mode in free-standing silicon membranes as a function of frequency. Experimental data of free-standing silicon membranes with thickness values ranging from approximately 194 to 8 nm (red dots)* [23] *and 222 nm (black dot)* [180]. *Green line: extrinsic boundary scattering processes. Blue line intrinsic three-phonon normal scattering processes. The total contribution, calculated using Matthiessen's rule, is shown by the solid black-dashed line. Adapted from J. Cuffe et al.* [23].

5.2.2 Phonon lifetime: theoretical results

The nanoscale the phonon lifetime is limited mainly by extrinsic surface roughness scattering. As shown in Equations [3.16] to [3.19], this effect may be introduced through a boundary condition in the steady-state BTE, following Ziman's approach [7]. For the case of the first order dilatation mode, the extrinsic rate can be simplified as:

$$\tau_B^{-1} = \frac{\omega_L}{\pi} \tanh\left(\frac{2\eta^2 \omega_L^2}{v_L^2} \right) \qquad [5.2]$$

where $\omega_L = 2\pi f = \pi\, v_L/a$ is the phonon frequency of the first order dilatational mode, η surface roughness and v_L is longitudinal sound velocity.

The intrinsic acoustic phonon attenuation can be calculated using two different approaches: (*i*) Landau-Rumer and (*ii*) Akhieser mechanisms. The validity of each model will depend principally on the wavelength of the absorbed phonon, λ, and the mean free path of the thermal phonons, Λ_{mfp}.

If the λ of the acoustic wave is much larger than the typical Λ_{mfp} of the thermal phonons, i.e., $f\tau_{TH} << 1$, where f is the phonon frequency and τ_{TH} the lifetime of the thermal phonons, we can assume that the acoustic wave interacts with the whole spectrum of thermal phonons. This range is known as the Akhieser regime. But if λ is much less than Λ_{mfp}, i.e.,$f\tau_{TH} >> 1$, then the phonon attenuation can be better described in the Landau-Rumer formalism and the phonon attenuation is due to three-phonon interactions processes.

The difference between Landau-Rumer and Akhieser model is basically the approach to describe of the phonon absorption. In the Landau-Rumer approach the acoustic phonon is described as a particle and the absorption is due to collisions between the phonons. The calculation is based on quantum mechanical perturbation theory, given by the Fermi golden rule and for low frequency phonons, it can be considered as pure N-processes. To apply the Landau-Rumer approach is necessary that the uncertainty in the conservation of the energy, $\Delta E \sim \hbar/\tau_{TH}$, will be smaller than the energy of the absorbed phonon, $E = \hbar\omega$, i.e., $E > \hbar/\tau_{TH}$ or $\omega\tau_{TH} > 1$. …"*This condition ensures that the thermal phonons exist sufficiently long in time or travel* *sufficiently far in space for them to endure a complete oscillation of the absorbed phonon and hence for them to establish a proper interference conditions in the space and time*"… [7]. Using the Equation [3.45], the lifetime of the first order dilatational mode can be simplified as:

$$\tau_{Ph}^{-1} = \frac{\hbar\gamma^2 v_L}{4\pi\rho v^2}\sum_{s',s''}\frac{1}{v_{s'}^2 v_{s''}^2}\left[\int \omega_{s'}^2(\omega_L+\omega_{s'})^2\,\frac{n(\omega_{s'})\big(n(\omega_L+\omega_{s'})+1\big)}{n(\omega_L)+1}\,d\omega_{s'} + \frac{1}{2}\int \omega_{s'}^2(\omega_L-\omega_{s'})^2\,\frac{n(\omega_{s'})n(\omega_L-\omega_{s'})}{n(\omega_L)}\,d\omega_{s'}\right] \qquad [5.3]$$

where the first and second term in the Equation [5.3] represent the class I and class II processes, respectively.

As the first order dilatational mode at $q_{//} = 0$ is a pure longitudinal mode, the possible interactions of this mode are: $L_1 + L_2 \rightarrow L_3$; $L_1 + T_2 \rightarrow L_3$; $L_1 \rightarrow L_2 + L_3$; $L_1 \rightarrow T_2 + T_3$; $L_1 \rightarrow L_2 + T_3$ and $L_1 \rightarrow T_2 + L_3$, where 1 denotes the low energy phonon, the dilatational one, 2 and 3 denote the higher frequency phonons and L and T are the longitudinal and transverse polarization, respectively. However, as shown in the inset of the Figure 5.5*b*, the processes which involves the decay of the phonon into two others phonons are negligible to the total relaxation time. That is due to the low phonon energy of this mode.

Although the collinear processes of the type $L_1 + L_2 \rightarrow L_3$ are often neglected or categorized as forbidden processes due to the dispersion of the branches. Early works have shown that these processes may occur as the finite lifetime of the branches compensates for the dispersion [17,93–95]. In addition, they can play a significant role especially at short wavevectors where the dispersion relation is Debye-like. We found that this processes contributes most to the total intrinsic phonon lifetime shown in Figure 5.5*a* and *b* and it also matches quite well the experimental data of Figure 5.4. The parameters used for the simulation are summarized in Table 3.3.

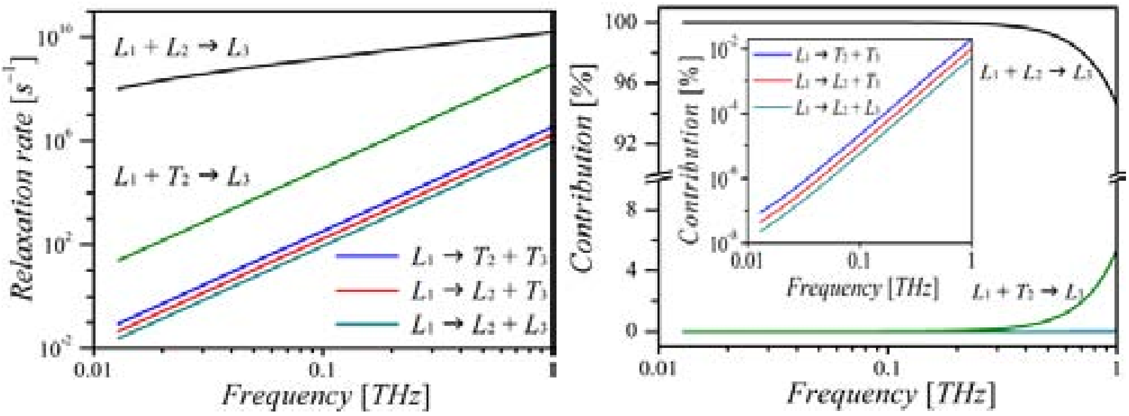

(*a*) (*b*)

Figure 5.5 *Phonon-phonon processes in Si membranes: (a) Intrinsic relaxation rate as function of the frequency. (b) Relative contribution to the total intrinsic lifetime of each phonon-phonon processes as a function of the frequency.*

The other mechanism to explain the intrinsic phonon attenuation is the Akhieser mechanism. In this model the mechanical wave is treated as a macroscopic strain field in the crystal, which produces a shift of the equilibrium distribution of thermal phonons. The latter tends to return to the equilibrium via phonon-phonon interaction, producing a time-dependence of the entropy of the system, which leads to the absorption of the mechanical wave.

The intrinsic phonon relaxation rate in the Akhieser regime can be expressed by using the Equation [3.46]. Although the theory of sound absorption in solids is well established, the alignment of damping models with experimental data still remains unfinished due to the complexity of the models themself. The use of adjustable parameters becomes inevitable. In particular, the Grüneisen parameter and the lifetime of the thermal phonons are often used as fitting parameters in the analysis of the experimental data. The flexibility with which the two parameters are varied has been considered acceptable because experimental data was unavailable. For example, the only experimental data known of the Grüneisen parameter are for modes at few high-symmetry points of the Brillouin zone [101]. In the case of the thermal phonon lifetime the Grüneisen parameter is identified as an average value over the whole spectrum of thermally excited phonons in the crystal. In some cases, a kink in the slope of the quality factor (Q-factor, $Q = \omega\tau$, where τ is the lifetime of the phonon mode with frequency ω)

and/or phonon attenuation against frequency is used as indicative of the frequency cut-off between the intrinsic damping models from which the lifetime of the thermal phonons is extracted [144,181,182]. However, it has been shown that this slope depends on the direction of the phonon propagation [183] and therefore such method can be misleading.

In Reference [23] we noticed that the Akhieser model did not describe the experimental data of mechanical mode decay in Si ultrathin membranes, when a single value of τ_{TH} was used regardless of the membranes thickness. As the real value of τ_{TH} is unclear, we used the constant value of τ_{TH} = 17 ps taken from Reference [108], which provided the best fit to acoustic attenuation in bulk silicon. However, as has been shown throughout this work, the thermal conductivity of thin layers and membranes, κ_{film}, decreases appreciably compared to the bulk counterpart, κ_{bulk}, as the membrane thickness decreases.

In order to correct this expression we suggest a modification of the τ_{TH} to take into account the shortening of the phonon mean free path due to diffuse scattering at the boundaries. By replacing κ by κ_{film} in the Equation [3.47] the lifetime of the thermal phonons can be expressed as:

$$\tau_{TH} = \frac{3\kappa_{film}}{C_V \bar{v}^2} \qquad [5.4]$$

and the intrinsic phonon relaxation rate in the Akhieser regime can be rewritten as:

$$\tau_{AK}^{-1} = 3T\frac{C_V}{\rho}\left(\frac{\bar{v}}{v_L}\right)^2 \frac{\omega_L^2(\kappa_{film}/C_V)}{(\bar{v}^4 + (3\omega_L\kappa_{film}/C_V)^2)}\bar{\gamma}^2$$

$$or \qquad [5.5]$$

$$\tau_{AK}^{-1} = 3TC_P\left(\frac{\bar{v}}{v_L}\right)^2 \frac{\alpha\omega_L^2}{(\bar{v}^4 + (3\alpha\omega_L)^2)}\bar{\gamma}^2$$

where $\alpha = \kappa_{film}/C_V$ is the thermal diffusivity, C_P the specific heat capacity and $\bar{\gamma}^2$ the average of the Grüneisen parameter.

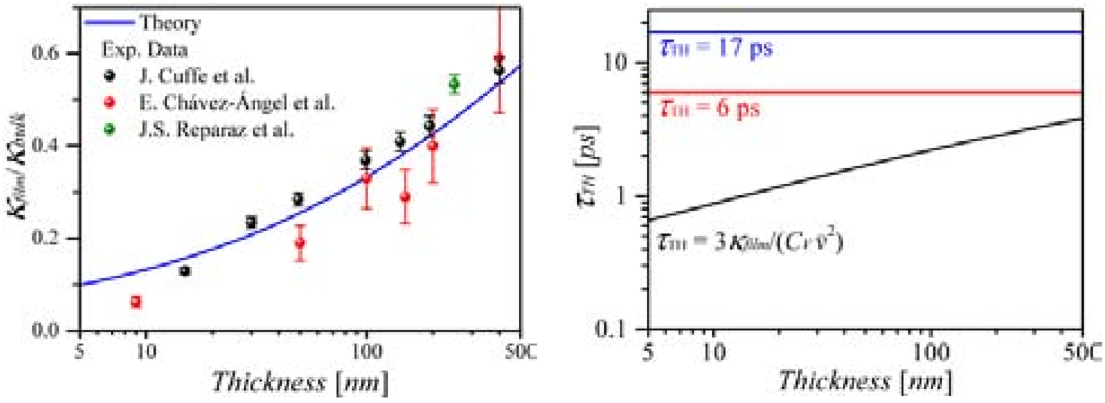

(*a*) (*b*)

Figure 5.6 *(a) Thermal conductivity of Si membranes normalized to the Si bulk value as function of the thickness. The experimental data were obtained from thermal transient gradient (black dots), Raman thermometry (red dots) and two-laser Raman thermometry (green dot) methods, respectively* [184–186]. *The theoretical description of the data using the Fuchs-Sondheimer model is shown in blue solid line. (b) Theoretical lifetime of the thermal phonon, τ_{TH}, as a function of thickness: black line includes modification of thermal phonon lifetime due to the decrease of the thermal conductivity, blue and red lines: constant thermal phonon lifetime of 17 and 6 ps are shown for comparison.*

Figure 5.6*a* shows the experimentally determined room-temperature thermal conductivity of Si membranes of thickness from ~ 400 nm to 9 nm [184–186] which undergoes decrease of about a factor of five with decreasing membrane thickness. The thermal conductivity model using the Fuchs-Sondheimer approach is seen to be in good agreement with the measured values. The details and the parameters used in the simulation are shown in the Appendix III.

An improved estimate of τ_{TH} can be obtained considering the thickness dependence of the thermal conductivity, κ_{film}, in the Equation [5.4]. Figure 5.6*b* shows the calculated τ_{TH} as a function of thickness together with the constant values τ_{TH} = 17 ps and 6 ps. While the first value was obtained in Reference [108] using τ_{TH} as an adjustable parameter, the second value is directly derived from Equation [5.4] by taking κ_{film} = 149 WK^{-1}m^{-1}. Then, once the dependence of τ_{TH} on membrane thickness is determined, the total effect on the intrinsic phonon attenuation is introduced through Equation [5.5].

Finally, the total lifetime, τ_T, of the silicon membranes was calculated considering the extrinsic surface-roughness boundary scattering, τ_B, and the intrinsic Akhieser damping effect, τ_{AK}. The values of C_V, v, and ρ used in these simulations were taken from the literature [101]. Since the Grüneisen parameter in silicon fluctuates between −1 and +1, it is possible to assume that the RMS variation of γ^2 is simply equal to 1. Although this approximation would fail at low temperatures where low frequency phonons with similar values of γ are excited, the vast majority of acoustic phonons are expected to be excited at room temperature and therefore the approach becomes reasonable [108]. A value of $\eta = 0.5$ nm for the roughness was taken from Reference [23].

The calculated total relaxation time using the τ_{AK} component with a constant $\tau_{TH} = 17$ ps and 6 ps or with a thickness-dependent $\tau_{TH} = 3\kappa_{film}/(C_V v^2)$ is shown in Figure 5.7. A better agreement with experimental data is obtained with the thickness-dependent τ_{TH}. As pointed out in Reference [23], at frequencies above 100 GHz (thickness < 50 nm) the measured total phonon lifetime is dominated by extrinsic boundary scattering. In contrast, the intrinsic Akhieser damping becomes the dominant process at lower frequencies (thicknesses > 50 nm).

Although in our previous work [23] the intrinsic phonon attenuation at low frequencies was simulated using the Landau-Rumer model, the modification of the thermal phonon lifetime was not taken into account.

The modified thermal phonon lifetime has a direct consequence for the intrinsic upper limit of the *Q*-factor of nano-mechanical resonators, namely, a decrease in thermal conductivity τ_{TH} can enhance or degrade the *Q*-factor depending on the frequency range. As is shown in the Figure 5.8*a*, at low frequencies the *Q*-factor scales as ~ $1/(\omega\tau_{TH})$ hence, smaller values of τ_{TH} result in higher *Q*-factor. However, at high frequencies, where the *Q*-factor scales as ~ $(\omega\tau_{TH})$, decreasing τ_{TH} leads to the deterioration of the *Q*-factor.

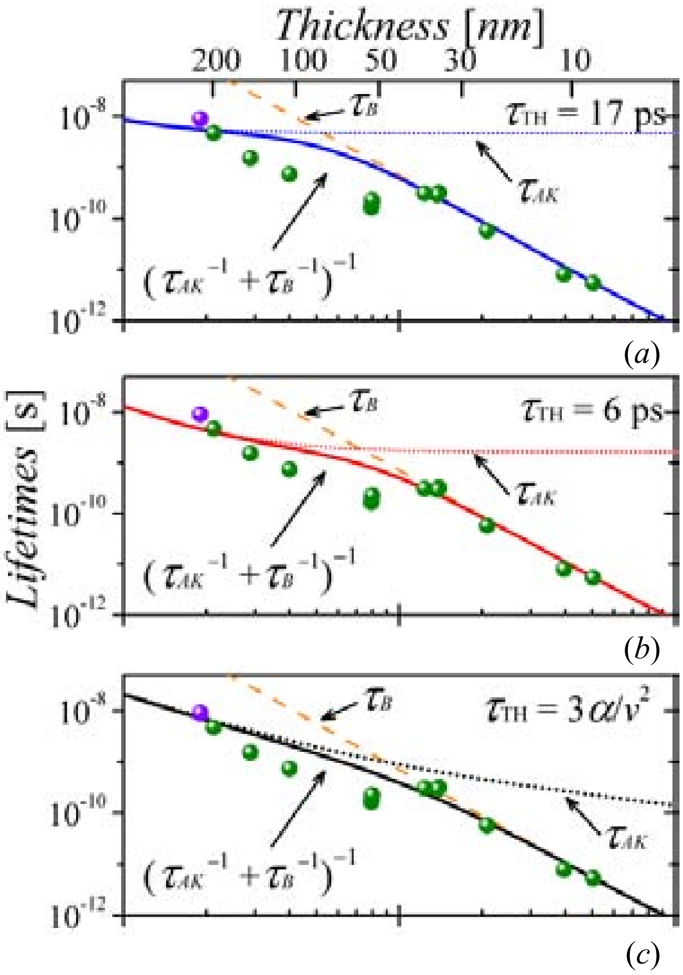

Figure 5.7 *Experimental and theoretical phonon lifetime of the first-order dilatational mode in free-standing silicon membranes as a function of frequency. Data of free-standing Si membranes with thickness ranging from 194 to 8 nm (green dots) were taken from Reference* [23] *and the data point for a 222 nm thick membrane (violet dot) was taken from reference* [180]. *Solid blue (a), red (b) and black lines (c) are the intrinsic Akhieser attenuation dependence calculated for thermal phonon lifetimes of 17 ps (a) and 6 ps (b), whereas (c) includes the thickness-dependent.*

In the example considered here, of a Si membrane for which both phonon lifetimes and thermal conductivities were already known, the validation of the modified Akhieser model becomes easier. Moreover, the connection established in the model between the mechanical mode lifetime and thermal conductivity means that thermal transport parameters could be obtained using contactless pump-and-probe measurements. This is particularly advantageous since standard electrical methods to measure κ require non-negligible processing and its calculation is far from straightforward due to the complex shape of nano/micro mechanical oscillators. Taking this into consideration, we propose the possibility to extrapolate the thermal conductivity from the experimental values of phonon lifetime or Q-factor of the nano/micro oscillators. Assuming that the phonon attenuation/damping of the system is dominated by pure Akhieser mechanism, it is possible to estimate the thermal conductivity/diffusivity from the phonon lifetime or Q-factor from Equation [5.5].

As an example, we calculate the thermal conductivity of a 1D optomechanical crystal [187]. The complexity of this structure makes the calculation of the reduction function almost unfeasible, see the inset of Figure 5.8*b*. If we assume that the quality factor of this system is just limited by the intrinsic Akhieser damping mechanism, then by fitting the Equation [5.5] with the experimental data of the Q-factor, it is possible to estimate the value of the thermal conductivity/diffusivity.

Figure 5.8*b* shows the experimental and theoretical quality factor as a function of the phonon frequency. The experimental data were taken from the Reference [187]. The determination of the thermal conductivity was extracted from the best fit to the experimental quality factor. The obtained value, κ_{wire} = 56.2 $WK^{-1}m^{-1}$, is in good agreement with a similar structure reported by Marconnet et al. [57].

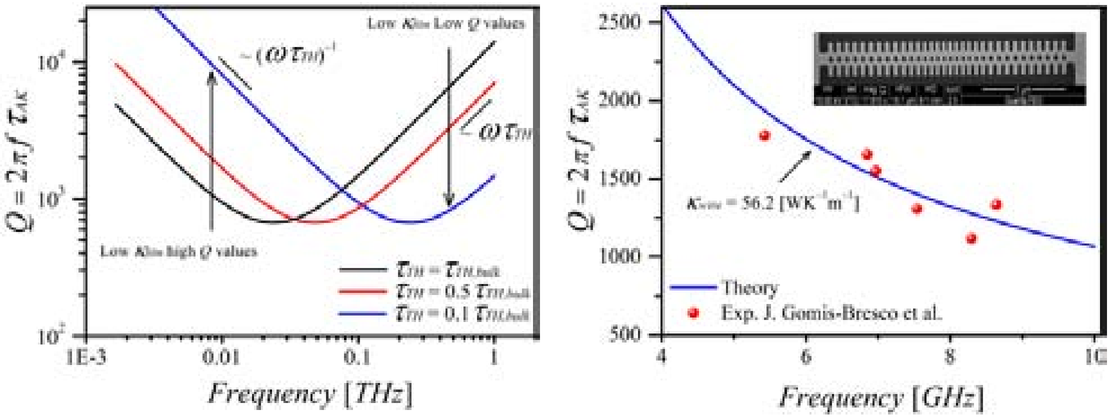

(*a*) (*b*)

Figure 5.8 *(a) Frequency dependence of the Q-factor for different values of the lifetime of the thermal phonon: bulk values,* $\tau_{TH,bulk} = 3\kappa_{bulk}/(C_V v^2)$*, 50% of the bulk value,* $\tau_{TH} = 0.5\,\tau_{TH,bulk}$ *and 10% of the bulk value,* $\tau_{TH} = 0.1\,\tau_{TH,bulk}$*. (b) Experimental and theoretical quality factor of different phonon modes in a Si nano-resonator. The experimental data (red dots) were taken from the Reference* [187]*, blue-solid line shows the best fit. Inset SEM image of the nano-resonator, courtesy of Dr. J. Gomis-Bresco.*

We have revisited the intrinsic damping mechanism limiting the performance of mechanical resonators in view of the modified thermal properties of nanostructured materials. This is illustrated with the example of Si nanomembranes for mechanical mode frequencies above 10 GHz, where a reformulated Akhieser model accounts very well for the measured decrease of the mechanical mode lifetime. We have demonstrated that for membranes it is not possible to assume a constant thermal phonon lifetime since modifications due to surface scattering have to be taken into account. The dependence of the lifetime on the thermal conductivity has a direct impact on the upper limit of the nano-resonators *Q*-factor which, depending on the frequency regime, could enhance or degrade the resonator performance.

In addition, we suggest the possibility to extract thermal conductivity values from lifetime measurements, which opens the possibility to use the *Q*-factor as indicative of the thermal conductivity/diffusivity of nano-resonators.

5.3 Thermal conductivity: measurements and simulations

The experimental determination of the thermal conductivity in nanostructures is one of the most difficult tasks. Contrary to the analogous charge in current, the heat current cannot be measured directly and the heat flux has to be determined assuming a given direction considering a particular geometry. Finally the thermal conductivity is extracted by assuming the diffusive behaviour, i.e., dominated by Fourier law.

In general in a bulk system, it is possible to use a heater and a sink to create a temperature gradient and a pair of thermocouples to measure it, see Figure 5.9, and its thermal conductivity is determined as $\kappa = (Q/A)/(\Delta T/\Delta L)$, where Q is the amount of heat passing through a cross sectional area A and ΔT the temperature difference between two points spaced by a distance ΔL.

However, in nanostructures miniature electrical heaters/thermometers have to be deposited on the sample and used to heat up and to measure the thermal gradient. In this sense, the dimensions of the heater/thermometer are one of the major challenges to measure the thermal properties in nanostructures. One typical example of this kind of technique it is the well-known 3ω method. Some inconveniences of this kind of techniques are the pre-processing stage of the samples preparation which sometime could lead to the modification of the system itself. In addition, the thermal resistance between the heater and the sample could lead to errors in the measurement. For this reason the uses of contactless techniques becomes increasingly attractive to study thermal properties at nanoscale. The lack of contact avoids the interaction between the heater and thermometer with the system.

In this section the measurement of the thermal conductivity as function of the membrane thickness will be described. The measurements were performed by using three contactless techniques: Single-Laser Raman Thermometry (1LRT), Two-Laser Raman Thermometry (2LRT) and Transient Thermal Grating (TTG) techniques.

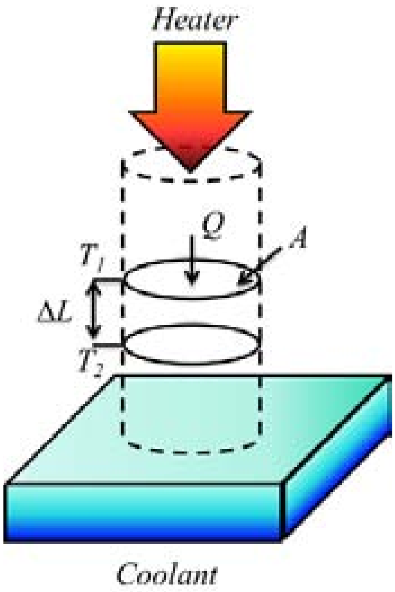

Figure 5.9 *Typical thermal conductivity measurement diagram*

The Raman-based measurements were performed in our laboratories with the collaboration of Dr. Juan Sebastian Reparaz and Dr. Francesc Alzina. The TTG measurements were developed as part of collaboration with groups of Prof. Dr. Gang Chen and Prof. Dr. Keith Nelson from the Massachusetts Institute of Technology, MIT. The TTG work was developed in collaboration with Dr. John Cuffe and Mr. Jeffrey Eliason.

5.3.1 Reduction of the thermal conductivity in free-standing silicon nano-membranes investigated by non-invasive Raman thermometry

As been shown the Section 4.2.3, the Raman thermometry technique is based on focusing a CW laser beam onto the membranes and monitoring the Raman shift (redshift) of the longitudinal optical (LO) phonon of Si as a function of the absorbed power. To correlate the change of temperature with the absorbed power it is possible to estimate the thermal conductivity of the system by solving the steady-state heat equation.

$$\kappa\nabla^2 T = -P_0(r,z) \qquad [5.6]$$

where κ is the thermal conductivity and $P_0(r, z)$ is the heat source term. Considering that the sample is illuminated by laser source, the heat source term can be written as product of irradiance of the laser (the power delivered by the beam on a unit area perpendicular to the beam) and an exponential decay in the z direction, which is

$$P_0(x,y,z) = \alpha_0(1-R)\frac{2P_I}{\pi b^2}\exp[-2r^2/b^2]\exp[-\alpha_0 z] \qquad [5.7]$$

where α_0 is the optical absorption coefficient, R the reflectivity, P_I the total laser incident power and b the spot laser radius. Considering that the lateral dimensions are so much larger than the thickness, the Equation [5.7] can be reduced just to one-dimensional equation along radial direction only, yielding:

$$\kappa\nabla_r^2 T = -\frac{(1-R-T)}{a}\frac{2P_I}{\pi b^2}\exp[-2r^2/b^2] \qquad [5.8]$$

This approximation is suitable for thin films, however for thicker membranes it is recommended to use the full three-dimensional equation.

The determination of the reflectance, $R = P_R/P_I$, transmittance, $T = P_T/P_I$, and absorptance, $A = 1 - R - T$, were performed by measuring the incident, P_I, transmitted, P_T, and reflected, P_R, powers after focusing the laser spot, with wavelength $\lambda = 514.5$ nm, on the surface of the membranes using a 50× (NA = 0.55) microscope objective. The power measurements were performed by using a home-made setup described in Section 4.2.3 and schematically in Figure 4.12.

The theoretical and experimental thickness dependent of R, T and A are shown in the Figure 5.10. The measurements of the optical coefficients were performed at low incident power to avoid any effect from local heating of the membranes. The effect of the scattering was also taken in consideration by using integrating spheres. However, the total contribution from the scattered light was negligible. Finally, the absorption coefficient was computed considering $A = 1 - R - T$ with absolute values and uncertainty lower than 1%. The theoretical modelling, solid lines show in the Figure 5.10, were performed in the group by Dr. Francesc Alzina. The simulations were carried out at room temperature applying the laws of reflection and refraction in a plane-parallel film and using the dielectric function of silicon reported in Reference [188]. From the graph we can note that at thicknesses smaller than, and/or in the order of, the wavelength of the incident light, the optical coefficient has an oscillatory behaviour. That is because membranes behave as Fabry-Pérot optical cavity. Therefore, an oscillatory behaviour is observed instead of a monotonous behaviour as in the case of bulk silicon [189].

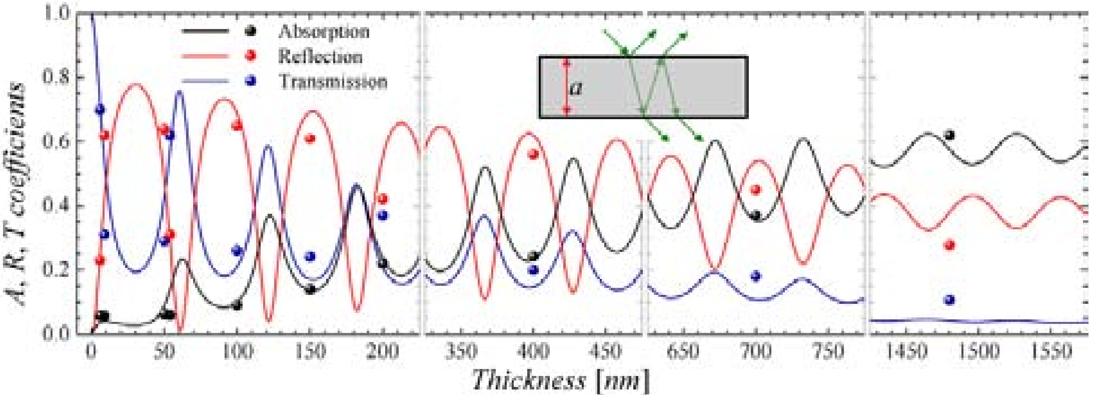

Figure 5.10 *Theoretical and experimental absorptance, A, reflectance, R, and transmittance, T, as a function of membrane thickness. The solids lines are calculation obtained from Fabry-Perot simulations, courtesy of Dr. Francesc Alzina. The solid dots are experimental data points. Inset: diagrammatic Fabry-Perot effect in membranes*

After the absorptance is determined, the temperature dependence of the Raman shift is determined. This dependence provides the calibration of the thermometer. The temperature dependence of the Raman shift is shown in Figure 5.11. The calibration curve was obtained using a cryostat to control the bath temperature. In addition, and for comparison, the data from the Reference [156] is also plotted. By fitting the experimental data, we can observe two ranges of temperature with a linear behaviour: the first range is 200 K $< T <$ 800 K with a slope of $dT/df = -$ 46 K/cm^{-1} and the second one is $T <$ 150 K with a slope of $dT/df = -$ 174 K/cm^{-1}. The temperature accuracy of the calibration is given by the spectral resolution of the equipment. In our case, we used T64000 Raman spectrometer manufactured by HORIBA Jobin Yvon. It was used in single grating mode with a spectral resolution better than 0.4 cm^{-1}, which gives a temperature resolution of ± 2 K.

Figure 5.12 shows the temperature of each membrane at the laser spot as function of the absorbed power, which was computed as $P_A = AP_l$. The Raman shift of the LO mode of the silicon was fitted using a Lorentzian function, which gives an accuracy better than ± 0.05 cm^{-1}. The solid lines are fits to the data using a linear relation.

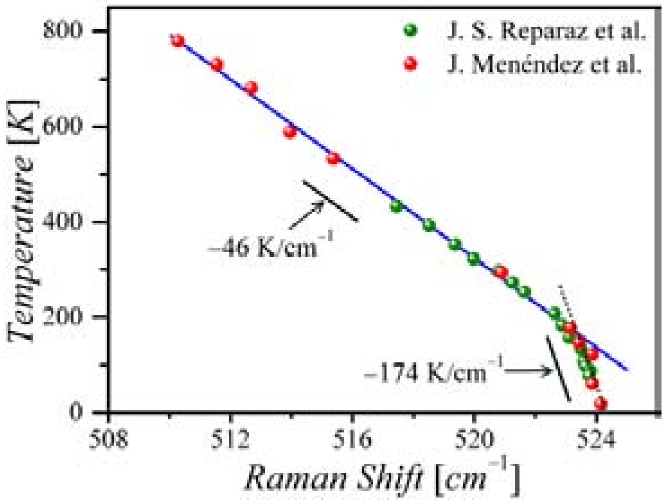

Figure 5.11 *Calibration of the Raman shift of the LO Si mode as function of the temperature: the red and green dots were extracted from the References* [156,186]*, respectively.*

Finally, the thermal conductivity of the sample is determined by solving the steady state heat equation using finite element method, FEM, with the commercial software COMSOL multiphysics. Since the typical thickness of the membranes is much smaller than the lateral dimensions, the heat equation was approximated by a two-dimensional expression.

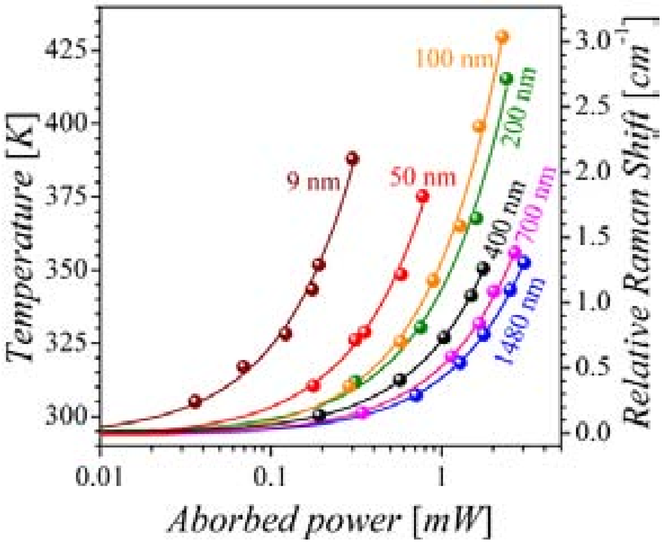

Figure 5.12 *Raman shift (right axis) of the longitudinal optical (LO) Si phonon of the membranes as a function of the absorbed power and membrane thickness. The left axis represent the temperature obtained from the temperature dependence of the LO mode extracted from the slope of the Figure 5.11.*

The heat equation was solved considering room temperature boundary conditions at the edges of the membranes. The values of the thermal conductivity were determined from the best fit to the temperature rise for each absorbed power and thicknesses. Figure 5.13 shows the normalized thermal conductivity, $\kappa_{film}/\kappa_{Bulk}$, for the Si membranes as a function of their thickness. For comparison experimental data of SOI films [2–4] and Si membranes from TTG measurements [184] are also shown. As expected, a systematic decrease of the thermal conductivity is observed with decreasing the thickness, reaching values as low as $\kappa \sim 9$ $WK^{-1}m^{-1}$ for the thinnest membranes, $a \sim 9$ nm.

From Figure 5.13 we note that the thermal conductivity of the SOI films is systematically larger than those of the free-standing membranes. This deviation could be associated to the Si-SiO_2 interface or with a different impurity concentrations, but these have not yet experimentally confirmed. A more logical explanation is to consider that in the case of the SOI samples, the substrate acts as an extra heat sink, thus, leading to a larger effective thermal conductivity.

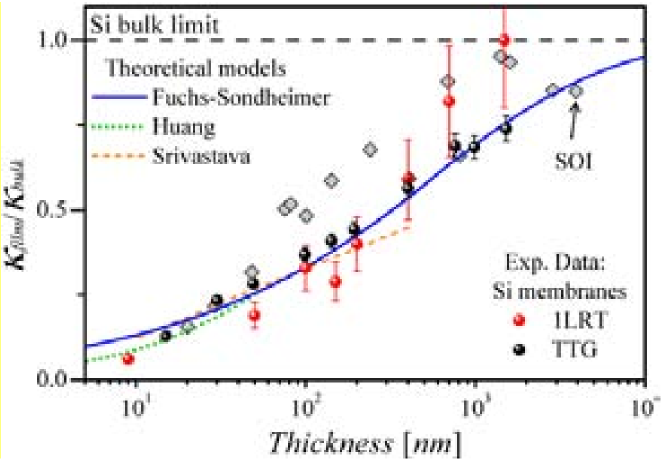

Figure 5.13 *Thermal conductivity of the membranes, $\kappa_{film}/\kappa_{bulk}$, normalized to the bulk Si value as a function of the thickness (solid red dots). As reference previous work in SOI* [2–4] *and membranes using TTG* [184] *are also shown. The theoretical description of the data using the modification of the dispersion relation, Srivastava and Fuchs-Sondheimer models are shown in green dotted, black dashed and blue solid lines, respectively.*

The measured thermal conductivity values were compared with the different theoretical models described in the Chapter IV: Fuchs-Sondheimer [120,122], Huang [46] and modified Debye-Callaway-Srivastava [17] models. All the simulations were performed by using the same Si parameters summarized in the Table 3.3.

While the implementation of each model gives us a correct interpretation of the experimental data, the computational cost makes a significant difference. For example, to calculate the thermal conductivity using the Huang model it is necessary to know the fully modify dispersion relation with the correct number of branches, see Equation [3.59]. The calculation of the required branches is not only a hard task but may also be incorrect.

To calculate the dispersion relation the elastic continuum model is often used. In this model, the discrete nature of the atomic lattice is ignored and the material is treated as a continuum. This model can be derived from the theory of lattice vibrations by considering that the lattice deformations vary slowly on a scale determined by the range of the inter-atomic forces [80], and is usually valid provided the wavelength of elastic waves, λ, is significantly larger than the atomic lattice constant, a_0, i.e., $\lambda/a_0 \geq 20$. This corresponds to wavelengths approximately longer than 10 nm, or frequencies smaller than approximately 100 GHz [81].

On the other hand, if we do not take into consideration the elastic limit, from the calculation of the specific heat capacity, see Figure 3.18 and Figure 3.20, we note that the effect of the modified dispersion relation is almost negligible at high temperatures ($T > 10$ K). However, if we use the criteria of the lattice thermal energy versus spacing energy between the branches, it is possible to find a temperature and thickness range where modified dispersion relation have to be taken into consideration. As shown in the Chapter III, if the energy spacing of the branches exceeds the lattice thermal energy, i.e., $\mathrm{T}a < \hbar\pi v_i/k_B$, the bulk dispersion relation is not the best approximation and modified dispersion relations have to be take into consideration. The effect of that can be seen in the Figure 5.13, which at smaller thicknesses, $a < 15$ nm, Fuchs-Sondheimer and Srivastava models does not exactly match. Anyway, it is very important to note that this **does not prove the validity of a model over the other**, because by using different impurity concentration, surface roughness or Grüneisen parameter each model can match properly in all the range of thicknesses.

In summary, the thickness dependence of the thermal conductivity in ultrathin free-standing Si membranes of high crystalline quality was investigated by using Raman thermometry. The power absorption coefficient of the membranes was determined experimentally and theoretically calculated. The expected reduction of the thermal conductivity with decreasing thickness was also observed. This was successfully modelled considering the modification of the dispersion relation and the shortening of the phonon mean free path due to the diffuse scattering at the boundaries. The thermal conductivity of the thinnest membrane with a = 9 nm resulted in $k_{film} \sim 9\pm2$ WK^{-1}m^{-1}, which could be argued approaches the amorphous limit while still maintaining a high crystalline quality.

5.3.2 A novel contactless technique for thermal field mapping and thermal conductivity determination: Two-Laser Raman Thermometry

Despite the single laser Raman thermometry suitability to determine thermal conductivity, there is substantial information that can be obtained studying the spatial dependence of the temperature distribution in the membranes, e.g., the type of heat transport regime. Recent studies found that phonons with mean free paths greater than 1000 nm contribute 50% of the bulk thermal conductivity of Si near of room temperature [8]. Similar observations were made in GaAs, GaN, AlN and 4H-SiC where phonons with MFPs greater than 230 ± 120 nm, 1000 ± 200 nm, 2500 ± 800 nm and 4200 ± 850 nm, respectively, contribute also to 50% of the bulk thermal conductivity respectively [190]. It is precisely these long MFP that open a world of possibilities to effectively control thermal transport in devices with similar dimensions.

In order to investigate the thermal transport regime, we used the 2LRT technique described in detail in Section 4.2.3. This technique is used to determine the in-plane thermal conductivity as well as its spatial distribution in Si membranes with thicknesses of 250 nm, 1 μm and 2 μm.

The membranes were single crystalline with a surface roughness Ra = 0.2 nm and rms = 0.15 nm, and were purchased from NORCADA Inc. The thermal conductivity was determined by solving the Fourier law analytically and also by using FEM simulations.

Figure 5.14 shows three-dimensional contour plot of the thermal field distribution of the 250 nm thick Si membrane. The maximum temperature reached at the center is $T_{max} \approx 830$ K and it decays symmetrically to 400 K at the edges as is shown in lower part of the Figure 5.14.

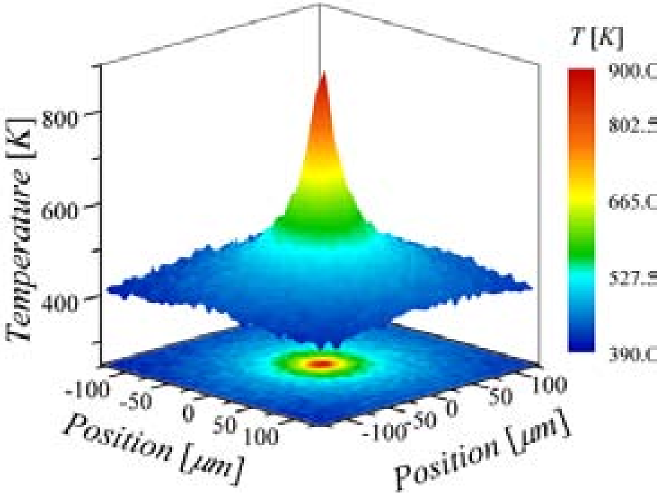

Figure 5.14 *Three-dimensional contour plot of the thermal field distribution of a 250 nm thick free-standing Si membrane. The isoline distribution of the thermal field is also shown in a lower plane. The colour bar indicates the maximum temperatures reaches.*

The symmetry of the thermal fields arises from the isotropic behaviour of the thermal properties of silicon. However, for anisotropic materials an asymmetric thermal decay is expected.

Figure 5.15 shows vertical and horizontal temperature cuts of the isoline thermal field distribution of a 250 nm thick free-standing Si membrane. It is noteworthy that the temperature field does not fully decay to the thermal bath temperature of ~ 300 K, and instead reaches only 400 K at 120 µm from the centre. The origin of this slow thermal bath temperature is due to a combination two effects: the low thermal conductivity of the membrane as well as the extra heating source from the probe laser.

Finally, by using the symmetric properties of the thermal field the determination of the thermal conductivity can be made using only single line scan between two arbitrary points, with one of them being the origin, i.e., the point of highest temperature rise.

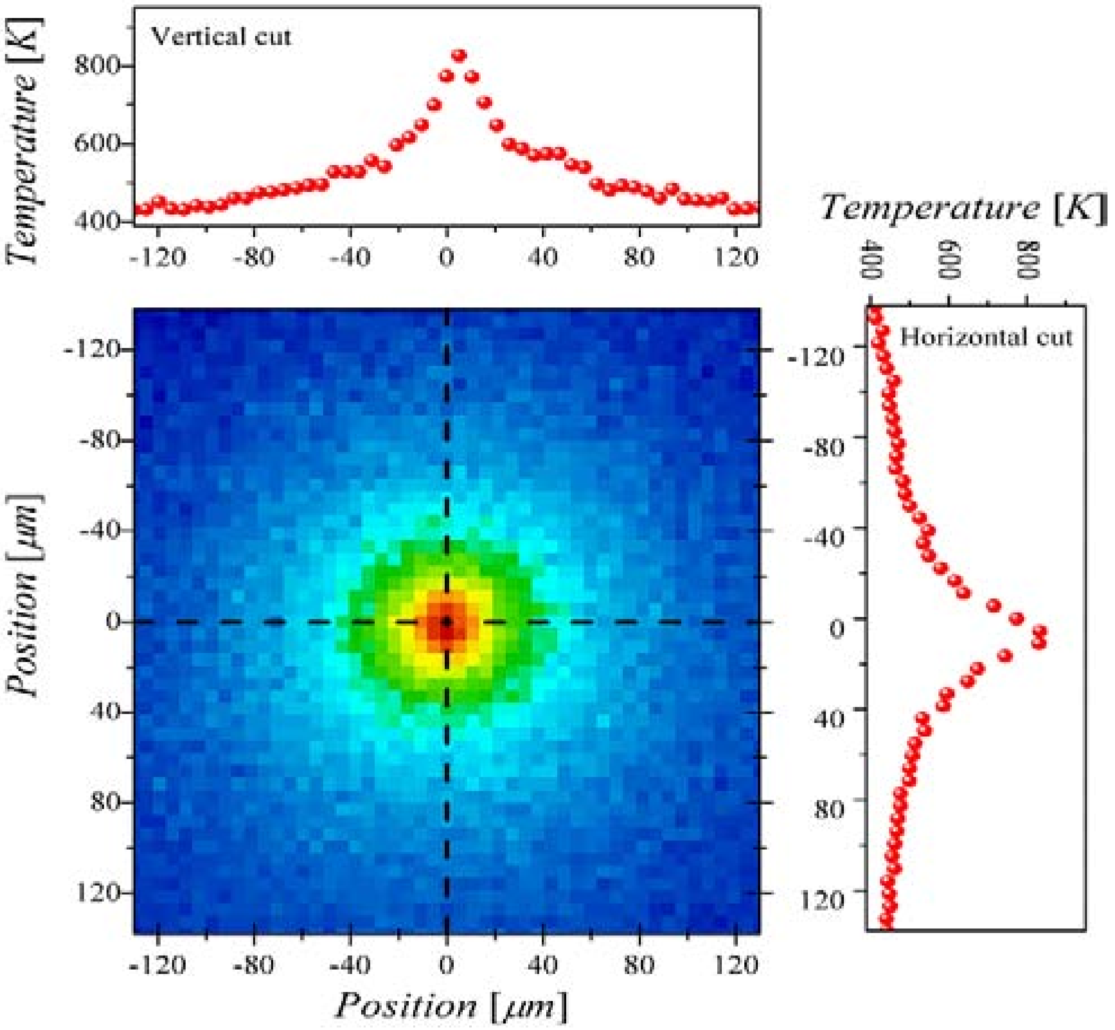

Figure 5.15 *Vertical and horizontal temperature cuts of the isoline thermal field distribution of a 250 nm thick free-standing Si membrane. Note the high symmetric distribution in temperature from both cuts.*

Figure 5.16 shows the temperature profile taken on a 1 μm thick Si membrane (blue dots). The heating laser location corresponds to the centre of the plot (0 μm) and the Raman signal is obtained by scanning the thermometer laser symmetrically on both sides of the source along a line. The Raman shift is converted to temperature using the calibrated temperature dependence of the Raman peak position (see Figure 5.11). A temperature rise of ~ 140 K is measured at the position of the source decaying slowly towards the edges of the membrane. The experimental and simulated temperature fields are shown in Figure 5.16, taking different values of κ_{film} ranging from the values normalized to the bulk thermal conductivity (1) decreasing progressively to 65% of it. The thermal conductivity and the temperature profiles were determined solving the Equation [5.7] using the finite element method. A compressive discussion of the simulation can be found in Appendix III.

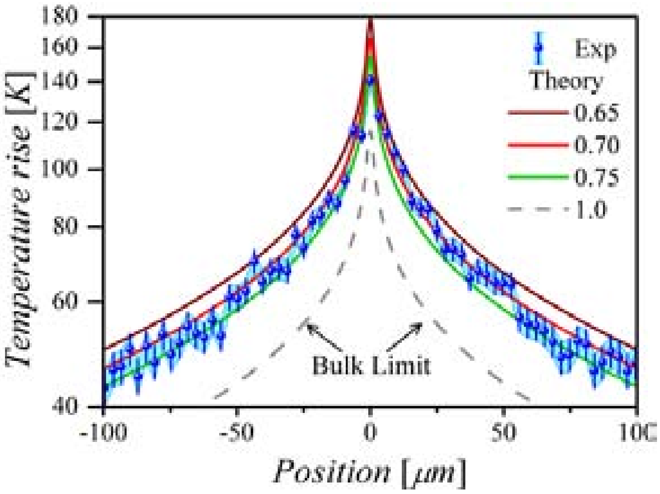

Figure 5.16 *Comparison of the temperature map measured and simulated for a 1 μm thick silicon membrane. The solid lines represent theoretical curves with different thermal conductivity values ranging from the bulk values (1) and decreasing progressively to 65% of the bulk values (0.65).*

A better agreement between experimental data and simulation is found when a decrease of the thermal conductivity in the membrane is included, $\kappa_{film} \approx 0.70\kappa_{bulk}$, i.e., $\kappa_{film} \approx 105$ WK^{-1}m^{-1}. This is better seen in Figure 5.17 where all the experimental points have been gathered. The decrease of the thermal conductivity matches very well the expected value in Figure 5.13. A similar analysis was performed for the 2 μm Si membrane, where the best fit was found to be $\kappa_{film} = 118$ WK^{-1}m^{-1}. The experimental and theoretical data are shown the Figure 5.18.

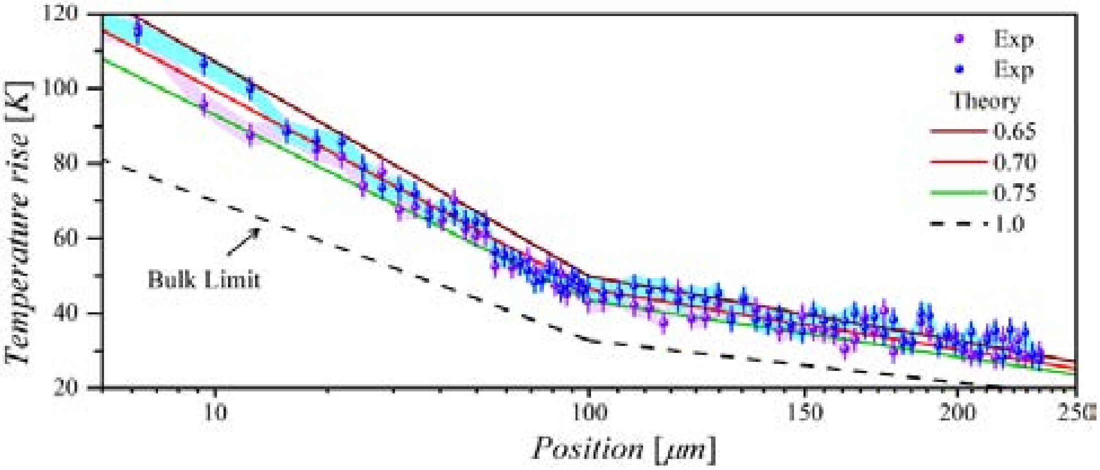

Figure 5.17 *Experimental temperature profile measured in a 1µm thick Si membrane (green and purple dots). The purple dots come from of the negative part of the Figure 5.16 mirror reflected to the right side.*

For the case of an ultra-thin membrane it is possible to obtain an analytical expression for the thermal field distribution. Following the work of J.S. Reparaz et al. [186], we can approximate the temperature distribution created by the excitation of a point like laser source to that shown in Figure 5.15. The solution of the heat equation is then simply given by integrating the Fourier Law: $Q = -\kappa(T)\nabla T$, where the total flux is given by the total power injected to the system, $P_A = AP_I$, divided by the cross sectional area of the membrane $A = 2\pi ra$ and the thermal conductivity can be considered constant or temperature-dependent ($\kappa_{film} \sim 1/T$). Finally, the temperature profile is for a constant thermal conductivity is given by:

$$T(r) = T_0 - \frac{P_A}{2\pi a \kappa_{film}} \ln[r/r_0] \rightarrow \kappa_{film} = const. \qquad [5.9]$$

$$T(r) = T_0 \left(\frac{r}{r_0}\right)^{-P_A/(2\pi a\beta)} \qquad \rightarrow \kappa_{film} \approx \beta / T \qquad [5.10]$$

where T_0 is the temperature of the bath at a distance r_0 from the heat source.

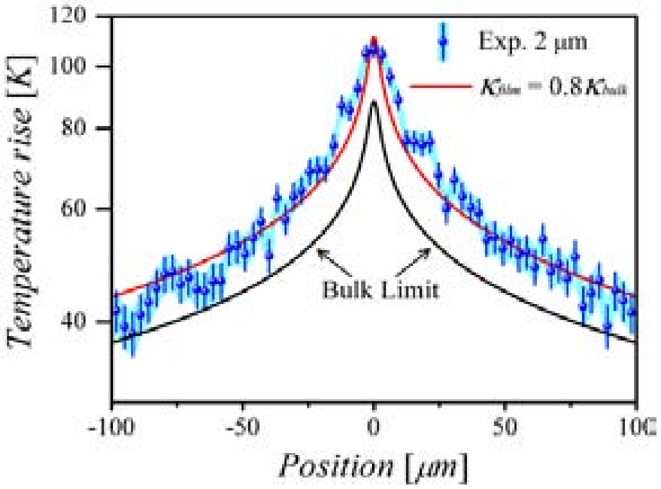

Figure 5.18 *Comparison of the temperature map measured and simulated for a 2 µm thick silicon membrane. The solid lines represent theoretical curves with thermal conductivity value of 118* $WK^{-1}m^{-1}$.

Figure 5.19 shows the experimental and theoretical results of a 250 nm thick Si membrane. The experimental data are shown in blue dots with errors bars of the same size of the dots. The red solid line represent the theoretical curve of the thermal field simulated with Equation [5.9], by assuming that the bath is at in the limit of the line scan, $r \sim 230$ µm and constant thermal conductivity. For comparison, the bulk limit is shown in black solid line.

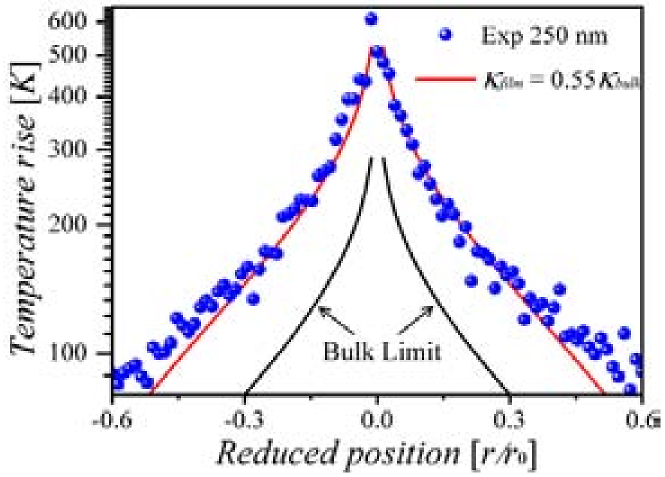

Figure 5.19 *Comparison of the measured and simulated temperature map for a 250 nm thick silicon membrane. The solid red line represents theoretical curves with thermal conductivity value of* $81 WK^{-1}m^{-1}$. *The bulk limit, black solid line, is shown by comparison.*

From the Figures 5.16 to 5.19, it is possible to note that the bulk limit for each case shows smaller temperature rise than the membranes. This difference between the thermal field distributions is a direct consequence of the low thermal conductivity of the membranes.

In summary, the values of the thermal conductivity of free-standing Si membranes were extracted from a novel contactless two-Laser Raman Thermometry, 2LRT. This technique is based on a two-laser approach to induce and probe the thermal field in the samples. The temperature resolution for Si samples is ~ ± 2K and the spatial resolution is defined by the optical diffraction limit which can be as low as 300 nm.

The experimental temperature profiles obtained with this technique for a Si membrane have been simulated by solving the thermal conduction equation within a finite element model as well as using an analytical approach. As expected, we found the reduction of the thermal conductivity matched quite well the theoretical prediction as well as the values in the literature, see Figure 5.20.

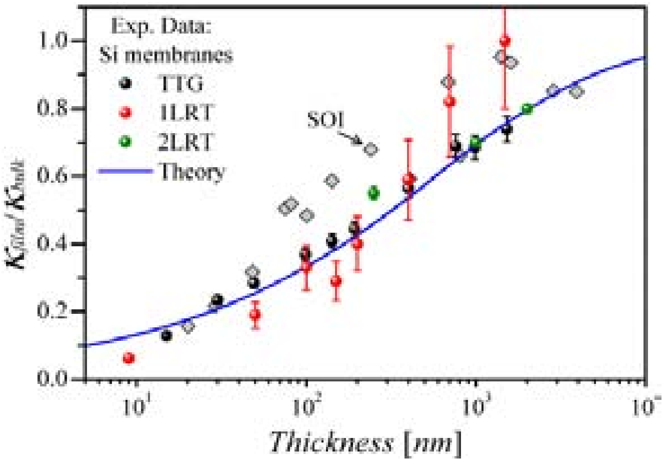

Figure 5.20 *Theoretical and experimental thermal conductivity of the Si membranes, normalized to the bulk Si value,* $\kappa_{film}/\kappa_{bulk}$, *as a function of thickness. The green solid dots show this work (2LRT) and as reference previous work data on SOI* [2–4] *and Si membranes using TTG* [184], *and Single-Raman thermometry, 1LRT, are also shown.*

5.3.3 Transient thermal grating measurements: temperature dependence of thermal diffusivity

Here, the temperature-dependence of the thermal diffusivity of 100 nm and 200 nm thick Si membranes is studied using TTG technique. This method was recently used to measure thermal transport in nanoscale silicon membranes, with thickness values ranging over two orders of magnitude from 15 nm to 1.5 µm [173,184]. A schematic TTG configuration is shown in Figure 4.15. Similarly to Raman thermometry, this technique does not require an absorbed metal transducer or any electrical heating. This means that no electrical or thermal contact resistances are introduced in the measurement or the analysis.

The main advantage of this technique compared with Raman thermometry is that the absolute injected power does not need to be measured. However, we have to take care that the finite size of the heat source does not affect the results, especially in Si, where a broad distribution of the phonon mean free path contributes to the thermal conductivity [8]. Therefore, it is crucial to vary the grating period in order to ensure diffusive transport.

Finally, since the thermal grating is defined in the plane of the membrane, in-plane thermal transport is assured. As described in section 4.2.3, the thermal diffusivity is extracted from the exponential fit to the time traces of the thermal grating. The decay time, τ, is inversely proportional to the thermal diffusivity, α, with a constant of proportionality given by the square of the grating wavevector q, i.e., $1/\tau = 4\pi^2\alpha/\Delta^2$ where Δ is the fringe spacing.

The thermal diffusivity as a function of grating spacing of a 200 nm thick Si membrane is shown in Figure 5.21. Data was collected for grating periods and temperatures ranging from 7.5 to 25 µm and 80 to 294 K, respectively. The diffusivity is seen to be constant as a function of grating spacing, indicating diffusive thermal transport. The slope shown at 80 and 90 K is due to non-diffusive effects.

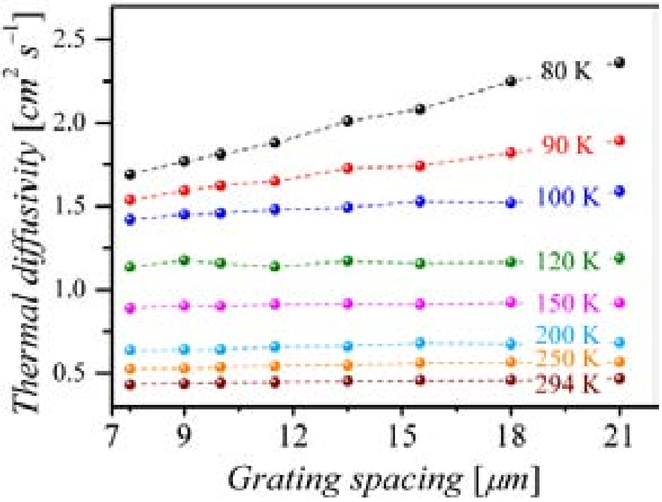

Figure 5.21 *Thermal diffusivity as a function of grating spacing in a 200 nm thick Si membrane at different temperatures.*

Figure 5.22 shows the thermal diffusivity as a function of the temperature for 100 nm and 200 nm thick in Si membranes. A dramatic decrease of the thermal diffusivity is found, down to values of at least an order of magnitude between the membranes and the bulk counterpart. This is reflected in the change of temperature-dependence of the thermal diffusivity from ~ $T^{-2.6}$ to $T^{-0.6}$.

Previous work in bulk Si has shown differences of one order of magnitude between lightly and highly doped samples [193]. However, in ultra-thin membranes the boundary scattering becomes the dominant processes. The change in the temperature-dependence reveals the impact of the boundary scattering, which becomes more significant with decreasing membrane thickness.

In summary, the temperature dependence of the thermal diffusivity in 100 nm and 200 nm thick free-standing Si membranes has been measured. As expected, the thermal diffusivity is substantially reduced in the thinnest membrane, reaching values as low as two orders of magnitude compared with their bulk counterpart at low temperature regime.

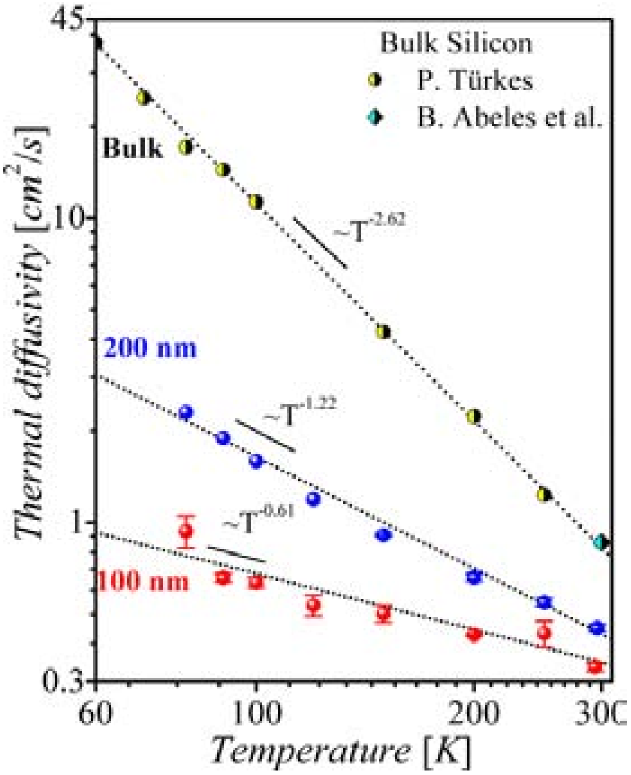

Figure 5.22 *Temperature dependence of the thermal diffusivity for 100 and 200 nm thick Si membranes. The Si bulk values are also shown for comparison* [191,192]

5.4 Thermal rectification

Similar to the electric charge diode, thermal rectification is a phenomenon where transport is preferred in one direction over the opposite. This effect could have widespread applications including electronics cooling and thermoelectrics with the improved ability to control thermal transport. This process requires simultaneously asymmetry and non-linearity [194]. Thermal rectification at the nano/microscale is attracting scientific attention due to its promising potential. Moreover, in analogy with electrical diodes, the thermal rectifier or thermal diode becomes an essential building block of future thermal logic circuits.

Thermal rectification is a phenomenon in which thermal transport properties, along a specific axis, depend upon the direction of the temperature gradient or heat current. In solid-state systems, at least five different rectifications mechanisms have been suggested: different thermal boundary resistance between two materials [195–197], anharmonic interatomic potentials [198], ballistic scattering in asymmetric nanostructures [199], asymmetric load mass [200], and different temperature dependence of the thermal conductivity of two connected different bulk materials [201–203]. Based on this last mechanism for thermal rectification, i.e., the combination of two dissimilar materials with different trends in their temperature dependence of the thermal conductivity in a certain temperature range, we have studied the control of the in- and out- of-plane heat conduction in laterally and vertically stacked Si and Ge thin films.

5.4.1 Modelling of thermal rectification in Si and Ge thin films

In the present work we have studied an extension of the classical thermal rectification, arising in certain cases from the contact of two dissimilar bulk materials with different temperature dependence of the thermal conductivity, to Si-Ge when boundary scattering effects are taken into account. Moreover, the directionality of the in-plane heat flow in a Si plate can be achieved by tuning the thickness and the impurity concentration along the cross section of the plate. We designed several potential structures with this function in mind and discussed the physics behind.

Based on the combination of two dissimilar materials with different trends in their temperature dependence of the thermal conductivity in a certain temperature range, we have studied the control of the in- and out- of-plane heat conduction in laterally and vertically stacked thin films, as shown in Figure 5.23. Moreover, the dependence of the thermal conductivity with film thickness provides a degree of freedom to optimize the rectification effect in Si-Ge system, when boundary effects are taken into account. In addition, the directionality of the in-plane heat flow in a Si plate can be achieved by tuning the thickness and the impurity concentration along the cross section of system.

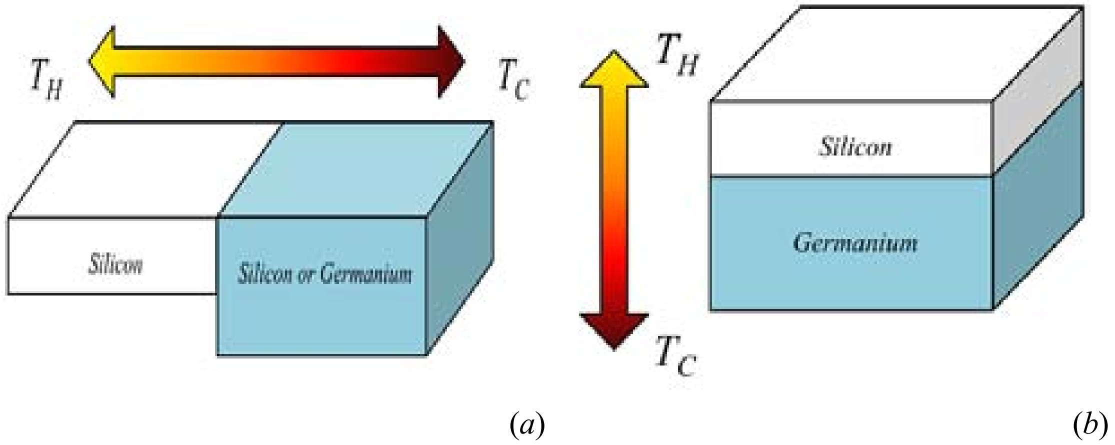

Figure 5.23 *Two-segment schemes for thermal rectification: (a) In-plane Si-Si or Si-Ge configuration. (b) Out-of- plane Si-Ge configuration.*

We start by deriving the lattice thermal conductivity in thin films, both in- and out-of-plane, based on a modified Callaway model with Fuchs-Sondheimer boundary corrections. Then the rectification factor of the different configurations is calculated. Estimated efficiencies of 10 % (at ΔT=60 K) and 12 % (at ΔT=40 K) are found in Si-Si and Si-Ge systems, respectively, for in-plane configuration. In the case of Si-Ge out-of-plane configuration, the thermal rectification reaches a maximum efficiency of around 3.6 % at room temperature with ΔT=200 K.

In general terms, the condition of rectification in a two- component system is typically related to the appearance of a crossing of the temperature-dependent thermal conductivities at a certain T, as a result of their different trend, i.e., different slope sign and/or value. Figure 5.24 shows different examples of tuned thermal conductivities of Si and Ge thin films where this condition applies. With the prospect of verifying the suitability of thin films in the configurations of Figure 5.23 as basic components for thermal rectification, we evaluated the heat flow of a two-segment system connected to two reservoirs at T_H and T_C, respectively, using the Fourier law approach. The temperature difference generates a heat flow ($Q_>$) in the direction of the temperature gradient. After exchanging the temperatures of the reservoirs, the thermal flux changes its direction ($Q_<$). If the magnitudes of the two fluxes are different, the device exhibits an effective thermal rectification, which is evaluated by the coefficient [202],

$$\varepsilon(T_H, T_C) = \frac{Q_> - Q_<}{Q_<} \qquad [5.11]$$

For simplicity, we have not considered interface resistances. The derivation of the thermal flux expressions and the methodology used to calculate it, follow the work of C. Dames [202] and references therein.

The thermal rectification coefficient was calculated in different configurations of laterally and vertically stacked Si and Ge thin films, according to Figure 5.23*a* and *b*. Different combination pairs of Si and Ge were tailored to present a crossing of the temperature-dependent thermal conductivities (Figure 5.24). In each case, the thermal rectification was calculated by fixing T_H and varying T_C in an adequate temperature range.

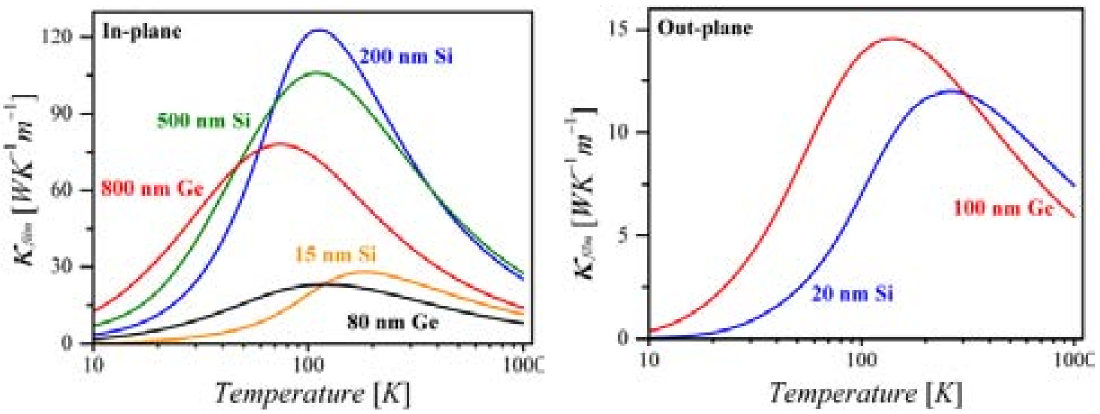

(*a*) (*b*)

Figure 5.24 *Temperature dependence of the in-plane (a) and out-of-plane (b) thermal conductivity of Si and Ge thin films. All curves were calculated with a mass-defect scattering parameter (Γ) reflecting the natural isotope concentration, with the exception of the 500 nm thick Si film for which an increased mass-defect scattering was introduced (10Γ).*

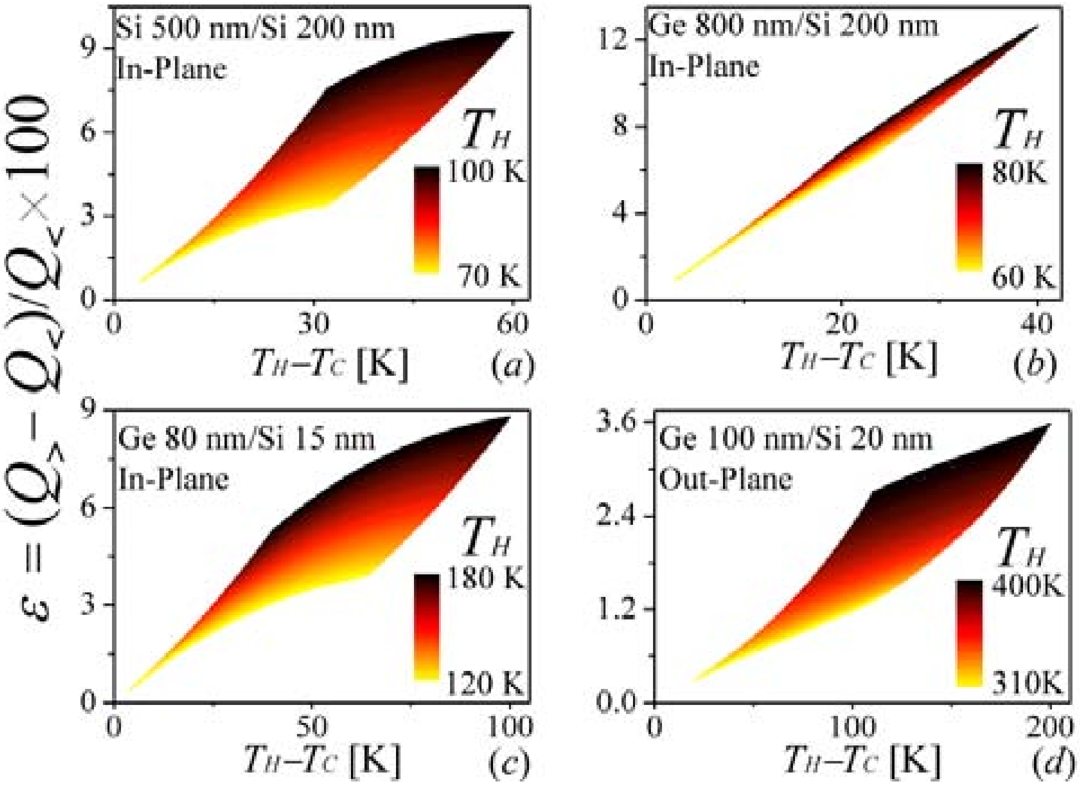

Figure 5.25 *Calculated in-plane thermal rectification coefficient of (a) 500-200 nm Si-Si, (b) 800-200 nm Ge-Si and (c) 80-15 nm Ge-Si systems. Calculated out-of-plane thermal rectification of a 100-20 nm Si-Ge system. For each configuration T_H, was fixed and the low temperature was varied.*

The first design of the type sketched in Figure 5.23*a* consists of a Si film with a natural isotope concentration, that is with a mass defect scattering parameter Γ, presenting a cross section comprised of a 500 nm thick section with high impurity concentration, 10Γ, followed by a 200 nm thick undoped Si section. The effect of the high-impurity concentration is to decrease the thermal conductivity of the 500 nm thick section, which becomes smaller than that of the 200 nm thick section for temperatures above 70 K (green and blue curves in Figure 5.24a, respectively). As a consequence of the crossing of these two curves at this temperature and their different slopes around it, the laterally stacked Si-Si system exhibits an effective thermal rectification between 0.5 to 10 % for a ΔT ranging from 4 to 60 K, as the calculated rectification factor in Figure 5.25*a* reveals.

The second and third designs are again configured for in-plane thermal rectification (cf. Figure 5.23a) but using segments of different material, i.e., Si and Ge films, with a combination of thicknesses of 200-800 nm and 15-80 nm, respectively. For the first system, the crossing of the thermal conductivity was found around of T = 58 K (blue and red curves in Figure 5.24*a*). The thermal rectification was estimated to be between 0.4 to 12 % at a temperature difference ΔT ranging from 3 to 40 K, as is shown in Figure 5.25*b*. For the second system, the crossing was found around T = 118 K (black and orange curves in Figure 5.24*a*) yielding a thermal rectification factor between 0.4 to 9 % for a temperature difference ΔT ranging from 4 to 100 K (cf. Figure 5.25*c*).

The last design involves an out-of-plane configuration (see Figure 5.23*b*) composed of 20 and 100 nm thick Si and Ge films, respectively. In this case the thermal conductivities cross at around 300 K (blue and red curves in Figure 5.24*b*). The rectification factor was found between 0.3 to 3.6 % for a ΔT ranging from 20 to 200 K, as is shown in Figure 5.25*d*.

In summary, we have calculated the thermal rectification coefficient in structures containing Si and Ge layers using the well-known mechanism for thermal rectification based on the different temperature-dependence of the thermal conductivity in a two-component system. The crossing of the thermal conductivity curves of the two materials in either a horizontal or vertical stack establishes a condition to achieve thermal rectification. We have shown that by varying the film thicknesses and the impurity concentration we are able to tailor the temperature dependence of the thermal conductivities in order to maximize the rectification efficiency and, thus, tune the temperature operation of the devices. This concept was fully exploited in the first in-plane design in Si consisting of two Si sections (segments) with different impurity concentration and film thicknesses. The rectification factor founded is in the range of 0.5 to 10 %. In the second and third in-plane designs based on a two-component system (Si and Ge), the thermal rectification factor was estimated between 0.4 to 12 %. Whereas for the out-of-plane configuration the resulting thermal rectification factor is about 3.6 %.

CHAPTER VI: CONCLUSIONS AND FUTURE WORK

6.1 Thesis Summary

Staring with the hypothesis that phonon confinement plays an important role on thermal properties; we present an insightful theoretical and experimental study of the phonon properties of silicon nanomembranes. By using advance and novel contactless techniques the acoustic dispersion relation, phonon lifetime, thermal conductivity and thermal diffusivity transport have been measured and compared with theoretical predictions.

The acoustic dispersion relation was measured by using Inelastic Brillouin Light Spectroscopy. Modes between 1 to 3 GHz from the fundamental flexural mode were detected in 17 nm thick silicon membrane. The quadratic behaviour of the dispersion curves was observed and simulated using the elastic continuum approach, showing a good agreement with the experimental data. Additionally, we demonstrated that the fundamental flexural wave dispersion in ultra-thin membrane can be described with simple quadratic wavevector dependence. This behaviour leads to a dramatic decrease of the group/phase velocity and has implications for the thermal properties of the system, being stronger in the low temperature regime, where the fundamental flexural mode carries most of the heat. The impact of the quadratic dispersion relation was observed in a strong modification of the specific heat capacity at low temperature regime. We found that the temperature dependence of the specific heat in this regime departs from “3D behaviour” $C_V \sim T^3$ toward a “1D behaviour” $C_V \sim T$. This change is related to the large contribution from the fundamental flexural wave, which for small parallel wavevector has a quadratic dispersion relation. We found that in the low temperature regime the specific heat of membranes is larger than in the bulk.

The phonon lifetime and frequencies of first order dilatational mode, with frequency given by $f = v_L/(2a)$, were measured by state-of-the-art ultra-fast pump-probe technique known as Asynchronous Optical Sampling, ASOPS. We investigated a series of Si membranes with thicknesses ranging from ~ 8 nm to 200 nm. The thicknesses/frequency dependence of the phonon lifetime was observed and simulated. The experimental phonon lifetime was compared with theories considering intrinsic scattering and extrinsic surface roughness scattering. From this modelling, we have identified that at frequencies higher than 100 GHz or thickness < 50 nm, the total phonon lifetime is dominated by extrinsic boundary scattering, while a lower frequencies or thickness > 50 nm, the phonon lifetime is dominates by intrinsic scattering mechanisms.

Although previously [23], we modelled the intrinsic mechanism considering the Landau-Rumer approach, the modification of the lifetime of the thermal phonons, τ_{TH}, was not taken into account. Finally, we demonstrated that the intrinsic phonon-phonon interaction based on Landau-Rumer approach can fit better the experimental data. The poor fit between the Akhieser model and our experimental data can be attributed to the values of τ_{TH}. Due to the uncertainly in the value of the lifetime, we used the constant value of $\tau_{TH} = 17$ ps taken from Reference [108], which provided the best fit to the acoustic attenuation in bulk silicon. In order to correct this expression we suggested the modification of τ_{TH} due to the thicknesses dependence of the thermal conductivity in Si membranes. By expressing the lifetime of thermal phonon as $\tau_{TH} \approx 3\kappa_{film}/(C_V v^2)$, we found out that it is not possible to assume a constant lifetime of the thermal phonons and a more complex dependence has to be taken. Additionally, we showed the impact of the modification of τ_{TH} in the performance of the Q-factor of high frequency oscillators: depending on the frequency regime as well as on the values of the thermal conductivity, it is possible to enhance and/or degrade the Q-factor. At low frequencies the Q-factor scales ~ $1/(\omega\tau_{TH})$ and since the τ_{TH} scales directly proportional to the thermal conductivity, smaller values of the thermal conductivity lead to higher values of *Q*. However, at higher frequencies, where the *Q*-factor scales ~ $(\omega\tau_{TH})$, a smaller thermal conductivity leads to a decrease of the *Q*-factor. These results have important consequences for the performance of resonance based sensors as well as providing a firm foundation to study of the effect of thermal conductivity in the intrinsic limit of *Q*-factors.

The study of the in-plane thermal conductivity was measured by using three optical techniques: single-laser Raman thermometry, two-laser Raman thermometry and thermal transient gradient. As expected, a systematic decrease of the thermal conductivity was observed with decreasing membrane thickness, reaching values as low as $\kappa \sim 9$ WK^{-1}m^{-1} for the thinnest membranes, $a \sim 9$ nm. The measured thermal conductivity was also modelled considering the modification of the dispersion relation and the shortening of the phonon mean free path due to the diffuse scattering at the boundaries.

Finally, we calculated the thermal rectification coefficient in Si-Ge films-based systems using the well-known mechanism for thermal rectification based on the different temperature-dependence of the thermal conductivity in a two-component system. We have shown that by varying the film thicknesses and the impurity concentration we are able to tailor the temperature dependence of the thermal conductivities in order to maximize the rectification efficiency and, thus, tune the temperature operation of the devices. This has important consequences for the design of future thermal logic circuit and provides two different parameters for tuning the performance of thermal rectifiers.

The results of this thesis have demonstrated the strong impact of the reduction of the dimensionality on the thermal properties of the systems. The modification of acoustic phonon dispersion, lifetime, specific heat capacity and thermal conductivity and diffusivity was investigated and the effect of the reduction of the dimensionality was successfully demonstrated. However the impact of the modified dispersion relation on the thermal properties was not completely demonstrated. To further understand the effect of the modified dispersion relation in the thermal conductivity, new experiments in porous silicon membranes will be performed. In addition, research on the transitions between heat transport regimes (diffusive and/or ballistic) as a function of materials, dimensions and temperature will also be investigated.

6.2 Future work

Traditionally, the tuning of the thermal conductivity is achieved by varying the impurity concentration, surface roughness and grain boundaries or by the inclusion of nanoparticles or holes. This leads to increase of the phonon scattering and the shorting of the phonon mean free path. Among these means, the introduction of holes in a silicon structures has demonstrated to be one of the most effective ways to reduce the thermal conductivity which, depending of the porosity, can reach values as low as three orders of magnitude those of the non-porous material.

In this sense, the ordered fabrication of pores in a crystalline system gives rise to phononic crystals. Similarly to the concept of photonic crystal, the phononic crystal was conceived as periodic arrange of two dissimilar materials, e.g. silicon and holes, generating an artificial lattice with all the associated concepts to them such as: Brillouin zones, band gap, modification of the dispersion relation, and so on. The redefinition of the Brillouin zones and the modification of the dispersion lead to changes in all the frequencies dependent parameters of the system, which in turns has an impact on the thermal properties of the system.

However, for the particular case of the Si membranes, we have shown that the reduction of thermal conductivity can be attributed mainly to the shortening of the phonon mean free path due to the diffuse scattering of phonons at the boundaries. At room, the impact of the modification of the dispersion relation on the reduction of thermal conductivity is negligible.

This is because the quantization of the dispersion relation quickly reaches the continuum. However, for small dimensions (*d* < 15 nm) or at low temperature (*T* < 15 K), the modification of the dispersion relation should be taken into account, including its effects on group velocity, phonon density of states, heat capacity and so on.

From these results an open question emerges concerning the low thermal conductivity exhibited by phononic crystals at room: Is it just a consequence of increased extrinsic scattering (boundary and holes scattering) or is it due to the modification of the dispersion relation? This question also gives rise to others questions:

i. Is it possible to manipulate the thermal conductivity through modifications of the dispersion relation at room temperature?

ii. What is the role of the modification of the dispersion relation on the thermal conductivity at room temperature?

iii. If the low thermal conductivity in a phononic crystal is just due to extrinsic scattering: does it make sense to work on a proper design of phononic crystal (including acoustic band gap and stop bands)?

In order to answer these questions and study the real effect of the modification of the dispersion relation future experiments will be performed. The main idea is to compare three similar membranes: two porous membranes with an order and disorder pattern (see Figure 6.1*a* and *b*, respectively) and one without any nanostructuring. Measurements of dispersion relation, phonon lifetime and thermal conductivity would be performed and the results compared among them.

Measurements of the temperature-dependence of the thermal conductivity may also be performed. This experiment would allow us to establish the temperature regime where the modification of the dispersion relation becomes relevant for the thermal management.

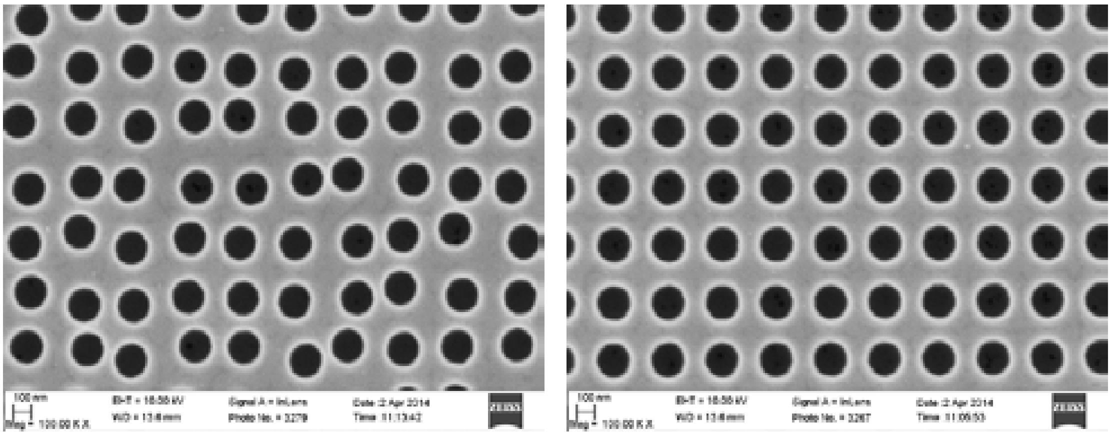

(*a*) (*b*)

Figure 6.1 *SEM image of the ordered (a) and disorder (b) phononic crystal for thermal properties analysis. Courtesy of Dr. Marianna Sledzinska.*

Others important questions rise from the dynamics of high frequency phonons in the surface and interfaces. The influence of constant or frequency-dependent surface roughness parameter still remains as open question and the experimental measurements of the phonon decay as function of roughness are necessaries. Future experiments of the phonon-lifetime may also be performed by using ultra-fast pump-and-probe technique (ASOPS).

The study of the phononic and thermal properties of suspended membranes is the key to determining the thermal behaviour of more elaborated structures leading to advanced electronic and photonics devices based on SOI and other thin film stacks. These include opto-mechanical crystals and advanced opto-NEMS, obtained by engineering the mechanical and photonic properties of such devices, which exploit the strong interaction between photons and phonons and that at room temperature are extremely sensitive to thermo-optical effects. It can be argued that several solid state variables are intrinsically linked to phonon properties when it comes to dissipation, coherence and low-power operation.

Appendices

APPENDIX I: ELASTIC CONTINUUM MODEL

In a solid material, the acoustic waves, cause changes to the positions of the atoms. These displacements can be described in terms of the *strains*, *S*. In presence of the *strain*, the materials generate internal forces that return the material to its original positions, i.e. the equilibrium state. These forces are expressed in terms of the *stresses* (*T*). Finally the acoustic waves can be described using *strain* and *stress* tensors.

I.1 Strain

In an equilibrium state, the particle[*] can be located at the point $X = (x, y, z)$. When the material is not in its equilibrium state, this particle is displaced by an amount $u = (u_1, u_2, u_3)$, where the components u_1, u_2 and u_3 are functions of the coordinates x, y and z[†]. Under the Lagrangian description [204], it is possible to write an expression for the transformations of any infinitesimal line element ΔX from the original state, equilibrium, to the corresponding infinitesimal line element Δu in the displacement state. This transformation is given by the equation:

$$\Delta u = \Im \Delta X \tag{I.1}$$

where $\Im$ is the 3×3 Jacobian matrix of the transformation, i.e., $\Im_{ij} = \partial u_i / \partial x_j$. The line elements ΔX and Δu are to be treated as column vectors. The transposed operation in [I.1] is $\Delta u^* = \Delta X^* \Im^*$ and the square of the length of the displacement line element is:

---

[*] The term *particle* can be associated to infinitesimal element of a solid continuum media.

[†] For mathematical convenience x, y and z variables will be changed by x_1, x_2 and x_3 respectively.

$$\Delta u^2 = \Delta u^* \cdot \Delta u = \Delta X^* \Im^* \cdot \Im \Delta X \qquad [I.2]$$

For any rigid body motion, the length of all line elements remains unaltered and hence the product $\Im^* \cdot \Im$ must be equal to E_3, the unit matrix of order 3. Thus, for an arbitrary displacement, the difference between Δu and ΔX can be expressed as:

$$\begin{aligned} \Delta u^2 - \Delta X^2 &= \Delta X^* \Im^* \Im \Delta X - \Delta X^* \Delta X \\ \Delta u^2 - \Delta X^2 &= \Delta X^* (\Im^* \Im - E_3) \Delta X \\ \Delta u^2 - \Delta X^2 &= \Delta X^* 2 S^L \Delta X \end{aligned} \qquad [I.3]$$

where S^L is Lagrangian finite strain tensor:

$$S^L = \frac{1}{2}\left(\Im^* \Im - E_3\right) \text{ or } S^L_{ij}(x_1, x_2, x_3) = \frac{1}{2}\left(\frac{\partial u_i}{\partial x_j}\frac{\partial u_j}{\partial x_i} - \delta_{ij}\right) \qquad [I.4]$$

Now, defining ΔX in terms of Δu, $\Delta X = \Im' \Delta u$ with $\Im'_{ij} = \partial x_i / \partial u_j$ and doing the same that in [I.2] and [I.3], it is found that:

$$\begin{aligned} \Delta u^2 - \Delta X^2 &= \Delta u^* \Delta u - \Delta u^* \Im'^* \, \Im' \Delta u \\ \Delta u^2 - \Delta X^2 &= \Delta u^* (E_3 - \Im^* \Im) \Delta u \\ \Delta u^2 - \Delta X^2 &= \Delta X^* 2 S^E \Delta X \end{aligned} \qquad [I.5]$$

where S^E is Eulerian-Almansi finite strain tensor:

$$S^E = \frac{1}{2}\left(E_3 - \Im^* \Im\right) \; or \; S^E_{ij}(x_1, x_2, x_3) = \frac{1}{2}\left(\delta_{ij} - \frac{\partial x_i}{\partial u_j}\frac{\partial x_j}{\partial u_i}\right) \qquad [I.6]$$

Both strain tensors can be expressed in terms of the displacement gradient tensor. For this first is defined an arbitrary displacement, μ, as difference between strained coordinates and unstrained coordinates, $\mu(x, t) = u(x, t) - X$ or $\delta_{ij} U_j = u_i - \delta_{ij} x_j$, where U_j represents a component of the arbitrary displacement. Then, differentiating with respect to unstrained coordinates is found that:

$$\begin{array}{l} \nabla_x \mu = \Im - E_3 \\ \Im = \nabla_x \mu + E_3 \end{array} \quad \text{or} \quad \begin{array}{l} \delta_{ij} \dfrac{\partial U_j}{\partial x_k} = \dfrac{\partial u_i}{\partial x_k} - \delta_{ij} \dfrac{\partial X_j}{\partial x_k} \\ \dfrac{\partial u_i}{\partial x_k} = \delta_{ij} \left(\dfrac{\partial U_j}{\partial x_k} + \delta_{jk} \right) \end{array} \qquad [I.7]$$

replacing [I.7] in [I.4], the Lagrangian finite strain tensor is expressed as:

$$S^L = \frac{1}{2} \left(\nabla_x \mu + (\nabla_x \mu)^* - \nabla_x^* \mu \nabla_x \mu \right) \text{ or } S_{kl}^L = \frac{1}{2} \left(\frac{\partial U_k}{\partial x_l} + \frac{\partial U_l}{\partial x_k} - \frac{\partial U_m}{\partial x_k} \frac{\partial U_m}{\partial x_l} \right) \qquad [I.8]$$

similarly, the Eulerian-Almansi finite strain tensor,

$$S_{ij}^E = \frac{1}{2} \left(\frac{\partial U'_i}{\partial u_j} + \frac{\partial U'_j}{\partial u_i} - \frac{\partial U'_k}{\partial x_i} \frac{\partial U'_k}{\partial x_j} \right) \qquad [I.9]$$

Neglecting higher products than those of first order (i.e. linear materials), the Lagrangian and Eulerian-Almansi finite strain matrix then reduce to the usual definition.

$$S_{kl}^{L(E)} = \frac{1}{2} \left(\frac{\partial U_k{}^{(\prime)}}{\partial x_l} + \frac{\partial U_l{}^{(\prime)}}{\partial x_k} \right) \qquad [I.10]$$

With this definition, the strain is a second-rank tensor and is clearly symmetrical, thus only six of the nine components are independent [205]. This can write conveniently as:

$$S = \frac{1}{2} \begin{bmatrix} 2\dfrac{\partial u}{\partial x} & \dfrac{\partial u}{\partial y} + \dfrac{\partial v}{\partial x} & \dfrac{\partial v}{\partial z} + \dfrac{\partial w}{\partial y} \\ \dfrac{\partial u}{\partial y} + \dfrac{\partial v}{\partial x} & 2\dfrac{\partial v}{\partial y} & \dfrac{\partial w}{\partial x} + \dfrac{\partial u}{\partial z} \\ \dfrac{\partial v}{\partial z} + \dfrac{\partial w}{\partial y} & \dfrac{\partial w}{\partial x} + \dfrac{\partial u}{\partial z} & 2\dfrac{\partial w}{\partial z} \end{bmatrix} \qquad [I.11]$$

where *u*, *v*, *w* are the components *x*, *y*, *z* of displacement vector.

I.2 Stress

Consider a general body subject to arbitrary (concentrated and distributed) external loadings, as shown in Figure I.1. It is define traction or stress vector as the average of surface forces, ΔF, acting on an element, ΔA, defined by:

$$T^n(x,n) = \lim_{\Delta A \to 0} \frac{\Delta F}{\Delta A} \qquad [I.12]$$

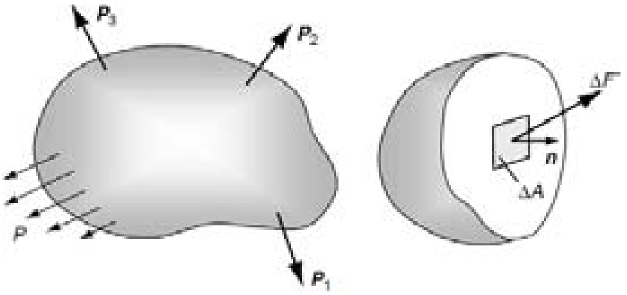

Figure I.1 *Sectioned solid under external loading*

where n is a unit normal vector to the surface under study. Now, considering that exists a special case in which ΔA coincides with each of the three coordinates planes with the unit normal vectors pointing along positives coordinate axes (see Figure I.2).

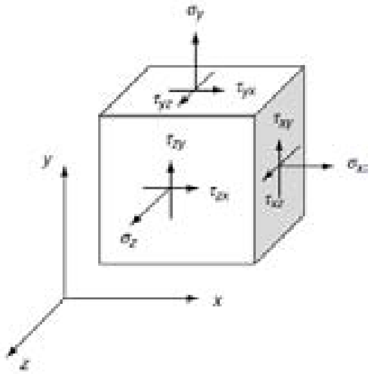

Figure I.2 *Stress components*

The traction vector on each face can be written as:

$$\begin{aligned} T^n(x, n = e_1) &= \sigma_x e_1 + \tau_{xy} e_2 + \tau_{xz} e_3 \\ T^n(x, n = e_2) &= \tau_{yx} e_1 + \sigma_y e_2 + \tau_{yz} e_3 \\ T^n(x, n = e_3) &= \tau_{zx} e_1 + \tau_{zy} e_2 + \sigma_z e_3 \end{aligned} \qquad [I.13]$$

where e_1, e_2 and e_3 are the unit vectors along of each coordinate direction. The nine quantities $\{\sigma_x, \sigma_y, \sigma_z, \tau_{xy}, \tau_{yx}, \tau_{zy}, \tau_{zx}, \tau_{xz},\}$ are the components of the stress vector on each of three coordinate planes, with σ_i referred to normal stresses and τ_{ij} called shearing stresses. Commonly the components of the stress on an oblique plane with arbitrary orientation (see Figure I.3), with unit normal vector, n, it can be written as:

$$T_i^n = \sigma_{ji} n_j = \begin{bmatrix} \sigma_x & \tau_{xy} & \tau_{xz} \\ \tau_{yx} & \sigma_y & \tau_{yz} \\ \tau_{zx} & \tau_{zy} & \sigma_z \end{bmatrix} \cdot \begin{bmatrix} n_x \\ n_y \\ n_z \end{bmatrix} \qquad [I.14]$$

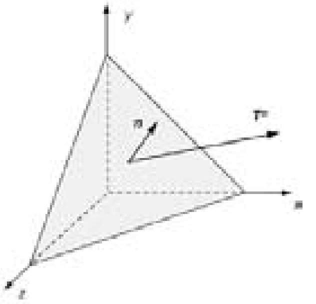

Figure I.3 *Traction on arbitrary orientation*

where n_x, n_y, n_z are the direction cosines of the unit vector n relative to the given coordinate system. Whereas that inside of the body all the forces have to satisfy the static equilibrium, i.e. forces and torque equal cero. This defines closed and in equilibrium subdomain, with volume V and surface A, where the conservation of linear momentum implies that the average of all the forces acting over this region must vanish, i.e.,

$$\iint_A T_i^n dA + \iiint_V F_i dV = 0 \text{ or } \iint_A \sigma_{ji} n_j dA + \iiint_V F_i dV = 0 \qquad [I.15]$$

which, applying the divergence theorem can be expressed as:

$$\iiint_V (\nabla \cdot \sigma_{ji} + F_i)dV = 0 \text{ or } \iiint_V (\sigma_{ji,j} + F_i)dV = 0 \qquad [I.16]$$

doing the same with angular momentum, torque equilibrium:

$$\iint_A \varepsilon_{ijk} x_j \sigma_{lk} n_l dA + \iiint_V \varepsilon_{ijk} x_j F_k dV = 0 \qquad [I.17]$$

where $\varepsilon_{ijk}\, x_j\, \sigma_{lk}\, n_l$ represents the vectorial product between an arbitrary distance x_j and the force $\sigma_{lk}\, n_l$, with ε_{ijk} the Levi-Civita tensor*. Applying again the divergence theorem:

$$\iiint_V ((\varepsilon_{ijk} x_j \sigma_{lk})_{,j} + \varepsilon_{ijk} x_j F_k)dV = 0 \qquad [I.18]$$

and expanding the terms of Equation [I.18] and using the Equation [I.16], it is obtained that:

$$\iiint_V (\varepsilon_{ijk} \delta_{jl} \sigma_{lk} + \varepsilon_{ijk} x_j \underbrace{(\sigma_{lk,l} + F_k)}_{0})dV = 0 \to \iiint_V \varepsilon_{ijk} \sigma_{jk} dV = 0 \qquad [I.19]$$

Due to the region V is arbitrary, the only possible solution to Equation [I.19] is that integrand must vanish, i.e. $\varepsilon_{ijk}\sigma_{jk} = 0$. Considering that ε_{ijk} is antisymmetric in the indices jk, i.e. $\varepsilon_{ijk} = -\varepsilon_{ikj}$, the only possible solution is that the product term of σ_{jk} must be symmetric, i.e.,

$$\sigma_{ij} = \sigma_{ji} \to \begin{matrix} \tau_{xy} = \tau_{yx} \\ \tau_{yz} = \tau_{zy} \\ \tau_{zx} = \tau_{xz} \end{matrix} \qquad [I.20]$$

This reduces the number of independent stress components to only six, instead of the original nine.

---

[*] The vectorial product of two arbitrary vector, $\vec{a} \times \vec{b} = \vec{c}$, can be expressed as: $c_i = \varepsilon_{ijk}\, a_j\, b_k$.

I.3 Hooke's law

To construct a general three-dimensional constitutive law for linear elastic materials, it is possible to assume that each stress components is linearly related to each strain component such as:

$$\begin{aligned}
\sigma_x &= C_{11}S_{11} + C_{12}S_{22} + C_{13}S_{33} + 2C_{14}S_{12} + 2C_{15}S_{23} + 2C_{16}S_{31} \\
\sigma_y &= C_{21}S_{11} + C_{22}S_{22} + C_{23}S_{33} + 2C_{24}S_{12} + 2C_{25}S_{23} + 2C_{26}S_{31} \\
\sigma_x &= C_{31}S_{11} + C_{32}S_{22} + C_{33}S_{33} + 2C_{34}S_{12} + 2C_{35}S_{23} + 2C_{36}S_{31} \\
\tau_{xy} &= C_{41}S_{11} + C_{42}S_{22} + C_{43}S_{33} + 2C_{44}S_{12} + 2C_{45}S_{23} + 2C_{46}S_{31} \\
\tau_{yz} &= C_{51}S_{11} + C_{52}S_{22} + C_{53}S_{33} + 2C_{54}S_{12} + 2C_{55}S_{23} + 2C_{56}S_{31} \\
\tau_{zx} &= C_{61}S_{11} + C_{62}S_{22} + C_{63}S_{33} + 2C_{64}S_{12} + 2C_{65}S_{23} + 2C_{66}S_{31}
\end{aligned} \qquad [I.21]$$

The factor two arises because of the symmetry of the strain tensor. This relation can be write conveniently as

$$\begin{bmatrix} \sigma_x \\ \sigma_y \\ \sigma_z \\ \tau_{xy} \\ \tau_{yz} \\ \tau_{zx} \end{bmatrix} = \begin{bmatrix} C_{11} & C_{12} & \cdot & \cdot & \cdot & C_{16} \\ C_{21} & \cdot & \cdot & \cdot & \cdot & \cdot \\ \cdot & \cdot & \cdot & \cdot & \cdot & \cdot \\ \cdot & \cdot & \cdot & \cdot & \cdot & \cdot \\ \cdot & \cdot & \cdot & \cdot & \cdot & \cdot \\ C_{61} & \cdot & \cdot & \cdot & \cdot & C_{66} \end{bmatrix} \cdot \begin{bmatrix} S_{11} \\ S_{22} \\ S_{33} \\ 2S_{12} \\ 2S_{23} \\ 2S_{31} \end{bmatrix} \qquad [I.22]$$

Using this notation, the relationship between stress and strain can be written reduce form such as:

$$T_{ij} = C_{ijkl}S_{kl} \qquad [I.23]$$

with C_{ijkl} fourth order tensor called elastic modulus tensor, which has 81 components, but only 36 of these components are independent, because elastic modulus tensor is symmetrical, i.e,

$$\begin{aligned} C_{ijkl} &= C_{jikl} \\ C_{ijkl} &= C_{ijlk} \end{aligned} \qquad [I.24]$$

In the isotropic case the stress-strain relations, the elastic modulus tensor must be the same under rotation operations, based in this point Chandrasekharaiah [206] found that for isotropic case the elastic modulus can be written as:

$$C_{ijkl} = \alpha\delta_{ij}\delta_{kl} + \beta\delta_{ik}\delta_{jl} + \gamma\delta_{il}\delta_{jk} \qquad [I.25]$$

where α, β and γ are constants, then introducing Equation [I.25] in Equation [I.23] the stress-strain relation gives:

$$T_{ij} = \lambda S_{kk}\delta_{ij} + 2\mu S_{ij} \qquad [I.26]$$

where α, β and γ have relabelled using Lamé's, λ, and shear modulus, μ, constants. Equation [I.26] is known as generalized Hooke's law for linear isotropic elastic solids. Robert Hooke was the first in propose that the deformation of an elastic structure is proportional to the applied forces. Equation [I.26] is possible to note that, for isotropic media, only two independent elastics constant are necessary to describe its behaviour. Commonly the strain components are written as:

$$S_{ij} = \frac{1+\nu}{E} T_{ij} - \frac{\nu}{E} T_{kk}\delta_{ij} \qquad [I.27]$$

where E $= \mu(3\lambda + 2\mu)/(1+ \mu)$ and is called Young's modulus, and $\nu = 1/(2(\lambda + \mu))$ is called Poisson's ratio.

I.4 From strain-stress relation to equations of motion

A simple and illustrative application of elastic continuum model is found in the case LA mode propagating trough of one dimensional (1-D) structure. Taking $u(x, t)$ as an elastic displacement can be described the longitudinal displacement of the infinitesimal element dx. Then, taken the strain and stress definition, it will define 1–D strain as $e = du/dx$ and 1–D stress as $T(x)$, then, taking one-dimensional Hooke's law, $T = Ye$, and 1–D Newton's law, $F = ma$, the following equations can be formed:

$$\rho A dx \frac{\partial^2 u}{\partial t^2} = \underbrace{[T(x+dx)-T(x)]}_{\frac{\partial T}{\partial x}dx} A \qquad [I.28]$$

where $\rho A dx$ is the mass associated to element dx and $\partial^2 u/\partial t^2$ the force. Now introducing Hooke's law is found that:

$$\rho \frac{\partial^2 u}{\partial t^2} = \frac{\partial}{\partial x}\left(Y \frac{\partial u}{\partial x} \right) \to \frac{\partial^2 u}{\partial t^2} = \frac{Y}{\rho} \frac{\partial^2 u}{\partial x^2} \qquad [I.29]$$

The Equation [I.29] is called one-dimensional wave equation and their solutions can be expressed in terms of plane waves, i.e. $u(x,t) = \xi \exp(i(qx - \omega t))$, where q is the wavevector, $q = 2\pi/\lambda$ and ω is 2π the frequency of the wave, $\omega = 2\pi f$.

Following the same approach, the three-dimensional equation can be carried out using the generalized displacement field, i.e. $U(x, y, z) = (u, v, w)$, and the tensorial Hook's law, i.e. Equation [I.26].

Due to the strain, stress and elastic modulus tensors are symmetric; their index can be compressed using the Voigt's notation, i.e. 1 = 11, 2 = 22, 3 = 33, 4 = 23, 5 = 31 and 6 = 12.

$$\begin{aligned} T_1 &= \lambda(S_1+S_2+S_3)+2\mu S_1 = \lambda\Delta+2\mu S_1 \\ T_2 &= \lambda(S_1+S_2+S_3)+2\mu S_2 = \lambda\Delta+2\mu S_2 \\ T_3 &= \lambda(S_1+S_2+S_3)+2\mu S_3 = \lambda\Delta+2\mu S_1 \\ T_4 &= \mu S_4, \qquad T_5 = \mu S_5, \qquad T_6 = \mu S_6 \end{aligned} \qquad [I.30]$$

where $\Delta = \partial u/\partial x + \partial v/\partial y + \partial w/\partial z$. Then, the generalization for three-dimensional system is given by the equations:

$$\begin{aligned} \rho\frac{\partial^2 u}{\partial t^2} &= \frac{\partial T_1}{\partial x}+\frac{\partial T_6}{\partial y}+\frac{\partial T_5}{\partial z} = (\lambda+\mu)\frac{\partial\Delta}{\partial x}+\mu\nabla^2 u \\ \rho\frac{\partial^2 v}{\partial t^2} &= \frac{\partial T_6}{\partial x}+\frac{\partial T_2}{\partial y}+\frac{\partial T_4}{\partial z} = (\lambda+\mu)\frac{\partial\Delta}{\partial y}+\mu\nabla^2 v \\ \rho\frac{\partial^2 w}{\partial t^2} &= \frac{\partial T_5}{\partial x}+\frac{\partial T_4}{\partial y}+\frac{\partial T_3}{\partial z} = (\lambda+\mu)\frac{\partial\Delta}{\partial z}+\mu\nabla^2 w \end{aligned} \qquad [I.31]$$

These can be written straightforwardly as the single vector equation

$$\frac{\partial^2 U}{\partial t^2} = v_T^2\nabla^2 U + (v_L^2 - v_T^2)\nabla\cdot(\nabla U) \qquad [I.32]$$

where $U = (u, v, w)$ is the amplitude of the displacement vector, $v_L = [(l + 2\mu)/\rho]^{1/2}$ and $v_T = (\mu/\rho)^{1/2}$ are longitudinal and transversal sound velocities, respectively.

I.5 Boundary conditions and Lamb waves

As seen in the Chapter II, the introduction of boundary conditions to infinite media changes the nature of the acoustic propagation. Following the Rayleigh's work, Lamb introduced a semi-infinite and isotropic system subject to a stress free on both surfaces as a boundary condition.

To calculate the dispersion relation is proposed a new dimensionless variable in order to eliminate the thicknesses dependence of the problem.

$$Q_l = aq_l/2,\ Q_t = aq_t/2,\ Q_{//} = aq_{//}/2;\quad \Omega = a\omega/(2v_L) \qquad [I.33]$$

This permits to redefine the problem to calculate the perpendicular component of the wavevector (Q_l, Q_t) which are dependent on perpendicular component of the wavevector $Q_{//}$ and the dimensionless frequency Ω. Then, Equations [2.13] and [2.14] are given by:

$$F(Q_{//},\Omega) = \frac{4Q_{//}^2 Q_l Q_t}{(Q_t^2 - Q_{//}^2)^2} + \left(\frac{\tan(Q_t)}{\tan(Q_l)}\right)^{\pm 1} = 0 \qquad [I.34]$$

$$Q_l = \sqrt{\Omega^2 - Q_{//}^2},\ Q_t = \sqrt{r_S^2\Omega^2 - Q_{//}^2};\quad r_S = S_L / S_T \qquad [I.35]$$

Now, only one parameter which depends on the material is the ratio of transverse and longitudinal velocities (r_S).

The problem has symmetry with respect to the inversion of each variable then, if Q_i is a solution, so $-Q_i$ is solution too. This permits to restrict the study of equations just to values of $Q_i > 0$, where i = (//, *l*, *t*). The presence of the tangent function in the first of these equations suggests the existence of several branches of solutions.

To calculate the numerical solutions of the Equations [I.34] and [I.35], for symmetric and antisymmetric modes, is now relatively simple:

i. First the equations are solved to $Q_0 = 0$, this give us the first point on the dispersion relation, $\Omega_{0,n}$. Being $Q_0 = 0$, the only point with an analytical solution.

ii. The wavevector is slightly modified, $Q_1 = Q_0 + \Delta Q$, and dimensionless frequency near of the first solution is chosen, $\Omega_{1,n} = \Omega_{0,n} \pm \Delta\Omega$.

iii. Fixing Q_1 and varying slightly $\Omega_{1,n}$, the signs of the Equation [I.34], $F(Q_1,\Omega_{1,n})$, are evaluated. The idea is found an interval where the function F change of sign, i.e. the function cross the abscissa and exist a solution of the equation. F

iv. Once fixed the interval, it is possible to use any numerical algorithm like Newton-Raphson, Bisection, Regula-Falsi or Brent to find the best solution. The rest of the solutions are obtained using the same approach and changing $\Omega_{1,n}$ by $\Omega_{0,n}$ and Q_1 by Q_0.

An example of the typical curve of the non-linear equation is show in Figure I.4. In this graph the typical asymptotical behaviour given by the combination of tangential functions can be observed. For the simulation ratio sound velocity was taken as $r_s = 1.44$, corresponding to $v_L = 8440$ m/s and $v_T = 5845$ m/s longitudinal and transverse sound velocity, respectively.

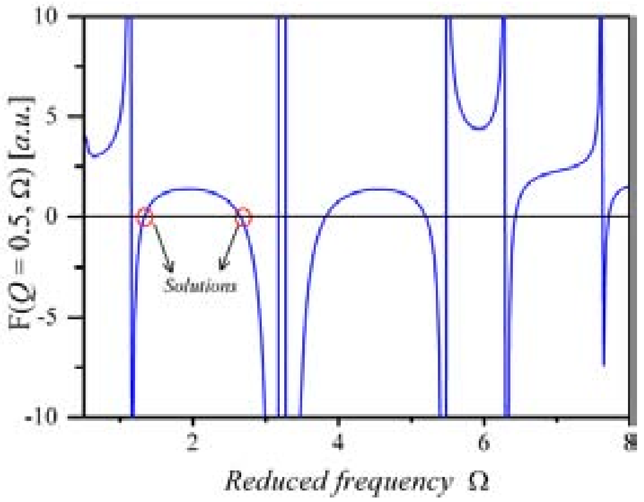

Figure I.4 *Typical graph of non-linear equation of dilatational waves for a fixed dimensionless wavevector, Q = 0.5, as a function of reduced frequency*

APPENDIX II: AHNARMONICITY AND THERMAL CONDUCTIVITY

II.1 Harmonic effect in crystals

The assumptions of small oscillations to describe the vibrations in almost all solids appear to be adequate and reasonable. But to describe more adequately a solid crystal is necessary to include high order terms in the Hamiltonian. A good example of this is the calculus of thermal expansion in a crystal. Using the Helmholtz free energy is possible to write the pressure of the system as state equation [207]:

$$P = -(\partial F / \partial V)_T, \; F = U - TS$$
$$P = -\frac{\partial}{\partial V}\left(U - T\int_0^T \frac{dT'}{T'} \frac{\partial U(T',V)}{\partial T'} \right)_T \qquad [II.1]$$

where F is Helmholtz free energy, V the total volume, U the internal energy, S the entropy and T the temperature. If is used small oscillations, i.e. harmonic approach, the internal energy is given by:

$$U = U^{eq} + 1/2\sum_{q,s}\hbar\omega_{qs} + \sum_{q,s}\hbar\omega_{qs}n_{qs} \qquad [II.2]$$

and the pressure:

$$P = -\frac{\partial}{\partial V}\left(U^{eq} + 1/2\sum_{q,s}\hbar\omega_{qs} \right) + \sum_{q,s} -\frac{\partial}{\partial V}(\hbar\omega_{qs})n_{qs} \qquad [II.3]$$

where U^{eq} the energy of the system in equilibrium, ω_{qs} is the frequency of mode q with polarization s and n_{qs} is the phonon distribution function.

According with the last equation, the equilibrium pressure depends on the temperature only because the normal modes depend on the equilibrium volume of the crystal. But if is used more rigorous expression for the harmonic potential of the form:

$$U = U^{eq} + 1/2 \sum_{R,R'} U(R) D(R - R') U(R') \qquad [II.4]$$

where D is force constants that are independent of $U(R)$, then the normal mode could have no volume dependence at all. This is due to the normal modes of harmonic crystal are not affected by the volume in equilibrium, and then the formulation of the pressure, Equation [II.3], depends only on the volume but not on the temperature. This means that the pressure required to maintain a given volume does not vary with temperature.

Other implications of this result are: the volume cannot vary with the temperature at fixed temperature and the coefficient of thermal expansion (α) must vanish:

$$\begin{gathered} \left(\frac{\partial V}{\partial T}\right)_P = -\frac{(\partial P/\partial T)_V}{(\partial P/\partial V)_T} \\ \alpha = \frac{1}{l}\left(\frac{\partial l}{\partial T}\right)_P = \frac{1}{3V}\left(\frac{\partial V}{\partial T}\right)_P = -\frac{1}{3V(\partial P/\partial V)_T}\left(\frac{\partial P}{\partial T}\right)_V \end{gathered} \qquad [II.5]$$

The absence of thermal expansion has other consequences as being equal in constant-volume and constant-pressure specific heats (C_P and C_V respectively).

$$C_P = C_V - \frac{T(\partial P/\partial T)_V^2}{V(\partial P/\partial V)_T} \qquad [II.6]$$

These anomalies is due to that in real crystals the force constants D in the harmonics approximation to the potential energy do depend on the equilibrium lattice about which the harmonic expansion is made.

II.2 Thermal conductivity models

Depending of the material, heat energy can be transported by different carriers such as: electrons, phonons, photons, magnons, etc. For the case of non-metals, semiconductors and alloys materials the dominant conduction mechanics is the lattice thermal conduction, i.e. phonons.

Thermal conductivity, κ, is defined as material's ability to conduct heat and, generally, the total thermal conductivity can be expressed as a sum of all carrier contribution, $\kappa = \sum_{\alpha}\kappa_{\alpha}$, where α denotes a type excitation.

The fundamental challenge for thermal transport is to capture the complexities of the systems. The models to capture these complexities can be derivate from Boltzmann transport equation, BTE. This equation determines the status of a particle via its localization, r, and velocity, v.

II.2.1 Boltzmann equation

The BTE is an equation for the temporal evolution of the non-equilibrium thermodynamic distribution function, $n_{qs}(r, v, t)$, in phase space.

If a particle travels with a velocity v in a time t, its velocity and position before a time $t + dt$ will vary in $v + dv$ and $r + dr$, i.e.,

$$\begin{aligned} &t \rightarrow t + dt \\ &r \rightarrow r + dr \rightarrow r + vdt \\ &v \rightarrow v + dv \rightarrow r + adt \end{aligned} \qquad [II.7]$$

In the absence of collisions, the probability to find a particle does not change with the time, then:

$$\frac{n_{qs}(r + vdt, v + adt, t + dt) - n_{qs}(r, v, t)}{dt} = 0 \qquad [II.8]$$

$$v\frac{\partial n_{qs}}{\partial r} + a\frac{\partial n_{qs}}{\partial v} + \frac{\partial n_{qs}}{\partial t} = 0 \text{ or } \frac{\partial n_{qs}}{\partial t} + \frac{p}{m}\nabla_r n_{qs} + F\nabla_p n_{qs} = 0 \qquad [II.9]$$

where a is the particle acceleration, F is the force field acting on the particles, m is the mass and p its momentum, the last equation is called Liouville equation. Now, if within this period there is a collision the Liouville equation is modified as:

$$\frac{\partial n_{qs}}{\partial t} + v\nabla_r n_{qs} + a\nabla_v n_{qs} = \left.\left(\frac{\partial n_{qs}}{\partial t}\right)\right|_{col} \qquad [II.10]$$

This expression is known as Boltzmann equation. The first term in BTE represents the net rate of particles over time, the second term is the convective inflow due to acceleration in physical space, and the third term is the net convective inflow due to acceleration in velocity and/or momentum space and right hand side term represents the net rate of change of particles due to collisions. Commonly in absence of external forces the third term vanish and the scattering term is approximated under the relaxation-time approach [17],

$$\frac{\partial n_{qs}}{\partial t} + v\nabla n_{qs} = \frac{n_{qs,0} - n_{qs}}{\tau_{eff}} \qquad [II.11]$$

where $n_{qs,0}$ is the thermodynamic distribution at equilibrium: Bose-Einstein distribution function for bosons and Fermi-Dirac distribution function for fermions particles.

Some of models can be derived from BTE are:

i. The Fourier model (Kinetic theory)

ii. The Cattaneo model

iii. The C- and F-process model for bridging Fourier to Cattaneo limits

iv. The equation of the phonon radiative transfer (EPRT)

v. The Callaway/Holland models and its modifications

In general these models are derived under the premise that system has local thermal dynamic equilibrium (LTE). The LTE implies that the second term in BTE can be expressed as □$n_{qs} = dn_{qs,0}/dT$□T, and then the BTE is given [68]

$$\frac{\partial n_{qs}}{\partial t} + \frac{dn_{qs,0}}{dT}\nabla T = \frac{n_{qs} - n_{qs,0}}{\tau} \qquad [II.12]$$

II.2.2 Kinetic theory

The basic law defining the relationship between the heat flow and the temperature gradient was developed for mathematics physicist Joseph Fourier.

The Fourier law is the simplest model for thermal transport valid for homogeneous and isotropic solids. In this approach phonon behaviour is approximated in acoustically thick limit, i.e. the size of the system, L, is much larger than the phonon mean free path, $L/\Gamma >> 1$, in addition, the temporal phenomena have to occur on time scale much larger than the phonon lifetime, t >> τ.

To describe the thermal conductivity, we need to define some characteristics quantities. Then taken the Equation [3.7] we can to describe the quantized phonon energy as:

$$E_n = \hbar\omega_{qs}\left(n_{qs,0} + 1/2\right) \qquad [II.13]$$

and the probability of a harmonic oscillator is an energy state E_n is giving by:

$$P(E_n) = (1/Z)\exp(-E_n / k_B T) \qquad [II.14]$$

with Z a normalization constant giving by $\sum_n P(E_n) = 1$, i.e. $Z = \sum_n \exp(-E_n/k_BT)$. Introducing the quantized energy expression, Equation [II.13], in the Z function definition:

$$Z(T) = \sum_{n=0}^{\infty}\exp\left[-\left(n_{qs,0} + 1/2\right)\hbar\omega_{qs} / k_B T\right] = \frac{\exp(-\hbar\omega_{qs} / 2k_B T)}{1 - \exp(-\hbar\omega_{qs} / k_B T)} \qquad [II.15]$$

Once obtained the form of probability, we can to find the contribution of the elastic waves to the average energy, which is giving by:

$$\begin{aligned}\left\langle U_{q,s}\right\rangle &= \sum_n \left(n_{qs,0} + 1/2\right)\hbar\omega_{qs} P(E_n)\\ &= (1/Z)\sum_n \left(n_{qs,0} + 1/2\right)\hbar\omega_{qs} e^{-\left(n_{qs,0}+1/2\right)\hbar\omega_{qs}/k_BT}\\ \left\langle U_{q,s}\right\rangle &= \tfrac{1}{2}\hbar\omega_{qs} + \hbar\omega_{qs}\frac{1}{(e^{\hbar\omega_{qs}/k_BT} - 1)} = \hbar\omega_{qs}\left(n_{qs,0} + 1/2\right)\end{aligned} \qquad [II.16]$$

The equilibrium phonon distribution function (EPDF), $n_{qs,0}$, represents the average number of phonons with wave vector q in equilibrium and at a given temperature T, the EPDF is described by the Bose-Einstein distribution:

$$n_{qs,0} = \frac{1}{\exp[\hbar\omega_{qs} / k_B T] - 1} \qquad [II.17]$$

According to the Boltzmann equation, in the presence of a temperature gradient $\vec{\nabla}T$, the steady state for phonons can be describes as:

$$\frac{n_{qs}-n_{qs,0}}{\tau_{qs}}=-\left(\vec{v}_{qs}\cdot\vec{\nabla}T\right)\frac{\partial n_{qs,0}}{\partial T} \qquad [II.18]$$

where $\vec{v}_{qs}$ is the phonon group velocity and τ_{qs} is the phonon scattering relaxation time. The heat flux in a dielectric solid is obtained by adding all the contribution of the *q* phonon in all possible *s* polarizations:

$$\vec{Q}=\frac{1}{N_0\Omega}\sum_{q,s}n_{qs}\hbar\omega_{qs}\vec{v}_{qs} \qquad [II.19]$$

substituting [II.18] into [II.19]:

$$\vec{Q}=\frac{1}{N_0\Omega}\sum_{q,s}\left[\hbar\omega_{qs}n_{qs,0}v_{qs}\langle\cos\theta\rangle-\hbar\omega_{qs}v_{qs}^2\langle\cos^2\theta\rangle\tau_{qs}\frac{\partial n_{qs,0}}{\partial T}\vec{\nabla}T\right] \qquad [II.20]$$

$$\vec{Q}=\frac{-1}{3N_0\Omega}\sum_{q,s}\hbar\omega_{qs}v_{qs}^2\tau_{qs}\frac{\partial n_{qs,0}}{\partial T}\vec{\nabla}T \qquad [II.21]$$

where θ is the angle between the group velocity and gradient of temperature: The first term in [II.20] is vanish due to integration over all the phase space. Once obtained the flux we can introduce this quantity in the Fourier's law to find the thermal conductivity:

$$\begin{aligned}\kappa&=-\frac{Q}{\vec{\nabla}T}\\&=\frac{1}{3N_0\Omega}\sum_{q,s}\hbar\omega_{qs}v_{qs}^2\tau_{qs}\frac{\partial n_{qs,0}}{\partial T}\\&=\frac{1}{3}\sum_{q,s}C_V v_{qs}^2\tau_{qs}\end{aligned} \qquad [II.22]$$

The differential heat conduction equation can be obtained considering energy-balance equation for small control volume, *V*, stated as [208]:

$$\begin{bmatrix}\text{Rate of heat entering through}\\ \text{the bounding surface of } V\end{bmatrix}+\begin{bmatrix}\text{rate of energy}\\ \text{generation in } V\end{bmatrix}=\begin{bmatrix}\text{rate of storage}\\ \text{of energy in } V\end{bmatrix} \qquad \text{[II.23]}$$

The first term of the Equation [II.23] can be evaluated as:

$$\begin{bmatrix}\text{Rate of heat entering through}\\ \text{the bounding surface of } V\end{bmatrix}=-\int_A Q\cdot\hat{n}dA=-\int_V \nabla\cdot QdV \qquad \text{[II.24]}$$

with A the surface area of the volume V, $\hat{n}$ is the outward normal unit vector to the surface element dA. The sign minus is included to ensure that the heat flow is into the volume. The other terms in are evaluated as:

$$\begin{bmatrix}\text{Rate of energy}\\ \text{generation in } V\end{bmatrix}=-\int_V g(r,t)dv \qquad \text{[II.25]}$$

$$\begin{bmatrix}\text{Rate of energy}\\ \text{storage in } V\end{bmatrix}=-\int_V \rho C_V\frac{\partial T(r,t)}{\partial t}dv \qquad \text{[II.26]}$$

where $g(r, t)$ is the heat generation rate in the medium and C_V is the heat capacity. The substitution of Equations [II.24], [II.25] and [II.26] in Equation [II.23] yields:

$$\int_v\left[-\nabla\cdot Q(r,t)+g(r,t)-\rho C_V\frac{\partial T(r,t)}{\partial t}\right]dv=0 \qquad \text{[II.27]}$$

taking $Q(r, t)$ from [II.22] into [II.27] and eliminating the integral, it is obtain the differential equation of heat conduction for a stationary, homogeneous, isotropic solid with heat generation within the body:

$$\nabla\cdot[\kappa\nabla T(r,t)]+g(r,t)=\rho C_V\frac{\partial T(r,t)}{\partial t} \qquad \text{[II.28]}$$

Normally the thermal conductivity is assumed as constant, i.e. independent of position, and then the Equation [II.28] is simplified as:

$$\nabla^2 T(r,t) + \frac{1}{\kappa} g(r,t) = \frac{1}{\alpha}\frac{\partial T(r,t)}{\partial t} \qquad \text{[II.29]}$$

where $\alpha = \kappa/\rho C_V$, is the thermal diffusivity. For a medium with constant thermal conductivity and no heat generation the equation [II.29] become in the Fourier equation.

$$\nabla^2 T(r,t) = \frac{1}{\alpha}\frac{\partial T(r,t)}{\partial t} \qquad \text{[II.30]}$$

II.2.3 Cattaneo equation: hyperbolic heat equation.

One of the problems of the Fourier equation is that the description of the velocity of heat propagation. The Fourier law assumes that the heat flow, Q, and the gradient of temperature, ∇T, appear at the same time instant t. This implies that thermal conductivity propagates with infinite speed which is incompatible with the physical laws. In addition, in a steady state the Equation [II.30] yields to erroneous results for the acoustically thin limit, where ballistic phonon transport effects are important [209]. To overcome these problems many scientists proposed an upgrade of the Fourier equation be using a hyperbolic form among which Cattaneo and phase-lagging models have found greater applications.

The Cattaneo equation is obtained using BTE under relaxation time, the temperature gradient approximation, Equation [II.12], and flux definition, Equation [II.22]. First the Equation [II.12] is multiplying by $v\hbar\omega_{qs}/N_0\Omega$ and sum over all frequency and polarization ranges to yield:

$$\frac{\partial n_{qs}}{\partial t} + v\frac{\partial n_{qs,0}}{\partial T}\nabla T = \frac{n_{qs,0} - n_{qs}}{\tau} \Bigg/ \cdot \sum_{q,s} \frac{v\hbar\omega_{qs}}{N_0\Omega} \qquad \text{[II.31]}$$

$$\tau\frac{\partial Q}{\partial t} + Q = -\kappa\nabla T \qquad \text{[II.32]}$$

The divergence of the Equation [II.29] and time derivate of the Equation [II.27] give two equations, which can be combined with the Equation [II.27] to eliminate the heat flux terms. The resulting differential equation for constant properties can be written as:

$$\tau\nabla\frac{\partial Q}{\partial t}+\nabla Q+\kappa\nabla^2 T=0 \qquad [II.33]$$

$$-\tau\frac{\partial\nabla Q}{\partial t}+\tau\frac{\partial g}{\partial t}-\tau\rho C\frac{\partial^2 T}{\partial t^2}=0 \qquad [II.34]$$

$$-\left(g+\tau\frac{\partial g}{\partial t}\right)+\frac{1}{\alpha}\frac{\partial T}{\partial t}+\frac{\tau}{\alpha}\frac{\partial^2 T}{\partial t^2}=\nabla^2 T \qquad [II.35]$$

This is the hyperbolic heat equation, which, in contrast to the Fourier equation, the wave speed is finite. Without heat generation the Equation [II.35] is known as telegraph or damped wave equation. The solution is propagating waves that its amplitude decays exponentially as it travels. The speed of this temperature in high-frequency limit is given by $v_{tw} = (\alpha/\tau)^{1/2}$.

II.2.4 Callaway model

The relaxation-time approximation assumes that the phonon distribution is restored to the equilibrium distribution at rate proportional to the departure from equilibrium. Assuming that scatters process are independent of one other the effective relaxation time is given by the Matthiessen's Rule. As been in the Chapter III, it is well known that the normal process cannot by themselves contribute to thermal conductivity, consequently, it is not legitimate add effective relaxation time. But it is incorrect assume that they do not influence the thermal conductivity, because they are capable of redistributing momentum and the energy. The resistive processes such as U processes tend to return the phonon system to equilibrium distribution, whereas N processes lead to a displaced this distribution. An investigation of the real effect of normal process was developed for Joseph Callaway in 1958 [68]. In his model is assumed that:

i. Debye-like phonon spectrum (linear dispersion relation).

ii. The medium is isotropic and homogeneous.

iii. No distinction between longitudinal and transverse phonons.

iv. One average of sound velocity.

v. Scattering mechanism only depends on of the frequency and temperature

From BTE in presence of gradient of temperature and for steady state for phonons can be describes as:

$$-\left(\vec{v}_{q,s}\cdot\vec{\nabla}T\right)\frac{\partial n_{qs,0}}{\partial T}=\left(\frac{\partial n_{qs}}{\partial T}\right)_{col}=\frac{n_{qs}(\lambda)-n_{qs}}{\tau_N}+\frac{n_{qs}-n_{qs,0}}{\tau_R} \quad \text{[II.36]}$$

where, τ_N is normal relaxation time and τ_R is the relaxation time for all the processes which do not conserve the momentum and $n_{qs}(\lambda)$ is the displaced Bose-Einstein distribution, which can be expressed as Fourier expansion:

$$n_{qs}(\lambda)=\left(\exp\left[\frac{\hbar\omega_{qs}-\lambda\cdot q}{k_BT}\right]-1\right)^{-1}\approx n_{qs,0}+\lambda\cdot q\frac{T}{\hbar\omega_{qp}}\frac{dn_{qs,0}}{dT}+\ldots \quad \text{[II.37]}$$

defining $n_1 = n_{qs} - n_{qs,0}$, and adding [II.37], The BTE, Equation [II.36], can be written as:

$$-\left(\vec{v}_{qs}\cdot\vec{\nabla}T\right)\frac{\partial n_{qs,0}}{\partial T}-(\tau_R^{-1}+\tau_N^{-1})n_1+\lambda\cdot q\tau_N^{-1}\frac{T}{\hbar\omega_{qs}}\frac{dn_{qs,0}}{dT}=0 \quad \text{[II.38]}$$

Now is defined the following parameters:

$$\tau_C^{-1}=\tau_R^{-1}+\tau_N^{-1} \quad \text{[II.39]}$$

$$n_1 = -\vartheta\left(\vec{v}_{q,s} \cdot \vec{\nabla} T\right)\frac{\partial n_{qs,0}}{\partial T} \qquad \text{[II.40]}$$

$$\lambda \cdot q = -\beta \frac{\hbar\omega}{T}\left(\vec{v}_{q,s} \cdot \vec{\nabla} T\right) \qquad \text{[II.41]}$$

where ϑ is the total relaxation time, λ is a constant vector in direction of temperature gradient, and β is parameter with the dimension of relaxation time. Substituting the Equations [II.39], [II.40] and [II.41] in [II.38] is simplifies to:

$$\frac{\vartheta}{\tau_C} - \frac{\beta}{\tau_N} = 1 \rightarrow \vartheta = \tau_C\left(1 + \frac{\beta}{\tau_N}\right) \qquad \text{[II.42]}$$

Using the assumed isotropic model, the thermal conductivity can be expressed in terms of the kinetic theory:

$$\kappa = \frac{1}{3}\sum_s \int \vartheta v_{q,s}^2 C_V dq^3 \qquad \text{[II.43]}$$

$$\kappa = v_g^2 \int \tau_C\left(1 + \beta / \tau_N\right) C_V D(\omega) d\omega \qquad \text{[II.44]}$$

where $D(\omega) = N_0\Omega\omega^2/2\pi^2 v^3_{qs}$ is the density of state in the Debye approach.

The term 1/3 is vanishing due to the summation in the polarization. The factor ($1+ \beta/\tau_N$) expresses the correction due to displaced of phonon distribution (N-processes contribution). To determinate the value of β is necessary utilize the fact that the N-processes conserve the momentum, therefore, the rate of change of the total phonon momentum due to N-processes have to be zero, i.e.,

$$\int \left(\frac{\partial n_{qs}}{\partial t}\right)_N q dq^3 = \int \frac{n_{qs}(\lambda) - n_{qs}}{\tau_N} q dq^3 = 0 \qquad \text{[II.45]}$$

Done the adequate substitution and introducing the variable $x = \hbar\omega/k_B T$ (the dimensionless phonon angular frequency), the Equation [II.45] becomes:

$$\int_0^{\theta_D/T} \frac{x^4 \exp(x)}{(\exp(x)-1)^2} \frac{(\vartheta-\beta)}{\tau_N} dx = 0 \qquad [II.46]$$

with θ_D is the Debye temperature. Inserting ϑ from the Equation [II.42] and solve for β which is independent of x:

$$\beta = \int_0^{\theta_D/T} \frac{x^4 \exp(x)\tau_C/\tau_N}{(\exp(x)-1)^2} dx \Bigg/ \int_0^{\theta_D/T} \frac{x^4 \exp(x)(1-\tau_C/\tau_N)}{\tau_N(\exp(x)-1)^2} dx \qquad [II.47]$$

Once that β is computed, it is substituted into [II.43], and the thermal conductivity is obtained. Note that if there is not U-process, i.e. $\tau_U \to \infty$, β becomes to infinity, and consequently the thermal conductivity is infinite.

Finally, in the Callaway model, the thermal conductivity is composed of two terms, one represents contributions of resistive processes, and the other represent the combined scattering rate which include the redistribution of the phonons due to N-processes.

$$\kappa_1 = v_g^2 \int \tau_C C_V D(\omega) d\omega \qquad [II.48]$$

$$\kappa_2 = v_g^2 \int \beta \tau_C \tau_N^{-1} C_V D(\omega) d\omega \qquad [II.49]$$

$$\kappa = \kappa_1 + \kappa_2 \qquad [II.50]$$

κ_2 is not only a correction term to κ_1, it is essential to counteract the effect of treating N-processes in τ_C as if they were entirely resistive. In the literature the contribution of term κ_2 remains below 1%, but for ultra-pure crystal the contribution increases to 20% of the total thermal conductivity. The magnitude of κ_2 is controlled by the concentration of point defects. However, when the N-processes become comparable to the resistive processes $\tau_N \approx \tau_R$, e.g. in very pure, defect free and isotopically pure samples, the κ_2 contribution to the total thermal conductivity is significant [210].

II.2.5 Holland model

The consideration of no distinction between the phonon polarizations used in the Callaway model, can lead to mistakes in the calculation of the thermal conductivity, because this means that all the phonons have the same group velocity, in addition all the process are degenerated. An analysis of the contributions of each polarization was done by Holland in 1963 [104]. He included effects of dispersion relation, as well as the modification of the group velocity under the assumptions $\kappa_2 = 0$. Holland separated the contributions of transversal and longitudinal phonons, and includes a partial effect of non-linearity of dispersion relation by splitting each polarization in two zones at the middle the first Brillouin zone. For each polarization Holland assumed that the group velocity and the phase velocity are constant at each zone at each polarization.

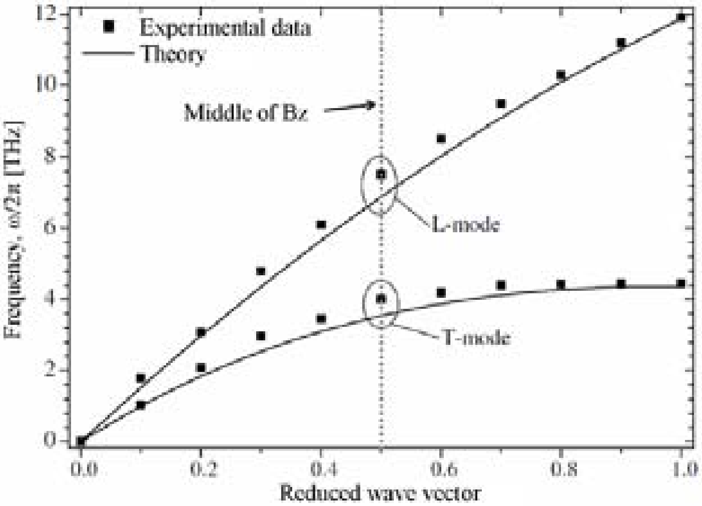

Figure II.1 *Silicon dispersion relation, adapted from* [211].

For bulk silicon, Holland calculated the group velocity as an average in each zone for transversal and longitudinal modes. The values are summarized as:

$$\text{For } 0 \le q < q_{\lim}/2$$

$$v_{g,j} = \begin{cases} 5860 \text{ m/s for } j = T \\ 8480 \text{ m/s for } j = L \end{cases} \qquad [II.51]$$

$$\text{For } q_{\lim}/2 \le q < q_{\lim}$$

$$v_{g,j} = \begin{cases} 2000 \text{ m/s for } j = T \\ 4240 \text{ m/s for } j = L \end{cases} \qquad [II.52]$$

where q_{lim} is the maximum wave vector, i.e. in the limit of the Brillouin zone.

The new formulation postulated that the thermal conductivity can be expressed as the sum of the contribution of longitudinal and transverse phonons:

$$\kappa = \kappa_1 = \frac{1}{3}\left(\frac{N_0\Omega}{2\pi^2}\right)\sum_p \int \frac{\tau}{v_{\omega,s}} C_V \omega^2 d\omega \qquad [II.53]$$

$$\kappa_T = \frac{2}{3}\int_0^{\theta_T/T} \frac{S_T \tau_T T^3 x^4 \exp(x)}{(\exp(x)-1)^2} dx \qquad [II.54]$$

$$\kappa_L = \frac{1}{3}\int_0^{\theta_L/T} \frac{S_L \tau_L T^3 x^4 \exp(x)}{(\exp(x)-1)^2} d\omega \qquad [II.55]$$

$$\kappa = \kappa_T + \kappa_L \qquad [II.56]$$

and

$$s = T, L;\; x = \hbar\omega_s / k_B T;\; \theta_s = k_B \omega_s / \hbar;\; S_s = (K^4 / 2\pi^2 \hbar^3 v_{\omega s}) \qquad [II.57]$$

the subscripts *T* and *L* refer to transversal and longitudinal phonons respectively.

The separation between two zones and the form of relaxation times used by Holland permits to divide the term κ_T into in two parts:

$$\kappa = \kappa_{T0} + \kappa_{TU} + \kappa_L \qquad [II.58]$$

$$\kappa_{T0} = \frac{2}{3}T^3 \int_0^{\theta_1/T} \tau_{T0} S_T x^4 \exp(x)(\exp(x)-1)^{-2} dx \qquad [II.59]$$

$$\kappa_{TU} = \frac{2}{3} T^3 \int_{\theta_1/T}^{\theta_2/T} \tau_{TU} S_T x^4 \exp(x)(\exp(x)-1)^{-2} dx \qquad [II.60]$$

$$\kappa_L = \frac{1}{3} T^3 \int_{0}^{\theta_3/T} \tau_L S_T x^4 \exp(x)(\exp(x)-1)^{-2} dx \qquad [II.61]$$

This division is because the U-processes such as $T + L \rightarrow L$ or $T + T \rightarrow L$ do not begin until $\omega > \omega_1$, because the shape of T branch. Figure II.2 shows the typical phonon spectrum of a material such as germanium or silicon. Note that U-processes start just for a minimum of frequency, under this limit there is absence of these processes.

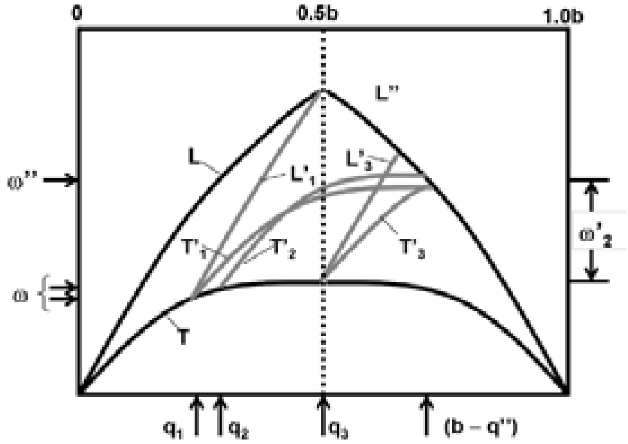

Figure II.2 *Schematic phonon spectrum showing zone division, 0.5b, and the extension into second Brillouin zone. Adapted from* [104].

Holland was the first who postulated that the modification of the acoustic dispersion relation could lead to modification of the thermal conductivity.

II.2.6 Holland-Callaway modifications

In general, the most used techniques for calculations of lattice thermal conductivity are based on Callaway or Holland models. These calculations are based on the linearized dispersion relation (Debye model) and involve certain of adjustable parameters.

As mentioned earlier, the lattice thermal conductivity is represented by the Equation [II.22]. It can be calculated through the sum over one longitudinal and two degenerate transverse phonon branches [II.56]. In the Callaway model the thermal conductivity can be expressed as a sum of two contributions [II.50]. Taking both models Asen-Palmer expressed the thermal conductivity as sum between transversal and longitudinal contribution and adding the Callaway correction to each contribution [210], i.e.,

$$\kappa = \kappa_{L_1} + \kappa_{L_2} + 2(\kappa_{T_1} + \kappa_{T_2}) \qquad \text{[II.62]}$$

$$\kappa_{i_1} = \frac{1}{3} S_i T^3 \int_0^{\theta_i/T} \tau_C^i(x)\Gamma(x)dx, \quad \Gamma(x) = \frac{x^4 \exp(x)}{\left(\exp(x)-1\right)^2} \qquad \text{[II.63]}$$

$$\kappa_{i_2} = \frac{1}{3} S_i T^3 \left[\int_0^{\theta_i/T} \Gamma(x) \frac{\tau_C^i(x)}{\tau_N^i(x)} dx \right]^2 \Bigg/ \int_0^{\theta_i/T} \frac{\Gamma(x)}{\left(\tau_N^i(x) + \tau_R^i(x)\right)} dx \qquad \text{[II.64]}$$

and

$$i = T, L;\ x = \hbar\omega / KT;\ \theta_i = K\omega_i / \hbar;\ S_i = (K^4 / 2\pi^2\hbar^3 v_i) \qquad \text{[II.65]}$$

where v_L and v_T are longitudinal and transversal sound velocity, respectively.

II. 3 Boundary scattering processes

This scattering process dominates at low temperature regime, because the phonons in this regime acquire long wavelengths. The boundaries of a crystal of finite size act as scatterings regions and limit the effective mean free path of the phonons. The formulations of this process can be find follow the treatment given by Ziman. Substituting the displaced Bose-Einstein distribution, Equation [II.37], in the steady state BTE, Equation [II.18]:

$$-\left(\vec{v}_{qs}\cdot\vec{\nabla}T\right)\frac{\partial n_{qs,0}}{\partial T}=\frac{\psi_{qs}(r)n_{qs,0}\left(n_{qs,0}+1\right)}{\tau_{qs}(bulk)}+\vec{v}_{qs}\cdot\vec{\nabla}\,\psi_{qs}(r)n_{qs,0}\left(n_{qs,0}+1\right) \qquad \text{[II.66]}$$

where $\psi_{qs}(r)$ is analogous to $\lambda\cdot q$, defined in the equation [II.37]. If it is considered the situation at very low temperature, when the relaxation time for bulk is very long compared with to boundary relaxation time, i.e. τ_{qs}(bulk) $\rightarrow\infty$. The equation [II.66] is reduced to:

$$\vec{v}_{qs}\cdot\vec{\nabla}\,\psi_{qs}(r)=-\left(\vec{v}_{qs}\cdot\vec{\nabla}T\right)\frac{\partial n_{qs,0}/\partial T}{n_{qs,0}\left(n_{qs,0}+1\right)} \qquad \text{[II.67]}$$

The solution of this first-order differential equation can be expressed as:

$$\psi_{qs}(r)=\frac{\partial n_{qs,0}/\partial T}{n_{qs,0}(n_{qs,0}+1)}\left(\vec{\nabla}T\cdot r\right)+\delta \qquad \text{[II.68]}$$

where δ is a constant of integration. This can be found by introducing suitable boundary conditions, i.e.,

$$\psi_{qs}(r_B)\Big|_{v_n}=-p\psi_{q's}(r_B)\Big|_{-v_n} \qquad \text{[II.69]}$$

Which assumes that the fraction p of all the phonons arriving at the surface r_B are reflected with the normal velocity v_n reversed. For purely diffuse scattering $p=0$ and the boundary condition is set in zero. This represents the Casimir limit in which all the phonons lose the sense of their directionality and obey the equilibrium distribution. For pure diffusive case the equation [II.68] becomes:

$$n_{qs,0}\left(n_{qs,0}+1\right)\psi_{qs}(r)=\frac{\partial n_{qs,0}}{\partial T}\vec{\nabla}T\cdot\left(r-r_B\right) \qquad \text{[II.70]}$$

Using the definition of the flux [II.19] over a cross-sectional area S_c, the heat current is

$$QS_c = \frac{1}{N_0\Omega}\sum_{q,s}\int \hbar\omega_{qs}\psi_{qs}(r)n_{qs,0}\left(n_{qs,0}+1\right)v_{qs}dS_c \qquad \text{[II.71]}$$

$$= \frac{1}{N_0\Omega}\sum_{q,p}\int \hbar\omega_{qs}\frac{\partial n_{qs,0}}{\partial T}\vec{\nabla}T\cdot(r-r_B)v_{qs}\cdot dS_c \qquad \text{[II.72]}$$

$$= \frac{1}{N_0\Omega}\sum_{q,p}\int\int \hbar\omega_{qs}\frac{\partial n_{qs,0}}{\partial T}\left|\vec{\nabla}T\right|\left|(r-r_B)\right|\left|v_{qs}\right|\cos^2(\theta)dS_c d\Omega \qquad \text{[II.73]}$$

where $(r - r_B)$ points in the solid angle $d\Omega$ and θ is the angle between $(r - r_B)$ and ∇T, and between v_{qp} and dS_c. The phonon velocity, $(r - r_B)$ and ∇T are in the direction of dS_c. Grouping terms the equation [II.73] can express as:

$$Q = \frac{1}{3}C_V v_{qs}L_0\left|\vec{\nabla}T\right| = \kappa\left|\vec{\nabla}T\right| \qquad \text{[II.74]}$$

where L_0 represents an effective boundary mean free path in the Casimir limit.

$$L_0 = \frac{3}{4\pi S_c}\iint\left|r-r_B\right|\cos^2(\theta)d\Omega dS_c \qquad \text{[II.75]}$$

Similarly to include the effect of specular reflection ($p \neq 0$) and the expression [II.68] is modified as [7]:

$$\begin{aligned} n_{qs,0}\left(n_{qs,0}+1\right)\psi_{qs}(r) = \frac{\partial n_{qs,0}}{\partial T}\vec{\nabla}T\cdot\Big[(1-p)\big\{(r-r_B)+p(r-r'_B)\\ +p^2(r-r''_B)+\ldots\big\}\Big] \end{aligned} \qquad \text{[II.76]}$$

where r'_B, r''_B, etc, are the points on the surface where specular reflections would have taken place before the point is r_B reached. With this expression the effective boundary men free path becomes:

$$L = \frac{3}{4\pi S_c}\iint\Big[(1-p)\big\{\left|r-r_B\right|+p\left|r-r'_B\right|+p^2\left|r-r''_B\right|\big\}\Big]\cos^2(\theta)d\Omega dS_c \qquad \text{[II.77]}$$

If it is assumed that the average position of r is in the middle on the circular cross section (for cylindrical sample), then $|r - r'_B| = 3|r - r_B|$; $|r - r''_B| = 5|r - r_B|$, etc. Then, the series is transformed in:

$$|r - r_B|\{1 + 3p + 5p^2 + \ldots + (2n+1)p^n\} = 2\sum_{n=0} np^n + \sum_{n=0} p^n = \frac{p+1}{(1-p)^2} \qquad \text{[II.78]}$$

with $p < 1$, finally the equation [II.77] can be expressed as:

$$L = \frac{1+p}{1-p} L_0 \qquad \text{[II.79]}$$

Thus the boundary MFP becomes longer when specular reflections are presents. The factor p depends on surface conditions and also of the temperature. With decreasing the temperature the phonon wavelength increase and the surface appears smoother. The phonon relaxation rate due to boundary scattering can be expressed as:

$$\tau_{qp}^{-1}(bp) = v_{qp} / L \qquad \text{[II.80]}$$

here L represents an effective boundary MFP.

APPENDIX III: MODELING OF THERMAL TRANSPORT

In this appendix the simulation of the thermal properties will be presented. The thermal conductivity calculation was done in our group by using original codes developed with the commercial software MATLAB and Mathematica. The finite element simulations were modelled by using the commercial software COMSOL multiphysics.

III.1 Calculation of thermal conductivity

Nomenclature

κ_L	Lattice thermal conductivity
$\hbar$	Planck constant divided by 2π
T	Temperature
k_B	Boltzmann constant
q	Wavevector
s	Phonon polarization
v_{qs}	Group velocity
ω_{qs}	Phonon frequency
n_{qs}	Bose-Einstein equilibrium phonon distribution function
τ_{qs}	Total relaxation time
D_{qs}	Phonon density of states
L	Effective diameter of the bulk sample
Γ	Impurity scattering parameter
V_0	Volume per atom
γ_s	Grüneisen parameter
$\theta_{D,s}$	Debye temperature of polarization s
M	Atomic mass average
δ_s	Inverse of Knudsen number
d	Film thickness.

Λ_s	Bulk mean free path
p_q	Wavevector dependent specularity parameter
x	Integration variable

The thermal conductivity simulation of free-standing membranes was carried out, first, by deriving the lattice thermal conductivity in Si (or Ge) bulk system using the modified Callaway model under the single mode relaxation time approximation. Then, once the thermal conductivity for bulk Si (or Ge) is determined, we introduced the effect of finite size through Fuchs-Sondheimer boundary corrections.

$$\kappa_{bulk} = \frac{\hbar^2}{3k_B T^2} \sum_s \int v_{qs}^2 \omega_{qs}^2 \tau_{qs} n_{qs} (n_{qs} + 1) D_{qs} dq \qquad \text{[III.1]}$$

$$\frac{\kappa_{film}}{\kappa_{bulk}} = 1 - \frac{3}{2} \frac{(1-p_q)}{\delta_s} \int_1^{\infty} (x^{-3} - x^{-5}) \frac{1 - e^{-x\delta_s}}{1 - p_q e^{-x\delta_s}} dx \qquad \text{[III.2]}$$

where $p_q = \exp(-4(\eta\omega_{qs}/v_{qs})^2)$ is the fraction of phonons that are specularly reflected by the boundaries, D_{qs} is phonon density of states and $\delta_s = d/\Lambda_s$ is the inverse of Knudsen number.

The dispersion relation, ω_{qs}, was determinate applying an analytical form from a second-order polynomial fit to the experimental data for (100) direction:

$$\omega = Aq + Bq^2 \qquad \text{[III.3]}$$

with A and B constants determined via numerical fitting of experimental values. The total bulk, τ_{qs}, relaxation time for each polarization, s, is limited by various scattering mechanisms such as: boundary $\tau_{B,qs}$, mass defect $\tau_{I,qs}$ and Umklapp phonon-phonon interactions $\tau_{U,qs}$. This can be obtained via the Matthiessen's rule as

$$\tau_{q,s}^{-1} = \tau_{B,qs}^{-1} + \tau_{I,qs}^{-1} + \tau_{U,qs}^{-1} \qquad \text{[III.4]}$$

where the relaxation times $\tau_{B,qs}$, $\tau_{I,qs}$ and $\tau_{U,qs}$ are given by [117,212,213]:

$$\tau_{B,qs}^{-1} = \frac{v_{qs}}{L} \qquad \text{[III.5]}$$

$$\tau_{I,qs}^{-1} = \frac{V_0 \Gamma}{4\pi c_{qs}^{3}} \omega_{qs}^{4} \qquad \text{[III.6]}$$

$$\tau_{U,qs}^{-1} = \frac{\hbar \gamma_s^2}{M c_{qs}^2 \theta_{D,s}} \omega_{qs}^{2} \exp\left[-\theta_{D,s}/(3T)\right] \qquad \text{[III.7]}$$

Figure III.1*b* compares the thermal conductivity of bulk Si and Ge obtained by the Equation [III.1], from Eqs. [III.5] to [III.7] and substituting into Eq. [III.1], with reported experimental values [18], showing a good agreement. The main parameters used in the calculations are displayed in Table III.1.

Material	γ_L	γ_T	θ_L (K)	θ_T (K)	Γ (10^{-4})	L (mm)
Silicon	1.14	0.56	591	213	2.01	5.0
Germanium	1.14	0.56	330	117	5.88	4.8

Table III.1 *Silicon and Germanium parameters used in the calculations.*

With the thermal conductivity determined, the effect of the finite size is introduced using the Equation [III.2]. The surface roughness surface parameter, η, was fixed in 0.5 nm taken from the estimated value in Reference [23] for Si membranes.

In order to avoid the infinite limit of the Equation [III.2], we suggest a change of variables of the form:

$$x = (1+y)/(1-y) \qquad \text{[III.8]}$$

This mathematical trick turns the infinite range of integration, $x \in [1, \infty)$, into a finite range of integration in the new integration variable, $y \in [0, 1]$, i.e.,

$$\begin{aligned} y \to 0 &\Rightarrow x \to 1 \\ y \to 1 &\Rightarrow x \to \infty \end{aligned} \qquad \text{[III.9]}$$

Then, the new integral is given by:

$$\frac{\kappa_{film}}{\kappa_{bulk}} = 1 - \frac{3}{2}\frac{(1-p_q)}{\delta_s}\int_0^1 \left(f(y)^{-3} - f(y)^{-5}\right)\frac{1-e^{-f(y)\delta_s}}{1-p_q e^{-f(y)\delta_s}}\frac{2}{(1-y)^2}dy \qquad \text{[III.10]}$$

where $f(y) = (1+y)/(1-y)$ and the factor $2/(1-y)^2$ arises from the Jacobian associated to the change of variables.

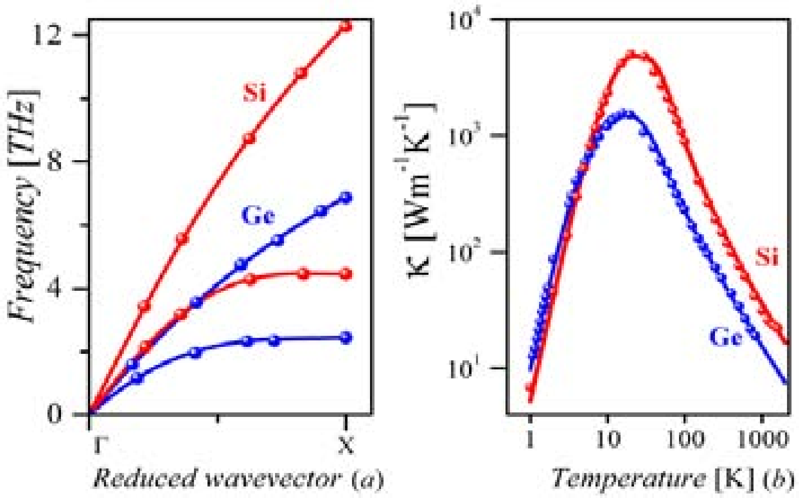

Figure III.1 *(a) Phonon dispersion relation of bulk silicon and germanium systems: experimental results (red and blue dots) from Ref.* [176] *and second-order polynomial fit (red and blue solid line). (b) Red and blue lines: calculated temperature-dependence of the lattice thermal conductivity of bulk silicon and germanium, respectively. Red and blue dots: the experimental data of silicon and germanium bulk respectively obtained from Ref.* [70]

III.2 Modelling of thermal transport: 2LRT and FEM simulations

To calculate the temperature distribution inside laser-heated Si membrane we must solve the two-dimensional heat flow equation illuminated by laser source, i.e., the heat source term is written as product of irradiance of the laser (the power carried by beam across a unit area perpendicular to the beam) and an exponential decay in the z direction, given by:

$$\kappa \nabla_r^2 T = -\alpha_0 (1-R) \frac{2P_I}{\pi b^2} \exp[-2r^2/b^2] \exp[-\alpha_0 z] \qquad \text{[III.11]}$$

where κ is the thermal conductivity, α_0 is the optical absorption coefficient[*], R the reflectance, P_I the total laser incident power and b the spot laser radius. Depending on the thickness of the sample the Equation [III.11] can be reduced to one-dimensional equation along radial direction with a uniformly distributed heat source along of z-direction:

$$\kappa \nabla_r^2 T = -\frac{(1-R-T)}{d} \frac{2P_I}{\pi b^2} \exp[-2r^2/b^2] \qquad \text{[III.12]}$$

where d is the thickness of the membrane. However, if the absorption of the sample is very high it is recommendable to use the Equation [III.11] instead of the Equation [III.12], this will depend of the thickness of the membrane, the wavelength of the heating laser and the material. In our case, we use a heater laser with a wavelength of 407 nm (~ 3.05 eV), as silicon has indirect band gap of ~ 1.1 eV the absorption of the light with wavelength near of the UV range is very high. In bulk silicon the penetration depth of a monochromatic light with wavelength of 407 nm is ~ 130 nm, i.e., the light intensity has fallen to ~ 36% (1/*e*) of its original value after travel 130 nm.

Figure III.2 shows the intensity decay of monochromatic light with wavelength of 407 nm as a function of the travelled distance in bulk silicon. Three different points at 250, 1000 and 2000 nm are included to rough comparison with the thicknesses of the studied membranes. In the inset of the Figure III.2 we can note that light intensity falls to ~ 13% of its original value after travel 250 nm, while for longer distance (> 500 nm) the light is completely absorbed.

Due to the membranes behave as optical cavities (Fabry-Pérot optical cavity) it is not possible compare directly the bulk absorption with the membranes and the multiple reflection effect have to be take into consideration. Figure III.3 shows the thickness-dependence of the absorptance (*A*), reflectance (*R*) and transmittance (*T*) of monochromatic light with wavelength of 407 nm. The simulations were performed by Dr Francesc Alzina by applying the laws of reflection and refraction in a plane-parallel slab and using the data for the dielectric function of bulk silicon for a monochromatic incident light of 407 nm at 300 K.

---

[*] The absorption coefficient, in general given in 1/cm, determinates the depth at which light of a certain wavelength penetrates a medium.

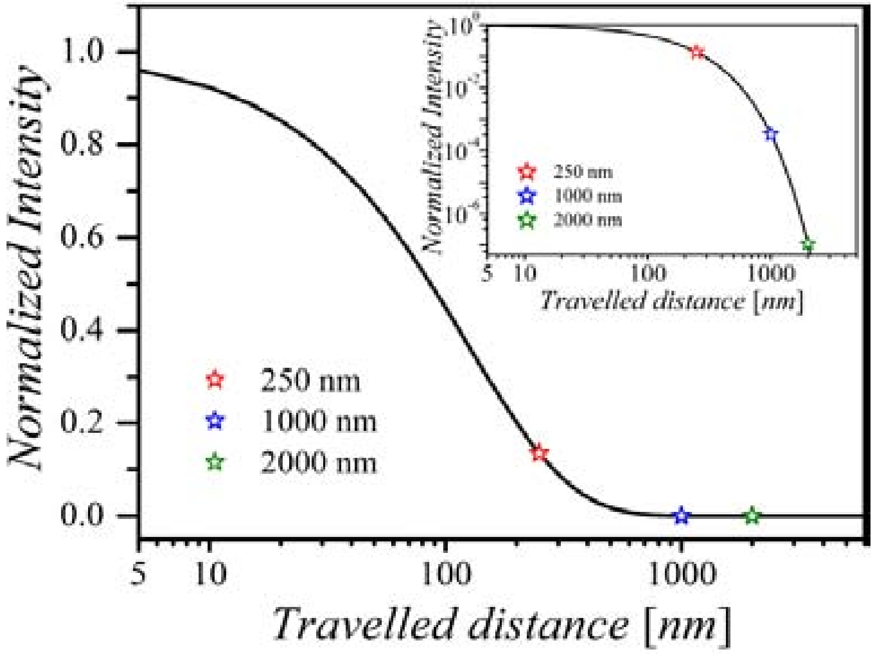

Figure III.2 *Normalized intensity of the monochromatic light with wavelength of 407 nm as a function of travelled distance in bulk silicon. Three different stars at 250 (red), 1000 (blue) and 2000 (green) nm are included to rough comparison with the thicknesses of the studied membranes. Inset: idem in double logarithmic scale for better visualization of the graph.*

From the Figure III.3*b* we can note that the values of the absorptance and reflectance for 1000 nm and 2000 nm thick membranes approaches to the bulk values, then the absorption coefficient, α_0, also approaches to the bulk values. This implies the incident light in the media will be absorbed totally in the first hundreds of nm of the travelled distance. Therefore, the assumption of a uniformly distributed heat source along z-direction it is not completely right in the thicker membranes. This forces us to use Equation [III.11] instead of the Equation [III.12].

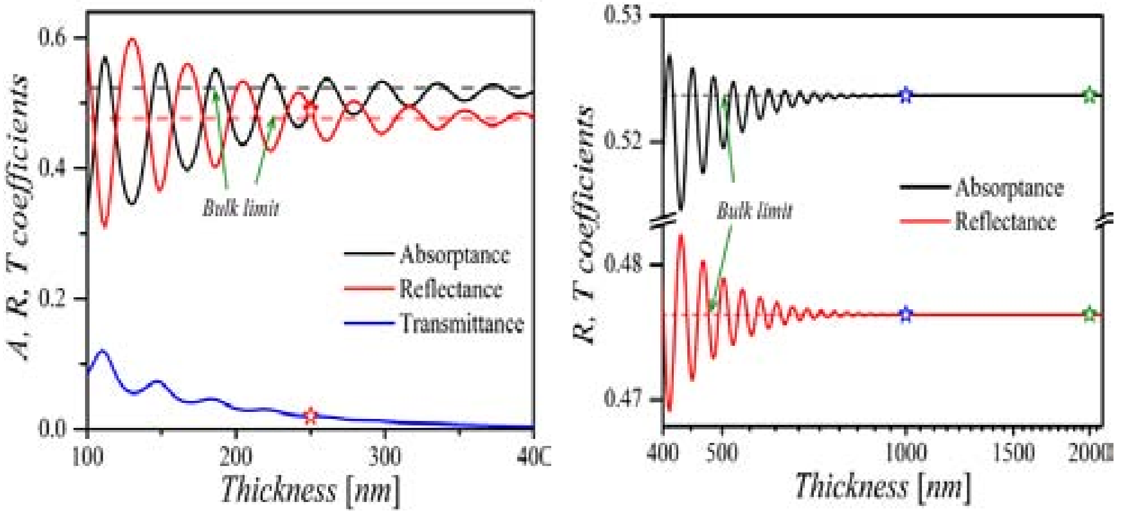

(*a*) (*b*)

Figure III.3 *Absorptance (A), reflectance (R), and transmittance (T) as a function of the thickness of the membranes. Solid black, red and blue lines are the calculated A, R and T coefficient considering the Fabry-Perot effect. For comparison the bulk limit of the A and R coefficients are shown in dashed grey and pink lines, respectively. Note that the oscillating behaviour is more appreciable at small thicknesses (a), while larger thicknesses the absorption reaches quietly the bulk values (b). Courtesy of Dr Francesc Alzina.*

Finally, the two-dimensional heat equation is solved using finite element method (FEM) of the commercial software COMSOL MultiPhysics (v4.3). The thermal conductivity of the membranes is assumed to be as:

$$\kappa_{film}(T) = \beta\kappa_{bulk}(T) \tag*{[III.13]}$$

where κ_{bulk} is the Si bulk thermal conductivity and β is a fitting factor that accounts for the reduction of the thermal conductivity of the membranes.

As is shown in the Figure III. 4, the thermal conductivity was determinate applying an analytical form from a second-order polynomial fit (solid blue line) to the experimental data silicon (red dots).

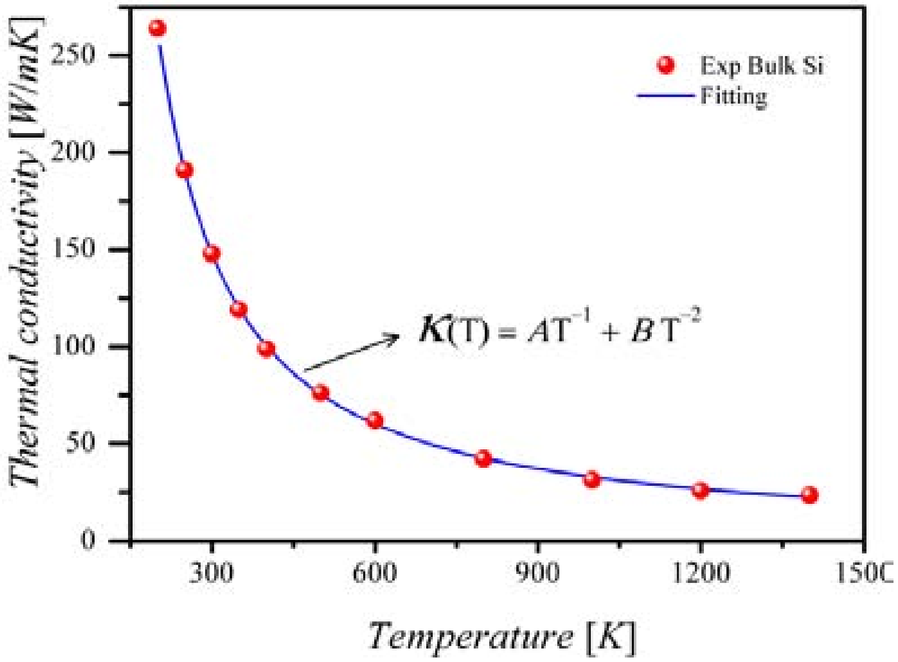

Figure III.4 *Temperature dependence of the bulk silicon thermal conductivity. The experimental data (red dots) were obtained from Ref.* [214]. *The solid blue line is a second-order polynomial adjust.*

The geometry of the sample used in the model is shown in Figure III.5*a*. A representative simulated temperature profile is displayed in Figure III.5*b*, where a circular membrane is heated in the centre by a Gaussian heating source. The temperature distribution on the membranes exhibits a maximum at the source position and gradually decays to room temperature towards the frame of the membrane, which is in contact with the substrate.

Finally the thermal conductivity of the membranes is obtained from the best fit between the experimental temperature profile and the simulated one.

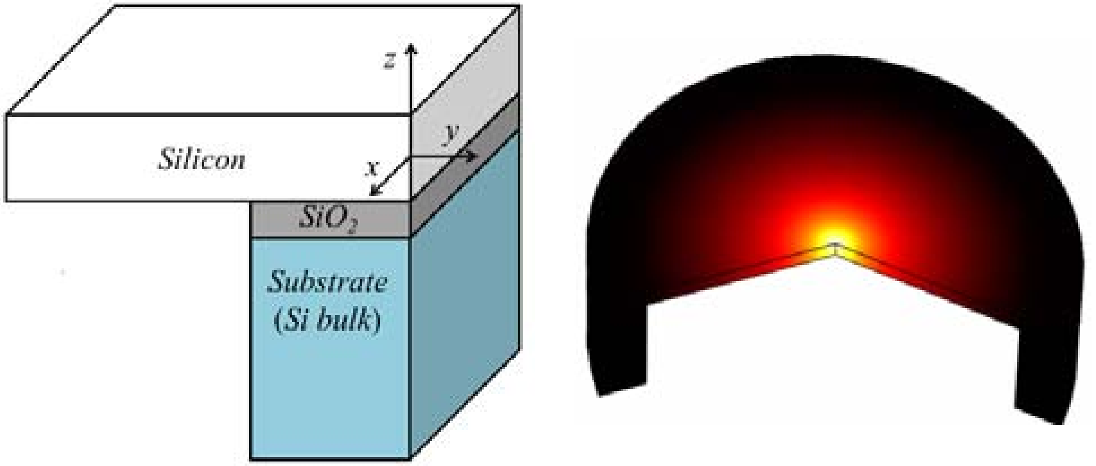
z
y
x
Silicon
SiO2
Substrate
(Si bulk)

(*a*) (*b*)

Figure III.5 *(a) Geometry of the sample used in the simulations. (b) Representative simulated temperature field.*

CURRICULUM VITAE

PERSONAL INFORMATION

- Place and birth date : Vallenar, Chile, December, 14th of 1985.
- Postal address : Carrer Sant Esteve 35b, Sant Cugat 08173, Barcelona, Spain.
- Phone (office) : +34 93 737 1615
- Personal phone number : +34 657407266
- E-mail : emigdio.chavez@icn.cat
  emigdio.chavez@gmail.com
- Google scholar profile : http://scholar.google.es/citations?user=-dHxodEAAAAJ&hl=es

ACADEMIC FORMATION

PhD student
2010-present. Universitat Autònoma de Barcelona and Catalan Institute of Nanoscience and Nanotechnology ICN2, Campus UAB, 08193 Bellaterra (Barcelona), Spain. Research project: "*Confined acoustics phonons in silicon nanomembranes: thermal properties*".

M.Sc. in Physics
2008-2010. Universidad Católica del Norte (UCN), Antofagasta, Chile. Master's thesis: "*Measurement of ferroelectric properties of barium titanate prepared by hydrothermal synthesis*"

B.A. in Physics with mention in Astronomy
2004-2008. Universidad Católica del Norte (UCN), Antofagasta, Chile.

FELLOWSHIPS AND AWARDS

- **2010.** Fellowship granted by National Commission for Scientific and Technological Research (CONICYT) to carry out PhD studies 2010-2014.
- **2009.** Fellowship granted by National Commission for Scientific and Technological Research (CONICYT) to carry out master studies during academic year 2009.
- **2008.** Outstanding student, Physics Department, Faculty of Sciences. Universidad Católica del Norte, Antogasta, Chile.
- **2008.** First graduate of my promotion, Universidad Católica del Norte, Antofagasta, Chile.
- **2004.** Financial Support from Educational Ministry, "Juan Gómez Millas Scholarship".

REFERENCES

[1] C. P. Poole and F. J. Owens, *Introduction to Nanotechnology* (John Wiley & Sons, 2003).

[2] M. Asheghi, Y. K. Leung, S. S. Wong, and K. E. Goodson, Appl. Phys. Lett. **71**, 1798 (1997).

[3] Y. S. Ju and K. E. Goodson, Appl. Phys. Lett. **74**, 3005 (1999).

[4] W. Liu and M. Asheghi, J. Appl. Phys. **98**, 123523 (2005).

[5] P. Chantrenne and J.-L. Barrat, Superlattices Microstruct. **35**, 173 (2004).

[6] M. Asheghi, M. N. Touzelbaev, K. E. Goodson, Y. K. Leung, and S. S. Wong, J. Heat Transfer **120**, 30 (1998).

[7] J. M. Ziman, *Electrons and Phonons: The Theory of Transport Phenomena in Solids* (Oxford University Press, USA, 1960).

[8] K. T. Regner, D. P. Sellan, Z. Su, C. H. Amon, A. J. H. McGaughey, and J. A. Malen, Nat. Commun. **4**, 1640 (2013).

[9] W. Bao, F. Miao, Z. Chen, H. Zhang, W. Jang, C. Dames, and C. N. Lau, Nat. Nanotechnol. **4**, 562 (2009).

[10] A. Shchepetov, M. Prunnila, F. Alzina, L. Schneider, J. Cuffe, H. Jiang, E. I. Kauppinen, C. M. Sotomayor Torres, and J. Ahopelto, Appl. Phys. Lett. **102**, 192108 (2013).

[11] D. Rugar, R. Budakian, H. J. Mamin, and B. W. Chui, Nature **430**, 329 (2004).

[12] J. Chaste, A. Eichler, J. Moser, G. Ceballos, R. Rurali, and A. Bachtold, Nat. Nanotechnol. **7**, 301 (2012).

[13] C. C. Striemer, T. R. Gaborski, J. L. McGrath, and P. M. Fauchet, Nature **445**, 749 (2007).

[14] P. Eriksson, J. Y. Andersson, and G. Stemme, J. Microelectromechanical Syst. **6**, 55 (1997).

[15] G. Siringo, E. Kreysa, A. Kovács, F. Schuller, A. Weiß, W. Esch, H.-P. Gemünd, N. Jethava, G. Lundershausen, A. Colin, R. Güsten, K. M. Menten, A. Beelen, F. Bertoldi, J. W. Beeman, and E. E. Haller, Astron. Astrophys. **497**, 945 (2009).

[16] D. Wilson, C. Regal, S. Papp, and H. Kimble, Phys. Rev. Lett. **103**, 207204 (2009).

[17] G. P. Srivastava, *The Physics of Phonons* (Taylor & Francis, 1990).

[18] N. Bannov, V. Aristov, V. Mitin, and M. A. Stroscio, Phys. Rev. B **51**, 9930 (1995).

[19] A. A. Balandin and K. L. Wang, J. Appl. Phys. **84**, 6149 (1998).

[20] M.-J. Huang, T.-M. Chang, C.-K. Liu, and C.-K. Yu, Int. J. Heat Mass Transf. **51**, 4470 (2008).

[21] J. Cuffe, E. Chávez, A. Shchepetov, P.-O. Chapuis, E. H. El Boudouti, F. Alzina, T. Kehoe, J. Gomis-Bresco, D. Dudek, Y. Pennec, B. Djafari-Rouhani, M. Prunnila, J. Ahopelto, and C. M. Sotomayor Torres, Nano Lett. **12**, 3569 (2012).

[22] E. Chávez, J. Cuffe, F. Alzina, and C. M. S. Torres, J. Phys. Conf. Ser. **395**, 012105 (2012).

[23] J. Cuffe, O. Ristow, E. Chávez, A. Shchepetov, P.-O. Chapuis, F. Alzina, M. Hettich, M. Prunnila, J. Ahopelto, T. Dekorsy, and C. M. Sotomayor Torres, Phys. Rev. Lett. **110**, 095503 (2013).

[24] A. Majumdar, Science **303**, 777 (2004).

[25] G. D. Mahan and H. B. Lyon, J. Appl. Phys. **76**, 1899 (1994).

[26] V. Goyal, D. Teweldebrhan, and A. A. Balandin, Appl. Phys. Lett. **97**, 133117 (2010).

[27] P. Ghaemi, R. S. K. Mong, and J. E. Moore, Phys. Rev. Lett. **105**, 166603 (2010).

[28] M. F. Silva, J. F. Ribeiro, J. P. Carmo, L. M. Gonçalves, and J. H. Correia, in *Scanning Probe Microscopy Nanoscience Nanotechnology 3*, edited by B. Bhushan (Springer Berlin Heidelberg, Berlin, Heidelberg, 2013), pp. 485–528.

[29] A. I. Boukai, Y. Bunimovich, J. Tahir-Kheli, J.-K. Yu, W. A. Goddard, and J. R. Heath, Nature **451**, 168 (2008).

[30] A. I. Hochbaum, R. Chen, R. D. Delgado, W. Liang, E. C. Garnett, M. Najarian, A. Majumdar, and P. Yang, Nature **451**, 163 (2008).

[31] K. Davami, J. S. Lee, and M. Meyyappan, Trans. Electr. Electron. Mater. (TEEM) **12**, 227 (2011).

[32] T. Markussen, Nano Lett. **12**, 4698 (2012).

[33] Z. Li, Q. Sun, X. D. Yao, Z. H. Zhu, and G. Q. (Max) Lu, J. Mater. Chem. **22**, 22821 (2012).

[34] D. Broido and T. Reinecke, Phys. Rev. B **51**, 13797 (1995).

[35] Z. Aksamija and I. Knezevic, in *2012 Int. Silicon-Germanium Technol. Device Meet.* (IEEE, 2012), pp. 1–2.

[36] S. Cecchi, T. Etzelstorfer, E. Müller, A. Samarelli, L. Ferre Llin, D. Chrastina, G. Isella, J. Stangl, and D. J. Paul, J. Mater. Sci. **48**, 2829 (2012).

[37] P. Jha, T. D. Sands, P. Jackson, C. Bomberger, T. Favaloro, S. Hodson, J. Zide, X. Xu, and A. Shakouri, J. Appl. Phys. **113**, 193702 (2013).

[38] J.-K. Yu, S. Mitrovic, D. Tham, J. Varghese, and J. R. Heath, Nat. Nanotechnol. **5**, 718 (2010).

[39] J. Tang, H.-T. Wang, D. H. Lee, M. Fardy, Z. Huo, T. P. Russell, and P. Yang, Nano Lett. **10**, 4279 (2010).

[40] I. El-Kady, M. F. Su, C. M. Reinke, P. E. Hopkins, D. Goettler, Z. C. Leseman, E. A. Shaner, and R. H. Olsson III, in *SPIE OPTO*, edited by A. Adibi, S.-Y. Lin, and A. Scherer (International Society for Optics and Photonics, 2011), pp. 794615–794615–9.

[41] P. E. Hopkins, L. M. Phinney, P. T. Rakich, R. H. Olsson, and I. El-Kady, Appl. Phys. A **103**, 575 (2010).

[42] C. M. Reinke, M. F. Su, B. L. Davis, B. Kim, M. I. Hussein, Z. C. Leseman, R. H. Olsson-III, and I. El-Kady, AIP Adv. **1**, 041403 (2011).

[43] E. Dechaumphai and R. Chen, J. Appl. Phys. **111**, 073508 (2012).

[44] A. Balandin and K. Wang, Phys. Rev. B **58**, 1544 (1998).

[45] D. Li, Y. Wu, P. Kim, L. Shi, P. Yang, and A. Majumdar, Appl. Phys. Lett. **83**, 2934 (2003).

[46] M.-J. Huang, T.-M. Chang, W.-Y. Chong, C.-K. Liu, and C.-K. Yu, Int. J. Heat Mass Transf. **50**, 67 (2007).

[47] I. J. Maasilta, AIP Adv. **1**, 041704 (2011).

[48] P. Hyldgaard and G. D. Mahan, in *Thermal Conductivity 23*, edited by K. E. Wilkes, R. B. Dinwiddie, and R. S. Graves (Technomics, 1996), pp. 172–182.

[49] W. Liu and M. Asheghi, Appl. Phys. Lett. **84**, 3819 (2004).

[50] G. H. Tang, Y. Zhao, G. X. Zhai, and C. Bi, J. Appl. Phys. **110**, 046102 (2011).

[51] J. Zou and A. Balandin, J. Appl. Phys. **89**, 2932 (2001).

[52] S. G. Walkauskas, D. A. Broido, K. Kempa, and T. L. Reinecke, J. Appl. Phys. **85**, 2579 (1999).

[53] J. Ma, B. R. Parajuli, M. G. Ghossoub, A. Mihi, J. Sadhu, P. V Braun, and S. Sinha, Nano Lett. **13**, 618 (2013).

[54] S. Grauby, E. Puyoo, J.-M. Rampnoux, E. Rouvière, and S. Dilhaire, J. Phys. Chem. C **117**, 9025 (2013).

[55] T. Claudio, G. Schierning, R. Theissmann, H. Wiggers, H. Schober, M. M. Koza, and R. P. Hermann, J. Mater. Sci. **48**, 2836 (2012).

[56] J. P. Feser, J. S. Sadhu, B. P. Azeredo, K. H. Hsu, J. Ma, J. Kim, M. Seong, N. X. Fang, X. Li, P. M. Ferreira, S. Sinha, and D. G. Cahill, J. Appl. Phys. **112**, 114306 (2012).

[57] A. M. Marconnet, T. Kodama, M. Asheghi, and K. E. Goodson, Nanoscale Microscale Thermophys. Eng. **16**, 199 (2012).

[58] J. M. Weisse, A. M. Marconnet, D. R. Kim, P. M. Rao, M. A. Panzer, K. E. Goodson, and X. Zheng, Nanoscale Res. Lett. **7**, 554 (2012).

[59] B. Kim, J. Nguyen, P. J. Clews, C. M. Reinke, D. Goettler, Z. C. Leseman, I. El-Kady, and R. H. Olsson, in *2012 IEEE 25th Int. Conf. Micro Electro Mech. Syst.* (IEEE, 2012), pp. 176–179.

[60] J. Fang, C. B. Kang, Y. Huang, S. H. Tolbert, and L. Pilon, J. Phys. Chem. C **116**, 12926 (2012).

[61] X. Liu, X. Wu, and T. Ren, Appl. Phys. Lett. **98**, 174104 (2011).

[62] Z. Wang, J. E. Alaniz, W. Jang, J. E. Garay, and C. Dames, Nano Lett. **11**, 2206 (2011).

[63] G. S. Doerk, C. Carraro, and R. Maboudian, ACS Nano **4**, 4908 (2010).

[64] M. Schmotz, P. Bookjans, E. Scheer, and P. Leiderer, Rev. Sci. Instrum. **81**, 114903 (2010).

[65] Z. Hao, L. Zhichao, T. Lilin, T. Zhimin, L. Litian, and L. Zhijian, in *2006 8th Int. Conf. Solid-State Integr. Circuit Technol. Proc.* (IEEE, 2006), pp. 2196–2198.

[66] Y. S. Ju, Appl. Phys. Lett. **87**, 153106 (2005).

[67] P. G. Klemens, Proc. R. Soc. A Math. Phys. Eng. Sci. **208**, 108 (1951).

[68] J. Callaway, Phys. Rev. **113**, 1046 (1959).

[69] A. H. Nayfeh, *North-Holland Series in Applied Mathematics and Mechanics Vol. 39: Wave Propagation in Layered Anisotropic Mediawith Applications to Composites* (North-Holland, 1995).

[70] C. J. Glassbrenner and Glen A. Slack, Phys. Rev. **134**, 1058 (1964).

[71] A. AlShaikhi and G. Srivastava, Phys. Rev. B **76**, 195205 (2007).

[72] N. W. Ashcroft and N. D. Mermin, *Solid State Physics* (Saunders College, 1976).

[73] G. Agrawal, *Nonlinear Fiber Optics* (Academic Press, New York, 2001).

[74] L. Rayleigh, Proc. London Math. Soc. **s1-17**, 4 (1885).

[75] H. Lamb, Proc. R. Soc. A Math. Phys. Eng. Sci. **93**, 114 (1917).

[76] G. Fasol, M. Tanaka, H. Sakaki, and Y. Horikoshi, Phys. Rev. B **38**, 6056 (1988).

[77] M. Grimsditch, R. Bhadra, and I. Schuller, Phys. Rev. Lett. **58**, 1216 (1987).

[78] X. Zhang, R. Sooryakumar, and K. Bussmann, Phys. Rev. B **68**, 115430 (2003).

[79] C. M. Sotomayor Torres, A. Zwick, F. Poinsotte, J. Groenen, M. Prunnila, J. Ahopelto, A. Mlayah, and V. Paillard, Phys. Status Solidi **1**, 2609 (2004).

[80] C. Kittel, *Introduction to Solid State Physics* (Wiley, 2004).

[81] B. Max and K. Huang, *Dynamical Theory of Crystal Lattices* (Oxford University Press on Demand, 1954).

[82] B. A. Auld, *Acoustic Fields and Waves in Solids* (Wiley, Florida, 1973).

[83] M. Sadd, *Elasticity Theory, Applications, and Numerics* (Academic Press, Oxfrord, 2004).

[84] J. L. Rose, *Ultrasonic Waves in Solid Media* (Cambridge University Press, 2004).

[85] A. E. H. Love, *Some Problems of Geodynamics: Being an Essay to Which the Adams Prize in the University of Cambridge Was Adjudged in 1911* (Cambridge University Press, Cambridge, 1967).

[86] K. Sezawa, Tokyo Bull. Earthq. Res. Inst. **3**, 1 (1927).

[87] T. Kühn and I. J. Maasilta, J. Phys. Conf. Ser. **92**, 012082 (2007).

[88] R. Stoneley, Proc. R. Soc. A Math. Phys. Eng. Sci. **106**, 416 (1924).

[89] W. T. Thomson, J. Appl. Phys. **21**, 89 (1950).

[90] L. Knopoff, Bull. Seismol. Soc. Am. **54**, 431 (1964).

[91] L. Donetti, F. Gámiz, J. B. Roldán, and A. Godoy, J. Appl. Phys. **100**, 013701 (2006).

[92] R. Peierls, Ann. Phys. **395**, 1055 (1929).

[93] R. Nava, R. Azrt, I. Ciccarello, and K. Dransfeld, Phys. Rev. **134**, A581 (1964).

[94] R. Nava, R. Callarotti, H. Ceva, and A. Martinet, Phys. Rev. **185**, 1177 (1969).

[95] H. J. Maris, Philos. Mag. **9**, 901 (1964).

[96] D. Ecsedy and P. Klemens, Phys. Rev. B **15**, 5957 (1977).

[97] N. W. Ashcroft and N. D. Mermin, *Solid State Physics* (Saunders College, 1976).

[98] J. E. Parrott, Proc. Phys. Soc. **81**, 726 (1963).

[99] G. P. Srivastava, Pramana **3**, 209 (1974).

[100] G. P. Srivastava, Philos. Mag. **34**, 795 (1976).

[101] O. Madelung, U. Rössler, and M. Schulz, editors, *Group IV Elements, IV-IV and III-V Compounds. Part a - Lattice Properties* (Springer-Verlag, Berlin/Heidelberg, 2001).

[102] D. T. Morelli and G. A. Slack, in *High Thermal Conductivity Materials*, edited by S. L. Shindé and J. S. Goela (Springer-Verlag, New York, 2006), pp. 37–68.

[103] H. J. McSkimin and P. Andreatch, J. Appl. Phys. **35**, 2161 (1964).

[104] M. Holland, Phys. Rev. **132**, 2461 (1963).

[105] L. D. Landau and G. Rumer, Phys. Z. Sowjet. **11**, 18 (1937).

[106] A. Akhieser, J. Phys. USSR **1**, 277 (1939).

[107] H. J. Maris, in *Physical Acoustics: Principles and Methods*, edited by W. P. Mason and R. N. Thurston (Academic Press, 1971), pp. 279–345.

[108] B. C. Daly, K. Kang, Y. Wang, and D. G. Cahill, Phys. Rev. B **80**, 174112 (2009).

[109] A. S. Nowick and B. S. Berry, in *Anelastic Relaxation in Crystalline Solids* (Academic Press, New York & London, 1972), pp. 493–523.

[110] G. G. Sahasrabudhe, J. Acoust. Soc. Am. **104**, 81 (1998).

[111] G. G. Sahasrabudhe and S. D. Lambade, J. Phys. Chem. Solids **60**, 773 (1999).

[112] T. Woodruff and H. Ehrenreich, Phys. Rev. **123**, 1553 (1961).

[113] P. Debye, Ann. Phys. **344**, 789 (1912).

[114] J. D. Chung, A. J. H. McGaughey, and M. Kaviany, J. Heat Transfer **126**, 376 (2004).

[115] P. E. Hopkins, P. T. Rakich, R. H. Olsson, I. F. El-kady, and L. M. Phinney, Appl. Phys. Lett. **95**, 161902 (2009).

[116] G. P. Srivastava, MRS Bull. **26**, 445 (2011).

[117] H. B. G. Casimir, Physica **5**, 495 (1938).

[118] A. C. B. Lovell, Proc. R. Soc. A Math. Phys. Eng. Sci. **157**, 311 (1936).

[119] J. J. Thomson, Proc. Cambridge Philos. Soc. **11**, 120 (1901).

[120] K. Fuchs, Math. Proc. Cambridge Philos. Soc. **34**, 100 (1938).

[121] R. G. Chambers, Proc. R. Soc. A Math. Phys. Eng. Sci. **202**, 378 (1950).

[122] E. H. Sondheimer, Adv. Phys. **1**, 1 (1952).

[123] D. Stewart and P. M. Norris, Microscale Thermophys. Eng. **4**, 89 (2000).

[124] X. Lü, W. Z. Shen, and J. H. Chu, J. Appl. Phys. **91**, 1542 (2002).

[125] R. S. Prasher and P. e. Phelan, Int. J. Heat Mass Transf. **42**, 1991 (1998).

[126] K. Johnson, M. Wybourne, and N. Perrin, Phys. Rev. B **50**, 2035 (1994).

[127] T. Iida, T. Itoh, D. Noguchi, and Y. Takano, J. Appl. Phys. **87**, 675 (2000).

[128] M. M. Roberts, L. J. Klein, D. E. Savage, K. A. Slinker, M. Friesen, G. Celler, M. A. Eriksson, and M. G. Lagally, Nat. Mater. **5**, 388 (2006).

[129] G. Gopalakrishnan, D. A. Czaplewski, K. M. McElhinny, M. V. Holt, J. C. Silva-Martínez, and P. G. Evans, Appl. Phys. Lett. **102**, 033113 (2013).

[130] D. Wang, H. Nakashima, J. Morioka, and T. Kitamura, Appl. Phys. Lett. **91**, 241918 (2007).

[131] W. Demtröder, *Laser Spectroscopy: Vol. 1: Basic Principles* (Springer, 2008).

[132] G. Benedek and K. Fritsch, Phys. Rev. **149**, 647 (1966).

[133] R. Loudon and J. R. Sandercock, J. Phys. C Solid State Phys. **13**, 2609 (1980).

[134] S. M. Lindsay, M. W. Anderson, and J. R. Sandercock, Rev. Sci. Instrum. **52**, 1478 (1981).

[135] J. R. Sandercock, Opt. Commun. **2**, 73 (1970).

[136] J. Cuffe, Phonon-Photon Interactions in Nanostructures, National University of Ireland, Cork, 2011.

[137] J. Cuffe, E. Chávez, A. Shchepetov, P.-O. Chapuis, E. H. El Boudouti, F. Alzina, Y. Pennec, B. Djafari-Rouhani, M. Prunnila, J. Ahopelto, and C. M. Sotomayor Torres, in *Vol. 9 Micro- Nano-Systems Eng. Packag. Parts A B* (ASME, 2012), p. 1081.

[138] Q. P. Unterreithmeier, T. Faust, and J. P. Kotthaus, Phys. Rev. Lett. **105**, 027205 (2010).

[139] J.-Y. Duquesne and B. Perrin, Phys. Rev. B **68**, 134205 (2003).

[140] T.-M. Liu, S.-Z. Sun, C.-F. Chang, C.-C. Pan, G.-T. Chen, J.-I. Chyi, V. Gusev, and C.-K. Sun, Appl. Phys. Lett. **90**, 041902 (2007).

[141] O. B. Wright and V. E. Gusev, Appl. Phys. Lett. **66**, 1190 (1995).

[142] C. Thomsen, J. Strait, Z. Vardeny, H. Maris, J. Tauc, and J. Hauser, Phys. Rev. Lett. **53**, 989 (1984).

[143] C. Thomsen, H. Grahn, H. Maris, and J. Tauc, Phys. Rev. B **34**, 4129 (1986).

[144] T. Zhu, H. Maris, and J. Tauc, Phys. Rev. B **44**, 4281 (1991).

[145] G. Rozas, M. F. P. Winter, B. Jusserand, A. Fainstein, B. Perrin, E. Semenova, and A. Lemaître, Phys. Rev. Lett. **102**, 15502 (2009).

[146] A. Bartels, R. Cerna, C. Kistner, A. Thoma, F. Hudert, C. Janke, and T. Dekorsy, Rev. Sci. Instrum. **78**, 35107 (2007).

[147] X. Zhang and C. P. Grigoropoulos, Rev. Sci. Instrum. **66**, 1115 (1995).

[148] D. Cahill, M. Katiyar, and J. Abelson, Phys. Rev. B **50**, 6077 (1994).

[149] M. G. Burzo, P. L. Komarov, and P. E. Raad, in *ITherm 2002. Eighth Intersoc. Conf. Therm. Thermomechanical Phenom. Electron. Syst. (Cat. No.02CH37258)* (IEEE, 2002), pp. 142–149.

[150] M. G. Burzo, P. L. Komarov, and P. E. Raad, Microelectronics J. **33**, 697 (2002).

[151] A. J. Schmidt, R. Cheaito, and M. Chiesa, Rev. Sci. Instrum. **80**, 094901 (2009).

[152] J. E. Graebner, Rev. Sci. Instrum. **66**, 3903 (1995).

[153] R. T. Swimm, Appl. Phys. Lett. **42**, 955 (1983).

[154] T. E. Beechem and J. R. Serrano, Spectroscopy **26**, 36 (2011).

[155] T. Hart, R. Aggarwal, and B. Lax, Phys. Rev. B **1**, 638 (1970).

[156] J. Menéndez and M. Cardona, Phys. Rev. B **29**, 2051 (1984).

[157] T. Hart, R. Aggarwal, and B. Lax, Phys. Rev. B **1**, 638 (1970).

[158] I. H. Campbell and P. M. Fauchet, Solid State Commun. **58**, 739 (1986).

[159] P. Mishra and K. Jain, Phys. Rev. B **62**, 14790 (2000).

[160] J. Camassel, L. Falkovsky, and N. Planes, Phys. Rev. B **63**, 035309 (2000).

[161] E. Chávez, S. Fuentes, R. A. Zarate, and L. Padilla-Campos, J. Mol. Struct. **984**, 131 (2010).

[162] S. Périchon, V. Lysenko, B. Remaki, D. Barbier, and B. Champagnon, J. Appl. Phys. **86**, 4700 (1999).

[163] S. Huang, X. Ruan, X. Fu, and H. Yang, J. Zhejiang Univ. Sci. A **10**, 7 (2009).

[164] S. Huang, X. Ruan, J. Zou, X. Fu, and H. Yang, Microsyst. Technol. **15**, 837 (2009).

[165] M. E. Siemens, Q. Li, R. Yang, K. A. Nelson, E. H. Anderson, M. M. Murnane, and H. C. Kapteyn, Nat. Mater. **9**, 26 (2010).

[166] C. Chiritescu, D. G. Cahill, N. Nguyen, D. Johnson, A. Bodapati, P. Keblinski, and P. Zschack, Science **315**, 351 (2007).

[167] G. Chen, D. Borca-Tasciuc, and R. G. Yang, Encycl. Nanosci. Nanotechnology, **7**, 429 (2004).

[168] R. Chen, A. I. Hochbaum, P. Murphy, J. Moore, P. Yang, and A. Majumdar, Phys. Rev. Lett. **101**, 105501 (2008).

[169] C. Chang, D. Okawa, H. Garcia, A. Majumdar, and A. Zettl, Phys. Rev. Lett. **101**, 075903 (2008).

[170] C. Chen, N. Hayazawa, and S. Kawata, Nat. Commun. **5**, 3312 (2014).

[171] A. Hartschuh, Angew. Chem. Int. Ed. Engl. **47**, 8178 (2008).

[172] D. Kan, T. Terashima, R. Kanda, A. Masuno, K. Tanaka, S. Chu, H. Kan, A. Ishizumi, Y. Kanemitsu, Y. Shimakawa, and M. Takano, Nat. Mater. **4**, 816 (2005).

[173] J. A. Johnson, A. A. Maznev, J. Cuffe, J. K. Eliason, A. J. Minnich, T. Kehoe, C. M. Sotomayor Torres, G. Chen, and K. A. Nelson, Phys. Rev. Lett. **110**, 025901 (2013).

[174] X. Zhang, R. Bandhu, R. Sooryakumar, and B. Jonker, Phys. Rev. B **67**, 075407 (2003).

[175] B. Graczykowski, S. Mielcarek, A. Trzaskowska, J. Sarkar, P. Hakonen, and B. Mroz, Phys. Rev. B **86**, 085426 (2012).

[176] O. Madelung, U. Rössler, and M. Schulz, editors, *Collaboration: Authors and Editors of the LB Volumes III/17A-22A-41A1b: Germanium (Ge), Sound Velocities.* (Springer-Verlag, Berlin/Heidelberg, 2002).

[177] N. Mingo and D. Broido, Phys. Rev. Lett. **95**, 096105 (2005).

[178] M. M. Sadeghi, M. T. Pettes, and L. Shi, Solid State Commun. **152**, 1321 (2012).

[179] F. Hudert, A. Bruchhausen, D. Issenmann, O. Schecker, R. Waitz, A. Erbe, E. Scheer, T. Dekorsy, A. Mlayah, and J.-R. Huntzinger, Phys. Rev. B **79**, 201307 (2009).

[180] A. Bruchhausen, R. Gebs, F. Hudert, D. Issenmann, G. Klatt, A. Bartels, O. Schecker, R. Waitz, A. Erbe, E. Scheer, J.-R. Huntzinger, A. Mlayah, and T. Dekorsy, Phys. Rev. Lett. **106**, 77401 (2011).

[181] J. Hasson and A. Many, Phys. Rev. Lett. **35**, 792 (1975).

[182] A. A. Maznev, F. Hofmann, A. Jandl, K. Esfarjani, M. T. Bulsara, E. A. Fitzgerald, G. Chen, and K. A. Nelson, Appl. Phys. Lett. **102**, 041901 (2013).

[183] A. E. Duwel, J. Lozow, C. J. Fisher, T. Phillips, R. H. Olsson, and M. Weinberg, in *Proc. SPIE 8031, Micro- Nanotechnol. Sensors, Syst. Appl. III, 80311C (May 13, 2011)* (2011), p. 80311C–80311C–14.

[184] J. Cuffe, J. K. Eliason, A. Maznev, K. C. Collins, J. Johnson, A. Shchepetov, M. Prunnila, J. Ahopelto, C. M. Sotomayor Torres, G. Chen, and K. A. Nelson, Unpubl. Results (2014).

[185] E. Chávez-Ángel, J. S. Reparaz, J. Gomis-Bresco, M. R. Wagner, J. Cuffe, B. Graczykowski, A. Shchepetov, H. Jiang, M. Prunnila, J. Ahopelto, F. Alzina, and C. M. Sotomayor Torres, APL Mater. **2**, 012113 (2014).

[186] J. S. Reparaz, E. Chavez-Angel, M. R. Wagner, B. Graczykowski, J. Gomis-Bresco, F. Alzina, and C. M. Sotomayor Torres, Rev. Sci. Instrum. **85**, 034901 (2014).

[187] J. Gomis-Bresco, D. Navarro-Urrios, M. Oudich, S. El-Jallal, A. Griol, D. Puerto, E. Chavez, Y. Pennec, B. Djafari-Rouhani, F. Alzina, A. Martínez, and C. M. Sotomayor Torres, arXiv:1401.1691v2 (2014).

[188] J. Šik, J. Hora, and J. Humlíček, J. Appl. Phys. **84**, 6291 (1998).

[189] O. Madelung, U. Rössler, and M. Schulz, editors, *Group IV Elements, IV-IV and III-V Compounds. Part a - Lattice Properties* (Springer-Verlag, Berlin/Heidelberg, 2001).

[190] J. P. Freedman, J. H. Leach, E. A. Preble, Z. Sitar, R. F. Davis, and J. A. Malen, Sci. Rep. **3**, 2963 (2013).

[191] B. Abeles, D. Beers, G. Cody, and J. Dismukes, Phys. Rev. **125**, 44 (1962).

[192] P. Türkes, Phys. Status Solidi **75**, 519 (1983).

[193] M. N. Wyboune, in *Properties of Crystalline Silicon*, edited by R. Hull (IET, London, 1999), pp. 168–169.

[194] N. A. Roberts and D. G. Walker, Int. J. Therm. Sci. **50**, 648 (2011).

[195] G. F. C. Rogers, Int. J. Heat Mass Transf. **2**, 150 (1961).

[196] R. W. Powell, R. P. Tye, and B. W. Jolliffe, Int. J. Heat Mass Transf. **5**, 897 (1962).

[197] A. M. Clausing, Int. J. Heat Mass Transf. **9**, 791 (1966).

[198] M. Terraneo, M. Peyrard, and G. Casati, Phys. Rev. Lett. **88**, 094302 (2002).

[199] J. Lee, V. Varshney, A. K. Roy, J. B. Ferguson, and B. L. Farmer, Nano Lett. **12**, 3491 (2012).

[200] C. W. Chang, D. Okawa, A. Majumdar, and A. Zettl, Science **314**, 1121 (2006).

[201] W. Kobayashi, Y. Teraoka, and I. Terasaki, Appl. Phys. Lett. **95**, 171905 (2009).

[202] C. Dames, J. Heat Transfer **131**, 061301 (2009).

[203] D. B. Go and M. Sen, J. Heat Transfer **132**, 124502 (2010).

[204] J. R. Drabble, in *Semicondtor and Semimetals Vol 2*, edited by R. K. Willardson and A. C. Beer (Academic Press Inc, 1966), pp. 75–114.

[205] V. E. Sauma, *Lectrures Notes: Introduction to Continuum Mechanics and Elements of Elasticity/structural Mechanics*, Draft (University of Colorado, 1998).

[206] D. S. Chandrasekharaiah and L. Debnath, *Continuum Mechanics* (Academic Press, New York, 1994).

[207] R. K. Pathria and P. D. Beale, *Statistical Mechanics* (Academic Press, 2011), p. 744.

[208] M. N. Ozisik, *Heat Conduction* (Wiley, 1993).

[209] A. A. Joshi and A. Majumdar, J. Appl. Phys. **74**, 31 (1993).

[210] M. Asen-Palmer, K. Bartkowski, E. Gmelin, M. Cardona, A. Zhernov, A. Inyushkin, A. Taldenkov, V. Ozhogin, K. Itoh, and E. Haller, Phys. Rev. B **56**, 9431 (1997).

[211] D. Baillis and J. Randrianalisoa, Int. J. Heat Mass Transf. **52**, 2516 (2009).

[212] P. G. Klemens, Proc. Phys. Soc. Sect. A **68**, 1113 (1955).

[213] G. Slack and S. Galginaitis, Phys. Rev. **133**, A253 (1964).

[214] D. Morelli, J. Heremans, and G. Slack, Phys. Rev. B **66**, 195304 (2002).